eman ta zabal zazu

Universidad del País Vasco

Euskal Herriko Unibertsitatea

University of the Basque Country

Ph. D. Thesis

Design and development of mixed metal oxides for high temperature thermochemical energy storage in active thermal barrier coating applications

Yasmina Portilla Nieto

Bilbao, September 2022

CIC energiGUNE

MEMBER OF BASQUE RESEARCH & TECHNOLOGY ALLIANCE

Tekniker

MEMBER OF BASQUE RESEARCH & TECHNOLOGY ALLIANCE

eman ta zabal zazu
UPV EHU
ZIENTZIA ETA TEKNOLOGIA FAKULTATEA
FACULTAD DE CIENCIA Y TECNOLOGÍA
50 URTE AÑOS 1968 - 2018
Biba Zientzia! Ciencia Viva

Departamento de Física

Programa de Doctorado:

Física

Physics

Ph. D. Thesis

Design and development of mixed metal oxides for high temperature thermochemical energy storage in active thermal barrier coating applications

Presented by:

Yasmina Portilla Nieto

Supervisors:

Dr. Stefania Doppiu

Dr. Estibaliz Aranzabe Basterrechea

A mis padres,

a mi abuela

“In three words

I can sum up everything

I have learned about life:

It goes on.”

-Robert Frost-

Acknowledgements

As most of the people who have accompanied me on this trip are Spanish speakers, let me write most of these part in Spanish.

Llegado el momento de redactar estas líneas me acuerdo de todos los compañeros, familiares y amigos que me han acompañado en esta travesía, complicada en algunos momentos puntuales, pero también gratificante.

Quería empezar acordándome de los dos centros que me dieron la oportunidad de realizar la tesis: CIC energiGUNE y TEKNIKER. Gracias a CIC energiGUNE por todo el apoyo mostrado, tanto personal como profesional, y por todos los recursos dedicados a la consecución de este trabajo. Gracias a TEKNIKER por depositar su confianza en mí para realizar esta tesis y por poner a mi alcance todos los recursos necesarios.

Este trabajo no hubiera sido posible sin la supervisión de mis directoras Stefania Doppiu y Estibaliz Aranzabe. Gracias por el esfuerzo y dedicación mostrado durante todo el camino. Gracias Esti por guiar el timón cuando parecía que todo se venía abajo y por protegerme. Gracias Stefania por acomodarte a la dirección de la tesis siguiendo las líneas pautadas y mejorando el trabajo. Otra persona que ha sido parte fundamental en la consecución de esta tesis es Elena Palomo. Gracias Elena por facilitar el cambio de dirección haciendo que yo prácticamente no tuviera consecuencias y por aportar un prisma resolutivo al trabajo. Ha sido un placer trabajar con vosotras.

Infinitas gracias a mi tutor en la Universidad del País Vasco (UPV/EHU), Gabriel Alejandro López por guiarme y por facilitarme tanto todos los temas

burocráticos. Gracias a todo el departamento de Física por el apoyo y la dedicación mostrada durante este periodo.

I would also like to thank the German Aerospace Center (DLR) for the treatment and support received during my stay in Stuttgart. Especially, I would like to thank Dr.-Ing. Marc Linder, for his absolute dedication and personal support received, both before, during and after the stay. It has been a pleasure to work with you Marc. I would not want to forget my co-workers Christian Brack and Julian Kaess, without whom it would have been impossible to achieve results. Thanks also to the rest of my colleagues who made my stay there very pleasant.

On behalf of CIC energiGUNE, I would like to thank Ali for guiding me during that first year. I was fortunate to be able to work with you and learn a lot of things from you both personally and professionally. Thanks also to Abdo for that first year. I felt really comfortable working with you. Gracias especiales a Sergio (compañero y amigo infatigable de batallas diurnas y nocturnas), a Leticia, Yagmur, Cristina, Mikel I, Angel, Mikel D., Asier O., Dani, Luis, Iñigo, Yarik, Peru, Francesco, María, etc. ¡¡Gracias a todo TES!! Ha sido un placer trabajar y convivir con vosotros.

Por parte de TEKNIKER quería agradecer especialmente a las personas que han estado conmigo incansablemente: Amaia, Haizea, Cris e Itzi. Llegar a trabajar y encontrarte con gente que te quiere y apoya personal y profesionalmente de esa manera es un privilegio. ¡Os adoro! Señor Alberto Villar, gracias por toda esa sabiduría durante los descansos. Me llevo otro libro de frases célebres. Nere, gracias por todo el soporte con la TGA, trabajar contigo es genial, eres la reina del laboratorio. Gracias a Iker Elexpe y Jon Etxarri, sin los que ese recubrimiento no hubiera quedado tan bien. Gracias al resto de mis compañeros de QSN por toda la ayuda y los los momentos vividos: Angela, Esti G, Marta, Vane, Karmele, Aritz R, Eneko, Leire, etc.

A mis chicos de la Palapa, en especial a Alba, Beatriz y Mikel, por apoyarme y dejarme ser, sin presionar y sin juzgar. ¡Os adoro!

A mi gente de Justel, en especial a Aldara (la mejor diseñadora de portadas), Silvia (compañera de tantas y tantas cosas), Adrián (mi mejor psicólogo), David (si, lee que sí que estás, simpático, no podías faltar en estas líneas), Rubén (aunque a veces quieras matarme) y Johny (aunque quieras ponerme a hacer rutas "graciosas" por el monte). Pasar tiempo con vosotros en el mejor lugar del mundo es oro. Gracias por todo el apoyo, consejos y anécdotas vividas.

A mi familia, en especial a mis Nieto's: Melanie, Lidia, Daniel, Nerea, Pablo, Ander y Martin. Os quiero.

Adrián, lo mejor que me llevo de este camino eres tú. Gracias por todo el cariño, la ayuda, el apoyo y el aguante todo este tiempo. Te quiero hasta en modo nubarrón.

A alguien que ya no está, pero que si viera esto estaría muy feliz y orgullosa. Abuela, allá donde estés, esta va por ti. Te quiero.

Por último y más importante, mi más sincero agradecimiento a las personas más importantes de mi vida, a mis padres, Iñaki y Charo, sin los que nada de esto hubiera sido posible. Mil gracias por inculcarme estos valores y esta educación recibida. Gracias por darme los medios (con mucho esfuerzo y sacrificio) para poder llegar hasta aquí. Os quiero mucho.

Abstract

Thermal storage technologies (TES) will play a major role in the integration of renewable energies and in the increase of the industrial processes' efficiency. Among them, thermochemical storage (TcES) is the least developed, as it is mostly at laboratory scale, being one of the most promising due to: (i) it covers a wide temperature range, (ii) it has high energy densities, (iii) heat can be stored at room temperature and (iv) heat is released at constant temperature, being adjustable according to reaction conditions.

Thus, the endothermic reaction is used to store heat when it is available and the exothermic reaction is used to release that heat when it is needed. In this regard, Redox reactions of metal oxides have been widely studied for high temperature TES applications. These Redox systems require suitable materials in terms of (i) complete reversibility, (ii) suitable reaction temperature, (iii) high energy density, (iv) high reaction enthalpy, (v) no-toxicity and (vi) good thermal stability during cycling in the temperature range of the application.

Traditionally, high-temperature thermochemical systems have been mostly proposed for concentrated solar power (CSP) plants, as substitutes for the current molten salt-based technology. Another possible application, at a very preliminary stage of development (less than 5 publications in literature), is the development of active thermal barrier coatings (TBC) using thermochemical materials. Thus, thermochemical reactions, which have the side effect of stabilizing the temperature while the reaction takes place, are responsible for

damping the temperature variations of the metallic components in service in processes at high and variable temperatures, in order to extend their lifetime.

This work details: (i) the development of new mixed metal oxides based on pure Co_3O_4 in order to adjust their reaction temperature without greatly impairing their high reaction enthalpy, (ii) The improvement of the stability and cyclability of the mixed metal oxides has been carried out by the addition of SiO_2 particles. (iii) A kinetic study has been completed for both materials, pure and added with SiO_2 particles. Subsequently, (iv) the study has been centered in the active thermal barrier coating application, where the formulation and the layer-by-layer application process has been optimized. To conclude, (v) the coatings have been assessed both at laboratory scale and on a test bench.

Resumen

Las tecnologías de almacenamiento térmico (TES) van a jugar un papel destacado en la integración de las energías renovables y en el incremento de las eficiencias de los procesos industriales. Entre ellas, el almacenamiento termoquímico (TcES) es la menos desarrollada, ya que se encuentra en la mayoría de casos a escala de laboratorio, siendo una de las más prometedoras puesto que: (i) abarca un amplio rango de temperaturas, (ii) tiene altas densidades energéticas, (iii) se puede almacenar el calor a temperatura ambiente y (iv) el calor se libera a temperatura constante, siendo ajustable según las condiciones de reacción.

Así, la reacción endotérmica se utiliza para almacenar el calor cuando está disponible y la reacción exotérmica se utiliza para liberar dicho calor cuando se necesita. En este sentido, las reacciones Redox de los óxidos metálicos han sido ampliamente estudiadas para aplicaciones TES a alta temperatura. Estos sistemas Redox requieren materiales adecuados en términos de (i) reversibilidad completa, (ii) temperatura de reacción adecuada, (iii) alta densidad energética, (iv) alta entalpía de reacción, (v) no tóxico y (vi) buena estabilidad térmica durante el ciclado en el rango de temperatura de la aplicación.

Tradicionalmente, los sistemas termoquímicos a alta temperatura se han propuesto en su mayoría para las plantas solares de concentración (Concentrated Solar Power, CSP), como sustitutos de la tecnología actual basada en sales fundidas. Otra posible aplicación, en una fase muy preliminar

de desarrollo (menos de 5 publicaciones al respecto en literatura), es el desarrollo de recubrimientos activos de barrera térmica (Thermal Barrier Coating, TBC) utilizando materiales termoquímicos. Así, las reacciones termoquímicas, que tienen como efecto secundario la estabilización de la temperatura mientras transcurre la reacción, se encargan de amortiguar las variaciones de temperatura de los componentes metálicos en servicio en procesos a altas y variables temperaturas, con el fin de alargar su vida útil.

En este trabajo se detalla: (i) el desarrollo de nuevos óxidos mixtos metálicos basados en Co_3O_4 puro con el fin de ajustar su temperatura de reacción sin perjudicar en gran medida su alta entalpía de reacción, (ii) La mejora de la estabilidad y ciclabilidad de los óxidos mixtos metálicos que se ha realizado mediante la adición de partículas de SiO_2, (iii) La realización de un estudio cinético para ambos materiales, puro y adicionado con partículas de SiO_2. Posteriormente, (iv) el estudio se ha centrado en la aplicación de los materiales como recubrimientos activos de barrera térmica, donde se ha optimizado una formulación y proceso de aplicación layer-by-layer. Para concluir, (v) los recubrimientos se han caracterizado tanto a escala de laboratorio como en un banco de ensayos.

Laburpena

Biltegiratze termikoko teknologiek (TES) paper nabarmena izango dute energia berriztagarrien integrazioan eta prozesu industrialen efizientzien hazkundean. Horien artean, biltegiratze termokimikoa (TcES) da gutxien garatua, gehienetan laborategiko eskalan baitago, eta oparoenetako bat da, izan ere: (I) tenperatura-tarte handia hartzen du, (ii) energia-dentsitate handiak ditu, (iii) beroa giro-tenperaturan gorde daiteke, (iv) beroa tenperatura konstantean askatzen da, erreakzio-baldintzen arabera doigarria izanik.

Erreakzio endotermikoa beroa biltegiratzeko erabiltzen da, eta erreakzio exotermikoa aldiz, bero askatzeko erabiltzen da. Zentzu horretan, TES aplikazioetarako oxido metalikoen Erredox erreakzioak sakonki aztertuak izan dira. Tenperatura altuko Erredox sistema hauek, honako baldintzak bete behar dituzte: (i) itzulgarritasun osoa, (ii) erreakzio-tenperatura egokia, (iii) dentsitate energetiko handia, (iv) erreakzio-entalpia altua, (v) ez-toxikoa eta (vi) aplikazio tenperatura tartean egonkorra izatea.

Tradizionalki, tenperatura altuko sistema termokimikoak eguzki-planta kontzentratuetarako (CSP) proposatu izan dira, gatz urtuetan oinarritutako egungo teknologiaren ordezko gisa. Beste aplikazio posible bat, oso aurretiazko garapen-fase batean aurkitzen dena (5 argitalpen baino gutxiago literaturan), material termokimikoak erabiliz, hesi termiko estaldura aktiboak (TBC) garatzea da, honen helburua tenperatura aldaketak egonkortu eta materialen bizitza luzatzea izanik.

Lan honetan honakoa zehazten da: (I) Co_3O_4 puruan oinarritutako oxido misto metaliko berrien garapena, erreakzio-tenperatura doitzeko helburuarekin,

erreakzio-entalpia handiari kalte egin gabe; (ii) Oxido misto metalikoen egonkortasunaren eta ziklagarritasunaren hobekuntza SiO_2 partikulak gehituz (iii). Ondoren, bi materialen azterketa zinetikoa egin da, material purua eta material konposatuarena (SiO_2 partikuladuna) hurrenez hurren. (iv) Jarraian, material hauek estaldura aktibo bezala aztertu dira eta horretarako formulaketa eta geruzaz geruzako aplikazioa optimizatu da. Amaitzeko, (v) estaldurak laborategiko eskalan nahiz saiakuntza-banku batean karakterizatu dira.

Abbreviations and symbols

Abbreviations

ASTM	American society for testing and materials
BET	Brunauer-Emmett-Teller
BSED	Backscattered electron detector
CAES	Compressed air energy storage
CaL	Calcium looping
CHP	Combined heat and power (cogeneration)
CSP	Concentrating solar power
DIN	Deutsches Institut für Normung (German institute for standardization)
DSC	Differential scanning calorimetry
EDX	Energy dispersive X-ray spectroscopy
ETD	Everhart-Thornley detector
GD	Glow discharge
HEN	Heat exchanger network
HTF	Heat transfer fluid
ISO	International organization for standardization
LHS	Latent heat storage
OES	Optical emission spectrometer
PCM	Phase change material

PEC	Photoelectrochemical
PH	Pumped hydro
RF GD-OES	Glow discharge optical emission spectroscopy
SB	Sestak- Berggren
SEM	Scanning electron microscopy
SHS	Sensible heat storage
SOEC	Solid oxide electrolyzer
SOFC	Solid oxide fuel cell
TBC	Thermal barrier coating
TCS	Thermochemical storage
TcES	Thermochemical energy storage
TcHS	Thermochemical heat storage
TCM	Thermochemical material
TEC	Thermal expansion coefficient
TEM	Transmission electron microscopy
TEOS	Tetraethyl orthosilicate
TES	Thermal energy storage
TGA	Thermogravimetric analysis
UTM	Universal micro tribometry
XRD	X-ray diffraction
YSZ	Yttria-stabilized zirconia

Symbols

α	Conversion ratio
A	Preexponential factor
ΔH	Reaction enthalpy
Δq	Latent heat of fusion
ΔS	Gibbs free enthalpy
C_p	Specific heat
C_{pL}	Specific heat of the liquid phase
C_{pS}	Specific heat of the solid phase
E_a	Activation energy
f	Melt fraction
$f(\alpha)$	Reaction model
m	Mass of heat storage medium
m_0	Initial mass
m_f	Final mass
m_t	Mass at a time t
n_A	mols of reactant
ρ	density
Q_{bind}	Binding heat
Q_{cond}	Heat of condensation

Q_{des}	Desorption heat
Q_s	Quantity of heat stored
Q_{sens}	Sensible heat
R	Gas noble constant
θ	Generalized time
T_f	Final temperature
T_i	Initial temperature
T_m	Melting temperature
t	Time

Distribution

This manuscript includes the Doctoral Thesis of D. Yasmina Portilla Nieto, entitled "Design and development of mixed metal oxides for high temperature thermochemical energy storage in active thermal barrier coating applications", which aims to provide an advance in knowledge about the development of thermochemical materials with lower reaction temperatures for improving the energy efficiency of industrial processes and active thermochemical coatings aimed at extending the lifetime of the materials used.

The research work has been carried out between the research center CIC energiGUNE and the technological center Fundación Tekniker, in close collaboration with the Department of Physics of the UPV/EHU. A pre-doctoral stay has also been carried out at the German Aerospace Center (DLR), more specifically in the Institute of Engineering Thermodynamics, located in Stuttgart.

The thesis report is presented as a compendium of publications in accordance with the criteria set out in the Regulations for the Management of Doctoral Studies of the University of the Basque Country/Euskal Herriko Universtitatea (UPV/EHU).

In line with the above, the thesis document is divided in three main sections as follows:

Chapter 1:

The present section encompasses both the thematic unit of the research work and a state of the art on thermal storage systems, focusing on thermochemical

systems, where the main reactions, the main metal oxides for redox reactions and their potential applications are detailed. Among the applications, protective coatings are specially detailed. In addition, the characteristics of the main synthesis routes for metal oxides are presented and the effect of sintering is explained.

This section also contains the definition of the objectives of the experimental work and a summary of the most relevant results. A detailed explanation of the experimental methodologies carried out as well as the characterization tools used is also presented. The section concludes with a list of references.

Chapter 2:

This section summarizes the main conclusions obtained during this thesis work in regard to the development and optimization of the mixed metal oxides and to the thermal coating obtention and analysis. It includes a sub-section describing the possible future works to continue with the research on this topic.

Chapter 3:

This section consists of the annexes. The first annex shows the dissemination of the research work, the second annex describes the unpublished experimental results, including the enthalpy studies and the third one contains the five publications obtained during the thesis work (three published and two submitted)

General index

List of Figures

List of Tables

Chapter 1

1. Background

The global energy demand continues increasing as a consequence of population and economic growth. This high energy consumption leads to a considerable increase in the pollution of the planet, due to the large quantities of CO_2 released into the atmosphere as a result of the overproduction of energy from non-renewable energy sources to meet society's demands.

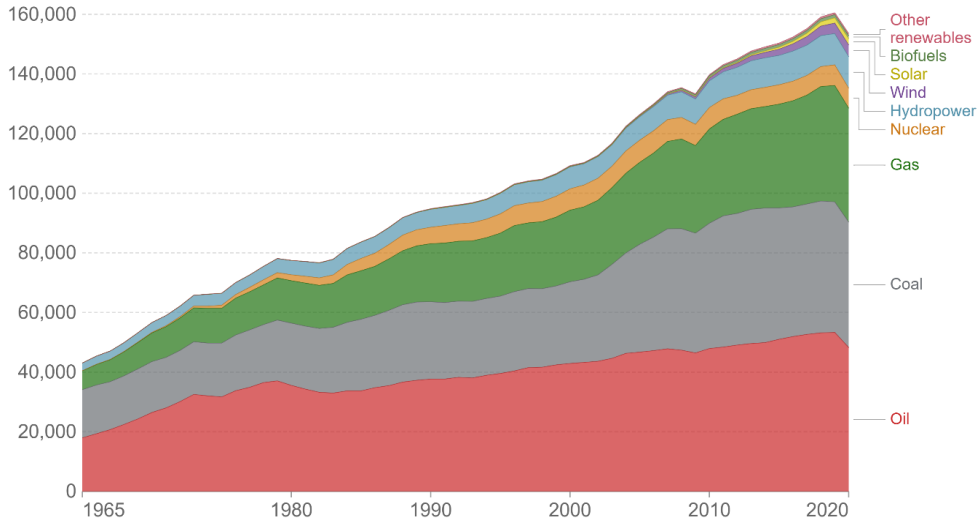

Figure 1.1. *Evolution of the energy consumption by source in the world [1,2]. The consumption is measured in terawatt-hours (TWh). "Other renewables" include geothermal, biomass and waste energy.*

The upward trend in energy consumption can be observed in Figure 1.1. It was slowed by 4.5 % in 2020 by the COVID-19 pandemic that swept the globe [1].

The lockdowns imposed around the world reduced the transport energy demand. Three-quarters of the total decrease in energy demand was due to the drop in oil demand [1]. During 2021, the gradual return to normality led to an increase in energy demand to values close to those of 2019 [3].

In this scenario of increasing demand, with growing tension between different countries over non-renewable energy resources, the use of the available sources of energy is a critical factor to solve both environmental and economic problems.

Two of the alternatives for meeting energy demand without generating major environmental impacts are: the commitment to renewable energies and the increase of the efficiency of industrial processes, both from the energy side and from increasing the life time to the materials side.

These aspects are introduced in The Energy Hierarchy, which presents levels of priority in terms of actions to be taken by policy makers, industry and consumers in the use of energy sources. The list is presented in order from the most sustainable to the least sustainable, as it is depicted in Figure 1.2.

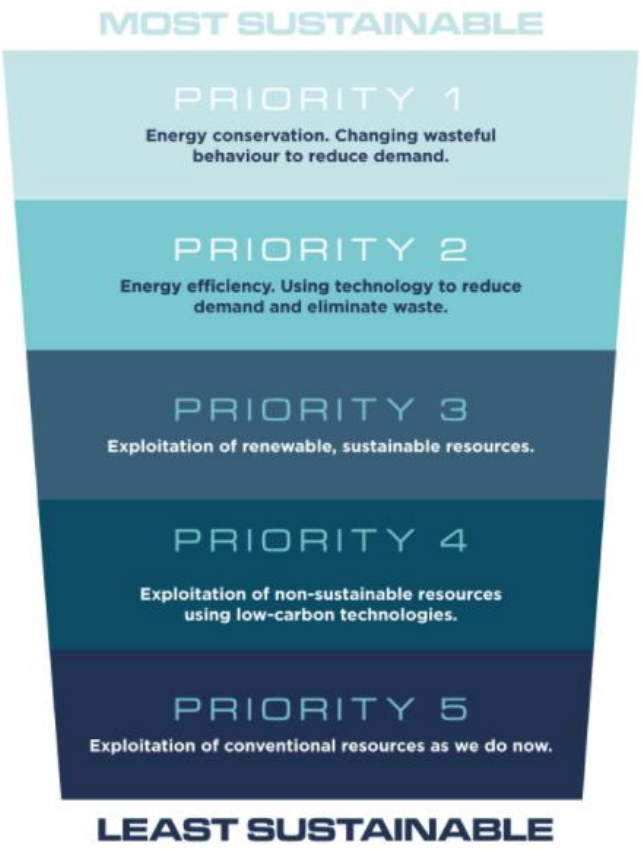

Figure 1.2. *The energy Hierarchy list [4].*

This list prioritizes reducing energy demand by taking preventive measures to conserve energy, then moves on to improving energy efficiency and the use of renewable energies, and finally it introduces the use of non-renewable energy sources with low CO_2 emissions and classic energy sources. It places importance on sustainability, not just in how energy is generated but also in how we use it as a resource [4].

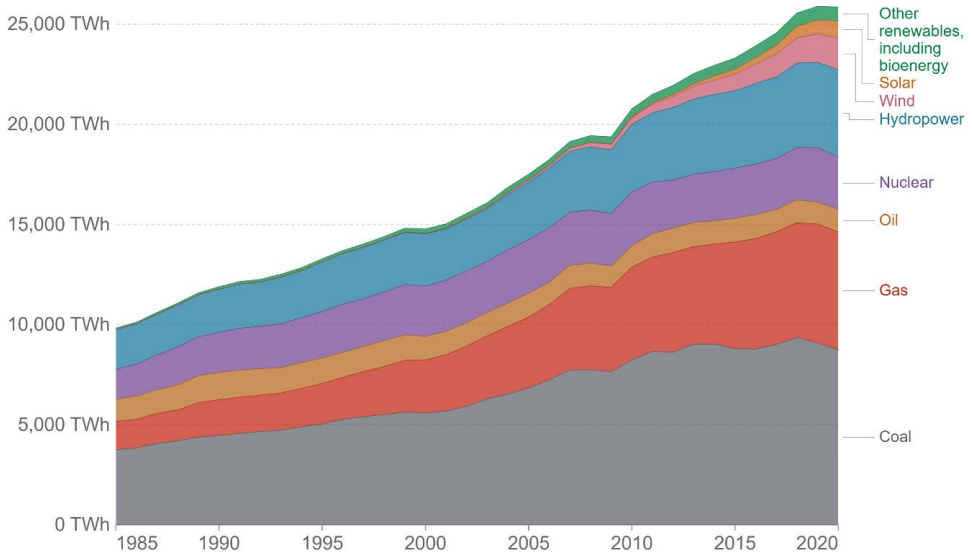

Figure 1.3. *Evolution of the global electricity production by source [1,2]. "Other renewables" slot includes biomass and waste, geothermal, wave and tidal.*

Following the Energy Hierarchy demand, the increase in renewable energy use has been evident over the years (Figure 1.3). During 2020, with the pandemic hitting the global economy, renewables continued to grow strongly. Especially solar and wind capacity grew by 238 GW, 50% more than in previous years [1]. In addition, wind and solar power fed into the global power mix reached record highs, as it is shown in Figure 1.4. Moreover, the immunity shown by the renewable energy over the events of 2020 is promising.

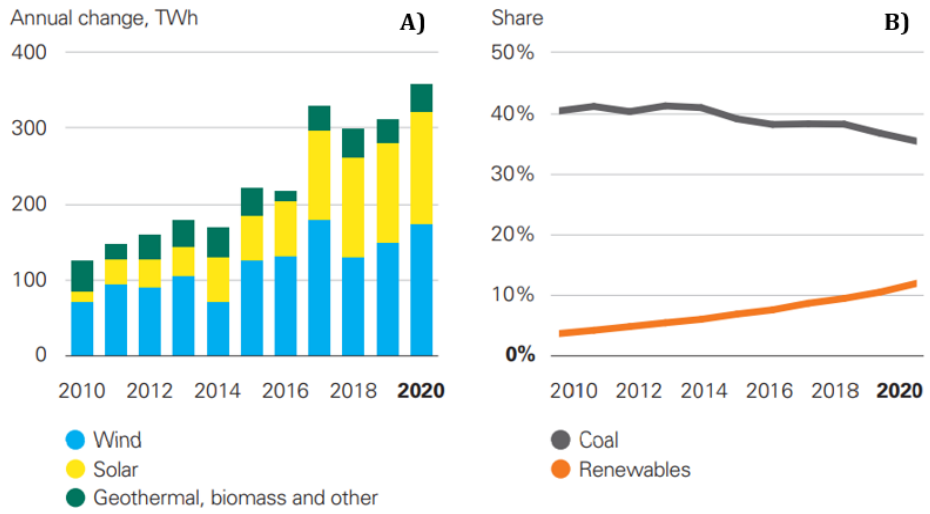

Figure 1.4. *A) Renewable power generation by source, and B) Share of renewables and coal in the global power generation [1].*

The commitment to renewables also allows the reduction in greenhouse gas emissions, essentially CO_2. During 2020, emissions were reduced by 6%, a value similar to what is needed to be reduced per year over the next 30 years to meet the objectives of the Paris agreement [1].

The challenges of renewable energies are the intermittency of production and that in most cases, electrical production does not match electricity demand. The use of electricity from renewable sources such as solar or wind for heat production, coupled with the use of thermal energy storage (TES) systems, can provide the necessary flexibility for the growth of renewables. Power to heat to power technology is a very promising alternative [5,6].

The heat is the center of the universal energy chain, linking primary and secondary sources of energy. The TES conversion, transfer and storage processes account for 90% of the whole energy budget worldwide [7]. The TES is capable of addressing all elements of the energy nexus, including mechanical,

electrical, fuel and light modules, through heat loss mitigation, waste recovery and energy saving approaches to improve system performance [8].

Thermal storage systems will also play a key role in improving the efficiency of industrial processes. These systems allow the storage of waste heat from the process and reuse it in another part of the process where it is needed [9,10]. In addition, they allow the temperature of the outgoing streams to the atmosphere to be lowered, thus reducing the impact on global warming.

Another way of increasing the efficiency of the industrial processes is improving the lifetime of the materials. The damage and deterioration of pipes, valves and fittings are a widespread problem of industries around the world [11]. These problems occur due to corrosion, erosion, thermal cycling and chemical attack. The insulation of the equipment to prevent heat loss and increase efficiency is key factor to save energy costs and reduce waste [11].

Thermal barrier coatings (TBCs) [12–14] are an efficient thermal protection technology. Normally, TBCs are formed by ceramic material with high-temperature resistance, corrosion resistance and good thermal insulation properties [15–19]. Thermal barrier coatings protect the superalloy materials from high temperature, oxidation and corrosion isolating them from the heat source [20]. Thermal coatings have been used widely in gas turbines and engines [21,22].

A new concept of active thermal barrier coatings based in the use of TES reactions has been recently proposed. The main objective of this concept is to delay or avoid the thermal fatigue at which are exposed process materials, solar receivers or other electronic devices at high temperatures [23–26], thus maintaining a high system efficiency for a prolonged time and increasing the lifetime of the process materials.

2. Introduction

2.1. Thermal Energy Storage (TES)

Thermal energy storage (TES) technologies are based on the storage of thermal energy by heating and cooling a storage medium [27]. The energy stored can be used later for applications such as heating/cooling [28], power generation or materials protection [24].

TES technologies allow to manage the generation and demand of energy which is out of phase and improve the performance and thermal reliability of the systems, but also, they increase in overall efficiency from 50% to around 70 to 100% [29], leading to better economics, reductions in investment and running costs, etc. [30].

Thermal storage systems can be used for short-, medium- and long-term storage applications. Thus, short and medium term refers to hours or days and long term or seasonal refers to energy storage for several months and can be used when needed [8].

These systems are used commonly in buildings and in industrial processes [28,31,32], improving the energy efficiency of the whole process and reducing the environmental impact by storing the waste heat, as those quantities of heat are usually dissipated to the environment, turning them into waste and also

causing an increase in the global warming effect. They are also used in combination with concentrating solar power (CSP) for the storage of electricity [27].

Thermal energy storage technologies can be divided into three principles of storage, as it is depicted in Figure 1.5, differing in the fundamental way they store thermal energy [28,33–35]:

- Sensible heat storage (SHS): This is the most extended TES technology and it is based on the raising and lowering the temperature of a liquid or solid medium to store/release thermal energy for low/medium temperature applications. The most common material used is water.
- Latent heat storage (LHS): This technology is based in the absorption or release of energy at a constant temperature during the phase change of a material. The most commonly phase change used is the solid/liquid transition but the solid-solid is used too.
- Thermochemical heat storage (TcHS): This technology operates in two ways: chemical reactions and sorption processes. The first ones store the energy as the heat of reversible reactions. In the second ones, the energy is stored either through adsorption or absorption processes.

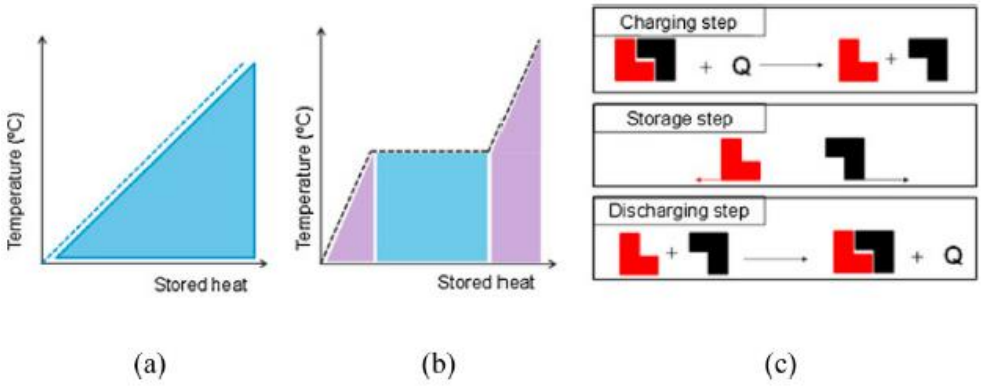

Figure 1.5. *Thermal energy storage systems: (a) sensible heat; (b) latent heat; (c) thermochemical reactions [36].*

The main characteristics of the different TES systems in comparison with other storage technologies are listed in Table 1.1.

Table 1.1. Characteristics of the different TES technologies [37].

Storage technologies	Pumped hydro plant	Compressed air energy storage	Batteries	TES systems		
				SHS	LHS	TcHS
Energy storage form	Mechanical	Mechanical	Electrochemical	Thermal	Thermal	Thermochemical
Efficiency (%)	50-85 (Electrical)	27-70 (Electrical)	75-95 (Electrical)	50-90 (Thermal)	75-90 (Thermal)	75-100 (Thermal)
Initial capital cost (kW)	500-4600	500-1500	300-3500	3400-4500	6000-15000	1000-3000
Energy cost (USD/kWh)	80-100	50-100	150-2500	0.1-13	10-56	8-100
Durability (years)	40-100	20-100	3-20	10-30 +	10-30 +	10-30 +
Durability (cycles)	10000-30000	8000-12000	1000-10000	2000-14600	2000-14600	2000-14600
Energy storage density (kWh/m3)	0.5-1.5	3-6	15-600	25	100	~500
Energy storage density (kWh/tonne)	0.5-1.5	30-60	10-250	10-50	50-150	~120-250
Storage capacity (MW)	100-5000	1-400	0.001-50	0.1-300	0.1-300	0.1-300

The bibliographic references for Table 1.1 are: efficiency: [38]; initial capital cost: [38,39]; energy cost: [38,40]; durability: [39–41]; energy storage density: [38,39,41]; storage capacity: [41].

2.1.1. Sensible Heat Storage (SHS)

Sensible heat storage is the most developed and simplest TES technology. It stores heat using the temperature difference on a liquid or solid medium. The SHS system stores the heat energy while increasing the temperature and releases the heat energy by decreasing the temperature [42]. A typical SHS system consists of a storage medium, a container and input/output devices. Containers must both retain storage material and prevent loss of thermal energy [43,44].

The main advantages of SHS are the prize - is the cheapest TES technology-, and the lack of risk associated with the use of toxic materials [28]. The main drawbacks are the low energy density and the variable discharging temperature [27,45,46], as it is shown in Figure 1.6, where it can also be observed that the energy density of SHS is the lowest among all TES systems.

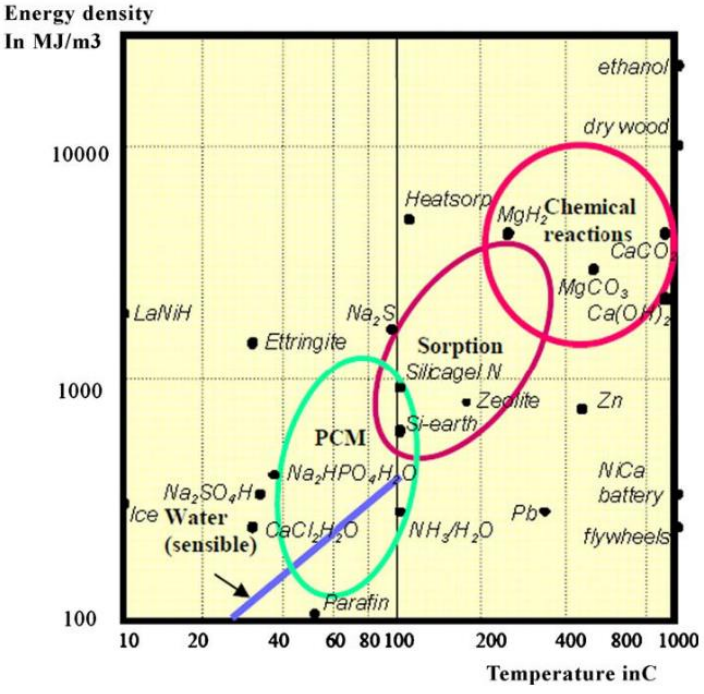

Figure 1.6. *Energy density of thermal energy storage methods [47].*

The quantity of heat stored depends on the amount of storage material, the specific heat of the medium and the temperature change [12], according to the following equation:

$$Q_s = \int_{T_i}^{T_f} m\ Cp\ dt = m\ Cp\ (T_f - T_i) \quad (1)$$

Where Q_s is the amount of heat stored, m is the mass of heat storage medium, C_p is the specific heat, T_i is the initial temperature and T_f the final temperature.

The materials for SHS should have high specific heat capacity, leading to increase the overall efficiency of the storage process and reduce the size of the storage tank, having as a consequence the reduction of the total investment cost [42]. The most commonly used materials for this TES technology are mainly: water, molten salts, nanofluids, sand, rock, brick, gravel, concrete [43,48,49]. Water is the cheapest option and has a number of industrial and residential applications. Above 100 ºC, oils, molten salts and liquid metals are used. Rock bed type storage materials are used for air heating applications. Another typical applications of SHS technology is the underground storage in both liquid and solid media [28] and the molten salt-based SHS system installed in all commercial CSP plants with the TES storage system [42].

2.1.2. Latent Heat Storage (LHS)

Latent heat storage systems provide the possibility of storing a large amount of heat at a constant temperature, the phase-change temperature [28,31]. The materials used for LHS systems are known as phase-change materials (PCM) due to their capability of releasing or absorbing energy with a change in physical state [28]. LHS systems have larger energy storage densities and smaller volume than SHS systems.

The storage capacity is described by the following equations [49]:

$$Q_s = \int_{T_i}^{T_m} m\ Cp\ dt + m\ f\ \Delta q + \int_{T_m}^{T_f} m\ Cp\ dt \quad (2)$$

$$Q_s = m\left[Cp_s(T_m - T_i) + f\ \Delta q + Cp_L\left(T_f - T_m\right)\right] \quad (3)$$

Where T_m is the melting temperature, m is the mass of PCM, Cp_s is the average specific heat of the solid phase between T_i and T_m, Cp_L is the average specific heat of the liquid phase between T_m and T_f, f is the melt fraction and Δq is the latent heat of fusion.

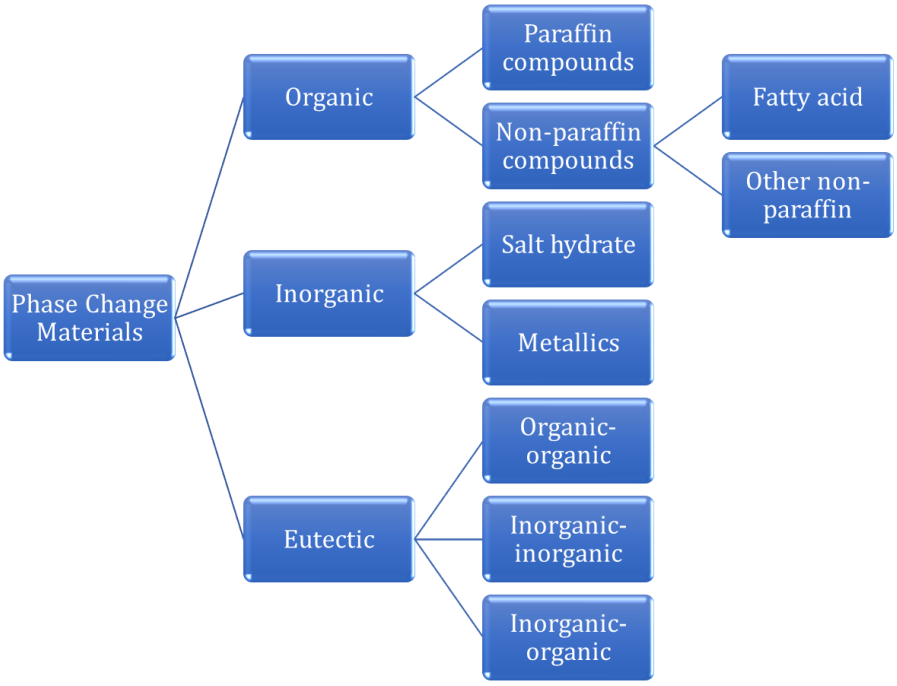

Figure 1.7. *Classification of phase change materials [31].*

The different types of PCMs are schemed in Figure 1.7. The organic phase change materials are adapted for low temperature applications but the prize and the flammability are their main drawbacks. PCMs have larger heat of phase change and are commonly used for high temperature applications [50]. The eutectic materials are a combination of organic and inorganic materials with

similar melting and freezing points. Their latent and specific heat capacities are usually low [31,51].

The temperatures of the LHS materials are listed in the decreasing orders: solid-solid > solid-liquid > liquid gas [42]. The solid-solid has generally the lower latent heat and the liquid-gas the highest, but its high volume change during the phase change is its main drawback for a commercial application [52]. Among organic materials, sugar alcohols show solid-liquid transitions with enthalpies from 165 to 357 J/g [53–55] and plastic crystals have solid-solid transitions with enthalpies from 110 to 300 J/g [56]. In the case of the inorganic materials, the salts and salt hydrates show heats of fusion ranging from 150 to 2678 J/g [57,58] and the metals show heats of fusion from 23 to 498 J/g [58].

LHS systems, as SHS ones, can be divided into direct and indirect systems. The heat transfer of the first ones is obtained by immediate contact between the heat transfer fluid (HTF) and the LHS material. In indirect systems, the HTF and the storage material are separated by a solid heat transfer edge, in which heat can be delivered to a container filled with PCM or an encapsulated material [33].

This technology is suitable for applications that do not allow big temperature differences. Each application requires a suitable PCM, whose phase change temperature is in the range of the application. So far, the main application of LHS systems is in buildings [59–61].

2.1.3. Thermochemical Heat Storage (TcHS)

Thermochemical heat storage (TcHS) is the less developed TES technology and has the highest energy storage density (up to 500 kWh/m^3) [62,63]. TcHS systems can store heat in two ways: chemical reactions and sorption processes [64]. The term “sorption” was firstly proposed in 1909 as a general expression

for covering adsorption and absorption [65]. The use of chemical reactions was purposed by Goldstein at first instance for solar heat storage [66]. Afterwards it was proposed for energy storage in general [67,68].

Chemical reactions and sorption processes can store large amounts of heat. In the case of the sorption processes (Figure 1.8), heat is stored by breaking the binding force between the sorbent and the sorbate in terms of chemical potential [69].

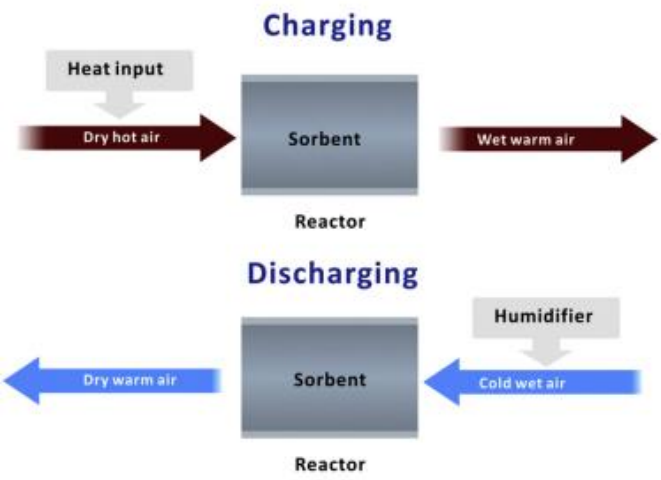

Figure 1.8. *Operating principle of a sorption thermal storage system [70].*

Thermochemical storage is based on gas-gas, gas-solid or solid-solid reactions. There are two phases involved in a TcHS system, as it is schemed in Figure 1.9: A charging step, where an endothermic reaction is involved for storing excess or waste heat [37,71,72], and a discharging step, where an exothermic reaction is used to release the stored energy for further applications [73]. If the reactions are completely reversible, all the energy stored should be recovered [74].

The general reaction taking place in a TcHS system can be described as [71]:

$$A + Q \leftrightarrow B + C \qquad (4)$$

During the charging step, the thermal energy activates the endothermic reaction where the compound "A" is transformed into the reaction products ("B" and "C") [75]. The compounds "B" and "C" can be stored separately [76]. The exothermic reverse reaction is obtained by the recombination of the reaction products ("B" and "C") releasing the heat of reaction. Theoretically, this reverse cycle guarantees a thermal energy storage without heat losses. The products of both steps can be stored at ambient temperature [71].

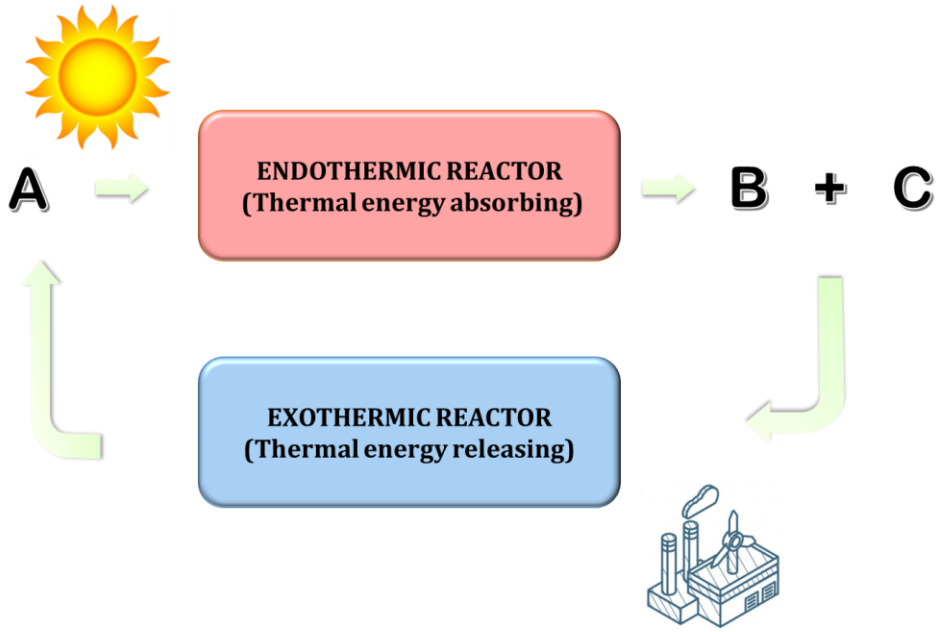

Figure 1.9. *Schematic diagram of a thermochemical heat storage system based on Wu et. al [37].*

The energy stored in this kind of systems can be calculated as [71]:

$$Q = n_A \cdot \Delta H \qquad (5)$$

Where n_A is the number of mol of reactant A and ΔH is the reaction enthalpy.

The main advantages of TcHS technologies are [46,68,71,77–79]:

- They present the highest energy storage density among all the TES technologies, up to 15 times greater than the SHS storage density and 6 times greater than the LHS one.
- High operation flexibility, being suitable for a wide range of applications due to the large number of available reversible reactions at different temperatures.
- Theoretically, the storage duration and transport distance are unlimited, as the systems do not present thermal energy losses.
- It can be achieved a stable heat source with constant temperature because the discharge reactions take place at constant temperatures.

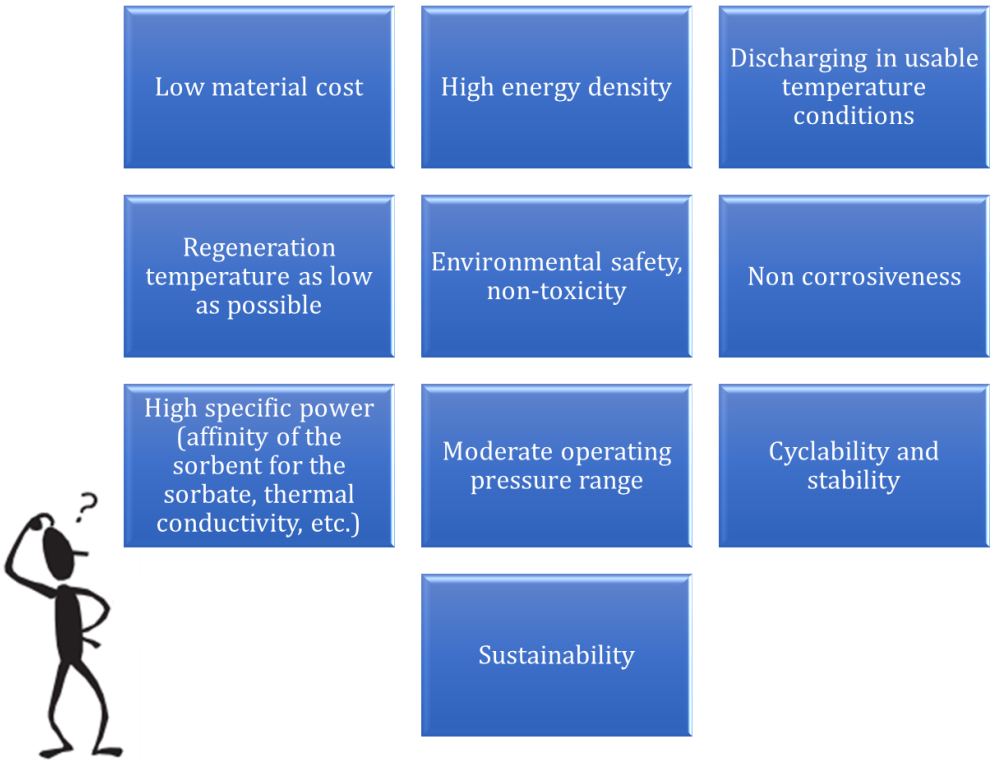

Figure 1.10. *Material selection criteria for thermochemical heat storage, based on N'Tsoukpoe et. al [80].*

The criteria for the selection of the material candidates for thermochemical energy storage is depicted in Figure 1.10. The most important requirements are:

- Complete reaction reversibility
- Suitable reaction temperature
- High storage density
- High reaction enthalpy
- No-toxicity
- Good thermal stability during cycling in the operation temperature range
- Low cost

The selection of thermochemical materials should be made in compliance with as many requirements as possible.

2.2. Thermochemical energy storage (TcES)

As thermochemical energy storage is the less developed and most complex TES technology, further studies are needed. This section deals with the classification of the different reactions and most promising materials.

2.2.1. Classification by type of reactions

The thermochemical reversible reactions used for storing energy can be grouped in four categories depending on the state of the materials involved [81]: gas-gas, liquid-gas, liquid-liquid, solid-gas and solid-solid reversible reactions [82–85]. Between them, solid-gas reactions have attracted more interest because of their wide range of turning temperature and the easy separation of the reactants [82,86,87].

The most studied systems in the medium-high temperature range are depicted in the Figure 1.11.

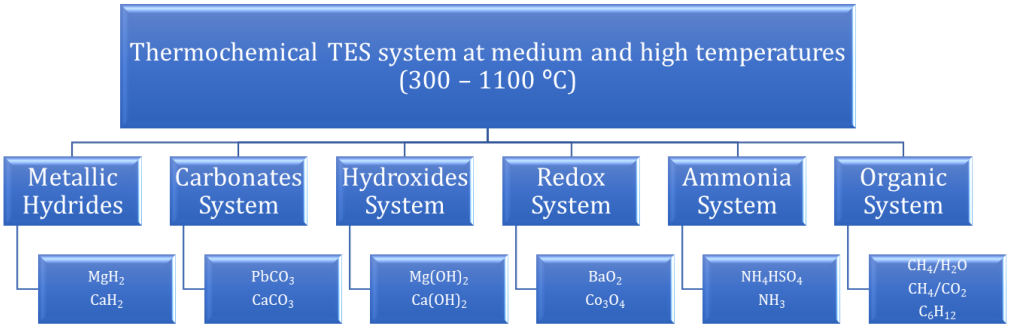

***Figure 1.11**. Thermochemical storage (TCS) systems studied in the past [71].*

There are various candidates for thermochemical energy storage but some of them are not considered for the final application because of their harmful nature to human beings. Thus, its development is not considered in many cases, as $PbCO_3$ due to the presence of Pb. In other cases, the toxicity of the sulfates linked to the corrosiveness of the resulting gaseous reaction products (sulfur oxides) in the gas-solid reactions makes them not suitable [37].

In other cases, the use of reactants such as CO_2 or H_2O makes separation or evaporation necessary, as is the case for carbonates, hydroxides and organic

systems [10]. The ammonia system suffers from high pressure requirements, slow ramp rates for ammonia synthesis and high exergetic losses [88]. All this complicates energy storage.

The main solid-gas reactions and sorption processes studied for thermochemical energy storage (TcES) are detailed in this section.

2.2.1.1. Sorption processes

The sorption thermal storage consists in a sorption followed by a desorption. The mechanism followed by this process for the basic cycles can be described as [70]:

Charging: $$A \cdot (m+n)B + heat \rightarrow A \cdot mB + nB \quad (6)$$

Discharging: $$A \cdot mB + nB \rightarrow A \cdot (m+n)B + heat \quad (7)$$

Where A is the sorbent and B is the sorbate.

In the charging step (desorption), a supply of heat is needed to remove the sorbate from the sorbent. The heat required must be higher than that associated with the evaporation or condensation heat of the pure sorbate. Explained in the mechanism, the heat breaks the binding force between A and B in A·(m+n)B and a part of B is released from A. The energy is stored in chemical potential while the mass fraction of B decreases.

In the discharging step (sorption), the sorbent and the sorbate must be in contact so the binding force can be stored. Explained in the mechanism, A·mB is in contact with B to form A·(m+n)B, and the chemical potential is transferred into thermal energy while the fraction of B increases [70]. The sorption process can be of adsorption (physisorption) and of absorption (chemisorption).

In a liquid absorption process, A·(m+n)B represents a solution with a lower concentration of A than A·mB. In a solid adsorption process, A·(m+n)B

represents the enrichment of B on the surface of A as (m+n) mole B is adsorbed [70].

The sorption process of a salt hydrate, for example, can be described as [89]:

$$Salt \cdot nH_2O(s) + heat \leftrightarrow Salt(s) + nH_2O \quad (8)$$

The types of sorption processes are classified in Figure 1.12, distinguishing between solid sorption and liquid absorption processes.

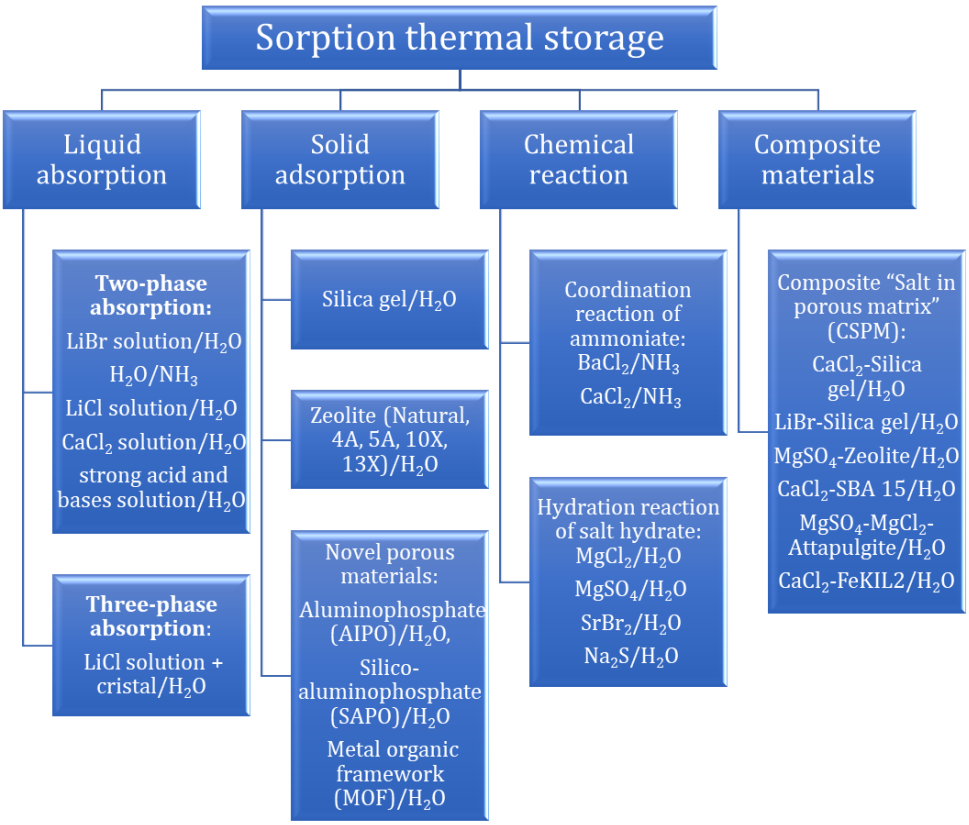

Figure 1.12. *Classification of sorption thermal storage [70].*

The energy involved in the sorption storage systems can be described as [70,90]:

$$Q_{char} = Q_{sens} + Q_{cond} + Q_{bind} \quad (9)$$

$$Q_{des} = Q_{cond} + Q_{bind} \quad (10)$$

Where the sensible heat (Q_{sens}) is a prerequisite energy to heat up the reactor to a required desorption temperature. The heat of condensation (Q_{cond}) is the liquid-gas phase change heat at a specific temperature which is assumed constant. The binding heat (Q_{bind}) represents the difference between the desorption heat (Q_{des}) and the condensation heat (Q_{cond}) [70].

The system configuration of the sorption processes can be closed or open [91–93]. The closed systems, isolated from the atmospheric environment, have been widely studied for refrigeration, heat pump and energy storage applications. This kind of systems is suitable for small-scale applications where compact and highly efficient devices are needed [94,95]. The open systems, contrary, are exposed to ambient environment to allow the release and sorption of the sorbate. Only water can be used [70]. This type of system has lower investment costs as well as better mass and heat transfer conditions. Therefore, practical projects are developed using open systems for thermal energy storage [92,93]. From a design point of view, open processes have more benefits than closed processes, as they have less auxiliary elements such as condensers, evaporators, water storage reservoirs, system pressure maintenance and complex system control, avoiding maintenance costs or failure of these auxiliaries [96–100].

Typical compounds used as thermochemical materials (TCMs) are salt hydrates, but as far as it is known, all hygroscopic salts are sensitive to some instability issues, so it is necessary to consider some stabilization ways. Matrix encapsulation with polymer coatings is one of the most commonly considered solution. Polymeric coatings can provide high water vapor permeabilities with reversible deformability, minimizing resistance to water transport and accommodating volumetric changes of the TCM during repetitive (de)hydration processes. [101]. The porous structure may have some influence on TCM thermodynamics [102].

Salt hydrates have advantages for storing low-grade heat, which include high energy storage density, suitable tuning temperature, self-separation of reactants and using water vapor as a safe and cheap gaseous reactant [81,82,86,87,103–105]. Their requirements for storing thermal energy, as in the case of the other thermochemical materials studied, are depicted in Figure 1.13.

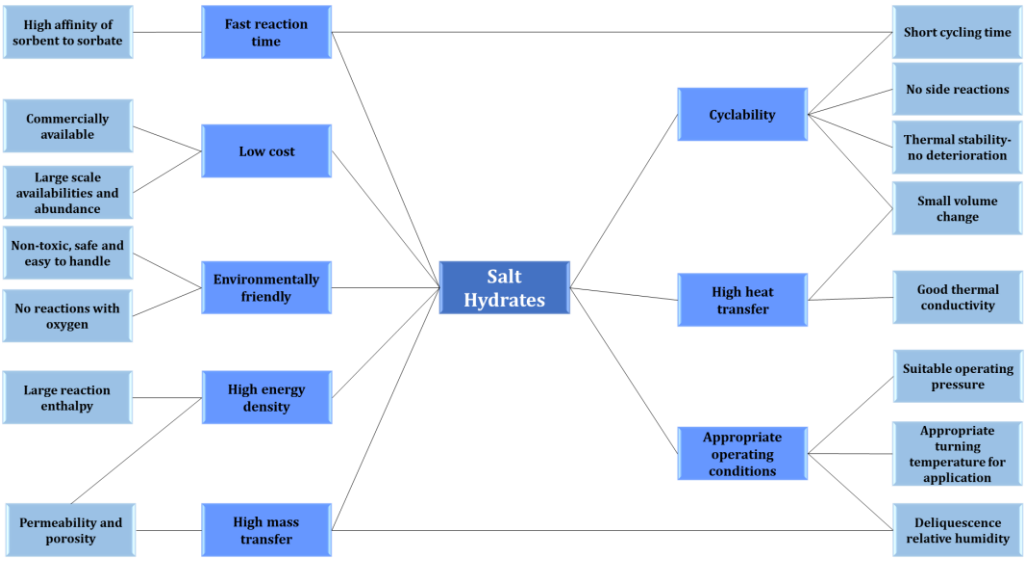

Figure 1.13. *Salt requirements for storing low-grade thermal energy [81].*

2.2.1.2. Hydration processes

The use of reversible hydration/dehydration of metal oxides can be used near atmospheric pressures at medium-high temperature, depending on the oxide used, for thermal energy storage. The charging and discharging reactions can be represented as follows (M=metal) [106]:

Exothermic reaction: $MO_{(s)} + H_2O_{(v)} \rightarrow M(OH)_2 + \Delta H$ (11)

Endothermic reaction: $M(OH)_2 + \Delta H \rightarrow MO_{(s)} + H_2O_{(v)}$ (12)

The H_2O partial pressure and the temperature drive the hydration/dehydration reactions [71].

The energy density of the given hydration reaction is given by [107]:

$$\frac{Q}{V} = \rho_H \frac{Q}{m} = \frac{\rho_H}{M_H} \Delta H_r = \frac{\rho_H}{M_H} n \Delta H_w \qquad (13)$$

The subscripts H and D refer to hydrated ($M(OH)_2$) and dehydrated (MO) phases of the compounds, Q/V [J/m³], Q/m [J/kg], ΔH_r [J/mol] are the energy storage densities per volume, mass and mole. ρ_H [kg/m³] and M_H [kg/mol] are density and molar mass of the hydrated state and ΔH_w [J/mol] is the reaction enthalpy per mole water.

The undesirable properties of the materials for the hydration reactions are common with all other thermochemical materials: deterioration during cycling, non-suitability in the application temperature range, side chemical reactions, corrosion, pulverization and deliquescence issues [107]. In an ideal case, the activity stable state is reached after several cycles of hydration and dehydration. Sometimes macro-crystals get cracked during the cycles, so it is necessary to look for additional stabilizing material.

Typical hydroxides are cheap, abundant and nontoxic [108]. The most studied ones are calcium hydroxide (Figure 1.14) and magnesium hydroxide for high-temperature TcES applications and chemical heat pump, respectively, due to their high volumetric energy density (up to ~600 MJ/m³) [109].

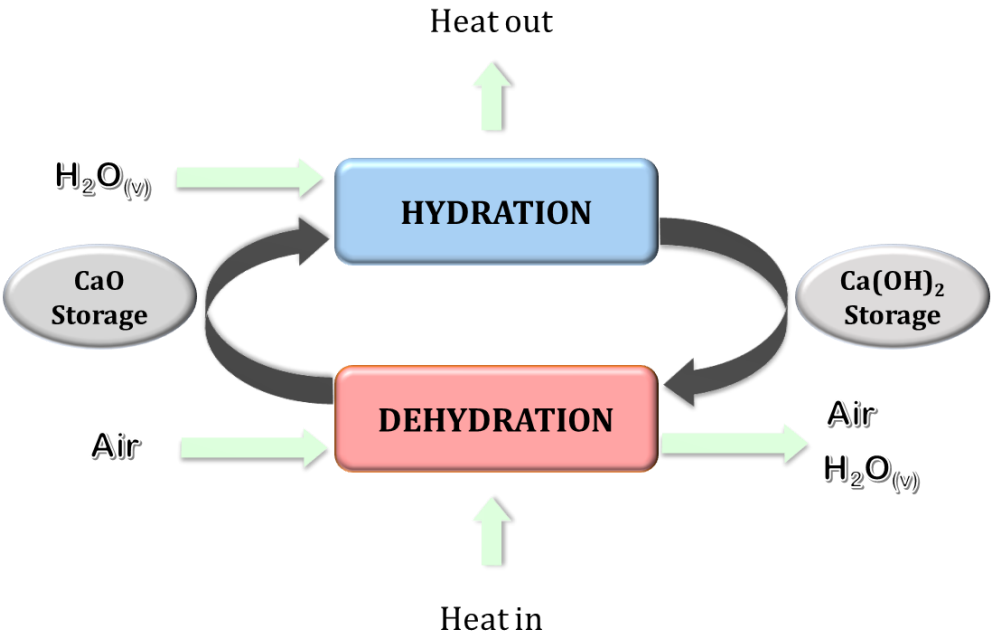

Figure 1.14. *$CaO/Ca(OH)_2$ thermochemical energy storage process concept [110].*

2.2.1.3. Carbonation processes

The alkaline-earth metal carbonates are suitable materials for thermochemical applications due to their high turning temperature, high energy density, and low price [83,111]. Initially, these compounds were used for CO_2 capture. The calcination-carbonation chemical looping is a cyclic process which can be used to achieve the desired storage temperature (above 800 ºC), energy density and discharging rates [112].

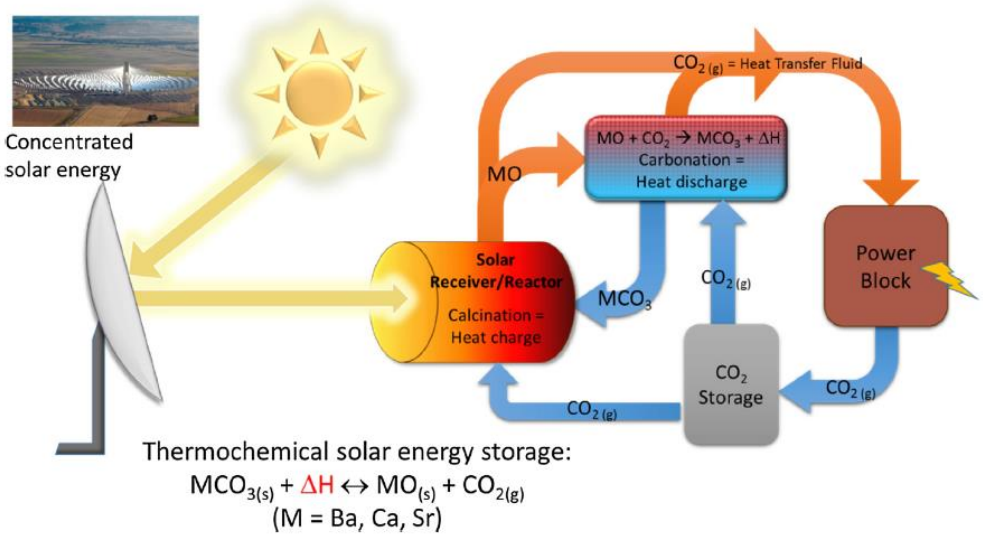

***Figure 1.15**. Operating principle of thermochemical energy storage based on carbonates in CSP plants [112].*

Figure 1.15 shows the operating principle of a carbonation process based on thermochemical reactions is used in a CSP plant.

The calcination/carbonation reactions can be described as [113]:

$$MCO_{3_{(s)}} + \Delta H_r \leftrightarrow MO_{(s)} + CO_{2_{(g)}} \qquad (14)$$

Carbonates are decomposed through the endothermic calcination reaction, where M represents Ca, Sr, Ba, etc. The reaction takes place in a solid-gas reactor under near-to-ambient pressure. The temperature of the reaction depends on the equilibrium partial pressure of CO_2. Once the calcination is completed, CO_2 and the metal oxide are stored separately after passing through a heat exchanger network (HEN) to reduce its storage temperature. Sometimes, the CO_2 is compressed to liquid state to reduce the storage volume [113]. When the energy needs to be recovered, the metal oxide and the CO_2 are sent to a solid-gas reactor where carbonation takes place, releasing the previously stored energy.

The main problem of carbonates is the sintering occurring after multiple calcination/carbonation cycles at high temperature [114–116]. The techniques used to solve this problem by increasing the active surface area and the stability of the pore structure are: the use of rigid porous materials as support, the use of additives to improve the thermal stability, the reduction of the particle size and the synthesis of materials with microporous structure[112,117].

Between the carbonation reactions, the best stablished system is the Calcium Looping (CaL) process based on calcium carbonate ($CaCO_3$/CaO) [118], but there are other alternatives using barium carbonate ($BaCO_3$/BaO) [119], strontium carbonate ($SrCO_3$/SrO) [120] or magnesium carbonate ($MgCO_3$/MgO) [121].

2.2.1.4. Redox processes

The technical issues associated with metal oxide redox systems are less than those of other TcES processes, since they have advantages such as: high reaction temperatures, non-corrosive products and no need for gas storage [37]. High operation temperatures are of great importance for power cycle applications as it increases the upper limit of the thermodynamic efficiency achievable according to Carnot principles [122].

The redox reactions involved in this process can be described as [74]:

Reduction: $$M_xO_y \rightarrow M_xO_{y-1} + {}^1/_2\, O_2 \qquad \Delta H > 0 \qquad (15)$$

Oxidation: $$M_xO_{y-1} + {}^1/_2\, O_2 \rightarrow M_xO_y \qquad \Delta H < 0 \qquad (16)$$

Initially, metal oxides are reduced by the endothermic reaction at high temperature storing external thermal energy. Later the reduced metal oxides are re-oxidized to the initial state by the exothermic reaction and release the previously stored energy. The oxidation is carried out by a source of oxygen. If

this oxygen source is water or CO_2, this phase produces H_2 or CO respectively [123]. The most common oxygen source is air. During the charging process, the reduction can be performed either by solar irradiation of the metal oxide or by heating an HTF. When air is used as oxygen source, the HTF and the oxygen source are the same. A scheme of the redox process is depicted in Figure 1.16.

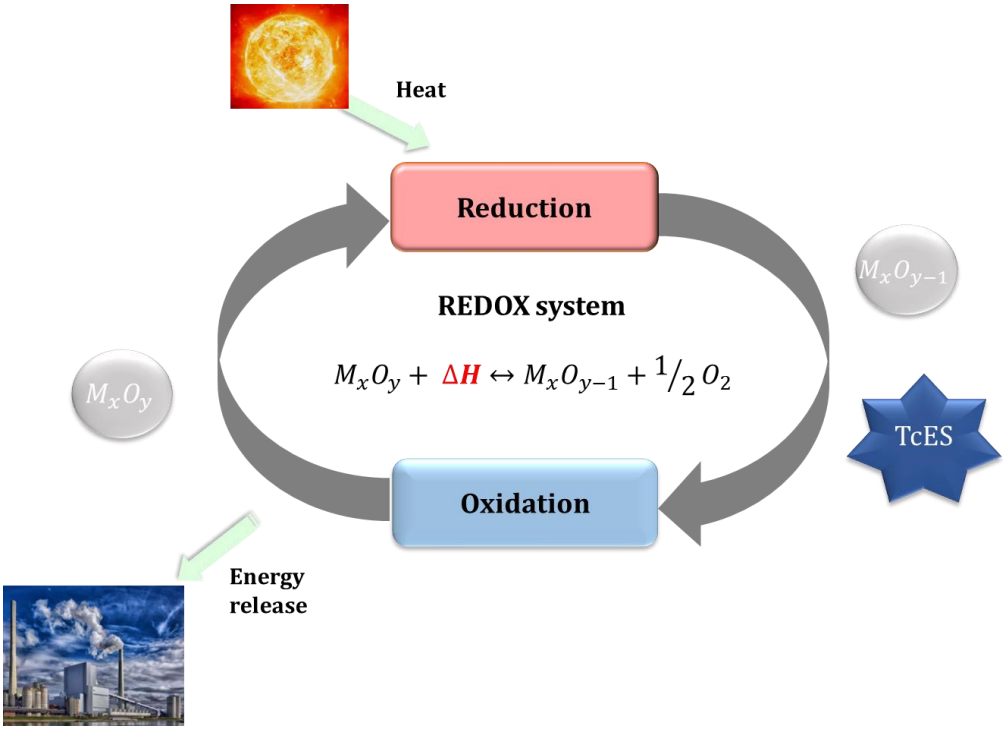

Figure 1.16. *Scheme of a typical redox process using air as HTF and oxygen source for thermochemical energy storage.*

Some of the advantages of this technology reported in the literature are [10,74,124–130] :

- The high operating temperatures, ranging from 350 ºC to 1100 ºC, are beneficial to boost the efficiency of CSP plants and make the redox process suitable for many applications.
- When air is used as HTF and reactant, there is no need to store the reactant gas.

- As the reaction is gas-solid, there is no necessity for products separation.
- Metal oxides have medium to high energy storage densities (230-850 kJ/kg).
- The reactions are simple and, in general, no catalysts are required.
- Environmental impact is relatively small for most redox couples.

There are three main properties to determine if a metal oxide is suitable for redox energy storage [37,71,77,84,126,131]:

- Turning temperature: The temperature at which the Gibbs free energy (ΔG) equals to zero (Figure 1.17), the formation of reactants or products is not thermodynamically favored.
- Energy storage density: The amount of energy stored by the endothermic reaction per unit volume or unit mass.
- Reaction reversibility: The evaluation of the redox degree of completion after cycling.

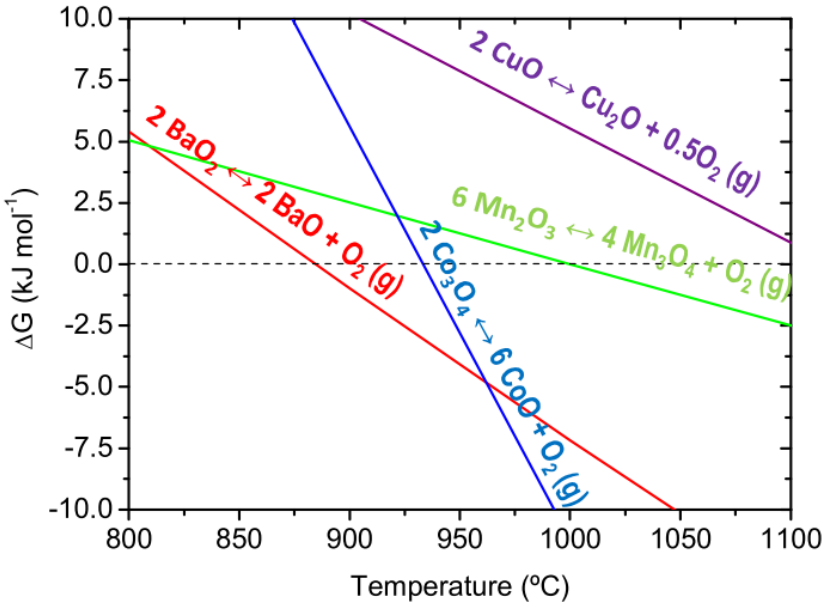

Figure 1.17. *Gibbs free energy (ΔG) against temperature for the most common metal oxides redox reactions [125].*

The redox systems can be classified into two groups depending on the number of metal oxides involved: pure and mixed metal oxide redox systems. In the pure oxide system only one metal element is included in oxides, e.g., CoO/Co_3O_4 redox couple. In the mixed oxide redox systems more than one metallic element is included in the oxide, for instance Co_3O_4 doped Mn_3O_4 system ($Co_{3-x}Mn_xO_4$). Normally, the synthesis of the pure redox systems is easier but the mixed ones have advantages such as reversibility and low cost [37].

Table 1.2 summarizes the advantages and disadvantages of each thermochemical process commented above.

Table 1.2. Advantages and disadvantages of the main thermochemical processes.

Process	Advantages	Disadvantages	Materials	Ref.
Sorption	- High efficiency - Low cost - Low auxiliary elements - Low maintenance cost - Suitable tuning temperature	- Small scale - Instability issues - Corrosion	- Salt hydrates	[81,82,92–95,132]
Hydration	- Cheap materials - Abundant materials - High volumetric energy density - Nontoxic materials	- Instability issues - Corrosion - Possible deliquescence	- Calcium hydroxide - Magnesium hydroxide	[107–110]
Carbonation	- High turning temperature - High energy density - Low price	- Sintering issues - Need to store reactant gas	- Calcium carbonate - Strontium carbonate - Barium carbonate - Magnesium carbonate	[83,111,113–116,118–121]
Redox	- High operation temperature - Non-corrosive products - No need of gas storage - Medium-high energy densities - No catalyst - Simple reactions	- High cost - Sintering issues	- Cobalt oxide - Manganese oxide - Copper oxide - Barium oxide - Iron oxide	[10,37,74,124–130]

2.2.2. Materials for Redox systems

Suitability studies have been conducted for years to determine which redox pairs have the best thermochemical storage performance [133–135]. Some oxides have been eliminated as their redox temperatures are too low (Cr_5O_{12}, Li_2O_2, Mg_2O), because of the presence of critical raw materials in their composition, because of their high processing cost (PtO_2, Rh_2O_3, UO_3) or because their non-reversibility (PbO_2) [136].

The most promising ones, due to their suitable operating temperature ranges, energy storage densities and acceptable cost and kinetics, are BaO_2/BaO, CuO/Cu_2O, Fe_2O_3/Fe_3O_4, Mn_2O_3/Mn_3O_4, and Co_3O_4/CoO [37,137]. Figure 1.18 shows a distribution of the different redox couples as a function of reaction temperature and energy density.

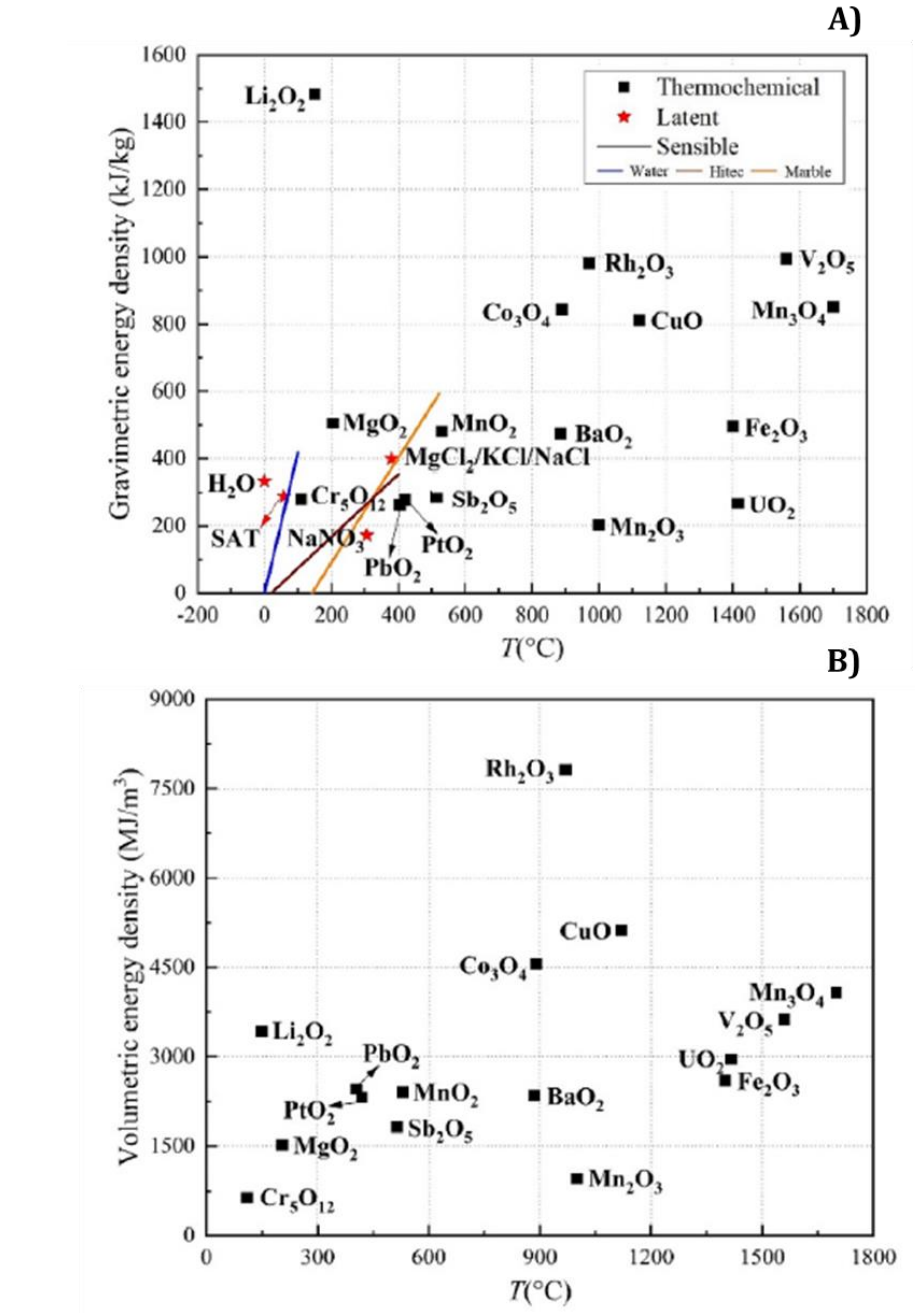

Figure 1.18. *Energy density versus energy storage temperature for A) metal oxide and some typical sensible and latent heat storage systems [137–143]; B) metal oxide systems [137,138].*

Table 1.3 lists the advantages and disadvantages of the most relevant metal oxides in the TcES field. The details of each metal oxide system are described below.

Table 1.3. Advantages and drawbacks of the most commonly studied metal oxides for thermochemical energy storage [138].

Material	Reaction temperature (°C)	Energy storage density (kJ/kg)	Advantages	Disadvantages	Ref.
BaO_2/BaO	738/880	390/526	- Abundance - Wide range of working temperatures - Moderate energy density	- Poor reversibility	[71,77,125,137,144–146]
CuO/Cu_2O	1042.5/1021.1	652/811	- High energy storage density - No catalyst required - Fast reduction kinetics - Flexibility in system design and operation - Low cost	- Melting - Slow oxidation	[137,147,148]
Fe_2O_3/Fe_3O_4	1145/1361	485	- Abundance - Low cost - Moderate energy storage density	- Strong sintering - Poor reversibility - High reaction temperatures	[77,147]
Mn_2O_3/Mn_3O_4	928/768	231	- Low cost - Not harmful - No catalyst required	- Slow oxidation - Low energy density - Incomplete reaction - Low cycling stability - Low toxicity	[147,149–152]
Co_3O_4/CoO	896/863	600/844	- High energy storage density - Good cycling stability - No catalyst required - Complete and reversible reaction - Fast reaction kinetics	- High cost - Toxic - Sintering	[9,147,149,150,153,154]

2.2.2.1. BaO_2/BaO

The barium oxide redox couple (BaO_2/BaO) was the first redox couple studied for TcES activities [146]. The research done on this material is very limited and the experiments were done in a small-scale furnace or in thermogravimetric analyzer (TGA). The material stability is not well determined because the maximum number of cycles tested is less than 30 [37].

The redox reaction that takes place can be described as:

$$2BaO_2 + \Delta H \leftrightarrow 2BaO + O_2 \quad (17)$$

Previous research works determine an energy storage density of these materials in the range from 390 kJ/kg to 526 kJ/kg [77,125,137,144,146]. The impurity of the materials, incomplete conversion or heat losses may be the possible causes of such deviation [125]. The theoretical weight loss during the reduction process is of 9.45% but, under some conditions, it may be higher due to some side reactions [125].

The reaction temperature of barium oxide varies depending on the calculation method and the experimental conditions. The values presented in literature are 738 ºC, 844 ºC and 880 ºC [77,144,145]. The differences may be due to the formation of solid solutions with the small amount of water of the system resulting in BaO_2 + $Ba(OH)_2$ and BaO + $Ba(OH)_2$ [155]. Different approaches can be used to reduce the reaction temperature: by mixing BaO_2 with other metal oxides, such as 10% CuO, MnO_2 or Fe_2O_3 [146,156] or by applying vacuum condition or reducing the total atmosphere pressure or oxygen partial pressure [125].

The kinetics of the material shows that the oxidation tends to be slower than the reduction, being the limiting step of the cycle [125]. Some authors identified that the reversibility of the reaction is subject to the heating rate and maximum temperature of experiment [146]. The conversion rate of the material is reduced to 22% in only 20 cycles due to the apparent degradation caused by

the thick ash layer of BaO_2, which develops a diffusion resistance around the particles and makes the rest of the BaO not available for the reaction. Another effect of the thick ash layer of BaO_2 is the pores blocking [144]. The sintering can be avoided by carrying out the reactions in a fluidized bed using extremely fine powder, where the ash formation is avoided [144].

Recent research works have demonstrated that the addition of MgO as a dopant leads to improved stability and reactivity of BaO_2 but reduces the energy storage density. More specifically, a BaO_2/MgO sample with 33 wt.% shows a good storage capacity over 200 redox cycles obtaining an energy density of approximately 290 kJ/kg [157].

To sum up, barium oxides are abundant and less harmful than cobalt oxide. They exhibit a lower reduction temperature than Co_3O_4, Mn_2O_3 and CuO [37]. They have a wide range of working temperatures, moderate energy density but a poor reversibility in pure state [71,125].

2.2.2.2. CuO/Cu_2O

The copper oxide cost is more competitive than other metal oxide candidates for thermochemical applications. This linked to its wide availability, makes it a possible candidate for TES technologies [158].

The CuO/Cu_2O redox couple was initially investigated in 1989 [159]. Since then and until 2011, research interest declined because the melting point of Cu_2O was considered too close to the reaction temperature, leading to sintering problems [37].

The reaction describing the redox process of the material is:

$$2CuO + \Delta H \leftrightarrow Cu_2O + {}^{1}/_{2}\, O_2 \qquad (18)$$

Low oxygen concentration in the gas stream (inert gas or similar) and a low gas pressure promotes the reduction of CuO according to the Le Chatelier principle [158,160], which proclaims that a disturbance applied to a system will move the system from its equilibrium state, but will have a counteracting influence on the effect of the disturbance [161].

The energy density of the CuO/Cu_2O redox couple is 811 kJ/kg, which is higher than other redox couples except Co_3O_4/CoO (~ 844 kJ/kg) [137].

The reaction temperature ranges from 700 ºC to 1100 ºC depending on the research work [74,159]. In this system, the oxidation temperature is notably lower than the equilibrium transition temperature, which reduces the oxidation heating requirements, thus offering flexibility in system design and operation [137].

The main issue with CuO is that its melting point is 1235 ºC, close to the reduction temperature and a significant grain growth is detected after thermal cycling [74,147]. The degradation of the material and the gas bypassing the shrinking packed bed leads to a decrease of the O_2 capture capacity [162]. For avoiding the sintering, some authors proposed to use a rotary reactor, in which the particles kept rotating and mixing [74]. This may be a new approach for the practical use of this material as energy storage candidate.

Another alternative to improve the cycling stability performance is to support the CuO with other metal oxides such as ZrO_2, $MgAl_2O_4$, CeO_2 and La_2O_3. Recent research works have demonstrated that the best alternative is the support of CuO with $MgAl_2O_4$ and $MgAl_2O_4$/ La_2O_3, obtaining a better O_2 release/consumption capacity [163,164].

To sum up, the advantages of the CuO/Cu_2O redox pair are the high density and its abundance. The reduction of copper oxide is faster than the oxidation, but the two reactions are strongly affected by the O_2 concentration of the HTC [74,77,162].

2.2.2.3. Fe_2O_3/Fe_3O_4

The few research works done on the Fe_2O_3/Fe_3O_4 redox pair show that the main advantages of this pair are the abundance, low cost, and moderate energy storage density (~ 485 kJ/kg) [77].

The redox reaction can be described as:

$$3Fe_2O_3 + \Delta H \leftrightarrow 2Fe_3O_4 + {}^1/_2\, O_2 \qquad (19)$$

The reduction temperature is influenced by the gas used in the experiment. It varies from 1361 ºC, under a gas containing a 20% of O_2 to 1145 ºC under argon atmosphere. [77]. The main characteristic for considering iron oxide as a suitable candidate for thermochemical energy storage is the conversion rate of Fe_3O_4 to Fe_2O_3 (92%) [77], but the redox temperatures are too high for being suitable for any application.

One of the problems that this material presents is the strong sintering observed after only three thermal cycles, notably decreasing its reversibility [147].

In general, it can be said thar the pure Fe_2O_3/Fe_3O_4 redox pair shows poor reversibility after thermal cycling and requires extremely high temperatures. The application of this material for thermochemical energy storage can be done by using it as an additive of other metal oxides such as cobalt oxide or manganese oxide improving the cyclability and the kinetics [9,165].

2.2.2.4. Mn_2O_3/Mn_3O_4

Manganese-oxygen system has four stable oxides [137]. Their reduction sequence is:

$$MnO_2 \rightarrow Mn_2O_3 \rightarrow Mn_3O_4 \rightarrow MnO \qquad (20)$$

Not all the reduction phases are suitable for thermochemical energy storage. For example, the reduction of MnO_2 to Mn_2O_3 is irreversible at atmospheric

pressure and the transition temperature of Mn_3O_4 to MnO is too high (1700 ºC) for practical applications [136,166]. Only Mn_3O_4 shows a reversible behavior in the temperature range from 500 ºC to 1050 ºC [167], so Mn_2O_3/ Mn_3O_4 is the only redox couple that could be used as TCS material.

The reaction of this redox couple is:

$$3Mn_2O_3 + \Delta H \leftrightarrow 2Mn_3O_4 + {}^1/_2\, O_2 \qquad (21)$$

The most important problem of this redox couple is the poor kinetics which result in a slow oxidation. A possible solution is the use of a low cooling rate to enhance the oxidation as the residence time at higher temperatures is more prolonged [37,72].

The energy storage density of Mn_2O_3 is theoretically 202 kJ/kg [125], a value much lower than that presented by BaO_2 (432 kJ/kg) and Co_3O_4 (844 kJ/kg). However, it is considered promising for high temperature energy storage applications due to its low toxicity and low cost [72,168].

The reduction and oxidation temperatures range from 550 to 1000 ºC, being suitable for high-temperature applications [169], but the large temperature gap between reduction and oxidation may have a serious effect on the efficiency of energy storage. A cascade structure, which consists in employing cascades of various porous structures, incorporating different redox materials distributed as a function of their thermochemical properties and of the local temperature of the heat transfer medium, can be suitable to reduce the temperature gap and thus, boost the efficiency [170].

One variable that has a big influence in the reaction characteristics is the particle size. A large specific area of smaller-size particle is beneficial to reduce the oxidation temperature of Mn_3O_4, but also brings severe sintering problem. This is caused by the densification sintering mechanism. In contrast, the coarse particles lead to a more open structure with larger pores [171]. The sintering

problem can be avoided by the addition of metal oxides such as iron or lithium [137,172]. Some research works have demonstrated that the addition of 10-15% of iron improves the performance of the manganese oxide, obtaining lower sintering and maintaining almost 90% of its capacity constant after 500 cycles. The main drawback is that the iron addition increases the reaction temperature [147,154,165,171,173].

Recently, a research work has proposed the addition of SiO_2 and Si^{4+} by different synthesis and addition methods, obtaining promising results. The silica improves the cyclability of the material without harming the reaction temperatures [174].

The structural form of the materials has also a great influence on the reaction characteristics. Thus, manganese oxide has better reaction kinetics in pellet form than in powder due to the low pressure drop induced energy losses and the better heat transfer characteristics for the flow-through pellets [169]. The same effect is observed with other oxides such as cobalt oxide.

Summarizing, the Mn_2O_3/Mn_3O_4 redox couple has low energy storage density and slow kinetics, but the low cost and the reaction temperature range makes this metal oxide a promising redox energy storage material.

2.2.2.5. Co_3O_4/CoO

The high energy density and the reversibility are the main qualities that make the redox couple Co_3O_4/CoO the most promising one for high temperature redox energy storage. The main drawback of cobalt oxide is its high cost [175], linked to its scarcity and its potential carcinogenic character, being potentially dangerous for human health [77].

The redox reaction of Co_3O_4/CoO can be described as:

$$Co_3O_4 + \Delta H \leftrightarrow 3CoO + {}^1/_2\, O_2 \qquad (22)$$

In the initial stages of research on this system, more attention was given to storage systems using pure Co_3O_4 in powder form but, when the experiments were done in a realistic condition like a rotary kiln, it was observed thar the completion of the reduction reaction was limited to conversions of ~50% [176]. Subsequently, efforts were focused on the development of systems employing Co_3O_4 in pellets and honeycombs, etc.

Analyses of the Co_3O_4/CoO redox pair have been performed from a laboratory perspective (TGA) to packed beds or rotary kilns. The number of redox cycles tested ranges from 1 to 500. Table 1.4 lists the past studies done in regard to the Co_3O_4/CoO redox pair.

Table 1.4. Past studies on the energy storage capability of Co_3O_4/CoO [13].

Ref	Physical form	Heating condition	Testing temperature and heating/cooling rate	Atmosphere	Cycles	Findings
[153]	Powder	TGA	780-960 ºC 20 ºC/min	Air, O_2	100	No degradation and no change in the surface area was found for one sample cycled between 870 ºC and 955 ºC.
[137]	Powder	Packed bed	500-900 ºC 10, 30 ºC/min	Air, N_2	1	The redox couple achieved full oxidation at a cooling rate of 10 ºC/min.
[137]	Powder	Packed bed, TGA	700-900 ºC 1, 10, 30 ºC/min	Air, N_2	500	The energy storage feasibility was proved yet more studies should be done regarding the oxidation.
[128]	Powder	Solar-heated rotary kiln	Up to 1000 ºC	Air, N_2, O_2	9	Confirmed the feasibility of using a solar heated rotary kiln for redox energy storage.
[79]	Powder	TGA	600-1100 ºC 10 ºC/min	Air, Ar	30	Co_3O_4 underwent 30 successful redox cycles and achieved full reversibility between 800 and 1000 ºC.
[123]	Thermodynamic analysis		777-977 ºC	Air	/	Confirmed the thermodynamic feasibility of integrating Co_3O_4 energy storage system with Air Brayton cycle.
[177]	Powder	TGA	177-940 ºC 10, 20 ºC/min	O_2, Ar	10	The Activation Energy of reduction and oxidation were determined as 247.21 kJ/mol and 58.07 kJ/mol respectively.
[136]	Powder	TGA	25-1250 ºC 10 ºC/min	Air, N_2, O_2	5	The redox storage system was found to be feasible at temperatures between 480 and 630 ºC by changing the oxygen content of the gas atmosphere.
[10,124,129,176,178–181]	Powder, monolithic porous structures (e.g., porous foam, denser pellet, honeycomb, coated cordierite)	TGA, packed bed	800-1100 ºC 5, 15 ºC/min	Air, Ar	Up to 100	Monolithic, porous, structured samples were capable of cyclic redox. Structure monolithic bodies can lower system pressure drop and improve the kinetics of Co_3O_4 redox couple.
[158]	Based on Neisses et al.'s study					Co_3O_4/CoO transition can be practically complete regardless of the selected parameters.

The theoretical enthalpy for Co_3O_4/CoO redox couple is 816-844 kJ/kg [77,137], higher than the practical one, which ranges from 495 kJ/kg in powder to 549 kJ/kg in a honeycomb [169,176]. The practical enthalpy is influenced by the materials' morphology and physical shape [37].

The reactions of this redox couple take place between 700 ºC and 900 ºC. The temperature range is strongly influenced by both the experimental conditions and the gas atmosphere used [77]. Theoretically, under air atmosphere, the turning temperature is 935 ºC and the transition temperature is 790 ºC [77]. Experimentally, when the HTF is air, the reduction reaction occurs in the temperature range 896-930 ºC while the oxidation reaction takes place between 863 and 910 ºC [72,128,147,169,176]. Other authors obtained 885-905 ºC as reduction temperature and 772 ºC for the pure Ar atmosphere [77,79].

The oxidation reaction of Co_3O_4/CoO is strongly influenced by the heating and cooling rates. Lower cooling rates guarantee higher degrees of oxidation because the residence time at higher temperatures is prolonged and the oxidation reaction is faster at higher temperatures. The sintering is a result of the prolonged exposure to high temperatures but it is beneficial for the increase of the oxidation rate [38]. A promising solution is the use of the pressure swing reaction, in which the redox reactions can be performed at the same temperature [182].

The kinetics of this redox pair is limited and it is affected by the reaction temperature, O_2 partial pressure and physical form [177].

The thermodynamic driving force can be changed by the variation of the partial pressure of oxygen. With a higher O_2 partial pressure it is obtained a slower reduction reaction following the Le Chatelier principle [153].

Regarding the physical form, large-sized powdered CoO particles cannot obtain complete oxidation due to the Co_3O_4 layer formed on the particle surface [137].

The reduction and oxidation of the dense cobalt oxide pellets are faster than those of powdered cobalt oxide due to the more intensive heat transfer [169].

The pair Co_3O_4/CoO has an excellent reversibility. Some authors have studied the stability of this redox couple, determining that after 10 cycles the mass change kept stable and near the theoretical values [138,177] but the selection of an adequate temperature range is a critical aspect for obtaining a correct behavior during cycling [138]. Thus, powdered Co_3O_4 maintains almost constant the reactivity for 100 cycles between 870 and 955 ºC, without appreciating any change at the surface [153] but if the cycling temperature is increased to 1100 ºC, the sintering observed is evident, resulting in a decrease of the reaction rate [183]. The physical form of the material affects the cyclability too. So, cobalt oxide extruded foams maintain their integrity for 30 cycles because their pores absorb better the generated thermal and chemical stress [179,180]. In the case of the cobalt oxide coated cordierite foams, the redox and structural stability is guaranteed for 100 cycles. Contrary, the pellets deform after 10 redox cycles [129].

The thermodynamic analyses have confirmed the feasibility of utility-scale application of Co_3O_4 redox energy storage system. The integrated system of the energy storage system, a Brayton cycle and a CSP plant could achieve a maximum cycle efficiency of 44% [123].

The main challenges associated to the use of the Co_3O_4/CoO system are the cost reduction, the suitability of its use for utility-scale applications, and the toxicity reduction. One possibility could be to combine cobalt oxide with less harmful and low-cost metal oxides [149], that also can lead to the decrease of the sintering degree, improving thus its cyclability, which is critical for its final application.

2.2.2.6. Co_3O_4/CoO based mixed oxides

The use of metal oxides as a dopant for cobalt oxide can lead to an improvement of its thermochemical properties. The most studied systems are those using iron oxide, aluminum oxide and copper oxide [138] as dopants, although there are other systems detailed in this section.

The Fe_2O_3/Co_3O_4 oxides allow to reduce the cost and toxicity of the material compared to pure Co_3O_4, as the proportion of iron in the mixture is cheaper and less harmful than the cobalt oxide. The mixed oxide shows a more stable microstructure than the pure material at high temperature, as a mixed spinel phase is formed when x=0.87 (x=Co/(Fe+Co)). The stability of the microstructure has advantages in the long-term cyclability, as it favors reactivity and cycling stability. The thermal hysteresis of the mixed phase is 35 ºC lower than the pure Co_3O_4 (50 ºC) [72,184], thus, reducing energy losses during cooling [9]. The main drawback of the mixed Co-Fe oxide is the decrease of the energy density with increasing amounts of iron doping. If the Fe doping percentage is 40%, the energy density decreases from 597 kJ/kg for the pure material to 50.7 kJ/kg for the mixed phase [150,154,185].

The Al_2O_3/Co_3O_4, forming the phase $(Al_xCo_{1-x})_3O_4$, has limited grain growth and enhanced microstructural stability in comparison of the pure Co_3O_4 [137]. The main problem is the formation of a redox inactive mixed phase ($CoAl_2O_4$) lowering the redox activity [129] and delaying or even inhibiting the internal reaction, as the content of Co_3O_4 is reduced on the surface due to the presence of $CoAl_2O_4$, and the rest gets encapsulated into a stable $CoAl_2O_4$ shell [186]. However, Al_2O_3 doping accelerates the redox reaction kinetics, leading to a decrease in the thermal hysteresis of the pure cobalt oxide [169,187]. The enthalpy and structural stability of the Al_2O_3/Co_3O_4 based honeycombs remain high after a long-term cycling [188], but if the scale of the honeycombs is larger, the calcination causes the structure to collapse, which could be caused by the

removal of the organic content. Some more controlled calcination steps have been tried but the collapse of the structure has not been avoided [132].

The CuO/Co_3O_4, forming the phase $(Cu_xCo_{1-x})_3O_4$, lowers the sintering and stabilizes the structure of pure Co_3O_4 at high temperature (>1000 ºC) [183]. In long-term cycling processes, the mixed oxide improves the reaction kinetics, being faster than the pure cobalt oxide [183]. The addition of the copper affects the reaction temperature, making it lower than the one of the pure oxide, but the enthalpy of the mixed oxide decreases with increasing amounts of Cu [150,185]. It is possible to obtain a $CuCo_2O_4$ mixed phase if the Cu doping ratio is higher than 33%, resulting in the deactivation of the material [79].

Regarding other systems, Co-Mn mixed oxides show lower redox properties than pure cobalt oxides [149,150,183,189], Co-Zn oxides show problems of volatilization at high temperatures and Co-Mg oxides show very low oxidation rates and incomplete reactions [79]. The addition of Ce and YSZ does not guarantee structural stability in pellets form [129] and Co-Si based honeycombs suffer from serios structural deformations [87,187].

Table 1.5 and Table 1.6 list the characteristics of the different cobalt oxide-based systems found in bibliography.

Table 1.5. Comparison of the technical characteristics of cobalt oxide systems [138].

Material	Doping ratio	Physical form	Energy storage density	Reaction temperature (°C)		Thermal hysteresis (°C)	Charge and discharge times (min)		References
				Reduction	Oxidation		Charge	Discharge	
Co_3O_4/CoO	-	Powder	495-600	885-926.9	804.5-910	30-93.1	5.4-19	5.1-22	[9,10,183,79,136,149,150,153,154,169,181]
		Pellet	513-609	910	855	50	16-17	18-20	[129,169]
		Honeycomb	549	905	875	30	14	16.4	[10,176]
Co_3O_4+ Fe_2O_3	5% Fe	Powder	454	921	848	73	-	-	[150,183]
	10% Fe		365	931	896	35	-	-	
	13% Fe		433	927.7	916.5	8.2	9	7.9	
	25% Fe		244	933	914	19	-	-	
	33% Fe		165	934	927.9	6.1	12.1	13.9	
Co_3O_4 + Mn_2O_3	2% Mn	Powder	499.09	902	906	-4	8.5	7.6	[72,183]
	7% Mn		380	914	975	-61	7.4	13.2	
	10% Mn		293	935.3	906.9	28.4	10	12.7	
Co_3O_4 + CuO	3% Cu	Powder	461-574	893.6-896	860-871	22.6-36	7.8	7.4	[79,150,183]
	7% Cu		470	866.5	862.9	3.6	7.3	8.2	
	10% Cu		457-570	865.5-867	845-859.5	6-22	6.9	7.5	
	20% Cu		412-520	864-867.6	824-842.9	24.7-40	5.3	6.2	
Co_3O_4 + MgO	33% Mg	Powder	-	855	-	-	-	Very slow	[79]
Co_3O_4 + Al_2O_3	11.3% Al	Honeycomb	513	-	-	-	15.7	18.6	[176]
	20.8% Al		400	-	-	-	12.2	14.5	

Table 1.6. Comparison of the technical characteristics of cobalt oxide systems. Continuation [138].

Material	Physical form	Micro/macrostructural stability	Cycle life	Reversibility	Cost	Toxicity	References
Co_3O_4/CoO	Powder Pellet Honeycomb	High Deformation Deformation High (coated honeycomb)	>100 <10 >30 (coated honeycomb)	Good	Co_3O_4 (≥73%) $49600/Ton	High	[137,153,177,183,190] [129] [10,87,188,191]
Co_3O_4+ Fe_2O_3	Powder Pellet Honeycomb	Light sintering Slightly high Deformation	>500 >10 <29	Moderately good	Moderately high	Moderately high	[137,192] [129] [187]
Co_3O_4 + Mn_2O_3	Powder	Sintering	-	Good			[149,150,183,189]
Co_3O_4 + CuO	Powder	Light sintering	>40	Moderately good			[183]
Co_3O_4 + MgO	Powder	-	-	Moderately poor			[79]
Co_3O_4 + ZnO	Powder	Zn volatilization	-	Very poor			[79]
Co_3O_4 + SiO_2	Honeycomb	Deformation	<38	Good			[187]
Co_3O_4 + Al_2O_3	Powder Pellet Honeycomb	Light sintering High High	>500 >10 >104	Good			[137] [129] [154,183]

Based on the published research works it can be concluded that the addition of metal oxides to the cobalt oxide can improve the structural stability, improve the cyclability, reduce the cost, reduce the toxicity and change the thermal hysteresis by modifying the reaction temperatures. However, it is necessary to note that the enthalpy of the mixed oxides decreases with the amount of doping metal oxides. Therefore, the amount of dopant must be adjusted following a compromise between the energy density and the cycling efficiency.

2.2.3. Applications

Thermochemical storage can be suitable for applications which are supported by other types of thermal heat storage, not being a substitute for sensible or latent heat storage systems. The main application areas of TCS are [33]:

- Solar concentrated power plants (CSP). The molten solar salt formed by a mixture of sodium and potassium nitrates ($NaNO_3/KNO_3$, 60/40 wt.%) is typically used for storing heat in the operation range 290- 565 ºC [193–195], but some systems of CSP such as tower plants can reach temperatures up to 1000 ºC using adequate receivers [196–199]. The use of metal oxides could extend the temperature range in which solar energy from CSP plants can be harnessed.
- Industrial process heat. The reduction of thermal losses and the insulation of the industrial processes are essential. This can be achieved by the use of TcES technologies [200,201].
- Building engineering. The growth experimented in low/zero carbon buildings has promoted the development of thermochemical energy storage systems to reduce the excessive consumption of energy from fossil resources [202].

- Automotive thermal management. TcES systems are used to store the waste heat coming from the powertrain and to reuse it for heating purposes before or during the driving [203].
- Seasonal storage and peak-shifting. As the largest heat demand occurs during winter and the renewable energy production is highly produced in summer, thermochemical energy storage systems can store the energy excess in the summer and release it during the winter period [204].
- Industrial waste heat, by storing the energy in form of heat released in a part of the process and re-using it in another step of the process where an energy supply is needed.
- Buffer storage in district heating. Most of the times small scale district heating networks are heated by a gas fired CHP. To maximize the profit of the CHP, it will be switched on at moments of high electricity prize. As there is a mismatch between the heat and electricity demand, thermochemical storage systems can be used to sort the gap [205].
- Domestic heating, cooling and hot water applications. The use of thermochemical energy storage allows the development of efficient cooling and heating systems with lower power consumption, lower CO_2 emissions and better network stability [206].
- Thermochemical protection layer for temperature stabilization [23,24]. When the temperature of a metallic component increases, the thermochemical layer stores heat, buffering the temperature raise while the reaction is taking place. When the temperature of the component cools down, the oxidation reaction releases the stored heat and maintains the metallic component at higher temperature, resulting in a buffering of the temperature changes in the compound.

In addition to the thermochemical applications, metal oxide systems are commonly used in other fields such as [138]:

- Chemical looping with oxygen uncoupling [207].
- Separation of O_2 from air [153,208].
- Recycling of industrial flue gas heat [136].
- Solar hydrogen production [160,209–211].
- CO_2 splitting [212].
- Oxygen pumps [213].
- Heat pumps [214].

2.3. Thermal Barrier Coatings (TBC)

2.3.1. Traditional TBC

Thermal barrier coatings have been widely used in applications such as gas turbines and diesel engines for protecting purposes [215–219]. The function of the coating is to reduce the heat transfer from the high temperature gas to the metal surface. Thermal coatings act as insulators in hot sides increasing the temperature difference between the carrier (hot gas) and the coated metallic component increasing both the materials lifetime and the energy efficiency of the process. [220,221].

The criteria that a material must fulfill for TBC applications are: low thermal conductivity, no phase transformation between room temperature and application temperature, good sintering resistance, favorable chemical stability, matching thermal expansion coefficients (TEC) and toughness with the metallic substrate [216,222–224].

A typical thermal barrier coating consists of a multilayered structure consisting on: the bond coat and the top coat. The first one acts as oxidation resistant and the second one as thermal resistant [215]. The most widely used materials for these two layers are: a diffusion aluminide or overlay MCrAlY in the case of the bond coat and a 7-8 wt.% Y_2O_3-stabilized ZrO_2 (7YSZ) ceramic material in the case of the top coating [225,226].

Wokon et. al purposed a new concept of active thermal barrier coating [23,24] for reducing or retarding the thermal fatigue of the materials. The difference with the traditional ones is the principle of heat dissipation. In these new active coatings, chemical reactions are used to regulate the temperature of the metallic materials to be protected while in the traditional ones the main function of the coating is to isolate the material to be protected.

2.3.2. Thermochemical protection coatings for temperature stabilization

2.3.2.1. Operating principle

A side effect of the thermochemical reactions is the temperature stabilization during the course of the reaction. Metal oxides can be applied for dynamic buffering of processes or components sensitive to recurrent temperature changes, since they exhibit thermal hysteresis in the redox reaction and they present a high reactivity in the endothermic and exothermic reactions [23].

The objective of this type of coatings is to avoid or delay as much as possible the thermal fatigue of the metallic components. Protection is given by coating the metallic components to be protected with metal oxides to form “active ceramic coatings” [23,24]. When the reduction temperature is reached, the thermochemical material stores the heat in the form of reaction enthalpy, so

that the component coated with the thermochemical material does not suffer a variation of temperature until the reaction is completed. When the temperature of the system drops to the oxidation temperature, this reaction begins to release the heat, not allowing the temperature of the coated component to decrease. This results in a buffering effect on the temperature variation of the metallic component.

The metal oxides used for this application should be designed based on the temperature range of the thermal hysteresis, which should match the temperature range of the application.

A scheme of the two types of TBC is depicted in Figure 1.19. The main differences between the traditional and active TBCs are:

- Presence of reactions: The traditional thermal coatings protect the metallic materials by isolating them from the heat source. The new concept of reactive thermal coatings buffers the temperature change of the metallic materials by storing/releasing heat through thermochemical redox reactions.
- Nature of layers: The traditional thermal coatings are formed by two layers of different composition and purpose (bond-coat and top-coat). The reactive thermal coatings consist of a multilayered structure of identical composition and purpose. The number of layers depends on the necessities of heat dissipation as more layers result in higher heat dissipation.
- Distribution of the coating: While the protective materials are applied between the heat source and the metal component in the case of the traditional coatings, the protective materials of the active coatings are not applied in the side of the heat source, as in many cases the heat source does not have oxygen. Instead, the layers need to be coated on the side exposed to ambient or to a O_2 containing atmosphere to activate the redox reactions [23].

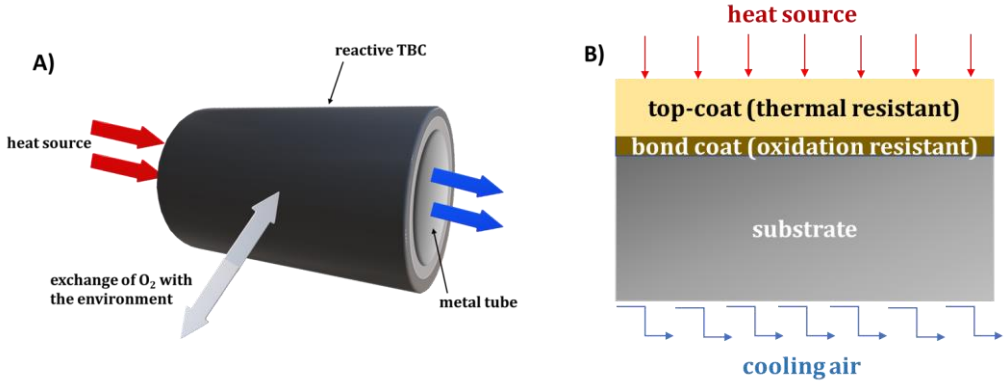

Figure 1.19. *Scheme of A) reactive ceramic TBC and B) traditional TBC.*

One of the most critical aspects for the selection of materials to formulate the new concept of reactive coatings is to obtain a high energy storage density, since the thickness of the applied layer is limited with the consequent limitation in the storage/buffering capacity [23].

Among metal oxide materials, cobalt oxide may be a suitable material for this application, but the long-term applicability and the safety issues related to its nature, make necessary to eliminate the possibility of spallation of the layer [23].

The main drawbacks of the novel active TBCs are:

- The degree of maturity of the technology: There are less than five research works dealing with this concept as the technology is at a very early stage.
- The way of deposition of the coatings: It is necessary to obtain a compromise between thermochemical activity and thermal and mechanical stability. This motivation leads to study different application methods and curing processes.
- The number of layers to be applied and their thickness, which is directly related to the storage capacity.

- The long-term behavior: There is no information regarding the behavior in a prolonged thermal cycling process involving chemical reaction.

2.3.2.2. Application examples

Previous research works have used the new active thermal barrier coating concept in applications such as protection of electronic devices and solar receivers.

In regard to the protection of electronic devices, some authors have applied the thermochemical energy storage in a system containing an active thermal barrier coating [26]. The system is composed of 3 layers with heat reflection, heat insulation and thermochemical heat storage purposes (Figure 1.20). This system has been designed to protect a black box from a high-temperature environment at 650 ºC.

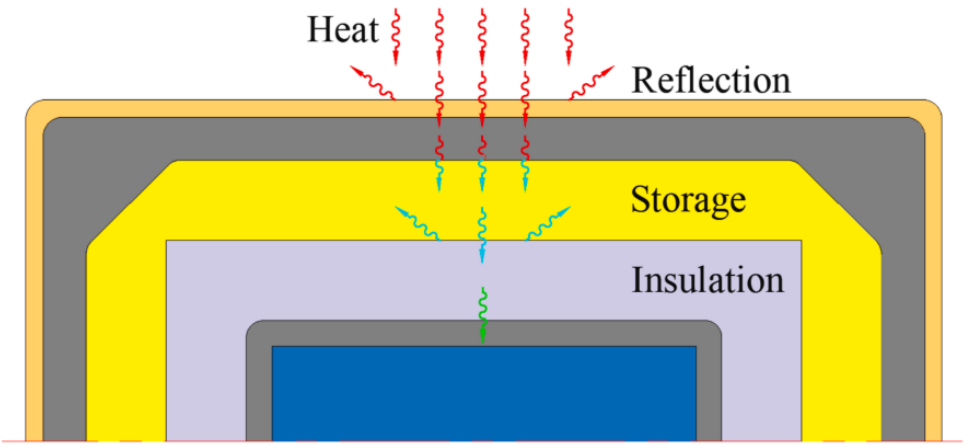

Figure 1.20. *Schematic diagram of the insulation-storage-reflection heat protection scheme [26].*

The system uses boric acid as thermochemical storage material with a decomposition temperature of 112.9 ºC, which is close to the thermal protection temperature of the circuit board, an aerogel with a thermal

conductivity of 0.0311 W/(m·K) as insulation material and a thick aluminum foil as reflection material. The experiment consisted in exposing the black box to an ambient temperature of 300 ºC. The heat flow increased rapidly at the beginning of the experiment but when the boric acid started to absorb heat, it quickly decreased to lower values than in the case of the same systems without thermochemical storage, reaching a buffering effect of the coating of 800 s at 100 ºC.

Regarding the protection of solar receivers, another research work proposes the use of thermochemical reactive coatings [25], as it is shown in Figure 1.21.

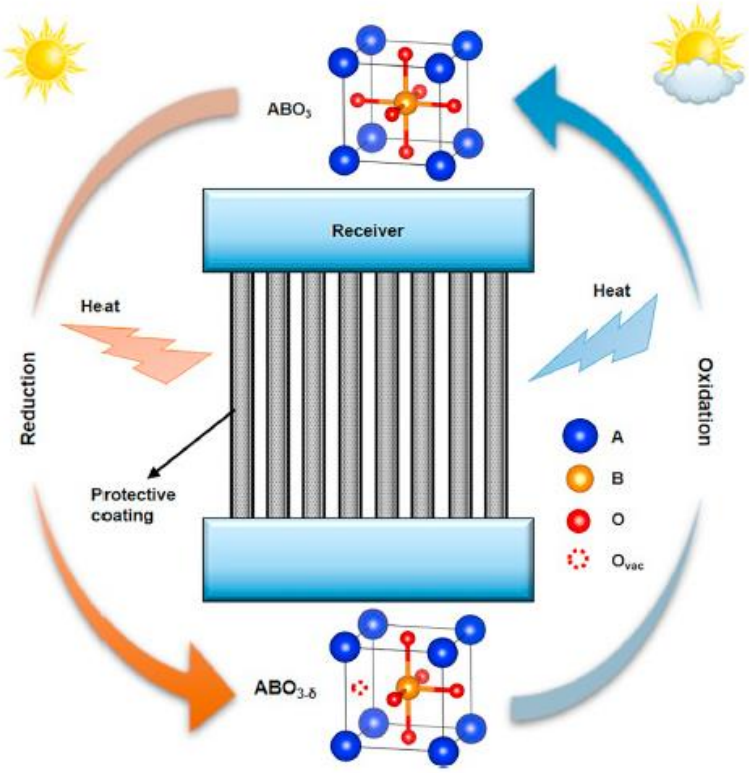

Figure 1.21. *Schematic illustration of thermochemical protective coating for molten salt receivers [25].*

The study focuses on the development of thermochemical barrier coatings using $BaCo_{1-x}Mn_xO_{3-\delta}$ perovskites, with reaction temperatures between 400 ºC and 700 ºC, as thermochemical material where x ranges from 0 to 0.4. One of the perovskites ($BaCo_{0.8}Mn_{0.2}O_{3-\delta}$) was tested in a laboratory-scale receiver. The average thickness of the coatings was 250 µm. The results demonstrate that the protective coating can alleviate the thermal shock of the receiver by changing the heating rate of the tubes, from 8.5 ºC/min without coating to 3 ºC/min with coating, in the first 2 min of experiment. On cooling, the rate of temperature change was reduced by 3.5 ºC/min in the first 2 min. However, the research work shows no evidence of a thermochemical reaction. The mechanical stability of the coatings was assessed in a tubular furnace in a temperature range of 600-700 ºC for 120 cycles [25].

2.3.3. Potential applications

There are some potential areas of application of the reactive ceramic coatings at high temperature [23].

- Exhaust manifolds installed downstream of internal combustion engines (e.g., in cars, motorcycles).
- Components for the construction of industrial furnaces and for heating engineering (e.g., temperature stabilization of gas jects).
- Components of solar receivers subjected to high temperatures [25].
- High temperature reversible solid oxide electrolyzer and fuel cells (SOEC/SOFC) [227].
- Protection of electronic devices [26].

2.4. Mixed metal oxides for TES applications

2.4.1. Preparation methods

The synthesis of materials with well-defined size and morphology, and controlled porosity are some of the critical aspects to obtain desirable physical and chemical properties [228–231]. Therefore, the synthesis of materials controlling all these aspects remains a major challenge. Traditional synthesis methods can be classified into dry methods (solid-state reaction method) and wet methods (co-precipitation, hydrothermal, sol-gel Pechini and sol-gel Stober). The main characteristics of each method are explained below.

2.4.1.1. Solid-state reaction method

The solid-state method, also named ceramic method, is commonly used to obtain a new solid material with a defined structure from solid starting materials. Possible products obtained by this route include polycrystalline materials, single crystals, glasses and thin-film materials [232].

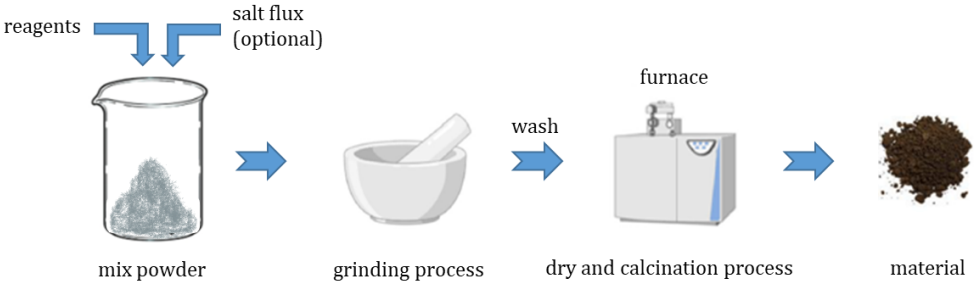

Figure 1.22. *Schematic process of a standard solid-state synthesis method [233].*

The process, depicted in Figure 1.22, consists of a reaction between the dry raw materials carried out by thermal treatments to accelerate the reaction [233]. For this purpose, the metallic compounds are combined in a milling process and heated at a controlled temperature for a certain time. Sometimes the conditions for synthesizing metal oxides and salts are very extreme, requiring high temperatures and pressures [232].

This route has simple reaction conditions, short synthesis time and allows mass production [234]. The main disadvantage is the extremely high sintering temperature (>1000 ºC) needed for the synthesis, associated with enormous energy consumption [235]. Another drawback is that irregularly shaped particles are obtained [233].

2.4.1.2. Co-precipitation method

Co-precipitation is a simple, efficient, large-scale and inexpensive method for the synthesis of powdered samples. This synthesis route is suitable for preparing composites and performing doping of materials [236].

The process consists of two stages [237]: (i) nucleation, which occurs when the concentration of species reaches critical supersaturation, and then, (ii) a slow nuclei growth by diffusion of the solutes to the crystal surface.

The size and shape of the materials is very influenced by the pH, ionic strength, temperature, nature of the salts and the ions concentration ratio, so for obtaining the desired materials it will be necessary to adjust all the parameters [238].

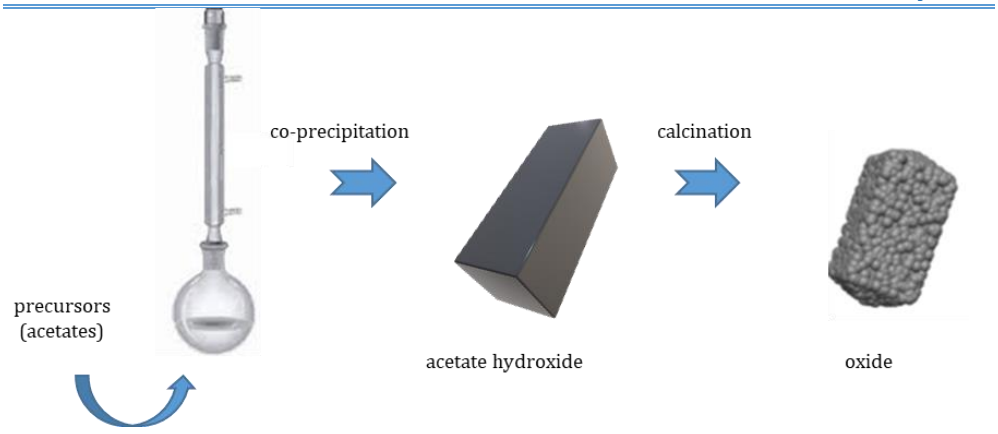

Figure 1.23. *Scheme of a co-precipitation process for the obtention of Ni-Co-Mn oxides [239].*

The main advantages of this route, which is shown in Figure 1.23, are: the great quantity of material obtained linked to the process scalability, the easiness, possibility to produce ultrathin powders, homogeneous and at relatively low temperatures [240]. However, the control of crystal size is strongly influenced by growth kinetics [241].

2.4.1.3. Hydrothermal method

The hydrothermal route is a controlled precipitation through water vapors heating. The material preparation is done by the formation of a solid phase in the transformation of a supersaturated solution into a saturated state [236]. The process is schemed in Figure 1.24.

The phases of the process are: nucleation, aggregation, coalescence and growth of particles. A heterogeneous reaction takes place in the nucleation forming clusters of molecules, which are the foundation of the aggregation of the particles. The aggregation of the particles is a basis for the nanostructure formation [236]. The most critical variables to control the size, crystallinity, shape and magnetic properties of the synthesized materials are the

temperature of the process, the precursors, the reaction time and the pressure [242].

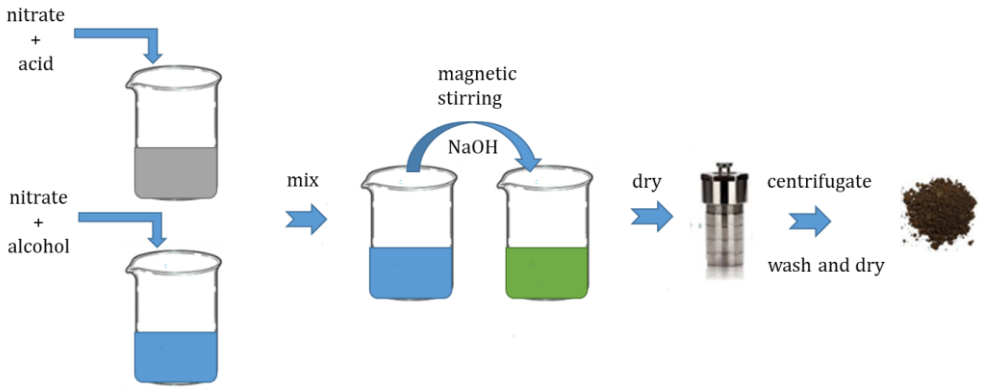

Figure 1.24. *Scheme of the hydrothermal synthesis of $CuBi_2O_4$ [243].*

It is necessary to point out that both in the co-precipitation process and in the hydrothermal synthesis process it is necessary to wash and dry the materials obtained, using high quantities of solvents [239,244].

The main drawback of this route is the use of a high vacuum step, increasing the cost of the process.

2.4.1.4. Sol-gel Pechini method

The sol-gel process, also known as chemical solution deposition, consists in solid particles suspended in a liquid forming the sol. When these particles are polymerized by partial evaporation of the solvent, or by addition of an initiator, the gel is formed, which is heated at high temperature to obtain the final solid products [245–248].

The Pechini route has been widely used to produce different morphologies of nanostructures including nanorods, nanoplates and nanoparticles.

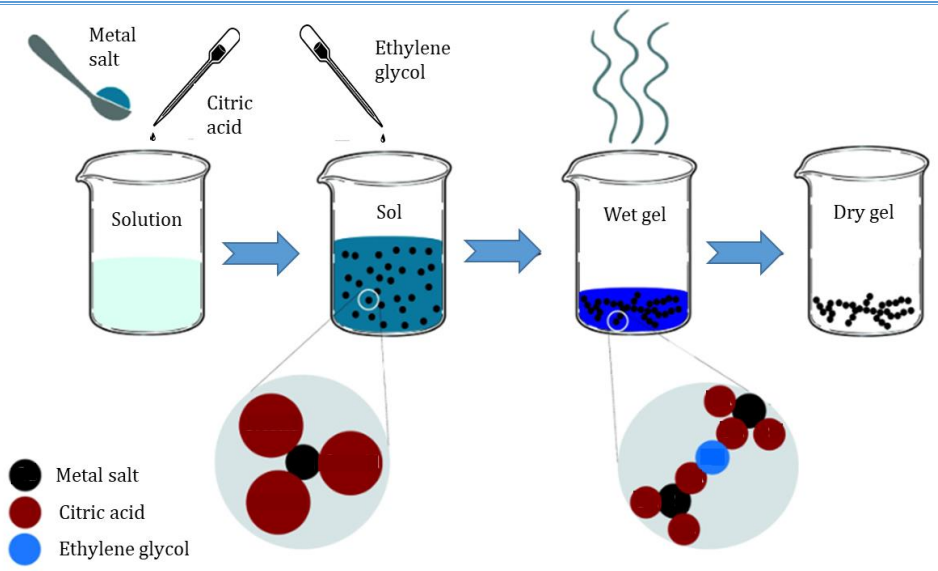

Figure 1.25. *Schematic diagram of the Pechini process for the synthesis of pure CuO [249].*

The Pechini route uses metal salts, ethylene glycol and citric acid to synthesize metal oxides [250], following the route described in Figure 1.25. The process is based on the chelation of metallic ions by citric acid, undergoing poly-esterification with polyhydroxyl alcohols such as ethylene glycol to form a polymeric precursor [251]. The process in detail is based in the polymerization of metal citrate by ethylene glycol. Firstly, the metal salt is dissolved and chelated by citric acid. This is produced by the combination of metal ions with citric acid with more than one bond. Subsequently, ethylene glycol interconnects these complexed molecules formed. Lastly, the condensation process takes place, creating large molecules [249,250].

Pechini is a well-known Sol-Gel route of preparation of nanoscale materials. This route is useful, simple, cost-effective and has a simple process for grain size and shape controlling of nanoscale materials using quite low annealing temperatures [236,252–254]. The materials obtained by this route are high purity powders with homogeneous compositions. Besides, the stoichiometric ratios can be controlled easily [249,250].

2.4.1.5. Sol-gel Stober method

A widely used method for obtaining colloidal silica nanoparticles is the sol-gel Stober route [255,256]. During the last decades, many research works have studied the features of Stober process. [255–259]. The growing interest in the Stober method in recent years has led to many opportunities and developments in the field of nanoscience and materials chemistry [260].

The process consists in the hydrolyzation and condensation of silica precursors, nucleation and aggregation processes for the growth of the silica. The sol-gel hydrolysis of tetraethyl orthosilicate (TEOS) is catalyzed by ammonia in the presence of water and low molecular weight alcohols such as ethanol. The hydrolysis is followed by a condensation reaction [260–265]. A schematic illustration of the whole process is depicted in Figure 1.26.

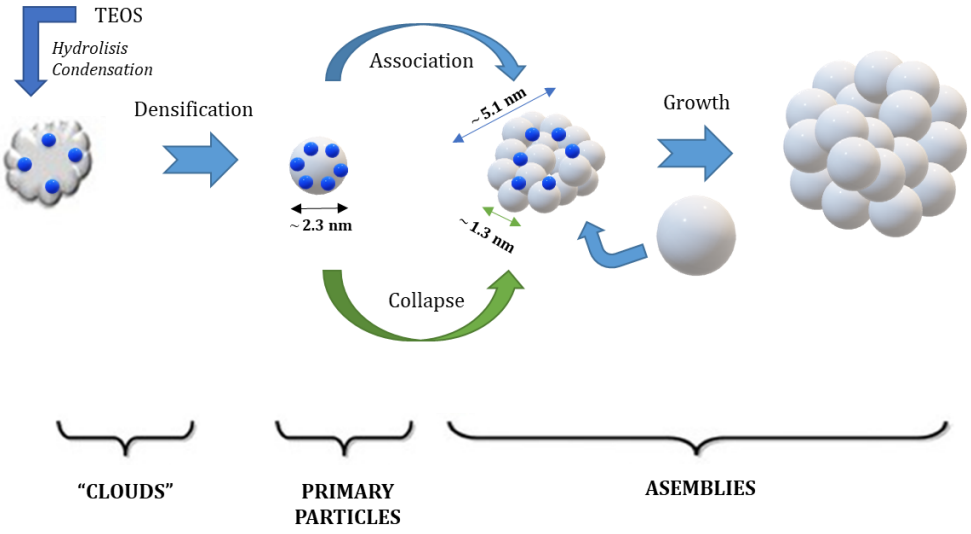

Figure 1.26. *Schematic illustration of proposed mechanism for formation of monodispersed silica colloids [260,266].*

After the publication of the Stober method, a pioneering work on the synthesis of colloidal silica nanoparticles, the research work focused on the control of

silica particle size for different initial reactant concentrations [267] and process temperatures [268].

It was demonstrated that in this synthesis method, the process temperature has a great impact on the final particle size. When the temperature is low, the nucleation rate of the particles is also low, resulting in fewer large particles. If the temperature is increased, the nucleation rate is faster, so the amount of smaller particles increases.

The main advantage of the Stober method is the possibility of controlling the particle size, distribution and morphology by the variation of the reaction parameters [269,270].

To sum up, Table 1.7 lists the main characteristics of each synthesis route.

Table 1.7. Summary of the characteristics of the wet and dry synthesis methods.

Synthesis route	Purity	Morphology	Advantages	Cost	References
Solid-state	High	Irregularly shaped particles, polycrystalline materials, single crystals, glasses and thin-film materials	Allows mass production	High: The calcination temperature is very high	[232–235]
Co-precipitation	Medium (it is necessary a washing step to reach high purity)	Powdered samples, composites and doped materials	The great quantity of material obtained, the easiness, possibility to produce ultrathin powders, homogeneous and at relatively low temperatures.	Medium: it is necessary to wash and dry the resulting material.	[236,239,240,244]
Hydrothermal	Medium (it is necessary a washing step to reach high purity)	Aggregated particles	It can be easily controlled the size, crystallinity, shape and magnetic properties of the synthesized materials	High: High pressure step is necessary and wash and dry the final material	[236,239,242,244]
Sol-gel Pechini	High	Nanoscale materials, multicomponent metal oxide materials	Simple process for grain size and shape control, easy control of stoichiometry and homogenous composition	Cheap	[236,249,250,252–254,271]
Stober	High	Nanoparticles (sferes)	Particle size, distribution and morphology easy control	Cheap	[269,270]

2.4.2. Sintering issues

Sintering is a phenomenon that occurs in almost all metal oxides used for thermochemical energy storage. This phenomenon occurs when the material is thermally cycled, as the material tends to densify when exposed to high temperatures. This results in a worsening of the cyclability of the materials, considerably reducing their activity, and therefore, the ability to store/release energy.

The investigations of the sintering phenomena are concentrated in the densification and microstructure development of the ceramic materials [272]. A sintering process can be defined as a thermal treatment used for bonding particles to form a solid structure via mass transport events occurring on the atomic scale. The bonds between particles improve the strength and lower the system energy [273]. The two main processes taking place in the sintering are depicted in Figure 1.27.

If two identical particles are in touch at high temperatures, the particles evolve to a new equilibrium shape, minimizing the total surface energy and grain boundary energy (the smaller ones start to shrink and disappear forming a large coarsened particle). This is reached by diffusional mass transport [274]. The motion of the surface and of the grain boundaries causes the particles to change in volume [274].

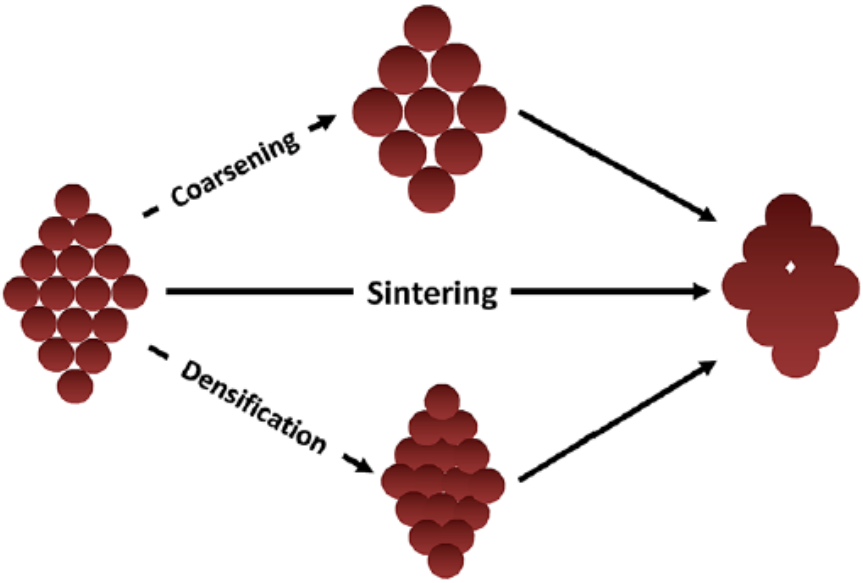

Figure 1.27. *Schematic view of the two main processes involved in the sintering: coarsening and densification [275].*

The green densities, pore size distributions and initial particle size have no influence on the grain growth, but affect pore growth and, as a consequence, the densification behavior of the material [272].

As already pointed out, in the case of powdered metal oxides used for thermochemical energy storage, sintering is an undesirable effect since it reduces the cyclability performance of the materials. To reduce the sintering effects triggered by the thermal repetitive cycles, two alternative routes can be followed: (i) the synthesis of mixed metal oxides, by doping another metal oxide in the host structure of an existent metal oxide, or (ii) the addition of particles/nanoparticles of a non-reactive material to the metal oxide, to stabilize the material.

3. Scope of the thesis

The present research work has been proposed based on the shortcomings observed in the state of the art regarding the existing solutions for the thermochemical energy storage at high-temperature.

The selection of redox reactions has been based on the wide temperature range they can cover (350 - 1100 °C), which makes them suitable for solar energy storage, but also for heat storage in a wide variety of processes.

The theoretical gravimetric energy densities of metal oxides are high (from 202 kJ/kg in the case of Mn_2O_3, up to 844 kJ/kg in the case of pure Co_3O_4) [276]. In addition, the use of air as HTF and as reactive gas at the same time makes the TES system design easier and cheaper. Another great advantage of this type of reactions is that they do not require catalysts and a subsequent separation of the products is not necessary, since the reaction that takes place is solid-gas.

The current challenges for these reactions are listed below.

- Challenge 1: There is an obvious lack of metal oxides working in the 600 - 900 ºC temperature range, as it can be observed in Figure 1.18. Having metal oxides that work in that temperature range would be interesting for applications such as CSP, industrial waste heat recovery or active thermal barrier coatings.
- Challenge 2: The cyclability of most metal oxides is strongly affected by the sintering that occurs in the material at high temperatures during the cycling processes.

- Challenge 3: The active thermal barrier coating concept based on thermochemical reactions is in a very early stage of development. In depth research is needed to make it suitable for real applications.

The main goal of this work is the development of novel Co_3O_4 based mixed oxides with lower reaction temperatures than pure Co_3O_4 for their application as active thermal barrier coatings. In order to achieve this main objective, based on the challenges observed in the state of the art, the following specific objectives have been formulated.

The **first objective** has been motivated by the challenge 1. It is based on the **obtention of mixed metal oxides with lower reaction temperatures** than in the case of pure metal oxide, while maintaining a good reversibility and high enthalpy. After a deep preliminary material selection, it has been decided to develop a solid solution between cobalt oxide and nickel oxide, as the Co_3O_4/CoO reaction temperature is around 900 °C, it has a high reaction enthalpy, adequate reversibility and no side reactions. The publication (DOI: 10.1016/j.solmat.2021.111194) entitled "Development of $Co_{3-x}Ni_xO_4$ materials for thermochemical energy storage at lower red-ox temperature" describes the achievement of this objective.

The **second objective** deals with the challenge 2. It has been centered on **improving the cyclability of the mixed metal oxides developed**. The literature details two main routes to accomplish this purpose, i) the development of doped structures with other metal oxides or ii) the use of additives of different nature to avoid the sintering. In this work, the second route was chosen, investigating the use of SiO_2 particles and nanoparticles, since a doping with metal oxides can interfere in the reaction temperatures, as detailed in the state of the art. The publication (DOI: 10.1016/j.est.2022.104876) entitled "Development and stabilization of $Co_{2.4}Ni_{0.6}O_4$ material for long-term thermochemical energy storage" details the research carried out on this topic.

To complete the study and provide useful information for a possible application, the **third objective** has been based on **the kinetic study of the materials** developed, both in their pure state and with added SiO_2 particles. The obtained results have been compared with the available published data for the pure cobalt oxide. The experimental results are presented in the publication (DOI: 10.3390/ma15103695) entitled "Development of a Kinetic Model for the Redox Reactions of $Co_{2.4}Ni_{0.6}O_4$ and $SiO_2/Co_{2.4}Ni_{0.6}O_4$ Oxides for Thermochemical Energy Storage".

Although the developed materials can be used as a heat storage medium in CSP solar plants or in other renewable energies that use power to heat to power technology, the present work has been focused on the development of novel protective active coatings.

The activity of the TBC is based on the redox reaction of the mixed oxides that constitute the coating, buffering the temperature changes of the metallic components exposed to high and variable temperatures, whether they are parts integrated in an industrial process, solar receivers, electronic devices, etc.

Thus, the **fourth objective** of the research work has been **the development of a novel active thermal barrier coating** using the thermochemical materials developed in this study, thus satisfying the need of the challenge 3. For this purpose, sol-gel solutions have been used to act as a binder of the thermochemical material but allowing the diffusion of the oxygen, necessary for the chemical reaction to take place. From this general objective, some secondary objectives have been defined:

- Obtaining a stable coating. For this purpose, the study of the formulation, deposition and curing protocol has been carried out. The thermochemical material/sol-gel ratios have been optimized and different routes of application and curing have been studied.

- Achieving the lab-scale performance of the coating (thermal cycling and mechanical stability) by testing the developed coating in thermogravimetric equipment in powder form and in a lab-scale furnace.
- Evaluating the performance of the coatings in a laboratory-scale test rig. For this purpose, a test rig, able to measure the temperature variations of the coated specimens, has been developed.
- Evaluating the performance of the coating in thermogravimetric equipment in coated form and comparing the results obtained in the test rig with them.

A new (the fourth) submitted publication entitled "Development of active thermochemical barrier coatings using metal oxides" shows the development and application of the thermal protective coating proposed in the fourth objective (more specifically, the first and second subgoals) and the thermal coating assessment has been presented in another submitted publication (the fifth) entitled "Active thermochemical barrier coatings using metal oxides – first experimental results", in line with the third and fourth subgoals of the fourth objective.

Figure 1.28 shows schematized the links between challenges, objectives and publications.

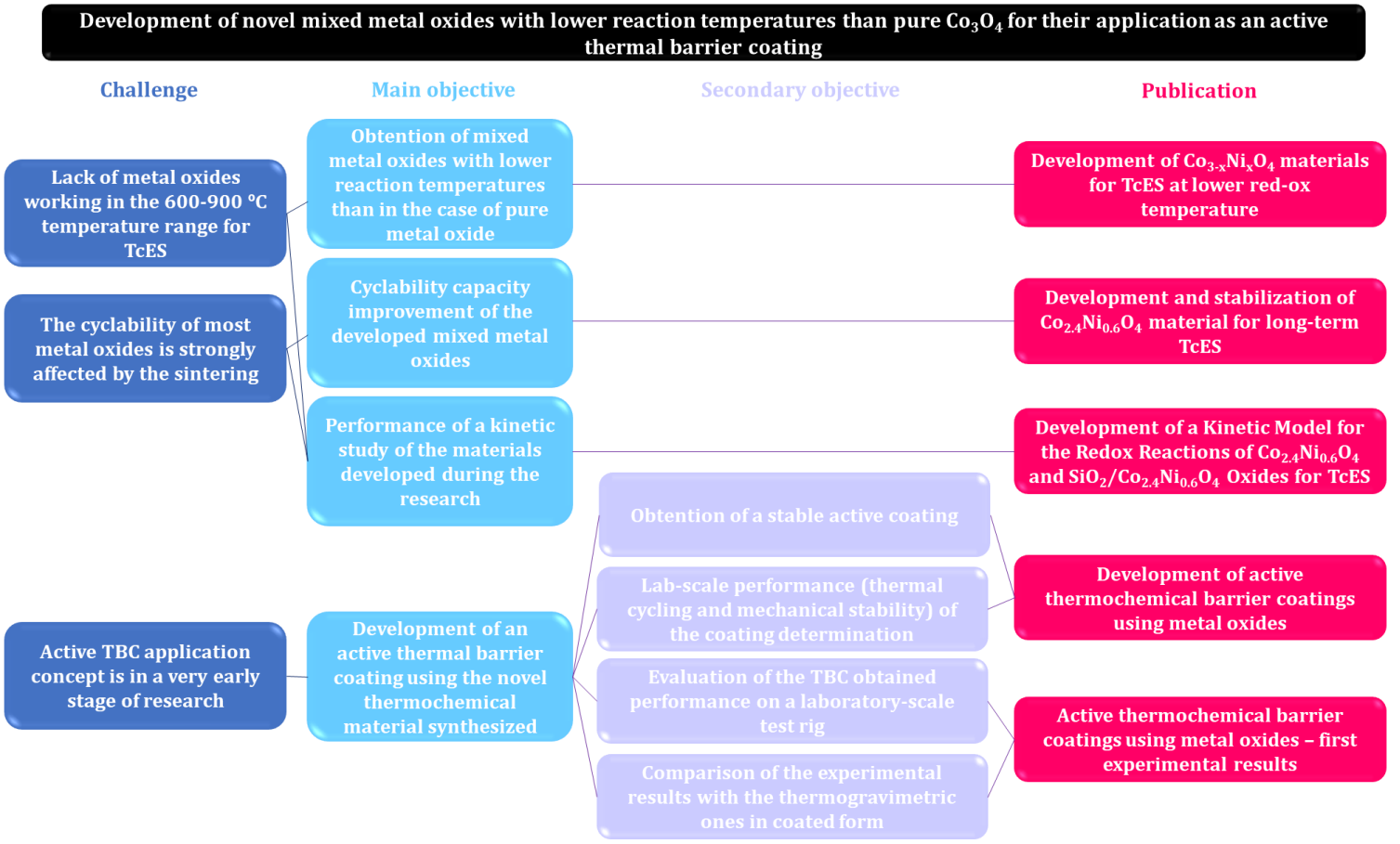

Figure 1.28. *Schematized structure of the research work in base of challenges, objectives and publications.*

4. Summary of the results

4.1. Selection of the Co-based mixed oxide

In order to lower the redox reaction temperatures, a suitable secondary metal oxide was selected for the formation of the mixed $Co_{3-x}M_xO_4$. The selection was made by analyzing the behavior of different combinations of materials.

For this purpose, the doping with 10% of different metal oxides in the cobalt oxide structure was performed following the Pechini route. The selection of the metal oxides was made based on the selection criteria of a suitable thermochemical material. The materials selected were: barium, iron, magnesium, manganese, zinc, nickel, chromium, strontium, copper and calcium.

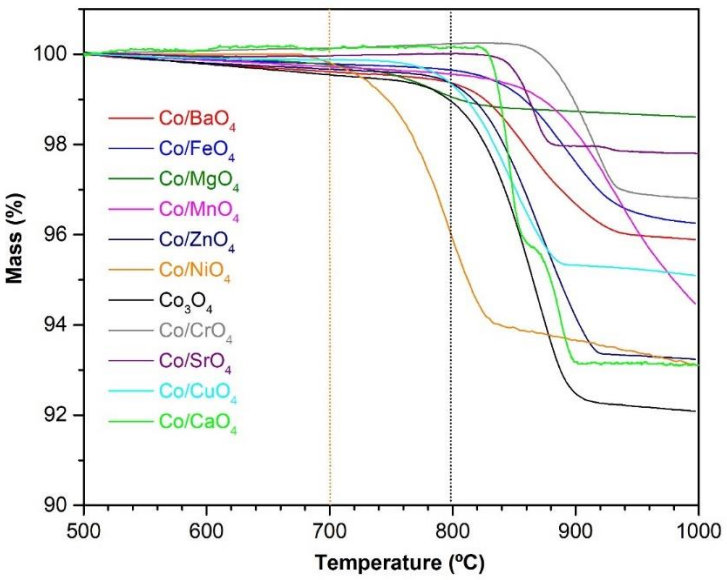

Figure 1.29. *Thermogravimetric curves of the cobalt mixed oxides.*

Figure 1.29 depicts the results obtained for the different doping combinations. As it can be observed, the most promising material was the one with nickel, as it shown a decrease of 100 ºC in the reduction temperature comparing with the pure cobalt oxide. The mass loss observed in the first attempt (~ 6%) was acceptable for a further study of the Co-Ni system.

4.2. Development of $Co_{3-x}Ni_xO_4$ mixed oxides

From the previous results, the cobalt-nickel mixed oxide was selected for a more in-depth study.

This study details the synthesis of $Co_{3-x}Ni_xO_4$ mixed oxides, with nickel contents (Ni^{2+}) (x) from 0 to 1. The main objective of the research work was lowering the reaction temperature, in comparison with pure cobalt oxide. The route selected for the synthesis of the mixed oxides was the Pechini sol-gel route. The resulting publication shows also the structural and morphological characterizations of the materials, including XRD, in-situ XRD and SEM.

XRD analyses confirmed the correct synthesis the mixed metal oxides from nickel contents (x) from 0 to at least 0.6. In the case of the compounds with nickel contents of 0.8 or 1, a high temperature irreversible phase of CoO·NiO was observed. In-situ XRD analyses showed the reversibility of the compounds with x lower or equal to 0.6 and a partial irreversibility of the compounds with x of 0.8 and 1.

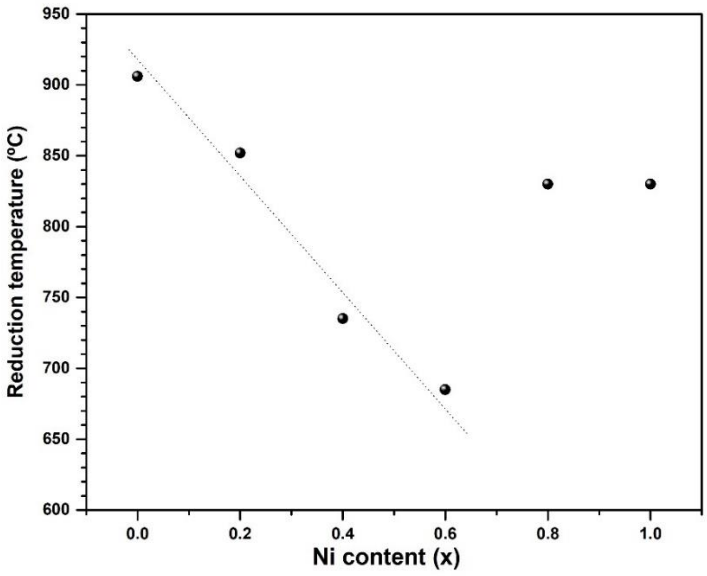

***Figure 1.30**. Reduction temperature evolution with the nickel content (x) in the $Co_{3-x}Ni_xO_4$ structure.*

The SEM images evidenced differences in the morphology of each composition, changing from foamy appearances to densified ones depending on the material, without following any criteria. The thermophysical characterization performed by TGA, showed good reversibility for the materials with nickel contents from 0 to at least 0.6. The materials with higher nickel content (from 0.8 to 1) showed low activity or irreversibility. The study shows how the nickel content in the cobalt oxide structure allow to tune the reduction temperature of the redox reaction, as in can be observed in Figure 1.30. In particular, the reduction temperature of the mixed oxides was lower (~ 200 ºC in some cases) than the one of pure Co_3O_4. The cyclability of the most promising mixed oxide ($Co_{2.4}Ni_{0.6}O_4$) was evaluated by performing a 100-cycle test.

The results obtained leads to propose the $Co_{2.4}Ni_{0.6}O_4$ mixed oxide as a suitable candidate for TcES. In-depth details of the research work are explained in the first publication in the Annex I section.

4.3. Stabilization of $Co_{2.4}Ni_{0.6}O_4$ for long-term TcES

This investigation aims to improve the cyclability of the mixed oxides selected ($Co_{2.4}Ni_{0.6}O_4$) by following two independent strategies. The first one consists of adding different percentages of SiO_2 particles and nanoparticles of different sizes to act as spacer and avoid the sintering. The second one consists of a post-calcination treatment of the materials (800 ºC 5h) with the aim of obtaining a stable morphology from the beginning, to achieve a constant cyclability in the whole experiment.

The results showed that the addition of silica particles keeps the reduction temperatures at lower values than in the case of pure $Co_{2.4}Ni_{0.6}O_4$. The cyclability of $SiO_2/Co_{2.4}Ni_{0.6}O_4$ was practically not affected in comparison with $Co_{2.4}Ni_{0.6}O_4$ in the short-term. Contrary, the extra-calcination step caused more sintering, which impaired cyclability. The XRD analyses demonstrated the absence of interactions between the SiO_2 particles and the mixed oxide, for at least 100 cycles. The SEM images showed that the mixed oxide with addition of SiO_2 particles had a particle size of 1-2 microns and exhibited sintering but in a minor degree than the material without addition.

The study is completed with a prediction of the behavior of the materials in 20 years (4000 cycles) based on the experimental results obtained (Figure 1.31). This confirms the best behavior in the case of $Co_{2.4}Ni_{0.6}O_4$ added with SiO_2 particles with an improvement in the conversion ratio of 12%.

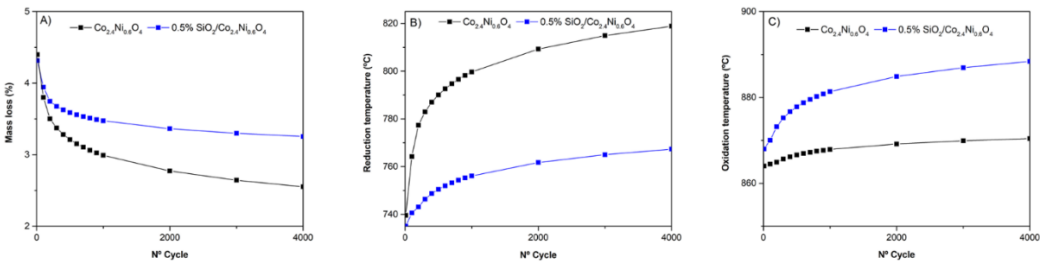

Figure 1.31. *Prediction results of A) Mass loss, B) Reduction temperature and C) Oxidation temperature for the materials $Co_{2.4}Ni_{0.6}O_4$ (black) and 0.5% $SiO_2/Co_{2.4}Ni_{0.6}O_4$ (blue).*

Based on these results, the addition of SiO_2 particles has better effect on stabilizing the mixed oxides than the post calcination step.

The details of the research are presented in the second publication which is attached in Annex I.

4.4. Kinetic model of $Co_{2.4}Ni_{0.6}O_4$ and $SiO_2/Co_{2.4}Ni_{0.6}O_4$ Oxides

To complete the study and to provide useful data in regard to the behavior of the mixed oxides for possible future scale up, a kinetic model of the $Co_{2.4}Ni_{0.6}O_4$ and $SiO_2/Co_{2.4}Ni_{0.6}O_4$ was developed.

This scientific work presents the kinetic study of pure $Co_{2.4}Ni_{0.6}O_4$ mixed oxide and $SiO_2/Co_{2.4}Ni_{0.6}O_4$ oxide. For the development of the kinetic study, multiple TGA tests were carried out, both in dynamic mode, varying the heating/cooling ramps, and in isothermal mode. Different gases were also used to vary O_2 partial pressures. The kinetic triplets of the two materials were obtained showing no modification of the activation energy in the case of the reduction step and an evident modification in the case of the oxidation step.

The mechanism describing the reduction step does not coincide in the two materials, observing good fittings of the experimental data with nucleation and growth mechanisms in the case of $Co_{2.4}Ni_{0.6}O_4$ and diffusion mechanisms for the 0.5% $SiO_2/Co_{2.4}Ni_{0.6}O_4$. Regarding the oxidation step, nucleation and growth mechanisms describe the behavior of the two materials.

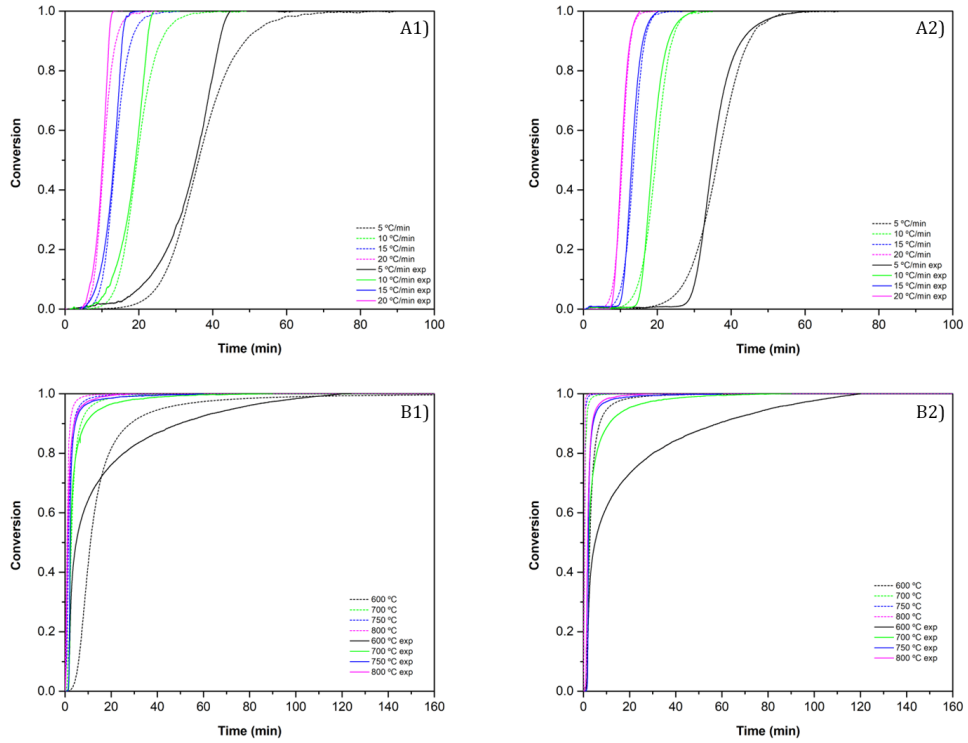

Figure 1.32. *Validation of A) Reduction conversion and B) Oxidation conversion for 1) $Co_{2.4}Ni_{0.6}O_4$ and 2) 0.5% SiO_2/ $Co_{2.4}Ni_{0.6}O$. The dotted lines correspond to the theoretical values and the solid ones to the experimental ones.*

The study was completed by adjusting the theoretical results of the kinetic study to the experimental results (Figure 1.32). For this purpose, the OCTAVE program was used and a good agreement between experimental and theoretical data was obtained.

The details of this research work are presented in the third publication attached in Annex I.

4.5. Development of active thermochemical barrier coatings using metal oxides

This research work shows the development of a stable active thermal barrier coating using thermochemical reactions to buffer the temperature changes of metallic components (Figure 1.33A).

The formulation of the active TBC is formed by metal oxides (Co_3O_4, $Co_{2.4}Ni_{0.6}O_4$ and 0.5% $SiO_2/Co_{2.4}Ni_{0.6}O_4$) as thermochemical materials and a sol-gel in silica base to act as a binder of the thermochemical material and give mechanical resistance to the resulting coating. For the optimization of the thermal coating formulation, commercial Co_3O_4 was used.

The compatibility between two types of stainless steel (AISI 310-s and AISI 304) and the thermal coating was analyzed to avoid the migration of Fe from the metallic component to the coating at high temperatures. The experiments showed better results in the high temperature stainless steel (AISI 310-s) as in the medium temperature AISI 304, the migration of Fe was clear.

The thermochemical material/sol-gel ratios and the sol-gel solids content were optimized, needing a 39.8% wt. of thermochemical material to reach a homogeneous coating and a sol-gel with a solids content of 10% to obtain a mechanical resistant coating to isothermal and dynamic treatments.

To avoid the delamination of the coating, the use of a protective interlayer was also studied and optimized. The best compromise between mechanical resistance and thermochemical activity was reached applying an interlayer of sol-gel with a solids content of 7.5 %.

Once the application of one layer was controlled, a layer-by-layer application process was designed based on spraying the thermochemical solution and

curing it with a CO_2 laser using a power of 15% to avoid the extreme sintering of the coating.

Cobalt, cobalt-nickel and cobalt-nickel-silica based coatings were deposited following the process designed previously. The new coatings were stable in terms of mechanical resistance and morphology. The thermochemical activity was assessed in TGA (Figure 1.33B) showing that all the coatings, fresh and thermal treated were active. However, the thermal treated samples suffered a decrease in activity in terms of conversion ratio, losing a 13.17% in the Co_3O_4 coating, a 27.83% in the $Co_{2.4}Ni_{0.6}O_4$ coating and a 5.75% in the 0.5% $SiO_2/Co_{2.4}Ni_{0.6}O_4$ coating.

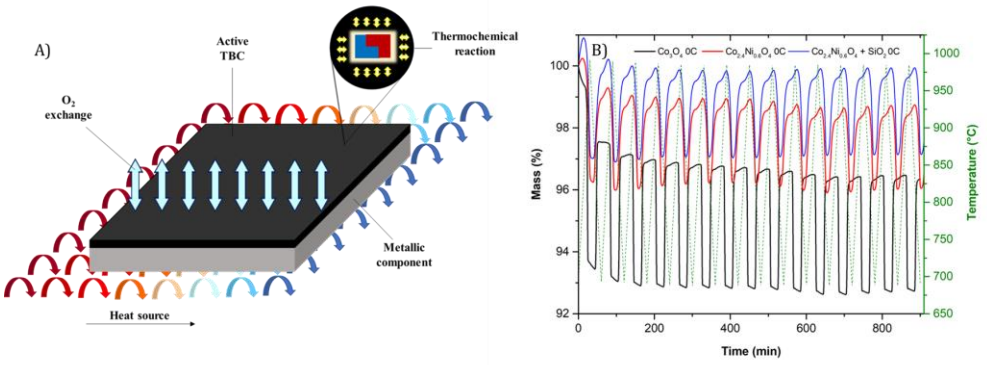

Figure 1.33. *A) Active thermal barrier coating activity principle and B) Thermogravimetric result of the Co_3O_4 (black), $Co_{2.4}Ni_{0.6}O_4$ (red) and 0.5% $SiO_2/Co_{2.4}Ni_{0.6}O_4$ (blue) coatings.*

The thickness of the three coatings was very similar, obtaining an average value of 129 µm in the case of the 2 layered coatings. The roughness was measured too, observing that the surface of the cobalt oxide coating is smoother than the ones of nickel cobaltite. The attrition measurements showed that the mechanical resistance level of the three coatings is very similar.

The details of the research work are shown in the fourth submitted publication attached in Annex I.

4.6. Active thermochemical barrier coatings using metal oxides – first experimental results

This research work evaluates the performance of the active thermal barrier coatings, using as thermochemical material Co_3O_4, $Co_{2.4}Ni_{0.6}O_4$ and wt. 0.5% $SiO_2/Co_{2.4}Ni_{0.6}O_4$, in a larger scale. The investigation details the TGA results in powder and coating configurations, as well as the development of a larger scale test rig and the experimental results obtained from it.

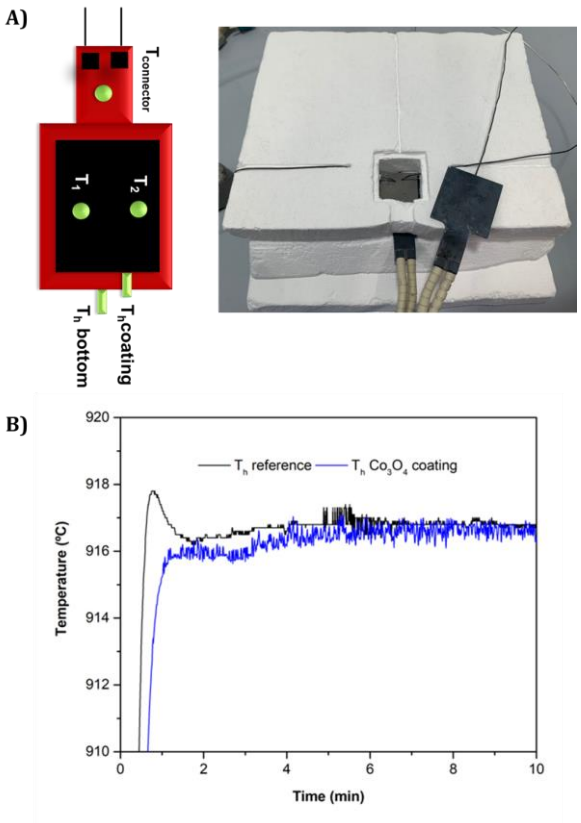

***Figure 1.34**. A) Detailed distribution of the thermocouples in the selected test rig configuration and B) the desired temperature damping effect on the metal components due to the action of the Co_3O_4 active coating.*

The assessment of the resistance of the coating in terms of delamination and fractures at the surface was done by performing dynamic thermal treatments. The three formulations withstood the tests without showing signs of fracture.

Thermogravimetric analyses of the powdered material showed that all the formulations (before and after thermal treatment) are active, but it can be observed a decrease in the performance of the thermal treated samples in terms of conversion ratio.

The test rig development was performed by using a distribution of two heaters, located in the upper and the bottom part of a small chamber. The lower heater aimed to control the temperature change of the reaction chamber and the upper heater aimed to reduce the heat fluxes of the test rig and stabilize the temperature in the whole chamber.

The analyses done on the test rig showed no damping effect in the case of the $Co_{2.4}Ni_{0.6}O_4$ coatings as their kinetics are slower than the pure Co_3O_4 ones, so the damping effect was hidden in the heat fluxes inherent to the test rig at high temperatures. The Co_3O_4 coating, on the contrary, showed a damping effect for 120 s maintaining temperatures below 916 ºC.

Thermogravimetric analyses of the coated material were conducted to study the performance of the coatings more precisely and to see the actual activity of the CoNi based coatings. The presence of reaction in the three coatings was demonstrated as mass gained/lost was observed in all the experiments.

The DSC signal shows almost no difference between the reference and the nickel cobaltites, despite obtaining a clear signal of mass variation, as the change in mass is very small and in the range of the measurement accuracy. In

the case of pure Co_3O_4, there is a clear difference between the coated sample and the reference, evidencing again the presence of a thermochemical reaction.

The in-depth details of the results are shown in the fifth publication attached in Annex III.

5. Materials and characterizations

This section describes the experimental methodologies followed during the research work. In the first part are detailed the methodologies used to obtain the different materials developed during the present study and the manufacturing of the reactive thermal coating. The details of the characterization techniques used are commented in the second part of this section. The techniques are divided between structural characterizations and thermophysical characterizations.

5.1. Experimental methodologies

5.1.1. Synthesis of mixed oxides

The $Co_{3-x}Ni_xO_4$ mixed metal oxides were synthesized following the sol-gel Pechini route, as the hydrothermal method requires high pressure equipment, increasing the cost [277], the co-precipitation method is not suitable for materials with exact stoichiometric ratios [278], and the solid state reaction

method presents a low efficiency [279]. The simplicity of the sol-gel Pechini route is a critical factor for the selection [280].

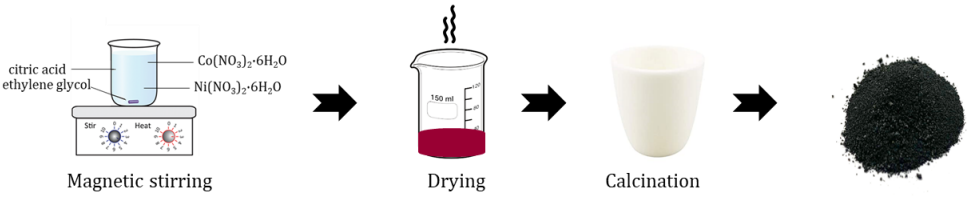

Figure 1.35. *Scheme of the sol-gel Pechini route for the synthesis of mixed oxides.*

The preparation of the materials following the general formula $Co_{3-x}Ni_xO_4$ is represented in Figure 1.35. The synthesis was done by mixing the appropriate quantities of $Co(NO_3)_2{\cdot}6H_2O$ and $Ni(NO_3)_2{\cdot}6H_2O$ nitrates. Firstly, the precursors were dissolved in 10 mL ethylene glycol under magnetic stirring to obtain a homogeneous solution. Stoichiometric citric acid, acting as chelating ligand, was added to the solution and the mixture was kept under gentle magnetic stirring for 60 min. The obtained mixture was dried overnight at 180 ºC. The resulting powders were grinded in an agate mortar with the aim of increasing the homogeneity and then calcined at 400 ºC for 10 h in air, to attain the mixed oxide with the right stoichiometry.

5.1.2. Synthesis of SiO_2 particles/nanoparticles

The formulation of the SiO_2 nanoparticles to inhibit the sintering of the mixed metal oxides was done following the Stober route [281] as it is represented in Figure 1.36. The precursors used for the synthesis of the SiO_2 nanoparticles were: tetraethyl orthosilicate, ammonia, distilled water and ethanol. Initially two solutions were prepared under magnetic stirring: i) 2/3 of ethanol with ammonia and distilled water (solution A); and ii) TEOS with 1/3 of ethanol (solution B). The solution A was heated under magnetic stirring at

temperatures from 25 to 80 ºC. Subsequently, the solution B was added to the solution A maintaining the whole system at the corresponding temperature under magnetic stirring. The resulting mixture was maintained under magnetic stirring at room temperature for 24 h for ageing. Once the particles were formed, the remaining solvent was removed in a rotary evaporator.

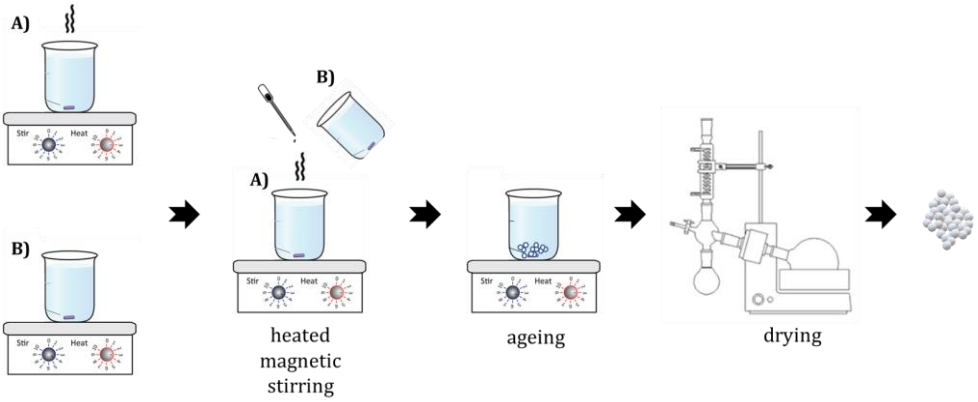

Figure 1.36. *Scheme of the Stober route for the synthesis of SiO_2 particles/nanoparticles.*

As the temperature of the process has a big influence in the final particle size, batches of particles from 26 nm (80 ºC) to 400 nm (25 ºC) were obtained. The size and morphology of the SiO_2 particles/nanoparticles was assessed by means of SEM and TEM, as it is depicted in Figure 1.37.

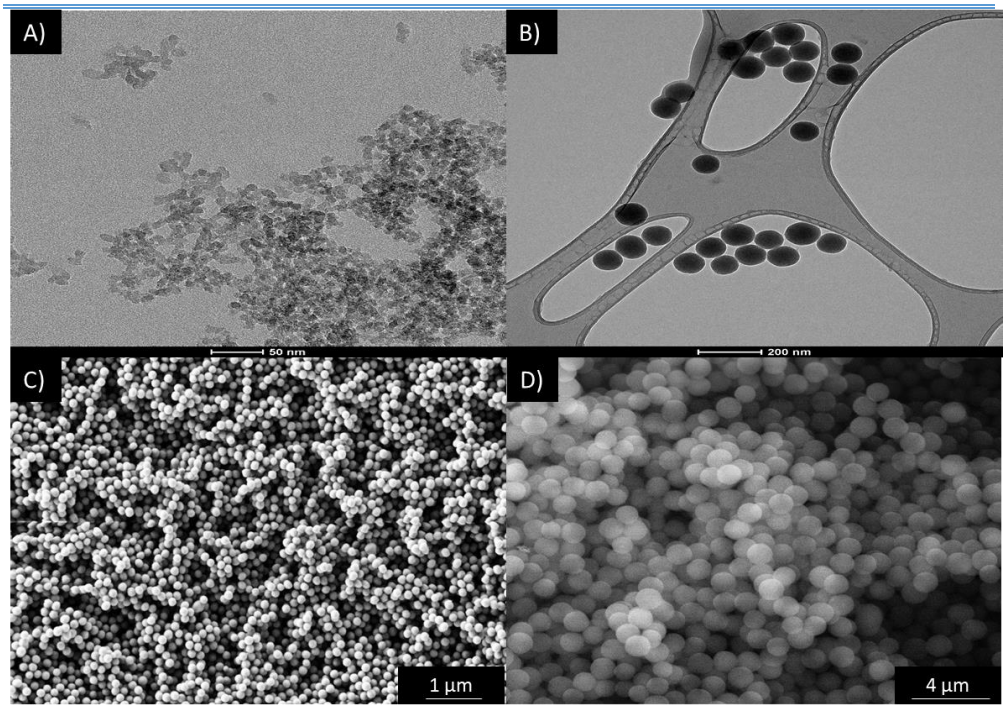

Figure 1.37. *A) TEM image of 26 nm SiO_2 nanoparticles, B) TEM images of 55 nm SiO_2 nanoparticles, C) SEM image of 210 nm SiO_2 particles and D) SEM images of 400 nm SiO_2 particles.*

The studies were done selecting the 26 nm SiO_2 nanoparticles and the 400 nm SiO_2 particles, to clearly observe the effect of the particle size in the cyclability stabilization. The BET surface area of the 26 nm SiO_2 nanoparticles is of 461.49 m^2/g and of 12.70 m^2/g in the case of the 400 nm SiO_2 particles.

5.1.3. Mixture of thermochemical materials and SiO_2 particles/ nanoparticles

The physical mixing of the thermochemical materials and the SiO_2 particles/nanoparticles was done by sonication. For this purpose, appropriate quantities of thermochemical materials and particles were weighed. Ethanol was added to this mixture as a dispersion medium. In order to homogeneously disperse the particles in the thermochemical material, the mixtures were sonicated for 1 min with an ultrasonic tip, using an amplitude of 50%. Solvent residues were removed at a rotary evaporator.

5.1.4. Thermal protective coating fabrication

The thermal coating was manufactured using a layer-by-layer process, where a thermochemical material and a silica-based sol-gel formulation were used as constituents.

The sol-gel formulation was developed by mixing TEOS, ethanol, distilled water and nitric acid. The following solutions were first prepared for the obtention of the final sol-gel: i) TEOS with 2/3 of ethanol (Solution A); and ii) 1/3 of ethanol with distilled water and nitric acid (Solution B). The solution A was kept under gentle stirring. Then, the solution B was added to the solution A drop by drop and was submitted to magnetic stirring for 24 h at room temperature for ageing.

The steps followed for the obtention of the new thermal protective coating are detailed in Figure 1.38:

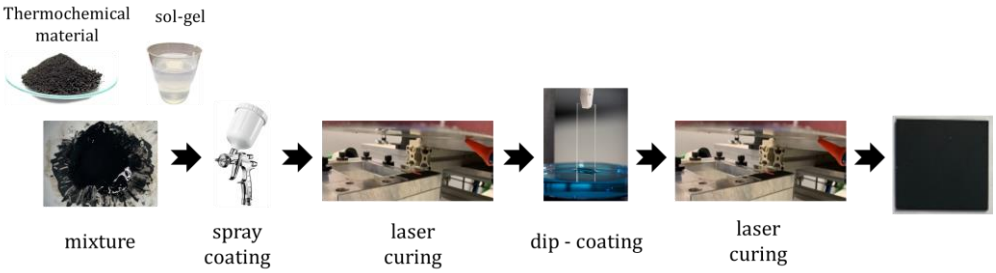

Figure 1.38. *Scheme of the thermal coating manufacturing process.*

Initially, the thermochemical material was grinded to afford a homogeneous particle size. Subsequently, appropriate quantities of thermochemical material and sol-gel solution were mixed. The mixture was applied in stainless steel sheets by spray coating. The obtained layer was cured by CO_2 solid-state laser. Afterwards, the dip-coating technique was used to apply a sol-gel protective layer, to act as a binder between thermochemical coating layers and was cured by CO_2 laser. The whole process was repeated to apply another complete layer (thermal coating + sol-gel protective layer). The thickness of the resulting coating is controlled by the number of layers applied.

5.2. Characterization techniques

5.2.1. Structural and morphological characterizations

5.2.1.1. X-ray diffraction analysis (XRD)

The X-ray diffraction non-destructive technique has been widely used in materials science to identify crystalline phases and the unit cell dimension of

the crystalline materials at room temperature [282]. This technique can provide the proportions of the crystalline phases both qualitatively and quantitatively when the Rietveld method is used.

When a certain wavelength X-ray beam interacts with a crystalline substance occurs the X-ray diffraction. The wavelength (λ) of the X-rays is of the same order as the cell parameters of a material's crystals. Thus, X-ray diffraction is based on the coherent scattering of the X-ray beam by matter, as the wavelength of the radiation is maintained, and on constructive interference of waves that are in phase and scatter in certain directions in space.

The Bragg law [283] describes the diffraction phenomena, predicting the direction of the constructive interference between the X-ray beams diffracted by a crystal. The law can be expressed as:

$$n\lambda = 2d_{hlk}sen\theta \qquad (22)$$

Where λ is the wavelength of the X-rays, θ is the incidence angle of the radiation and d_{hkl} is the distance between two consecutive planes defined by a vector of components hkl.

The XRD technique works with an initial generation of X-ray by a cathode ray tube. Subsequently, the monochromatic radiation is achieved by a monocromator. The collimator is used to narrow the beam and the X-rays are directed on the way to the sample. The interaction between the X-ray and the sample produces the diffraction peaks. The detector archives the X-rays and processes the signals to obtain a count rate. The patterns generated are characteristic of the substance analyzed and can be stared as a type of fingerprint [284]. One of the most commonly used sources of target materials is copper. The radiation of the CuKα1 source is 1.5418 Å.

Figure 1.39. *Image of the Bruker D8 Advance diffractometer used in the present research work.*

The diffractometer used in this research was a Bruker D8 Advance (Figure 1.39), equipped with a LYNXEYE detector using CuKα1 radiation (λ = 1.5418 Å) placed at CIC energiGUNE. The geometry used for the XRD analysis was θ-2θ. The data were collected at room temperature in the range 10-80 º with a step size of 0.02 º and a counting time of 8 s per step. The determination of the phase composition of the materials was done using the EVA software. The Rietveld method [285] was used for confirming the presence of the pure single structure of each material, using the Winplotr/Fullprof [286] package and the Maud package.

5.2.1.2. In-situ X-ray diffraction (in-situ XRD)

The in-situ XRD is a variant of the traditional XRD technique. In this case, the analysis is done as a function of the temperature. This allows to follow all the transformations (reactions, phase transitions, etc.) in the material during heating/cooling.

The equipment used was a Bruker D8 Advance diffractometer operating at 30 kV and 20 mA, equipped with a Cu tube (λ = 1.5418 Å), a Vantec-1 PSD detector and an Anton Parr HTK2000 high-temperature furnace, placed in the X-ray General Service of SGIker from UPV/EHU, Leioa. The powder patterns were recorded in 2θ steps of 0.04 º in the 15 ≤2θ ≤ 85 range, counting for 1.4 s per step. The heating rate used during the measurements was of 0.166 ºC s^{-1}.

5.2.1.3. Scanning Electron Microscopy (SEM)

The scanning electron microscopy (SEM) technique uses an electron beam instead of a light beam to obtain high resolution images of a sample surface by using electron-matter interactions. This kind of microscopes produce high resolution images and can study spatially close features in the sample at high magnification. The different generated signals show information about the morphology, topography and composition of the analyzed materials.

The main requirement for the sample preparation is that the materials must be conductive. If the samples are not conductive, they get charged by the electron beam. A possibility to avoid this effect is to coat the samples with a layer of carbon or metal to give them conductive properties.

The process is based in the scanning of the sample with a beam of accelerated electrons travelling through the barrel of a high vacuum column. A detector measures the amount of scattered electrons, being able to construct images which give information about the microstructure and morphology of the surface of the sample [287]. The electron column in vacuum prevents possible contamination and external disturbances, increasing the resolution of the image obtained, that could be below 1 nm, but normally between 1-20 nm. The resolution of the SEM images depends mainly on the electron spot size and the volume of the electron beam interaction with the sample.

When the beam of electrons interacts with the sample, it penetrates a few microns, depending on the accelerating voltage and the density of the samples,

producing secondary electrons, backscattered electrons and characteristic X-rays. The exchange of energy produced between the sample and the electron beam, in the case of inelastic scattering reflects secondary electrons, but in the case of the elastic scattering emits high energy electrons. The secondary electrons give high resolution images, backscattered electrons give information about the crystal structure [288] and the X-rays are used for the elemental analysis by energy dispersive X-ray spectroscopy (EDX).

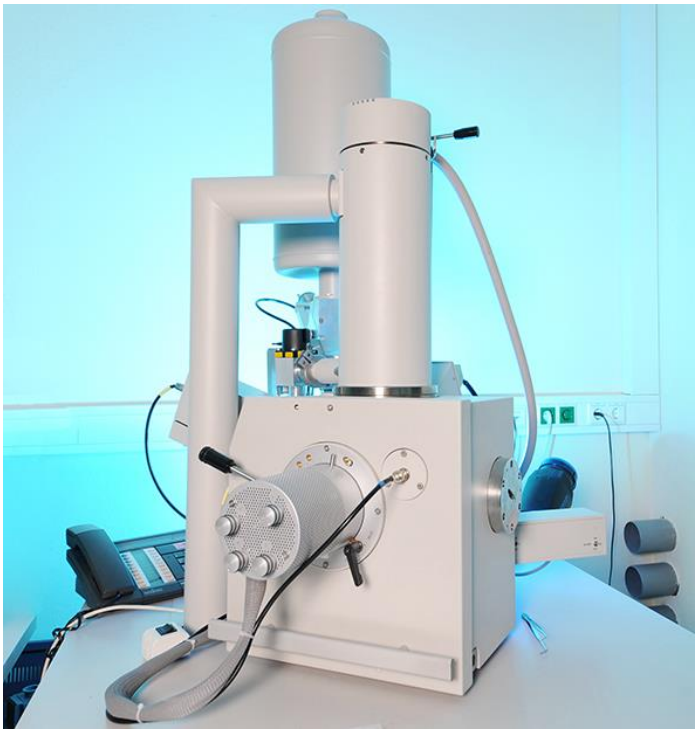

Figure 1.40. *Image of a FEI Quanta 200 FEG scanning electron microscope.*

The samples were analyzed using a scanning electron microscope FEI Quanta 200 FEG, which is shown in Figure 1.40, operated in high vacuum mode at 30 kV featured with a backscattered electron detector (BSED) and Everhart-Thornley Detector (ETD), placed in CIC energiGUNE. The elemental mapping analyses were carried out by energy-dispersive X-ray spectroscopy (EDX). SEM images were statistically analyzed for the evaluation of the pore size

distributions. At least 200 measurements were collected for each sample using ImageJ software.

5.2.1.4. Transmission electron microscopy (TEM)

In the transmission electron microscopy, a high-energy electron beam is transferred through a thin, suitably prepared sample. The interaction between the electron and the sample provides the image. This technique can also be used to classify the crystalline structure and the chemical composition of the materials. The images provided by TEM offer information both of crystalline and amorphous samples.

When the electrons collide with the sample, some of them are selectively scattered, depending on the thickness and the type of atoms forming the sample [289]. In other words, there is a progression between the electrons that pass directly through the sample and those that are totally deflected. All the electrons are conducted and modulated by lenses to form a final image, with thousands of magnifications, obtaining a definition unreachable for any other instrument. The magnifications that can reach the TEM ranges from 100X to 100,000X [290]. The image obtained is formed by different grey intensities that correspond to the degree of dispersion of the incident electrons.

Figure 1.41. *Image of a FEI Tecnai F20 electron microscope.*

The synthesized nanoparticles were analyzed by means of transmission electron microscopy (TEM), model FEI Tecnai F20 electron microscope, represented in Figure 1.41, which is operating at 200 kV, placed at CIC energiGUNE. The sample preparation was carried out by the dispersion of the solid nanoparticles in ethanol and small droplet of the sample was transferred onto a holey carbon film fixed on a 3 mm copper grid (200 mesh).

5.2.1.5. Brunauer - Emmett - Teller (BET) Analysis

BET analyses are used to determine the specific surface area and the pore size distribution of the materials. The physical adsorption of the gas molecules on the surface of the material and the adsorbed gas associated to the monomolecular layer on the surface are used to calculate the specific surface area of the materials. The forces taking place between the adsorbate gas molecules and the material surface are of Van der Walls.

BET analyses usually use test gases that do not react chemically with the material surfaces as adsorbates to do the measurements of specific surface area. The most commonly used absorbed gas for BET measurements is nitrogen. This is why standard BET analysis is most often performed at the boiling temperature of N_2 (77 K). Other adsorbates are also used, less frequently, being able to change the temperatures and scales of the measurement as argon, carbon dioxide or water [291].

Figure 1.42. *Image of a Quantachrome Autosorb IQ.*

The specific surface area of the nanoparticles/particles of SiO_2 was measured using an Autosorb IQ from Quantachrome placed at TEKNIKER and depicted in Figure 1.42. The N_2 (77K) physisorption data was recorded using particles/nanoparticles under vacuum at 300 ºC for 12 h.

5.2.1.6. 3D Optical Profilometry

3D Optical profilometry is a metrology technique non-destructive, non-contact rapid surface metrology technique.

These profilers are a type of microscope in which a beam splitter divides the light from a lamp into two paths. The first one directs the light onto the surface of the tested material and the other one directs the light to a reference mirror. Subsequently the reflections are recombined and projected onto an array detector. Interference can occur if the path difference between the recombined beams is in the order of a few wavelengths of light. The generated interference has the information about the surface contours of the tested material. The vertical resolution of the equipment can be of several angstroms. The lateral resolution is influenced by the used objective, but typically ranges from 0.3 to 8 microns [292]. Confocal profiling provides the highest lateral resolution that an optical profiler can achieve. The spatial sampling can be reduced to 0.10 μm, necessary for critical dimensions. High NA (0.95) and magnification (150X) objectives are available to measure surfaces.

Figure 1.43. *Image of the Sneox 3D Optical Profiler from SENSOFAR Metrology.*

The surface roughness of the coatings was measured with a Sneox 3D Optical Profiler from SENSOFAR Metrology placed at TEKNIKER (Figure 1.43). In the measurements 20X objectives were used.

5.2.2. Thermophysical characterizations

5.2.2.1. Thermogravimetric Analysis (TGA)

The thermogravimetric analysis is a characterization technique that allows to monitor the mass loss and gain of a sample as a function of the temperature or time, as the sample is subjected to a controlled temperature program in a controlled atmosphere during the analysis. The TGA curves are called thermograms and they offer information about the thermal stability, the composition and the reversibility of the sample and the products that can be generated in a heating/cooling process.

A typical TGA device consists on a sample pan that is supported by a precision balance. The pan is placed inside a furnace and is heated and cooled during the experiment. The precision balance monitories the sample mass during the experiment and a sample purge gas controls the environment of the measurement. This gas is usually an inert gas or a reactive gas that flows over the sample and exits through a vent [293].

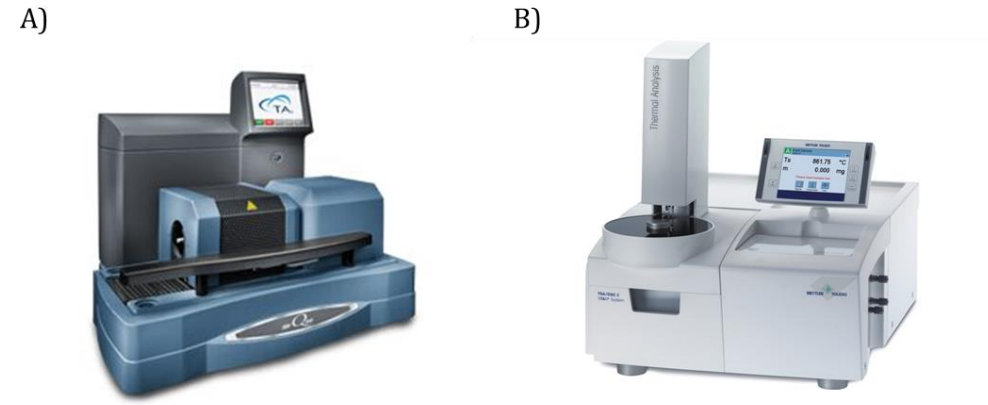

Figure 1.44. *A) Device SDT Q600-0802 TGA from TA Instruments and B) Device TGA/DSC 1 from Mettler Toledo.*

The samples were analyzed in a SDT Q600-0802 TGA from TA Instruments and in a TGA/DSC 1 from Mettler Toledo, using a sensor type DSC HSS2, a furnace LF heating until 1100 ºC, equipped with a sample robot standard, both instruments placed at TEKNIKER. The gas controller is the type GC 200. The conditions of the measurements are detailed in each article. Both equipments are depicted in Figure 1.44.

5.2.2.2. Differential Scanning Calorimetry (DSC)

The DSC is a thermal analysis technique that measures the heat flow into or out of a sample as a function of temperature or time, while the sample is subjected to controlled temperature variations [294]. It provides information on the endothermic (heat absorption) and exothermic (heat release) properties of materials during a physical transition process, thermodynamic process and reaction kinetics.

In the DSC technique, the sample and reference pans are placed in a thermoelectric sensor surrounded by a furnace. During the increase/decrease of temperature, the differential heat flux of the sample and reference is measured.

In the case of the mixed metal oxides, the temperatures needed to measure the enthalpies of reaction is very high for a conventional DSC, usually with a maximum working temperature of 600 ºC. This is the reason why DSC systems integrated in the TGA equipment are used, able to work at higher temperatures (up to 1000 ºC).

Figure 1.45. *Image of the STA 449 F3 Jupiter from Netzsch.*

The enthalpy measurements were done in a STA 449 F3 Jupiter from Netzsch placed at CIC energiGUNE and shown in Figure 1.45. The measurements were done using 40 mg of sample, under air and in the temperature range of 600-910 ºC, using a heating ramp of 10 ºC/min.

5.2.2.3. Glow Discharge Optical Emission Spectroscopy (RF GD-OES)

GD-OES technique combines a glow discharge (GD) and an optical emission spectrometer (OES). This analytical technique provides the surface depth profile and the bulk elemental composition of solid materials and layers, with high sensitivity to all elements.

The operating principle involves the controlled sputtering of an area of the sample, as it is depicted in Figure 1.46 A. This area is analyzed by the GD plasma and the simultaneous OES observation of the sputtered species. This technique is destructive as a crater is done in the sample after the analysis. The technique is fast and can reach a depth resolution of nm level if the sample is flat over the sputtered area [295].

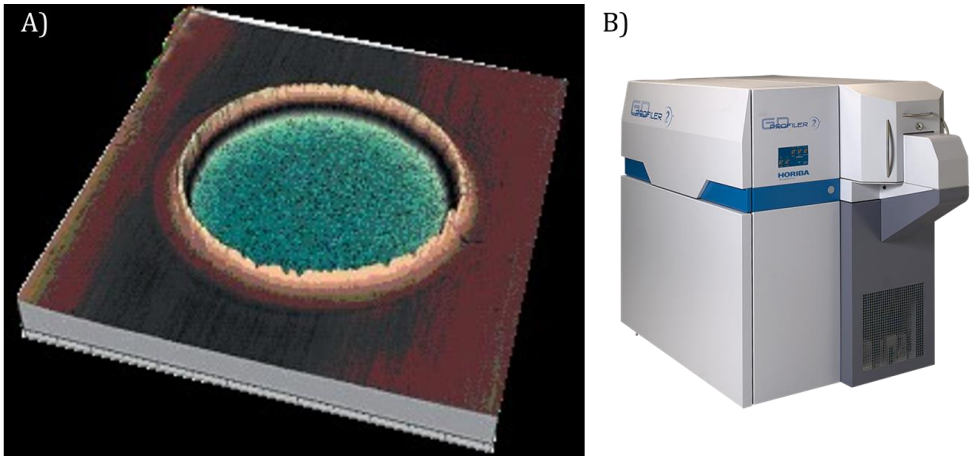

Figure 1.46. *A) 3D view of a resulting crater [295] and B) Image of a GD Profiler 2 from Horiba*.

The compatibility between the stainless steel and the reactive thermal coating was characterized in a GD Profiler 2 from Horiba Jobin-Yvon placed at TEKNIKER (Figure 1.46 B). The conditions used for the measurement were: a flushing time of 5 s, a pre-integration time of 100 s, a background of 5 s, a pressure of 650 Pa, a power of 35 W, a module of 7.2 V and a phase of 4.7 V.

5.2.3. Other characterization techniques

5.2.3.1. Stylus profilometry

The profilometry is used to extract topographical data from a surface. The data taken can be a single point, a linear scan or a three-dimensional scan (obtained with the 3D Optical profiler detailed above). The topographical data that can be obtained with a profilometer are the surface morphology, step heights and roughness of a surface. This information can be obtained using a physical probe (stylus profiler) or using light (optical profiler).

The stylus profilometers use a prove to detect the changes in the surface by physically moving a prove along the surface, acquiring the surface heights. These profilometers require force feedback and touch physically the surface of the sample, providing high Z resolution. This technique is sensitive to soft surfaces as the prove can be contaminated by the materials of the surface. A side effect is the destruction of some surfaces nonresistant to the prove. The measurement resolution can be influenced by the stylus tip size and shape [296].

Figure 1.47. *Image of the profilometer Dektak 8 from Veeco.*

The thickness of the reactive thermal coatings was measured with a Dektak 8 from Veeco (Figure 1.47), placed at TEKNIKER. The stylus used was the 0.7 one, with a force of 1 mg and a length of 2 mm. The data points per scan were 60,000.

5.2.3.2. Universal Micro Tribometry (UTM)

This technique allows to test samples mechanically under multiple wear patterns on a single test platform. UTM and its accessories can be configured to conduct over 20 standard ASTM, ISO or DIN tribology tests. The most widely used are: Pin/Ball-on-Disk, Disc/Plate-On-Disc/Plate, Indenter-on-Plate, Crossed Cylinders and 4-Ball Test. Al the test can be done dry or in liquid, under vacuum and under humidity, and at room temperature or at elevated temperatures [297].

Figure 1.48. *Image of the Universal Material Tester from Bruker-CETR.*

The evaluation of the attrition of the coatings was measured with a Universal Mechanical Tester from Bruker – CETR, placed at TEKNIKER and imaged in Figure 1.48. The configuration used was ball on disk. The ball selected for the test was of 440 steel, with a diameter of 10mm. The test conditions were 0.1 Hz, 2 min, 10 mm travel, ambient temperature and 0.5 kg load. The footprint generated during the measurement is evaluated with the 3D Optical profiler.

6. References

[1] BP Energy, Statistical Review of World Energy globally consistent data on world energy markets . and authoritative publications in the field of energy, BP Energy Outlook 2021. 70 (2021) 8–20.

[2] H. Ritchie, M. Roser, Energy, OurWorldInData.Org. (2020). https://ourworldindata.org/energy (accessed March 8, 2022).

[3] C. Moore, S. Brown, P. MacDonald, M. Ewen, H. Broadbent, European Electricity Review, (2022).

[4] C. Glasgow Science, The Energy Hierarchy, (2021). https://www.glasgowsciencecentre.org/our-blog/the-energy-hierarchy (accessed April 6, 2022).

[5] A. Bloess, W.P. Schill, A. Zerrahn, Power-to-heat for renewable energy integration: A review of technologies, modeling approaches, and flexibility potentials, Appl. Energy. 212 (2018) 1611–1626. https://doi.org/10.1016/j.apenergy.2017.12.073.

[6] A. Bloess, Modeling of combined heat and power generation in the context of increasing renewable energy penetration, Appl. Energy. 267 (2020) 114727. https://doi.org/10.1016/j.apenergy.2020.114727.

[7] Y. Li, Y. Jin, Y. Huang, F. Ye, X. Wang, D. Li, E. Al., Principles and new development of thermal storage technology (I), 2013.

[8] G. Sadeghi, Energy storage on demand: Thermal energy storage development, materials, design, and integration challenges, Energy Storage Mater. 46 (2022) 192–222. https://doi.org/10.1016/j.ensm.2022.01.017.

[9] T. Block, N. Knoblauch, M. Schmücker, The cobalt-oxide/iron-oxide binary system for use as high temperature thermochemical energy storage material, Thermochim. Acta. 577 (2014) 25–32. https://doi.org/10.1016/j.tca.2013.11.025.

[10] S. Tescari, C. Agrafiotis, S. Breuer, L. De Oliveira, M. Neises-Von Puttkamer, M. Roeb, C. Sattler, Thermochemical solar energy storage via redox oxides: Materials and reactor/heat exchanger concepts, Energy

Procedia. 49 (2014) 1034–1043. https://doi.org/10.1016/j.egypro.2014.03.111.

[11] Belzona, A Thermal Insulation Barrier Providing Corrosion Protection with "Cool-to-Touch" Properties, 2021. (n.d.). https://www.minexpodirectory.com/exhibitor-news/promotion/21603332/belzona-inc-a-thermal-insulation-barrier-providing-corrosion-protection-with-cooltotouch-properties (accessed April 6, 2022).

[12] A. Kumar, S.K. Shukla, A Review on Thermal Energy Storage Unit for Solar Thermal Power Plant Application, Energy Procedia. 74 (2015) 462–469. https://doi.org/10.1016/j.egypro.2015.07.728.

[13] S.T. Vagge, S. Ghogare, Thermal barrier coatings: Review, Mater. Today Proc. (2021). https://doi.org/10.1016/j.matpr.2021.11.170.

[14] K. Yan, Y. Xiang, H. Yu, Z. Li, Y. Wu, J. Sun, Effect of irregular microcracks on the hot corrosion behavior and thermal shock resistance of YSZ thermal barrier coatings, Surf. Coatings Technol. 431 (2022) 128038. https://doi.org/10.1016/j.surfcoat.2021.128038.

[15] E.J. Gildersleeve, S. Sampath, Dynamic interactions of ingested molten silicate particles with air plasma sprayed thermal barrier coatings, J. Mater. Res. 35 (2020) 2321–2334. https://doi.org/10.1557/jmr.2020.196.

[16] V. Kumar, B. Kandasubramanian, Processing and design methodologies for advanced and novel thermal barrier coatings for engineering applications, Particuology. 27 (2016) 1–28. https://doi.org/10.1016/j.partic.2016.01.007.

[17] G.R. Li, L.S. Wang, G.J. Yang, A novel composite-layered coating enabling self-enhancing thermal barrier performance, Scr. Mater. 163 (2019) 142–147. https://doi.org/10.1016/j.scriptamat.2019.01.010.

[18] N.P. Padture, Advanced structural ceramics in aerospace propulsion, Nat. Mater. 15 (2016) 804–809. https://doi.org/10.1038/nmat4687.

[19] H. Zhao, C.G. Levi, H.N.G. Wadley, Molten silicate interactions with thermal barrier coatings, Surf. Coatings Technol. 251 (2014) 74–86. https://doi.org/10.1016/j.surfcoat.2014.04.007.

[20] C. Deng, R. Zheng, L. Wang, S. Zhang, X. Lin, K. Ding, Construction of three-dimensional dynamic growth TGO (thermally grown oxide) model and stress simulation of 8YSZ thermal barrier coating, Ceram. Int. 48 (2022) 5327–5337. https://doi.org/10.1016/j.ceramint.2021.11.076.

[21] J. Huang, X. Chu, T. Yang, H. Fang, D. Ye, W. Wang, X. Zhang, W. Sun, R.

Huang, C.J. Li, Achieving high anti-sintering performance of plasma-sprayed YSZ thermal barrier coatings through pore structure design, Surf. Coatings Technol. 435 (2022) 128259. https://doi.org/10.1016/j.surfcoat.2022.128259.

[22] S.A.A. Jude, J.T.W. Jappes, M. Adamkhan, Thermal barrier coatings for high-temperature application on superalloy substrates - A review, Mater. Today Proc. (2022). https://doi.org/10.1016/j.matpr.2021.12.223.

[23] M. Wokon, Reversible Redox Reactions for High Temperature Thermochemical Energy Storage, 2020.

[24] M. Wokon, M. Linder, T. Bauer, Metallic component with a reactive thermal protective layer, its use and process for its production, DE 10 2013 214 396 B4, 2020.

[25] P. Yuan, C. Gu, H. Xu, Z. Ning, K. Cen, G. Xiao, Regulating thermochemical redox temperature via oxygen defect engineering for protection of solar molten salt receivers, IScience. 24 (2021) 103039. https://doi.org/10.1016/j.isci.2021.103039.

[26] J. Huang, W. Sun, Z. Zhang, Z. Ling, X. Fang, Thermal protection of electronic devices based on thermochemical energy storage, Appl. Therm. Eng. 186 (2021) 116507. https://doi.org/10.1016/j.applthermaleng.2020.116507.

[27] IEA ETSAP, IRENA, Thermal Energy Storage-Insights for Policy Makers, (2013) 9.

[28] I. Sarbu, C. Sebarchievici, A comprehensive review of thermal energy storage, Sustain. 10 (2018). https://doi.org/10.3390/su10010191.

[29] P. Denholm, J.C. King, C.F. Kutcher, P.P.H. Wilson, Decarbonizing the electric sector: Combining renewable and nuclear energy using thermal storage, Energy Policy. 44 (2012) 301–311. https://doi.org/10.1016/j.enpol.2012.01.055.

[30] I. Dincer, R.M. A., Thermal Energy Storage: Systems and Applications, 2011.

[31] A. Sharma, V. V. Tyagi, C.R. Chen, D. Buddhi, Review on thermal energy storage with phase change materials and applications, Renew. Sustain. Energy Rev. 13 (2009) 318–345. https://doi.org/10.1016/j.rser.2007.10.005.

[32] R. Tamme, D. Laing, W.D. Steinmann, Advanced thermal energy storage technology for parabolic trough, J. Sol. Energy Eng. Trans. ASME. 126 (2004) 794–800. https://doi.org/10.1115/1.1687404.

[33] J.-M. Durand, M.J. Duarte, P. Clerens, Joint EASE/EERA recommendations for a European Energy Storage Technology Development Roadmap Towards 2030, Int. Energy Storage Policy Regul. Work. (2017) 108.

[34] P. Pinel, C.A. Cruickshank, I. Beausoleil-Morrison, A. Wills, A review of available methods for seasonal storage of solar thermal energy in residential applications, Renew. Sustain. Energy Rev. 15 (2011) 3341–3359. https://doi.org/10.1016/j.rser.2011.04.013.

[35] M. Liu, N.H. Steven Tay, S. Bell, M. Belusko, R. Jacob, G. Will, W. Saman, F. Bruno, Review on concentrating solar power plants and new developments in high temperature thermal energy storage technologies, Renew. Sustain. Energy Rev. 53 (2016) 1411–1432. https://doi.org/10.1016/j.rser.2015.09.026.

[36] A. De Gracia, L.F. Cabeza, Phase change materials and thermal energy storage for buildings, Energy Build. 103 (2015) 414–419. https://doi.org/10.1016/j.enbuild.2015.06.007.

[37] S. Wu, C. Zhou, E. Doroodchi, R. Nellore, B. Moghtaderi, A review on high-temperature thermochemical energy storage based on metal oxides redox cycle, Energy Convers. Manag. 168 (2018) 421–453. https://doi.org/10.1016/j.enconman.2018.05.017.

[38] M. Lott, S.-I. Kim, D. Elzinga, C. Tam, S. Heinen, L. Munuera, U. Remme, Technology Roadmap: Energy Storage - 2014 edition, (2014) 64.

[39] A.D. Monde, A. Shrivastava, P.R. Chakraborty, Solar Thermal Energy Storage, Energy, Environ. Sustain. (2018) 131–162. https://doi.org/10.1007/978-981-10-7206-2_8.

[40] G.L. Kyriakopoulos, G. Arabatzis, Electrical energy storage systems in electricity generation: Energy policies, innovative technologies, and regulatory regimes, Renew. Sustain. Energy Rev. 56 (2016) 1044–1067. https://doi.org/10.1016/j.rser.2015.12.046.

[41] M. Beaudin, H. Zareipour, A. Schellenberglabe, W. Rosehart, Energy storage for mitigating the variability of renewable electricity sources: An updated review, Energy Sustain. Dev. 14 (2010) 302–314. https://doi.org/10.1016/j.esd.2010.09.007.

[42] N. Udayashankar, Investigation of new nanofluids based on molten salts and their corrosion mechanisms for thermal energy storage applications., (2019). https://addi.ehu.es/handle/10810/41974.

[43] I. Dincer, S. Dost, X. Li, Performance analyses of sensible heat storage systems for thermal applications, Int. J. Energy Res. 21 (1997) 1157–1171. https://doi.org/10.1002/(SICI)1099-

114X(19971010)21:12<1157::AID-ER317>3.0.CO;2-N.

[44] G.K. Pavlov, B.W. Olesen, Seasonal ground solar thermal energy storage - Review of systems and applications, 30th ISES Bienn. Sol. World Congr. 2011, SWC 2011. 6 (2011) 4864–4874. https://doi.org/10.18086/swc.2011.29.24.

[45] Swati Khare, A.K. Sharma, R.K. Ranjan, Shashank Khare, Energy Conservation through Energy Storage, Int. J. Curr. Res. 4 (2012) 144–148. http://www.iea-eces.org/homepage.html.

[46] A.H. Abedin, A Critical Review of Thermochemical Energy Storage Systems, Open Renew. Energy J. 4 (2011) 42–46. https://doi.org/10.2174/1876387101004010042.

[47] K.E. N'Tsoukpoe, H. Liu, N. Le Pierrès, L. Luo, A review on long-term sorption solar energy storage, Renew. Sustain. Energy Rev. 13 (2009) 2385–2396. https://doi.org/10.1016/j.rser.2009.05.008.

[48] S. Ayyappan, K. Mayilsamy, V. V. Sreenarayanan, Performance improvement studies in a solar greenhouse drier using sensible heat storage materials, Heat Mass Transf. Und Stoffuebertragung. 52 (2016) 459–467. https://doi.org/10.1007/s00231-015-1568-5.

[49] Y. Tian, C.Y. Zhao, A review of solar collectors and thermal energy storage in solar thermal applications, Appl. Energy. 104 (2013) 538–553. https://doi.org/10.1016/j.apenergy.2012.11.051.

[50] D. Liu, L. Xin-Feng, L. Bo, Z. Si-quan, X. Yan, Progress in thermochemical energy storage for concentrated solar power: A review, Int. J. Energy Res. 42 (2018) 4546–4561. https://doi.org/10.1002/er.4183.

[51] W. Su, J. Darkwa, G. Kokogiannakis, Review of solid-liquid phase change materials and their encapsulation technologies, Renew. Sustain. Energy Rev. 48 (2015) 373–391. https://doi.org/10.1016/j.rser.2015.04.044.

[52] G. Alva, Y. Lin, G. Fang, An overview of thermal energy storage systems, Energy. 144 (2018) 341–378. https://doi.org/10.1016/j.energy.2017.12.037.

[53] G. Barone, G. Della Gatta, D. Ferro, V. Piacente, Enthalpies and entropies of sublimation, vaporization and fusion of nine polyhydric alcohols, J. Chem. Soc. Faraday Trans. 86 (1990) 75–79. https://doi.org/10.1039/FT9908600075.

[54] R.A. Talja, Y.H. Roos, Phase and state transition effects on dielectric, mechanical, and thermal properties of polyols, Thermochim. Acta. 380 (2001) 109–121. https://doi.org/10.1016/S0040-6031(01)00664-5.

[55] M.M. Kenisarin, Thermophysical properties of some organic phase change materials for latent heat storage. A review, Sol. Energy. 107 (2014) 553–575. https://doi.org/10.1016/j.solener.2014.05.001.

[56] A. Serrano, M. Duran, J.L. Dauvergne, S. Doppiu, E.P. Del Barrio, Tailored transition temperature plastic crystals with enhanced thermal energy storage capacity, Sol. Energy Mater. Sol. Cells. 220 (2021) 110848. https://doi.org/10.1016/j.solmat.2020.110848.

[57] S. Doppiu, J.L. Dauvergne, A. Serrano, E.P. del Barrio, The Li2SO4-Na2SO4 system for thermal energy storage, Materials (Basel). 12 (2019). https://doi.org/10.3390/ma12223658.

[58] S.A. Mohamed, F.A. Al-Sulaiman, N.I. Ibrahim, M.H. Zahir, A. Al-Ahmed, R. Saidur, B.S. Yılbaş, A.Z. Sahin, A review on current status and challenges of inorganic phase change materials for thermal energy storage systems, Renew. Sustain. Energy Rev. 70 (2017) 1072–1089. https://doi.org/10.1016/j.rser.2016.12.012.

[59] A. Hassan, M.S. Laghari, Y. Rashid, Micro-encapsulated phase change materials: A review of encapsulation, safety and thermal characteristics, Sustain. 8 (2016). https://doi.org/10.3390/su8101046.

[60] A. De Gracia, E. Oró, M.M. Farid, L.F. Cabeza, Thermal analysis of including phase change material in a domestic hot water cylinder, Appl. Therm. Eng. 31 (2011) 3938–3945. https://doi.org/10.1016/j.applthermaleng.2011.07.043.

[61] F. Agyenim, N. Hewitt, The development of a finned phase change material (PCM) storage system to take advantage of off-peak electricity tariff for improvement in cost of heat pump operation, Energy Build. 42 (2010) 1552–1560. https://doi.org/10.1016/j.enbuild.2010.03.027.

[62] S. Kuravi, J. Trahan, D.Y. Goswami, M.M. Rahman, E.K. Stefanakos, Thermal energy storage technologies and systems for concentrating solar power plants, Prog. Energy Combust. Sci. 39 (2013) 285–319. https://doi.org/10.1016/j.pecs.2013.02.001.

[63] A. Gil, M. Medrano, I. Martorell, A. Lázaro, P. Dolado, B. Zalba, L.F. Cabeza, State of the art on high temperature thermal energy storage for power generation. Part 1-Concepts, materials and modellization, Renew. Sustain. Energy Rev. 14 (2010) 31–55. https://doi.org/10.1016/j.rser.2009.07.035.

[64] P. Tatsidjodoung, N. Le Pierrès, L. Luo, A review of potential materials for thermal energy storage in building applications, Renew. Sustain. Energy Rev. 18 (2013) 327–349. https://doi.org/10.1016/j.rser.2012.10.025.

[65] J.W. McBain, XCIX. The mechanism of the adsorption ("sorption") of hydrogen by carbon , London, Edinburgh, Dublin Philos. Mag. J. Sci. 18 (1909) 916–935. https://doi.org/10.1080/14786441208636769.

[66] M. Goldstein, Conference Solar Energy , Wind Power and Geothermal Energy, (1961).

[67] J.E. Funk, Thermochemical hydrogen production: Past and present, Int. J. Hydrogen Energy. 26 (2001) 185–190. https://doi.org/10.1016/S0360-3199(00)00062-8.

[68] E. Guy, Solar Heat Storage Using Chemical Reactions, J. Solid State Chem. 22 (1977) 51–61.

[69] A. Fopah Lele, State-of-Art of Thermochemical Heat Storage Systems, 2016. https://doi.org/10.1007/978-3-319-41228-3_2.

[70] N. Yu, R.Z. Wang, L.W. Wang, Sorption thermal storage for solar energy, Prog. Energy Combust. Sci. 39 (2013) 489–514. https://doi.org/10.1016/j.pecs.2013.05.004.

[71] P. Pardo, A. Deydier, Z. Anxionnaz-minvielle, S. Rougé, M. Cabassud, P. Cognet, P. Pardo, A. Deydier, Z. Anxionnaz-minvielle, S. Rougé, M. Cabassud, A review on high temperature thermochemical heat energy storage To cite this version : HAL Id : hal-01345714, (2016).

[72] A.J. Carrillo, J. Moya, A. Bayón, P. Jana, V.A. De La Peña O'Shea, M. Romero, J. Gonzalez-Aguilar, D.P. Serrano, P. Pizarro, J.M. Coronado, Thermochemical energy storage at high temperature via redox cycles of Mn and Co oxides: Pure oxides versus mixed ones, Sol. Energy Mater. Sol. Cells. 123 (2014) 47–57. https://doi.org/10.1016/j.solmat.2013.12.018.

[73] A.H. Abedin, M.A. Rosen, Assessment of a closed thermochemical energy storage using energy and exergy methods, Appl. Energy. 93 (2012) 18–23. https://doi.org/10.1016/j.apenergy.2011.05.041.

[74] E. Alonso, C. Pérez-Rábago, J. Licurgo, E. Fuentealba, C.A. Estrada, First experimental studies of solar redox reactions of copper oxides for thermochemical energy storage, Sol. Energy. 115 (2015) 297–305. https://doi.org/10.1016/j.solener.2015.03.005.

[75] M. Linder, Using thermochemical reactions in thermal energy storage systems, LTD, 2021. https://doi.org/10.1016/b978-0-12-819885-8.00016-4.

[76] A.J. Carrillo, J. González-Aguilar, M. Romero, J.M. Coronado, Solar Energy on Demand: A Review on High Temperature Thermochemical Heat Storage Systems and Materials, Chem. Rev. 119 (2019) 4777–4816. https://doi.org/10.1021/acs.chemrev.8b00315.

[77] L. André, S. Abanades, G. Flamant, Screening of thermochemical systems based on solid-gas reversible reactions for high temperature solar thermal energy storage, Renew. Sustain. Energy Rev. 64 (2016) 703–715. https://doi.org/10.1016/j.rser.2016.06.043.

[78] A.J. Carrillo, D.P. Serrano, D. Sastre, J.M. Coronado, P. Pizarro, Additional Material - Revisiting the BaO 2 /BaO redox cycle for solar thermochemical energy storage - Additional Material, Phys. Chem. Chem. Phys. 18 (2016) 8039–8048.

[79] C. Agrafiotis, M. Roeb, M. Schmücker, C. Sattler, Exploitation of thermochemical cycles based on solid oxide redox systems for thermochemical storage of solar heat. Part 1: Testing of cobalt oxide-based powders, Sol. Energy. 102 (2014) 189–211. https://doi.org/10.1016/j.solener.2013.12.032.

[80] K.E. N'Tsoukpoe, T. Schmidt, H.U. Rammelberg, B.A. Watts, W.K.L. Ruck, A systematic multi-step screening of numerous salt hydrates for low temperature thermochemical energy storage, Appl. Energy. 124 (2014) 1–16. https://doi.org/10.1016/j.apenergy.2014.02.053.

[81] R.J. Clark, A. Mehrabadi, M. Farid, State of the art on salt hydrate thermochemical energy storage systems for use in building applications, J. Energy Storage. 27 (2020) 101145. https://doi.org/10.1016/j.est.2019.101145.

[82] A. Solé, I. Martorell, L.F. Cabeza, State of the art on gas-solid thermochemical energy storage systems and reactors for building applications, Renew. Sustain. Energy Rev. 47 (2015) 386–398. https://doi.org/10.1016/j.rser.2015.03.077.

[83] T. Yan, R.Z. Wang, T.X. Li, L.W. Wang, I.T. Fred, A review of promising candidate reactions for chemical heat storage, Renew. Sustain. Energy Rev. 43 (2015) 13–31. https://doi.org/10.1016/j.rser.2014.11.015.

[84] M.A. Fahim, T.A. Al-Sahhaf, S.E.M. Hamam, Energy storage using the reaction cycle: Methyl alcohol/acetaldehyde, Int. J. Energy Res. 13 (1989) 289–296. https://doi.org/10.1002/er.4440130305.

[85] M. Fischer, S. Bruzzano, B. Egenolf-Jonkmanns, B. Zeidler-Fandrich, H. Wack, G. Deerberg, Thermal storage by thermoreversible chemical reaction systems, Energy Procedia. 48 (2014) 327–336. https://doi.org/10.1016/j.egypro.2014.02.038.

[86] G. Whiting, D. Grondin, S. Bennici, A. Auroux, Heats of water sorption studies on zeolite-MgSO4 composites as potential thermochemical heat storage materials, Sol. Energy Mater. Sol. Cells. 112 (2013) 112–119. https://doi.org/10.1016/j.solmat.2013.01.020.

[87] S. Tescari, A. Singh, C. Agrafiotis, L. de Oliveira, S. Breuer, B. Schlögl-Knothe, M. Roeb, C. Sattler, Experimental evaluation of a pilot-scale thermochemical storage system for a concentrated solar power plant, Appl. Energy. 189 (2017) 66–75. https://doi.org/10.1016/j.apenergy.2016.12.032.

[88] S.A. Kalogirou, Solar thermal collectors and applications, 2004. https://doi.org/10.1016/j.pecs.2004.02.001.

[89] L. Scapino, H.A. Zondag, J. Van Bael, J. Diriken, C.C.M. Rindt, Sorption heat storage for long-term low-temperature applications: A review on the advancements at material and prototype scale, Appl. Energy. 190 (2017) 920–948. https://doi.org/10.1016/j.apenergy.2016.12.148.

[90] L.F. Cabeza, Aran Solé, C. Barreneche, Review on sorption materials and technologies for heat pumps and thermal energy storage, (n.d.) 5–24.

[91] C. Bales, P. Gantenbein, D. Jaenig, H. Kerskes, M. van Essen, R. Weber, H. Zondag, Final Report of Subtask B "Chemical and Sorption Storage" : Report B7 of Subtask B, (2008) 21. http://www.iea-shc.org/publications/downloads/task32-c7.pdf.

[92] A. Hauer, Adsorption Systems for Tes—Design and Demonstration Projects, Therm. Energy Storage Sustain. Energy Consum. (2007) 409–427. https://doi.org/10.1007/978-1-4020-5290-3_25.

[93] A. Hauer, E.L. avemann, Open Absorption Systems for Air Conditioning and Thermal Energy Storage, Therm. Energy Storage Sustain. Energy Consum. (2007) 429–444. https://doi.org/10.1007/978-1-4020-5290-3_26.

[94] W. Wongsuwan, S. Kumar, P. Neveu, F. Meunier, A review of chemical heat pump technology and applications, 2001. https://doi.org/10.1016/S1359-4311(01)00022-9.

[95] F. Ziegler, Sorption heat pumping technologies: Comparisons and challenges, Int. J. Refrig. 32 (2009) 566–576. https://doi.org/10.1016/j.ijrefrig.2009.03.007.

[96] H. Kerskes, B. Mette, F. Bertsch, S. Asenbeck, H. Drück, Chemical energy storage using reversible solid/gas-reactions (CWS) - Results of the research project, Energy Procedia. 30 (2012) 294–304. https://doi.org/10.1016/j.egypro.2012.11.035.

[97] B. Mette, H. Kerskes, H. Drück, H. Müller-Steinhagen, New highly efficient regeneration process for thermochemical energy storage, Appl. Energy. 109 (2013) 352–359. https://doi.org/10.1016/j.apenergy.2013.01.087.

[98] H. Zondag, B. Kikkert, S. Smeding, R. de Boer, M. Bakker, Prototype

thermochemical heat storage with open reactor system, Appl. Energy. 109 (2013) 360–365. https://doi.org/10.1016/j.apenergy.2013.01.082.

[99] A. Hauer, F. Fischer, Open adsorption system for an energy efficient dishwasher, Chemie-Ingenieur-Technik. 83 (2011) 61–66. https://doi.org/10.1002/cite.201000197.

[100] G. Tanguy, F. Marias, S. Rouge, J. Wyttenbach, P. Papillon, Parametric studies of thermochemical processes for seasonal storage, Energy Procedia. 30 (2012) 388–394. https://doi.org/10.1016/j.egypro.2012.11.046.

[101] B.G.P. Van Ravensteijn, P.A.J. Donkers, R.C. Ruliaman, J. Eversdijk, H.R. Fischer, H.P. Huinink, O.C.G. Adan, Encapsulation of Salt Hydrates by Polymer Coatings for Low-Temperature Heat Storage Applications, ACS Appl. Polym. Mater. 3 (2021) 1712–1726. https://doi.org/10.1021/acsapm.0c01186.

[102] M. Steiger, S. Asmussen, Crystallization of sodium sulfate phases in porous materials: The phase diagram Na2SO4-H2O and the generation of stress, Geochim. Cosmochim. Acta. 72 (2008) 4291–4306. https://doi.org/10.1016/j.gca.2008.05.053.

[103] S. Hongois, F. Kuznik, P. Stevens, J.J. Roux, Development and characterisation of a new MgSO4-zeolite composite for long-term thermal energy storage, Sol. Energy Mater. Sol. Cells. 95 (2011) 1831–1837. https://doi.org/10.1016/j.solmat.2011.01.050.

[104] H.U. Rammelberg, T. Schmidt, W. Ruck, Hydration and dehydration of salt hydrates and hydroxides for thermal energy storage - Kinetics and energy release, Energy Procedia. 30 (2012) 362–369. https://doi.org/10.1016/j.egypro.2012.11.043.

[105] V.M. Van Essen, J. Cot Gores, L.P.J. Bleijendaal, H.A. Zondag, R. Schuitema, M. Bakker, W.G.J. Van Helden, Characterization of salt hydrates for compact seasonal thermochemical storage, Proc. ASME 3rd Int. Conf. Energy Sustain. 2009, ES2009. 2 (2009) 825–830. https://doi.org/10.1115/ES2009-90289.

[106] F. Desai, J. Sunku Prasad, P. Muthukumar, M.M. Rahman, Thermochemical energy storage system for cooling and process heating applications: A review, Energy Convers. Manag. 229 (2021) 113617. https://doi.org/10.1016/j.enconman.2020.113617.

[107] A.J. De Jong, L. Van Vliet, C. Hoegaerts, M. Roelands, R. Cuypers, Thermochemical Heat Storage - From Reaction Storage Density to System Storage Density, Energy Procedia. 91 (2016) 128–137. https://doi.org/10.1016/j.egypro.2016.06.187.

[108] S. Rougé, Y.A. Criado, O. Soriano, J.C. Abanades, Continuous CaO/Ca(OH)2 fluidized bed reactor for energy storage: First experimental results and reactor model validation, Ind. Eng. Chem. Res. 56 (2017) 844–852. https://doi.org/10.1021/acs.iecr.6b04105.

[109] J. Yan, C.Y. Zhao, Z.H. Pan, The effect of CO2 on Ca(OH)2 and Mg(OH)2 thermochemical heat storage systems, Energy. 124 (2017) 114–123. https://doi.org/10.1016/j.energy.2017.02.034.

[110] Y.A. Criado, M. Alonso, J.C. Abanades, Kinetics of the CaO/Ca(OH)2 Hydration/Dehydration Reaction for Thermochemical Energy Storage Applications, Ind. Eng. Chem. Res. 53 (2014) 12594–12601. https://doi.org/10.1111/j.1540-4560.1975.tb00737.x.

[111] Y. Duan, D.C. Sorescu, D. Luebke, Efficient theoretical screening of solid sorbents for CO2 capture applications, 28th Annu. Int. Pittsburgh Coal Conf. 2011, PCC 2011. 1 (2011) 661–677.

[112] L. André, S. Abanades, Evaluation and performances comparison of calcium, strontium and barium carbonates during calcination/carbonation reactions for solar thermochemical energy storage, J. Energy Storage. 13 (2017) 193–205. https://doi.org/10.1016/j.est.2017.07.014.

[113] C. Ortiz, Thermochemical energy storage based on carbonates: A brief overview, Energies. 14 (2021) 3–5. https://doi.org/10.3390/en14144336.

[114] I. Arvanitidis, D. Sichen, S. Seetharaman, A study of the thermal decomposition of BaCO3, Metall. Mater. Trans. B Process Metall. Mater. Process. Sci. 27 (1996) 409–416. https://doi.org/10.1007/BF02914905.

[115] N.R. Rhodes, A. Barde, K. Randhir, L. Li, D.W. Hahn, R. Mei, J.F. Klausner, N. Auyeung, Solar Thermochemical Energy Storage Through Carbonation Cycles of SrCO3/SrO Supported on SrZrO3, ChemSusChem. 8 (2015) 3793–3798. https://doi.org/10.1002/cssc.201501023.

[116] C. Qin, W. Liu, H. An, J. Yin, B. Feng, Fabrication of CaO-based sorbents for CO 2 capture by a mixing method, Environ. Sci. Technol. 46 (2012) 1932–1939. https://doi.org/10.1021/es203525y.

[117] J.M. Valverde, Ca-based synthetic materials with enhanced CO2 capture efficiency, J. Mater. Chem. A. 1 (2013) 447–468. https://doi.org/10.1039/c2ta00096b.

[118] C. Ortiz, J.M. Valverde, R. Chacartegui, L.A. Perez-Maqueda, P. Giménez, The Calcium-Looping (CaCO3/CaO) process for thermochemical energy

storage in Concentrating Solar Power plants, Renew. Sustain. Energy Rev. 113 (2019) 109252. https://doi.org/10.1016/j.rser.2019.109252.

[119] L. André, S. Abanades, Evaluation and performances comparison of calcium, strontium and barium carbonates during calcination/carbonation reactions for solar thermochemical energy storage, J. Energy Storage. 13 (2017) 193–205. https://doi.org/10.1016/j.est.2017.07.014.

[120] S. Zare Ghorbaei, H. Ale Ebrahim, Carbonation reaction of strontium oxide for thermochemical energy storage and CO2 removal applications: Kinetic study and reactor performance prediction, Appl. Energy. 277 (2020) 115604. https://doi.org/10.1016/j.apenergy.2020.115604.

[121] D. Mahon, G. Claudio, P. Eames, An experimental study of the decomposition and carbonation of magnesium carbonate for medium temperature thermochemical energy storage, Energies. 14 (2021). https://doi.org/10.3390/en14051316.

[122] J. Stekli, L. Irwin, R. Pitchumani, Technical challenges and opportunities for concentrating solar power with thermal energy storage, J. Therm. Sci. Eng. Appl. 5 (2013) 1–12. https://doi.org/10.1115/1.4024143.

[123] A.J. Schrader, A.P. Muroyama, P.G. Loutzenhiser, Solar electricity via an Air Brayton cycle with an integrated two-step thermochemical cycle for heat storage based on Co3O4/CoO redox reactions: Thermodynamic analysis, Sol. Energy. 118 (2015) 485–495. https://doi.org/10.1016/j.solener.2015.05.045.

[124] C. Agrafiotis, M. Roeb, C. Sattler, Hybrid Sensible/Thermochemical Solar Energy Storage Concepts Based on Porous Ceramic Structures and Redox Pair Oxides Chemistry, Energy Procedia. 69 (2015) 706–715. https://doi.org/10.1016/j.egypro.2015.03.081.

[125] A.J. Carrillo, D. Sastre, D.P. Serrano, P. Pizarro, J.M. Coronado, Revisiting the BaO2/BaO redox cycle for solar thermochemical energy storage, Phys. Chem. Chem. Phys. 18 (2016) 8039–8048. https://doi.org/10.1039/c5cp07777j.

[126] W.E. Wentworth, E. Chen, Simple thermal decomposition reactions for storage of solar thermal energy, Sol. Energy. 18 (1976) 205–214. https://doi.org/10.1016/0038-092X(76)90019-0.

[127] T. Kousksou, P. Bruel, A. Jamil, T. El Rhafiki, Y. Zeraouli, Energy storage: Applications and challenges, Sol. Energy Mater. Sol. Cells. 120 (2014) 59–80. https://doi.org/10.1016/j.solmat.2013.08.015.

[128] M. Neises, S. Tescari, L. de Oliveira, M. Roeb, C. Sattler, B. Wong, Solar-

heated rotary kiln for thermochemical energy storage, Sol. Energy. 86 (2012) 3040–3048. https://doi.org/10.1016/j.solener.2012.07.012.

[129] C. Pagkoura, G. Karagiannakis, A. Zygogianni, S. Lorentzou, M. Kostoglou, A.G. Konstandopoulos, M. Rattenburry, J.W. Woodhead, Cobalt oxide based structured bodies as redox thermochemical heat storage medium for future CSP plants, Sol. Energy. 108 (2014) 146–163. https://doi.org/10.1016/j.solener.2014.06.034.

[130] T. Kodama, N. Gokon, Thermochemical cycles for high-temperature solar hydrogen production, Chem. Rev. 107 (2007) 4048–4077. https://doi.org/10.1021/cr050188a.

[131] A. Castillo, D.F. Gayme, Grid-scale energy storage applications in renewable energy integration: A survey, Energy Convers. Manag. 87 (2014) 885–894. https://doi.org/10.1016/j.enconman.2014.07.063.

[132] G. Karagiannakis, C. Pagkoura, A.G. Konstandopoulos, S. Tescari, A. Singh, M. Roeb, M. Lange, J. Marcher, A. Jové, C. Prieto, M. Rattenbury, A. Chasiotis, Thermochemical storage for CSP via redox structured reactors/heat exchangers: The RESTRUCTURE project, AIP Conf. Proc. 1850 (2017). https://doi.org/10.1063/1.4984453.

[133] C. Zhou, K. Shah, E. Doroodchi, B. Moghtaderi, Equilibrium thermodynamic analyses of methanol production via a novel Chemical Looping Carbon Arrestor process, Energy Convers. Manag. 96 (2015) 392–402. https://doi.org/10.1016/j.enconman.2015.03.008.

[134] C. Zhou, K. Shah, B. Moghtaderi, Techno-economic assessment of integrated chemical looping air separation for oxy-fuel combustion: An Australian case study, Energy and Fuels. 29 (2015) 2074–2088. https://doi.org/10.1021/ef5022076.

[135] K. Shah, C. Zhou, H. Song, E. Doroodchi, B. Moghtaderi, A novel hybrid chemical-looping oxy combustor process for the combustion of solid and gaseous fuels: Thermodynamic analysis, Energy and Fuels. 29 (2015) 602–617. https://doi.org/10.1021/ef502389t.

[136] D. Müller, C. Knoll, W. Artner, M. Harasek, C. Gierl-Mayer, J.M. Welch, A. Werner, P. Weinberger, Combining in-situ X-ray diffraction with thermogravimetry and differential scanning calorimetry – An investigation of Co3O4, MnO2 and PbO2 for thermochemical energy storage, Sol. Energy. 153 (2017) 11–24. https://doi.org/10.1016/j.solener.2017.05.037.

[137] B. Wong, Thermochemical heat storage for concentrated solar power: Thermochemical system reactor design for thermal energy storage, Phase II Final Report for the period September 30, 2008 through April

30, 2011, (2011).

[138] X. Han, L. Wang, H. Ling, Z. Ge, X. Lin, X. Dai, H. Chen, Critical review of thermochemical energy storage systems based on cobalt, manganese, and copper oxides, Renew. Sustain. Energy Rev. 158 (2022) 112076. https://doi.org/10.1016/j.rser.2022.112076.

[139] T. Esence, A. Bruch, S. Molina, B. Stutz, J.F. Fourmigué, A review on experience feedback and numerical modeling of packed-bed thermal energy storage systems, Sol. Energy. 153 (2017) 628–654. https://doi.org/10.1016/j.solener.2017.03.032.

[140] H. Grirate, N. Zari, I. Elamrani, R. Couturier, A. Elmchaouri, S. Belcadi, P. Tochon, Characterization of several Moroccan rocks used as filler material for thermal energy storage in CSP power plants, Energy Procedia. 49 (2014) 810–819. https://doi.org/10.1016/j.egypro.2014.03.088.

[141] H. Michels, R. Pitz-Paal, Cascaded latent heat storage for parabolic trough solar power plants, Sol. Energy. 81 (2007) 829–837. https://doi.org/10.1016/j.solener.2006.09.008.

[142] A. Abhat, Low temperature latent heat thermal energy storage: Heat storage materials, Sol. Energy. 30 (1983) 313–332. https://doi.org/10.1016/0038-092X(83)90186-X.

[143] Q. Xiao, J. Fan, Y. Fang, L. Li, T. Xu, W. Yuan, The shape-stabilized light-to-thermal conversion phase change material based on CH3COONa·3H2O as thermal energy storage media, Appl. Therm. Eng. 136 (2018) 701–707. https://doi.org/10.1016/j.applthermaleng.2018.03.053.

[144] M. a Fahim, J.D. Ford, Energy storage using the BaO\textsubscript{2}/ BaO reaction cycle, Chem. Eng. J. 27 (1983) 21–28.

[145] O. Kubaschewski, C.B. Alcock, Metallurgical Thermochemistry, in: 5th ed., Oxford Pergamon press, 1979. https://doi.org/10.1063/1.3060816.

[146] R.G. Bowrey, J. Jutsen, Energy storage using the reversible oxidation of barium oxide, Sol. Energy. 21 (1978) 523–525. https://doi.org/10.1016/0038-092X(78)90078-6.

[147] T. Block, M. Schmücker, Metal oxides for thermochemical energy storage: A comparison of several metal oxide systems, Sol. Energy. 126 (2016) 195–207. https://doi.org/10.1016/j.solener.2015.12.032.

[148] M. Deutsch, F. Horvath, C. Knoll, D. Lager, C. Gierl-Mayer, P. Weinberger, F. Winter, High-Temperature Energy Storage: Kinetic Investigations of the CuO/Cu2O Reaction Cycle, Energy and Fuels. 31 (2017) 2324–2334. https://doi.org/10.1021/acs.energyfuels.6b02343.

[149] A.J. Carrillo, J. Moya, A. Bayón, P. Jana, V.A. De La Peña O'Shea, M. Romero, J. Gonzalez-Aguilar, D.P. Serrano, P. Pizarro, J.M. Coronado, Thermochemical energy storage at high temperature via redox cycles of Mn and Co oxides: Pure oxides versus mixed ones, Sol. Energy Mater. Sol. Cells. 123 (2014) 47–57. https://doi.org/10.1016/j.solmat.2013.12.018.

[150] L. André, S. Abanades, Investigation of metal oxides, mixed oxides, perovskites and alkaline earth carbonates/hydroxides as suitable candidate materials for high-temperature thermochemical energy storage using reversible solid-gas reactions, Mater. Today Energy. 10 (2018) 48–61. https://doi.org/10.1016/j.mtener.2018.08.007.

[151] A.J. Carrillo, D.P. Serrano, P. Pizarro, J.M. Coronado, Improving the thermochemical energy storage performance of the Mn2O3/Mn3O4 redox couple by the incorporation of iron, ChemSusChem. 8 (2015) 1947–1954. https://doi.org/10.1002/cssc.201500148.

[152] K. Randhir, K. King, N. Rhodes, L. Li, D. Hahn, R. Mei, N. AuYeung, J. Klausner, Magnesium-manganese oxides for high temperature thermochemical energy storage, J. Energy Storage. 21 (2019) 599–610. https://doi.org/10.1016/j.est.2018.11.024.

[153] K.N. Hutchings, M. Wilson, P.A. Larsen, R.A. Cutler, Kinetic and thermodynamic considerations for oxygen absorption/desorption using cobalt oxide, Solid State Ionics. 177 (2006) 45–51. https://doi.org/10.1016/j.ssi.2005.10.005.

[154] L. André, S. Abanades, L. Cassayre, High-temperature thermochemical energy storage based on redox reactions using Co-Fe and Mn-Fe mixed metal oxides, J. Solid State Chem. 253 (2017) 6–14. https://doi.org/10.1016/j.jssc.2017.05.015.

[155] L. Till, Thermochemical data of barium peroxide from thermogravimetric measurements, J. Therm. Anal. 3 (1971) 177–180. https://doi.org/10.1007/BF01904681.

[156] J. Kendall, F.J. Fuchs, THE CATALYTIC INFLUENCE OF FOREIGN OXIDES ON THE DECOMPOSITION OF SILVER OXIDE, MERCURIC OXIDE AND BARIUM PEROXIDE, J. Am. Chem. Soc. 43 (1921) 2017–2031. https://doi.org/10.1021/ja01442a005.

[157] F. Lei, A. Dyall, N. AuYeung, An in-depth investigation of BaO2/BaO redox oxides for reversible solar thermochemical energy storage, Sol. Energy Mater. Sol. Cells. 223 (2021) 110957. https://doi.org/10.1016/j.solmat.2021.110957.

[158] E. Alonso, A. Gallo, C. Pérez-Rábago, E. Fuentealba, Thermodynamic study of CuO/Cu2O and Co3O4/CoO redox pairs for solar energy

thermochemical storage, AIP Conf. Proc. 1734 (2016). https://doi.org/10.1063/1.4949102.

[159] D. Chadda, J.D. Ford, M.A. Fahim, Chemical energy storage by the reaction cycle CuO/Cu2O, Int. J. Energy Res. 13 (1989) 63–73. https://doi.org/10.1002/er.4440130107.

[160] J. Marugán, J.A. Botas, M. Martín, R. Molina, C. Herradón, Study of the first step of the Mn 2O 3/MnO thermochemical cycle for solar hydrogen production, Int. J. Hydrogen Energy. 37 (2012) 7017–7025. https://doi.org/10.1016/j.ijhydene.2011.10.124.

[161] K.H. Norwich, Le chatelier's principle in sensation and perception: Fractal-like enfolding at different scales, Front. Physiol. 1 JUN (2010) 1–7. https://doi.org/10.3389/fphys.2010.00017.

[162] M. Hänchen, A. Stiel, Z.R. Jovanovic, A. Steinfeld, Thermally driven copper oxide redox cycle for the separation of oxygen from gases, Ind. Eng. Chem. Res. 51 (2012) 7013–7021. https://doi.org/10.1021/ie202474s.

[163] D. Yilmaz, E. Darwish, H. Leion, Thermochemical energy storage performance of copper oxides: Effect of support materials, J. Energy Storage. 32 (2020) 102012. https://doi.org/10.1016/j.est.2020.102012.

[164] M. Arjmand, A. Azad, H. Leion, A. Lyngfelt, T. Mattisson, Prospects of Al2O3 and MgAl2O4-Supported CuO Oxygen Carriers in Chemical-Looping Combustion (CLC) and Chemical-Looping with Oxygen Uncoupling (CLOU), Energy and Fuels. 25 (2011) 5493–5502. https://doi.org/dx.doi.org/10.1021/ef201329x.

[165] M. Wokon, T. Block, S. Nicolai, M. Linder, M. Schmücker, Thermodynamic and kinetic investigation of a technical grade manganese-iron binary oxide for thermochemical energy storage, Sol. Energy. 153 (2017) 471–485. https://doi.org/10.1016/j.solener.2017.05.045.

[166] A. Steinfeld, P. Kuhn, A. Reller, R. Palumbo, J. Murray, Y. Tamaura, Solar-processed metals as clean energy carriers and water-splitters, Int. J. Hydrogen Energy. 23 (1998) 767–774. https://doi.org/10.1016/s0360-3199(97)00135-3.

[167] M.I. Zaki, M.A. Hasan, L. Pasupulety, K. Kumari, Thermochemistry of manganese oxides in reactive gas atmospheres: Probing catalytic MnOx compositions in the atmosphere of CO+O2, Thermochim. Acta. 311 (1998) 97–103. https://doi.org/10.1016/s0040-6031(97)00417-6.

[168] A.J. Carrillo, D.P. Serrano, P. Pizarro, J.M. Coronado, Manganese oxide-based thermochemical energy storage: Modulating temperatures of redox cycles by Fe-Cu co-doping, J. Energy Storage. 5 (2016) 169–176.

https://doi.org/10.1016/j.est.2015.12.005.

[169] G. Karagiannakis, C. Pagkoura, A. Zygogianni, S. Lorentzou, A.G. Konstandopoulos, Monolithic ceramic redox materials for thermochemical heat storage applications in CSP plants, Energy Procedia. 49 (2014) 820–829. https://doi.org/10.1016/j.egypro.2014.03.089.

[170] C. Agrafiotis, A. Becker, M. Roeb, C. Sattler, Hybrid sensible/thermochemical storage of solar energy in cascades of redox-oxide-pair-based porous ceramics, ASME 2015 9th Int. Conf. Energy Sustain. ES 2015, Collocated with ASME 2015 Power Conf. ASME 2015 13th Int. Conf. Fuel Cell Sci. Eng. Technol. ASME 2015 Nucl. Forum. 2 (2015) 1–10. https://doi.org/10.1115/ES2015-49334.

[171] A.J. Carrillo, D.P. Serrano, P. Pizarro, J.M. Coronado, Thermochemical heat storage based on the Mn 2 O 3 /Mn 3 O 4 redox couple: Influence of the initial particle size on the morphological evolution and cyclability, J. Mater. Chem. A. 2 (2014) 19435–19443. https://doi.org/10.1039/c4ta03409k.

[172] F. Varsano, C. Alvani, A. La Barbera, A. Masi, F. Padella, Lithium manganese oxides as high-temperature thermal energy storage system, Thermochim. Acta. 640 (2016) 26–35. https://doi.org/10.1016/j.tca.2016.07.018.

[173] A.J. Carrillo, D.P. Serrano, P. Pizarro, J.M. Coronado, Improving the thermochemical energy storage performance of the Mn 2 O 3 /Mn 3 O 4 redox couple by the incorporation of iron, ChemSusChem. 8 (2015) 1947–1954. https://doi.org/10.1002/cssc.201500148.

[174] D. Bielsa, A. Zaki, P.L. Arias, A. Faik, Improving the redox performance of Mn2O3/Mn3O4 pair by Si doping to be used as thermochemical energy storage for concentrated solar power plants, Sol. Energy. 204 (2020) 144–154. https://doi.org/10.1016/j.solener.2020.04.073.

[175] S.M. Babiniec, E.N. Coker, J.E. Miller, A. Ambrosini, Doped calcium manganites for advanced high temperature thermochemical energy storage, Int. J. Energy Res. 33 (2016) 280–284. https://doi.org/10.1002/er.

[176] C. Pagkoura, G. Karagiannakis, A. Zygogianni, S. Lorentzou, A.G. Konstandopoulos, Cobalt Oxide Based Honeycombs as Reactors/Heat Exchangers for Redox Thermochemical Heat Storage in Future CSP Plants, Energy Procedia. 69 (2015) 978–987. https://doi.org/10.1016/j.egypro.2015.03.183.

[177] A.P. Muroyama, A.J. Schrader, P.G. Loutzenhiser, Solar electricity via an

Air Brayton cycle with an integrated two-step thermochemical cycle for heat storage based on Co3O4/CoO redox reactions II: Kinetic analyses, Sol. Energy. 122 (2015) 409–418. https://doi.org/10.1016/j.solener.2015.08.038.

[178] A. Singh, S. Tescari, G. Lantin, C. Agrafiotis, M. Roeb, C. Sattler, Solar thermochemical heat storage via the Co3O4/CoO looping cycle: Storage reactor modelling and experimental validation, Sol. Energy. 144 (2017) 453–465. https://doi.org/10.1016/j.solener.2017.01.052.

[179] C. Agrafiotis, S. Tescari, M. Roeb, M. Schmücker, C. Sattler, Exploitation of thermochemical cycles based on solid oxide redox systems for thermochemical storage of solar heat. Part 3: Cobalt oxide monolithic porous structures as integrated thermochemical reactors/heat exchangers, Sol. Energy. 114 (2015) 459–475. https://doi.org/10.1016/j.solener.2014.12.037.

[180] C. Agrafiotis, M. Roeb, M. Schmücker, C. Sattler, Exploitation of thermochemical cycles based on solid oxide redox systems for thermochemical storage of solar heat. Part 2: Redox oxide-coated porous ceramic structures as integrated thermochemical reactors/heat exchangers, Sol. Energy. 114 (2015) 440–458. https://doi.org/10.1016/j.solener.2014.12.036.

[181] C. Agrafiotis, A. Becker, M. Roeb, C. Sattler, Exploitation of thermochemical cycles based on solid oxide redox systems for thermochemical storage of solar heat. Part 5: Testing of porous ceramic honeycomb and foam cascades based on cobalt and manganese oxides for hybrid sensible/thermochemical heat s, Sol. Energy. 139 (2016) 676–694. https://doi.org/10.1016/j.solener.2016.09.013.

[182] M. Silakhori, M. Jafarian, M. Arjomandi, G.J. Nathan, Thermogravimetric analysis of Cu, Mn, Co, and Pb oxides for thermochemical energy storage, J. Energy Storage. 23 (2019) 138–147. https://doi.org/10.1016/j.est.2019.03.008.

[183] T. Block, M. Schmücker, Metal oxides for thermochemical energy storage: A comparison of several metal oxide systems, Sol. Energy. 126 (2016) 195–207. https://doi.org/10.1016/j.solener.2015.12.032.

[184] A. Zaki, J. Carrasco, D. Bielsa, A. Faik, Tunable Redox Temperature of a Co3-xMn xO4 (0 ≤ x ≤ 3) Continuous Solid Solution for Thermochemical Energy Storage, ACS Appl. Mater. Interfaces. 12 (2020) 7010–7020. https://doi.org/10.1021/acsami.9b14369.

[185] L. André, S. Abanades, L. Cassayre, Mixed Metal Oxide Systems Applied to Thermochemical Storage of Solar Energy: Benefits of Secondary Metal Addition in Co and Mn Oxides and Contribution of Thermodynamics,

Appl. Sci. 8 (2018) 2618. https://doi.org/10.3390/app8122618.

[186] L. Ji, J. Lin, H.C. Zeng, Metal-Support Interactions in Co/Al2O3 Catalysts: A Comparative Study on Reactivity of Support, J. Phys. Chem. 104 (2000) 1783–1790. https://doi.org/10.1021/jp993400l.

[187] C. Pagkoura, G. Karagiannakis, E. Halevas, A.G. Konstandopoulos, Co3O4-based honeycombs as compact redox reactors/heat exchangers for thermochemical storage in the next generation CSP plants, AIP Conf. Proc. 1734 (2016). https://doi.org/10.1063/1.4949135.

[188] G. Karagiannakis, C. Pagkoura, E. Halevas, P. Baltzopoulou, A.G. Konstandopoulos, Cobalt/cobaltous oxide based honeycombs for thermochemical heat storage in future concentrated solar power installations: Multi-cyclic assessment and semi-quantitative heat effects estimations, Sol. Energy. 133 (2016) 394–407. https://doi.org/10.1016/j.solener.2016.04.032.

[189] C. Agrafiotis, M. Roeb, C. Sattler, Exploitation of thermochemical cycles based on solid oxide redox systems for thermochemical storage of solar heat. Part 4: Screening of oxides for use in cascaded thermochemical storage concepts, Sol. Energy. 139 (2016) 695–710. https://doi.org/10.1016/j.solener.2016.04.034.

[190] https://www.made-in-china.com, (n.d.) https://www.made-in-china.com.

[191] S. Tescari, A. Singh, L. De Oliveira, S. Breuer, C. Agrafiotis, M. Roeb, C. Sattler, J. Marcher, C. Pagkoura, G. Karagiannakis, A.G. Konstandopoulos, Experimental proof of concept of a pilot-scale thermochemical storage unit, AIP Conf. Proc. 1850 (2017). https://doi.org/10.1063/1.4984455.

[192] T. Block, N. Knoblauch, M. Schmücker, The cobalt-oxide/iron-oxide binary system for use as high temperature thermochemical energy storage material, Thermochim. Acta. 577 (2014) 25–32. https://doi.org/10.1016/j.tca.2013.11.025.

[193] A. Giaconia, I. Balog, G. Caputo, Article hybridization of CSP plants: Characterization of a molten salt heater for binary and ternary nitrate salt mixtures fueled with gas/biogas heaters, Energies. 14 (2021). https://doi.org/10.3390/en14227652.

[194] A. Giaconia, G. Iaquaniello, A.A. Metwally, G. Caputo, I. Balog, Experimental demonstration and analysis of a CSP plant with molten salt heat transfer fluid in parabolic troughs, Sol. Energy. 211 (2020) 622–632. https://doi.org/10.1016/j.solener.2020.09.091.

[195] K. Lovegrove, W. Stein, Concentrating Solar Power Technology–

Principles, Developments and Applications, ISBN 978-0, Sawston, UK, 2012. https://doi.org/10.1016/B978-1-84569-769-3.50020-0.

[196] R.P. Merchán, M.J. Santos, A. Medina, A. Calvo Hernández, High temperature central tower plants for concentrated solar power: 2021 overview, Renew. Sustain. Energy Rev. 155 (2022) 111828. https://doi.org/10.1016/j.rser.2021.111828.

[197] V.R. Patil, F. Kiener, A. Grylka, A. Steinfeld, Experimental testing of a solar air cavity-receiver with reticulated porous ceramic absorbers for thermal processing at above 1000 °C, Sol. Energy. 214 (2021) 72–85. https://doi.org/10.1016/j.solener.2020.11.045.

[198] A. Del Río, R. Korzynietz, J.A. Brioso, M. Gallas, I. Ordóñez, M. Quero, C. Díaz, Soltrec - Pressurized Volumetric Solar Air Receiver Technology, Energy Procedia. 69 (2015) 360–368. https://doi.org/10.1016/j.egypro.2015.03.042.

[199] M. Lubkoll, T.W. Von Backström, D.G. Kröger, Survey on Pressurized Air Receiver Development, 2nd South. African Sol. Energy Conf. 2014. 27 (2014).

[200] P. Pardo, A. Deydier, Z. Anxionnaz-Minvielle, S. Rougé, M. Cabassud, P. Cognet, A review on high temperature thermochemical heat energy storage, Renew. Sustain. Energy Rev. 32 (2014) 591–610. https://doi.org/10.1016/j.rser.2013.12.014.

[201] L. Kumar, M. Hasanuzzaman, N.A. Rahim, Global advancement of solar thermal energy technologies for industrial process heat and its future prospects: A review, Energy Convers. Manag. 195 (2019) 885–908. https://doi.org/10.1016/j.enconman.2019.05.081.

[202] Y. Ding, S.B. Riffat, Thermochemical energy storage technologies for building applications: a state-of-the-art review, Int. J. Low-Carbon Technol. 8 (2013) 106–116. https://doi.org/10.1093/ijlct/cts004.

[203] M. Nasri, I. Burger, S. Michael, H.E. Friedrich, Waste heat recovery for fuel cell electric vehicle with thermochemical energy storage, 2016 11th Int. Conf. Ecol. Veh. Renew. Energies, EVER 2016. (2016). https://doi.org/10.1109/EVER.2016.7476439.

[204] M. Schmidt, M. Linder, A Novel Thermochemical Long Term Storage Concept: Balance of Renewable Electricity and Heat Demand in Buildings, Front. Energy Res. 8 (2020) 1–12. https://doi.org/10.3389/fenrg.2020.00137.

[205] D. Vanhoudt, B. Claessens, R. Salenbien, J. Desmedt, The use of distributed thermal storage in district heating grids for demand side

management, (2017). http://arxiv.org/abs/1702.06005.

[206] A. Ahmad, Y. Ding, A thermochemical energy storage based cooling and heating system: Modelling, experimental validation and lab-scale demonstration, Energy Convers. Manag. 247 (2021) 114748. https://doi.org/10.1016/j.enconman.2021.114748.

[207] C.K. Clayton, H.Y. Sohn, K.J. Whitty, Oxidation kinetics of Cu2O in oxygen carriers for chemical looping with oxygen uncoupling, Ind. Eng. Chem. Res. 53 (2014) 2976–2986. https://doi.org/10.1021/ie402495a.

[208] P. Haseli, M. Jafarian, G.J. Nathan, High temperature solar thermochemical process for production of stored energy and oxygen based on CuO/Cu2O redox reactions, Sol. Energy. 153 (2017) 1–10. https://doi.org/10.1016/j.solener.2017.05.025.

[209] C. Agrafiotis, M. Roeb, A.G. Konstandopoulos, L. Nalbandian, V.T. Zaspalis, C. Sattler, P. Stobbe, A.M. Steele, Solar water splitting for hydrogen production with monolithic reactors, Sol. Energy. 79 (2005) 409–421. https://doi.org/10.1016/j.solener.2005.02.026.

[210] A.K. Singh, N.J. Auyeung, K. Randhir, R. Mishra, K.M. Allen, J. Petrasch, J.F. Klausner, Thermal Reduction of Iron Oxide under Reduced Pressure and Implications on Thermal Conversion Efficiency for Solar Thermochemical Fuel Production, Ind. Eng. Chem. Res. 54 (2015) 6793–6803. https://doi.org/10.1021/ie504402x.

[211] J.E. Lee, I. Shafiq, M. Hussain, S.S. Lam, G.H. Rhee, Y.K. Park, A review on integrated thermochemical hydrogen production from water, Int. J. Hydrogen Energy. 47 (2022) 4346–4356. https://doi.org/10.1016/j.ijhydene.2021.11.065.

[212] M.E. Gálvez, P.G. Loutzenhiser, I. Hischier, A. Steinfeld, CO2 splitting via two-step solar thermochemical cycles with Zn/ZnO and FeO/Fe3O4 redox reactions: Thermodynamic analysis, Energy and Fuels. 22 (2008) 3544–3550. https://doi.org/10.1021/ef800230b.

[213] M. Kawabe, H. Ono, T. Sano, M. Tsuji, Y. Tamaura, Thermochemical oxygen pump with praseodymium oxides using a temperature-swing at 403-873 K, Energy. 22 (1997) 1041–1049. https://doi.org/10.1016/S0360-5442(97)00044-3.

[214] S. Ströhle, A. Haselbacher, Z.R. Jovanovic, A. Steinfeld, Upgrading sensible-heat storage with a thermochemical storage section operated at variable pressure: An effective way toward active control of the heat-transfer fluid outflow temperature, Appl. Energy. 196 (2017) 51–61. https://doi.org/10.1016/j.apenergy.2017.03.125.

[215] G.R. Li, G.J. Yang, Structure evolution of multiscaled thermal barrier coatings during thermal exposure, Elsevier Inc., 2019. https://doi.org/10.1016/B978-0-12-813870-0.00007-3.

[216] N.P. Padture, M. Gell, E.H. Jordan, Thermal barrier coatings for gas-turbine engine applications, Science (80-.). 296 (2002) 280–284. https://doi.org/10.1126/science.1068609.

[217] R. Vassen, A. Stuke, D. Stöver, Recent developments in the field of thermal barrier coatings, J. Therm. Spray Technol. 18 (2009) 181–186. https://doi.org/10.1007/s11666-009-9312-7.

[218] J.T. DeMasi-Marcin, D.K. Gupta, Protective coatings in the gas turbine engine, Surf. Coatings Technol. 68–69 (1994) 1–9. https://doi.org/10.1016/0257-8972(94)90129-5.

[219] B. Gleeson, Thermal barrier coatings for aeroengine applications, J. Propuls. Power. 22 (2006) 375–383. https://doi.org/10.2514/1.20734.

[220] C.U. Hardwicke, Y.C. Lau, Advances in thermal spray coatings for gas turbines and energy generation: A review, J. Therm. Spray Technol. 22 (2013) 564–576. https://doi.org/10.1007/s11666-013-9904-0.

[221] D.R. Clarke, M. Oechsner, N.P. Padture, Thermal-barrier coatings for more efficient gas-turbine engines, MRS Bull. 37 (2012) 891–898. https://doi.org/10.1557/mrs.2012.232.

[222] L. Xu, H. Wang, L. Su, D. Lu, K. Peng, H. Gao, A new class of high-entropy fluorite oxides with tunable expansion coefficients, low thermal conductivity and exceptional sintering resistance, J. Eur. Ceram. Soc. 41 (2021) 6670–6676. https://doi.org/10.1016/j.jeurceramsoc.2021.05.043.

[223] X.Q. Cao, R. Vassen, D. Stoever, Ceramic materials for thermal barrier coatings, J. Eur. Ceram. Soc. 24 (2004) 1–10. https://doi.org/10.1016/S0955-2219(03)00129-8.

[224] A. Loganathan, A.S. Gandhi, Effect of phase transformations on the fracture toughness of t' yttria stabilized zirconia, Mater. Sci. Eng. A. 556 (2012) 927–935. https://doi.org/10.1016/j.msea.2012.07.095.

[225] A. Feuerstein, J. Knapp, T. Taylor, A. Ashary, A. Bolcavage, N. Hitchman, Technical and economical aspects of current thermal barrier coating systems for gas turbine engines by thermal spray and EBPVD: A review, J. Therm. Spray Technol. 17 (2008) 199–213. https://doi.org/10.1007/s11666-007-9148-y.

[226] R. Vaßen, M.O. Jarligo, T. Steinke, D.E. Mack, D. Stöver, Overview on advanced thermal barrier coatings, Surf. Coatings Technol. 205 (2010)

938–942. https://doi.org/10.1016/j.surfcoat.2010.08.151.

[227] S. Santhanam, M.P. Heddrich, M. Riedel, K.A. Friedrich, Theoretical and experimental study of Reversible Solid Oxide Cell (r-SOC) systems for energy storage, Energy. 141 (2017) 202–214. https://doi.org/10.1016/j.energy.2017.09.081.

[228] Q. Zhang, E. Uchaker, S.L. Candelaria, G. Cao, Nanomaterials for energy conversion and storage, Chem. Soc. Rev. 42 (2013) 3127–3171. https://doi.org/10.1039/c3cs00009e.

[229] A. Walcarius, Mesoporous materials and electrochemistry, Chem. Soc. Rev. 42 (2013) 4098–4140. https://doi.org/10.1039/c2cs35322a.

[230] M.C. Orilall, U. Wiesner, Block copolymer based composition and morphology control in nanostructured hybrid materials for energy conversion and storage: Solar cells, batteries, and fuel cells, Chem. Soc. Rev. 40 (2011) 520–535. https://doi.org/10.1039/c0cs00034e.

[231] M.R. Gao, Y.F. Xu, J. Jiang, S.H. Yu, Nanostructured metal chalcogenides: Synthesis, modification, and applications in energy conversion and storage devices, Chem. Soc. Rev. 42 (2013) 2986–3017. https://doi.org/10.1039/c2cs35310e.

[232] S. Aldrich, Solid State Synthesis, (n.d.). https://www.sigmaaldrich.com/ES/es/applications/materials-science-and-engineering/solid-state-synthesis (accessed March 7, 2022).

[233] N. Wang, J.Y.H. Fuh, S.T. Dheen, A. Senthil Kumar, Synthesis methods of functionalized nanoparticles: a review, Bio-Design Manuf. 4 (2021) 379–404. https://doi.org/10.1007/s42242-020-00106-3.

[234] K. Cui, M. Sun, J. Zhang, J. Xu, Z. Zhai, T. Gong, L. Hou, C. Yuan, Facile solid-state synthesis of tetragonal CuFe2O4 spinels with improved infrared radiation performance, Ceram. Int. (2021) 2–8. https://doi.org/10.1016/j.ceramint.2021.12.268.

[235] X. Wu, H. Yu, H. Dong, L. Geng, Enhanced infrared radiation properties of CoFe2O4 by single Ce3+-doping with energy-efficient preparation, Ceram. Int. 40 (2014) 5905–5911. https://doi.org/10.1016/j.ceramint.2013.11.035.

[236] D.P. Dubal, P. Gomez-Romero, B.R. Sankapal, R. Holze, Nickel cobaltite as an emerging material for supercapacitors: An overview, Nano Energy. 11 (2015) 377–399. https://doi.org/10.1016/j.nanoen.2014.11.013.

[237] M. Nawaz, Y. Sliman, I. Ercan, M.K. Lima-Tenório, E.T. Tenório-Neto, C. Kaewsaneha, A. Elaissari, Magnetic and pH-responsive magnetic nanocarriers, Elsevier Ltd., 2018. https://doi.org/10.1016/B978-0-08-

101995-5.00002-7.

[238] L. Babes, J. Jacques, L. Jeune, P. Jallet, Synthesis of Iron Oxide Nanoparticles Used as MRI Contrast Agents: A Parametric Study, J. Colloid Interface Sci. 482 (1999) 474–482. https://www.sciencedirect.com/science/article/abs/pii/S0021979798960532.

[239] J. Zhao, M. Li, J. Li, C. Wei, Y. He, Y. Huang, Q. Li, Porous Ni-Co-Mn oxides prisms for high performance electrochemical energy storage, Appl. Surf. Sci. 425 (2017) 1158–1167. https://doi.org/10.1016/j.apsusc.2017.07.261.

[240] M.A. Peña, J.L.G. Fierro, Chemical structures and performance of perovskite oxides, Chem. Rev. 101 (2001) 1981–2017. https://doi.org/10.1021/cr980129f.

[241] S. Laurent, D. Forge, M. Port, A. Roch, C. Robic, L. Vander Elst, R.N. Muller, Erratum: Magnetic iron oxide nanoparticles: Synthesis, stabilization, vectorization, physicochemical characterizations, and biological applications (Chemical Reviews (2008) 108 (2064)), Chem. Rev. 110 (2010) 2574. https://doi.org/10.1021/cr900197g.

[242] J. Li, X. Shi, M. Shen, Hydrothermal synthesis and functionalization of iron oxide nanoparticles for MR imaging applications, Part. Part. Syst. Charact. 31 (2014) 1223–1237. https://doi.org/10.1002/ppsc.201400087.

[243] Y. Wang, F. Cai, P. Guo, Y. Lei, Q. Xi, F. Wang, Short-time hydrothermal synthesis of CuBi2O4 nanocolumn arrays for efficient visible-light photocatalysis, Nanomaterials. 9 (2019) 16–21. https://doi.org/10.3390/nano9091257.

[244] Z.Q. Liu, Q.Z. Xu, J.Y. Wang, N. Li, S.H. Guo, Y.Z. Su, H.J. Wang, J.H. Zhang, S. Chen, Facile hydrothermal synthesis of urchin-like NiCo2O4 spheres as efficient electrocatalysts for oxygen reduction reaction, Int. J. Hydrogen Energy. 38 (2013) 6657–6662. https://doi.org/10.1016/j.ijhydene.2013.03.092.

[245] I.A. Neacşu, A.I. Nicoară, O.R. Vasile, B.Ş. Vasile, Inorganic micro- and nanostructured implants for tissue engineering, Nanobiomaterials Hard Tissue Eng. Appl. Nanobiomaterials. (2016) 271–295. https://doi.org/10.1016/B978-0-323-42862-0.00009-2.

[246] S.O. Kucheyev, M. Toth, T.F. Baumann, A. V. Hamza, J. Ilavsky, W.R. Knowles, C.K. Saw, B.L. Thiel, V. Tileli, T. Van Buuren, Y.M. Wang, T.M. Willey, Structure of low-density nanoporous dielectrics revealed by low-vacuum electron microscopy and small-angle X-ray scattering,

Langmuir. 23 (2007) 353–356. https://doi.org/10.1021/la0619729.

[247] J. Konishi, K. Fujita, S. Oiwa, K. Nakanishi, K. Hirao, Crystalline ZrO2 monoliths with well-defined macropores and mesostructured skeletons prepared by combining the alkoxy-derived sol-gel process accompanied by phase separation and the solvothermal process, Chem. Mater. 20 (2008) 2165–2173. https://doi.org/10.1021/cm703351d.

[248] R. Sui, J.L. Young, C.P. Berlinguette, Sol-gel synthesis of linear Sn-doped TiO2 nanostructures, J. Mater. Chem. 20 (2010) 498–503. https://doi.org/10.1039/b915349g.

[249] M. Zarei, M. Borhani Zarandi, M. Alizadeh, Preparation of CuO/CeO2 composites by the Pechini method and investigation of their structural and electrical properties, Ceram. Int. 45 (2019) 1991–1997. https://doi.org/10.1016/j.ceramint.2018.10.096.

[250] S. Sakka, Sol-Gel Processing of Thin Films with Metal Salts, Handb. Sol-Gel Sci. Technol. Process. Charact. Appl. (2018) ix. https://doi.org/10.1007/978-3-319-32101-1.

[251] S. Bayat, D. Ghanbari, M. Salavati-Niasari, Pechini synthesis of Co2SiO4 magnetic nanoparticles and its application in photo-degradation of azo dyes, J. Mol. Liq. 220 (2016) 223–231. https://doi.org/10.1016/j.molliq.2016.04.066.

[252] F. Ansari, F. Soofivand, M. Salavati-Niasari, Utilizing maleic acid as a novel fuel for synthesis of PbFe12O19 nanoceramics via sol-gel auto-combustion route, Mater. Charact. 103 (2015) 11–17. https://doi.org/10.1016/j.matchar.2015.03.010.

[253] A.B.S. Garcia, A.G. Bispo-Jr, S.A.M. Lima, A.M. Pires, Effects of the Pechini's modified synthetic route on structural and photophysical properties of Eu3+ or Tb3+-doped LaAlO3, Mater. Res. Bull. 143 (2021) 111462. https://doi.org/10.1016/j.materresbull.2021.111462.

[254] M. Aflaki, F. Davar, Synthesis, luminescence and photocatalyst properties of zirconia nanosheets by modified Pechini method, J. Mol. Liq. 221 (2016) 1071–1079. https://doi.org/10.1016/j.molliq.2016.06.067.

[255] Y. Han, Z. Lu, Z. Teng, J. Liang, Z. Guo, D. Wang, M.Y. Han, W. Yang, Unraveling the growth mechanism of silica particles in the stöber method: In situ seeded growth model, Langmuir. 33 (2017) 5879–5890. https://doi.org/10.1021/acs.langmuir.7b01140.

[256] W. Li, Z. Huo, X. Zhang, H. Zhao, Z. Cui, P. Fu, M. Liu, X. Qiao, W. Fan, X. Pang, New sight for in-situ monitoring of silica growth process: The incorporation of Stöber process and aggregation-induced emission (AIE)

technique, Dye. Pigment. 182 (2020) 108637. https://doi.org/10.1016/j.dyepig.2020.108637.

[257] T. Matsoukas, E. Gulari, Monomer-addition growth with a slow initiation step: A growth model for silica particles from alkoxides, J. Colloid Interface Sci. 132 (1989) 13–21. https://doi.org/10.1016/0021-9797(89)90210-5.

[258] T. Matsoukas, E. Gulari, Dynamics of growth of silica particles from ammonia-catalyzed hydrolysis of tetra-ethyl-orthosilicate, J. Colloid Interface Sci. 124 (1988) 252–261. https://doi.org/10.1016/0021-9797(88)90346-3.

[259] G.H. Bogush, C.F. Zukoski, Uniform Silica Particle Precipitation: An Aggregative Growth Model, J. Colloid Interface Sci. 142 (1991) 1–16. http://ac.els-cdn.com.ezp-prod1.hul.harvard.edu/002197979190030C/1-s2.0-002197979190030C-main.pdf?_tid=98719180-079c-11e4-a239-00000aab0f02&acdnat=1404933168_904c31bfb117db9b0bb754e209dc1b36%5Cnpapers2://publication/uuid/DF68F9E9-490B-4570-9586-76C081EBBA.

[260] P.P. Ghimire, M. Jaroniec, Renaissance of Stöber method for synthesis of colloidal particles: New developments and opportunities, J. Colloid Interface Sci. 584 (2021) 838–865. https://doi.org/10.1016/j.jcis.2020.10.014.

[261] W. Stober, A. Fink, Controlled growth of monodisperse silica spheres in the micron size range, J. Colloid Interface Sci. 26 (1968) 62–69. https://doi.org/10.1589/jpts.29.112.

[262] S. Lüdtke, T. Adam, K.K. Unger, Application of 0.5-µm porous silanized silica beads in electrochromatography, J. Chromatogr. A. 786 (1997) 229–235. https://doi.org/10.1016/S0021-9673(97)00600-6.

[263] C. López, L. Vázquez, F. Meseguer, R. Mayoral, M. Ocaña, H. Míguez, Photonic crystal made by close packing SiO2 submicron spheres, Superlattices Microstruct. 22 (1997) 399–404. https://doi.org/10.1006/spmi.1996.0313.

[264] K.K. Unger, Porous silica: its properties and use as support in column liquid chromatography, Journal of chromatography library- Volume 16, 1979.

[265] R. Ciriminna, A. Fidalgo, V. Pandarus, F. Béland, L.M. Ilharco, M. Pagliaro, The sol-gel route to advanced silica-based materials and recent applications, Chem. Rev. 113 (2013) 6592–6620. https://doi.org/10.1021/cr300399c.

[266] C.C.M.C. Carcouët, M.W.P. Van De Put, B. Mezari, P.C.M.M. Magusin, J. Laven, P.H.H. Bomans, H. Friedrich, A.C.C. Esteves, N.A.J.M. Sommerdijk, R.A.T.M. Van Benthem, G. De With, Nucleation and growth of monodisperse silica nanoparticles, Nano Lett. 14 (2014) 1433–1438. https://doi.org/10.1021/nl404550d.

[267] G.H. Bogush, M.A. Tracy, C.F. Zukoski, Preparation of monodisperse silica particles: control of size and mass fraction, J. Non. Cryst. Solids. 104 (1988) 95–106. https://doi.org/10.1016/0166-6622(88)80084-2.

[268] C.G. Tan, B.D. Bowen, N. Epstein, Production of monodisperse colloidal silica spheres: Effect of temperature, J. Colloid Interface Sci. 118 (1987) 290–293. https://doi.org/10.1016/0021-9797(87)90458-9.

[269] S.L. Greasley, S.J. Page, S. Sirovica, S. Chen, R.A. Martin, A. Riveiro, J. V. Hanna, A.E. Porter, J.R. Jones, Controlling particle size in the Stöber process and incorporation of calcium, J. Colloid Interface Sci. 469 (2016) 213–223. https://doi.org/10.1016/j.jcis.2016.01.065.

[270] I.A. Rahman, V. Padavettan, Synthesis of Silica nanoparticles by Sol-Gel: Size-dependent properties, surface modification, and applications in silica-polymer nanocompositesa review, J. Nanomater. 2012 (2012). https://doi.org/10.1155/2012/132424.

[271] G.A.M. Ali, O.A. Fouad, S.A. Makhlouf, Structural, optical and electrical properties of sol-gel prepared mesoporous Co3O4/SiO2 nanocomposites, J. Alloys Compd. 579 (2013) 606–611. https://doi.org/10.1016/j.jallcom.2013.07.095.

[272] J.L. Shi, Relation between coarsening and densification in solid-state sintering of ceramics: experimental test on superfine zirconia powder compacts, J. Mater. Res. 14 (1999) 1389–1397. https://doi.org/10.1557/JMR.1999.0189.

[273] R.M. German, Sintering of Advanced Materials, Woodhead Publishing Limited, 2010. https://doi.org/10.1533/9781845699949.1.110.

[274] F. Wakai, M. Yoshida, Y. Shinoda, T. Akatsu, Coarsening and grain growth in sintering of two particles of different sizes, Acta Mater. 53 (2005) 1361–1371. https://doi.org/10.1016/j.actamat.2004.11.029.

[275] A.J. Carrillo, D.P. Serrano, P. Pizarro, J.M. Coronado, Thermochemical heat storage at high temperatures using Mn2O3/Mn3O4 system: Narrowing the redox hysteresis by metal co-doping, Energy Procedia. 73 (2015) 263–271. https://doi.org/10.1016/j.egypro.2015.07.686.

[276] H.B. Dizaji, H. Hosseini, A review of material screening in pure and mixed-metal oxide thermochemical energy storage (TCES) systems for

concentrated solar power (CSP) applications, Renew. Sustain. Energy Rev. 98 (2018) 9–26. https://doi.org/10.1016/j.rser.2018.09.004.

[277] M. Outokesh, M. Hosseinpour, S.J. Ahmadi, T. Mousavand, S. Sadjadi, W. Soltanian, Hydrothermal synthesis of CuO nanoparticles: Study on effects of operational conditions on yield, purity, and size of the nanoparticles, Ind. Eng. Chem. Res. 50 (2011) 3540–3554. https://doi.org/10.1021/ie1017089.

[278] T. Got̲, M. Kada, Preparation of high-tc y-ba-cu-o superconducting filaments by suspension spinning method, Jpn. J. Appl. Phys. 26 (1987) 1527–1528. https://doi.org/10.1143/JJAP.26.L1527.

[279] P. Salame, R. Drai, O. Prakash, A.R. Kulkarni, IBLC effect leading to colossal dielectric constant in layered structured Eu2CuO4 ceramic, Ceram. Int. 40 (2014) 4491–4498. https://doi.org/10.1016/j.ceramint.2013.08.123.

[280] P.A.K. Nair, W.L. Vasconcelos, K. Paine, J. Calabria-Holley, A review on applications of sol-gel science in cement, Constr. Build. Mater. 291 (2021) 123065. https://doi.org/10.1016/j.conbuildmat.2021.123065.

[281] A. Kharchenko, O. Myronyuk, L. Melnyk, P. Sivolapov, Analysis of methods of regulation of silicon dioxide particles size obtained by the Stober method, Technol. Audit Prod. Reserv. 2 (2017) 9–16. https://doi.org/10.15587/2312-8372.2018.128571.

[282] F. Sima, C. Ristoscu, L. Duta, O. Gallet, K. Anselme, I.N. Mihailescu, Laser thin films deposition and characterization for biomedical applications, Elsevier Ltd, 2016. https://doi.org/10.1016/B978-0-08-100883-6.00003-4.

[283] C. Domingo, J. Saurina, An overview of the analytical characterization of nanostructured drug delivery systems: Towards green and sustainable pharmaceuticals: A review, Anal. Chim. Acta. 744 (2012) 8–22. https://doi.org/10.1016/j.aca.2012.07.010.

[284] M. Bimson, The examination of ceramics by X-ray powder diffraction, Stud. Conserv. 14 (1969) 83–89.

[285] S. Petrick Casagrande, R.C. Blanco, Método de Rietveld para el estudio de estructuras cristalinas, 2 (2004) 1–5.

[286] J. Rodríguez-Carvajal, Recent advances in magnetic structure determination by neutron powder diffraction, Phys. B Phys. Condens. Matter. 192 (1993) 55–69. https://doi.org/10.1016/0921-4526(93)90108-I.

[287] R.. Egerton, Physical Principles of Electron Microscopy, Springer, 2005.

[288] J. Henderson, Chemical analysis techniques, Encycl. Archaeol. (2008) 985–995. https://doi.org/10.1016/B978-012373962-9.00053-4.

[289] B. Misof, P. Roschger, P. Fratzl, 3.26 Imaging mineralized tissues in vertebrates, Compr. Biomater. II. 3 (2017) 549–578. https://doi.org/10.1016/B978-0-12-803581-8.09827-1.

[290] B. Misof, P. Roschger, P. Fratzl, Imaging mineralized tissues in vertebrates, Elsevier Ltd., 2011. https://doi.org/10.1016/b978-0-08-055294-1.00112-4.

[291] D.A.H. Hanaor, M. Ghadiri, W. Chrzanowski, Y. Gan, Scalable surface area characterization by electrokinetic analysis of complex anion adsorption, Langmuir. 30 (2014) 15143–15152. https://doi.org/10.1021/la503581e.

[292] Pennstate Materials Research Institute, Optical profilometry, (n.d.). https://www.mri.psu.edu/materials-characterization-lab/characterization-techniques/optical-profilometry (accessed March 25, 2022).

[293] Perkin Elmer, Thermogravimetric analysis (TGA), 2019. https://doi.org/10.46430/phen0083.

[294] Intertek, Differential Scanning Calorimetry (DSC), (n.d.). https://www.intertek.com/analysis/dsc/#:~:text=Differential Scanning Calorimetry (DSC) is,to a controlled temperature program. (accessed March 28, 2022).

[295] Horiba, What is Glow Discharge Optical Emission Spectroscopy GDOES?, (n.d.). https://www.horiba.com/int/glow-discharge-optical-emission-spectroscopy/?MP=2163-2162 (accessed March 25, 2022).

[296] NanoScience Instruments, Optical profilometry, (n.d.). https://www.nanoscience.com/techniques/optical-profilometry/#:~:text=Profilometry is a technique used,probe or by using light. (accessed March 25, 2022).

[297] Bruker Nano Surface Division, Universal Mechanical Tester — Proven Innovation, 2013. www.bruker.com.

Chapter 2

Conclusions and future works

Conclusions

The research carried out, to meet the objectives detailed in the previous chapters, has led to several conclusions, which are detailed in this section. They are presented in schematic form in response to the different aspects described in the objectives.

The initial objective based on the development of novel mixed metal oxides with lower reduction temperatures for thermochemical energy storage at high temperatures led to the following conclusions:

- A mixed oxide with the general formula $Co_{3-x}Ni_xO_4$ where $0<x<1$ can be successfully prepared by the sol-gel Pechini route. The maximum quantity of Ni in the Co_3O_4 structure is x=0.6, as for higher nickel contents, the XRD patterns show a secondary irreversible phase of CoO·NiO.
- The reactivity and the redox performance of the materials synthesized (with Ni contents (x) from 0 to 1) was determined by TGA/DSC measurements. It was observed that each mixed oxide shows a different behavior in terms of reduction temperature, oxygen loss ratio and reversibility. It can be highlighted that the mixed oxides with higher amount of nickel ($Co_{2.2}Ni_{0.8}O_4$ and Co_2NiO_4) show incomplete

reoxidations, indicating that the reduction/oxidation only takes place in a small fraction of the material.

- The study has confirmed that the reduction temperature of the nickel cobaltites is lower than in the case of the pure Co_3O_4. Moreover, the redox temperature is tunable depending on the amount of nickel in the cobalt oxide structure. The nickel content of the material leads to a substantial decrease of the redox temperature. In particular, the mixed oxide with a nickel content x=0.6, resulting in $Co_{2.4}Ni_{0.6}O_4$, presents a reduction temperature below 700 ºC, 200 ºC lower than in the case of the pure Co_3O_4.
- The preliminary cyclability of the mixed oxide with the best performance ($Co_{2.4}Ni_{0.6}O_4$) was assessed in a longer experiment (100 cycles) in TGA. An adequate behavior was observed, with a mass loss of 1.18% of between the first and the last cycle.
- The enthalpy values of the mixed oxides changes with the amount of nickel in the cobalt oxide structure. In general, the mixed metal oxides with higher nickel contents show lower values of enthalpy, ranging from 631.9 kJ/kg in the case of pure Co_3O_4 to 347.4 kJ/kg in the case of Co_2NiO_4. However, the enthalpy values obtained are high enough to be suitable for high temperature thermochemical energy storage.

The second objective dealt with the cyclability capacity improvement. The addition of selected particles and an intermediate high temperature calcination step were the routes chosen for the cyclability stability improvement. The results obtained lead to the following conclusions:

- The extra-calcination process produces a densification phenomenon harming the cyclability due to a slowdown of the redox reaction's kinetics. Contrary, the addition of silica particles slightly improves the stability of the material in the initial cycles of the experiments, reaching higher conversion ratio (+1.3%) than the material without addition but

increases slightly the redox temperatures. Moreover, the morphology of the mixed oxide with addition of silica particles is uniform, obtaining the 80% of the measurements in the range of 1-2 μm.

- The lack of interactions between $Co_{2.4}Ni_{0.6}O_4$ and SiO_2 was proved by XRD after 100 cycles.
- The optimization of the type of particles, their size and amount allowed to determine that 0.5 wt. % SiO2 of 400 nm is the best solution showing the best performance.
- The long-term prediction (20 years and 4000 cycles), based on the experimental results of both the material without and with silica particles shows a significant improvement with the presence of particles in the thermochemical material, as the conversion ratio of the nickel cobaltite with addition of SiO_2 particles loses a 12% less than the one of the pure nickel cobaltite. In addition, the reduction temperature is 32 °C lower than in the case of the $Co_{2.4}Ni_{0.6}O_4$ without addition of silica particles.
- The addition of SiO_2 particles does not decrease the enthalpy values of $Co_{2.4}Ni_{0.6}O_4$ (624 kJ/kg for 0.5% SiO_2/$Co_{2.4}Ni_{0.6}O_4$ and 594 kJ/kg for $Co_{2.4}Ni_{0.6}O_4$) due to the cyclability improvement caused in the material, reaching almost the enthalpy values of pure Co_3O_4 (631.9 kJ/kg).
- Enthalpy values are reduced with thermal cycling as a consequence of activity loss due to sintering, obtaining 624 kJ/kg in the case of the fresh 0.5% SiO_2/$Co_{2.4}Ni_{0.6}O_4$ and 554.1 kJ/kg in the 100 times cycled one.

In base of the results obtained, nickel cobaltites with addition of SiO_2 particles are suitable materials and potential future candidates for TcES applications at high temperature.

Once the second objective was completed, the third objective was defined to complete the study of the novel materials with the kinetic analysis of the

material with and without addition of SiO_2 particles. The main conclusions of the kinetic study are:

- The nickel substitution in the cobalt oxide structure and the addition of SiO_2 particles do not increase the reduction activation energy of the materials in comparison with the pure cobalt oxide (158-960 kJ/kg), obtaining 450 kJ/kg for $Co_{2.4}Ni_{0.6}O_4$ and 449 kJ/kg for 0.5% $SiO_2/Co_{2.4}Ni_{0.6}O_4$.
- The theoretical models *f(α)* describing the reduction experimental data are different for each material. Nucleation and growth mechanisms describe the experimental data in the case of $Co_{2.4}Ni_{0.6}O_4$ and diffusion models in the case of 0.5% $SiO_2/Co_{2.4}Ni_{0.6}O_4$.
- The activation energy of the oxidation reaction is affected by the substitution of nickel in the cobalt oxide structure, obtaining higher values for the mixed oxides (99 kJ/kg for $Co_{2.4}Ni_{0.6}O_4$ and 123 kJ/kg for 0.5% $SiO_2/Co_{2.4}Ni_{0.6}O_4$) than the ones listed in bibliography for the pure Co_3O_4 (~60 kJ/kg) but is in agreement with the values published for other mixed oxides (165 kJ/kg for 5% Al_2O_3/Co_3O_4).
- The same theoretical models *f(α)* of nucleation and growth mechanisms fit well with the experimental data of both materials when the conversion ratio is higher than 0.5. For the lower values the SB equation was used to obtain a reliable model in the whole conversion ratio.
- The agreement between the experimental and the theoretical data obtained with the model was good, showing some deviations that could be improved by studying the pressure effect on the kinetics.

The fourth objective of this research work was related with a new possible application of the novel materials developed. The research was focused on the obtention of an active thermal barrier coating to avoid or delay the thermal fatigue triggered by the temperature change of metallic components.

The accomplishment of the fourth objective included different aspects. First the formulation, deposition, curing protocol and initial characterization of the mechanical and thermal properties of the coating. The main conclusions on this case are:

- The quantities of thermochemical material/sol-gel of the coating formulation were adjusted to a 39.8% wt. for the obtention of a homogeneous coating.
- The curing process was studied to reach a compromise between mechanical resistance and activity, obtaining the best performance with a CO_2 solid state laser at a 15% of its maximum power.
- Two types of stainless steel were studied. The compatibility between them (AISI 310-s and AISI 304) and the thermal coating was analyzed by means of GD-OES, showing better results in regard to Fe migration from the stainless steel to the coating in the high temperature one (AISI 310-s).
- The coating formulation was developed with the goal of reaching a compromise between thermochemical activity and resistance to obtain the best performance. It was obtained when using a sol-gel with a solid content of 10 % and a protective interlayer with a solid content of 7.5 %, guaranteeing a correct resistance and not hindering the cyclability of the coating.
- The optimized formulation was used to manufacture coatings of cobalt oxide, nickel cobaltite pure and nickel cobaltite with addition of silica particles. 2 layered coatings with a thickness of 129 μm and good mechanical resistance were obtained.
- The results showed that all the coatings, fresh or thermal treated, were active. However, there was a decrease of activity in the case of the thermal treated ones. The conversion ratios decreased of 13.17 % in the

Co_3O_4 coating, a 27.83% in the $Co_{2.4}Ni_{0.6}O_4$ coating and of 5.75 % in the 0.5 % $SiO_2/Co_{2.4}Ni_{0.6}O_4$ coating.

- The measurements of the coating's roughness showed that the surface of the cobalt oxide coatings is smoother than the one of the nickel cobaltite coatings. Attrition measurements were carried out to assess the mechanical resistance, obtaining similar friction coefficient values for all the coatings.
- In base to all the detailed results, it can be concluded that the layer-by-layer protocol designed is a valid option for manufacturing high temperature active thermal barrier coatings. The thermochemical materials used for the coating formulation during this thesis could be suitable for applications such as: exhaust manifolds installed downstream of internal combustion engines, components for the construction of industrial furnaces, heating engineering, components of solar receivers at high temperatures, electrolyzer and fuel cells, etc.

The second aspect deals with the characterization of the active thermal barrier coating on a thermogravimetric analyzer and on a laboratory-scale test rig. The main conclusions on this case are:

- The coatings have good resistance to the dynamic thermal treatment. They do not show signs of fracture or delamination.
- The thickness of the three formulations is very similar, obtaining an average value of 129 μm.
- The thermogravimetric analysis of the three coating formulations (in powdered form) shows that all the fresh and cycled samples are active. However, treated samples show a decrease in the mass gained/lost. In the case of the Co_3O_4 coatings, the activity decreases a 13%, the $Co_{2.4}Ni_{0.6}O_4$ coatings show an activity decrease of 27% and the 0.5% $SiO_2/Co_{2.4}Ni_{0.6}O_4$ coating shows a decrease of 6%.

- A test rig with the distribution of two heaters (upper and bottom) was selected in order to reduce as much as possible the heat fluxes generated at high temperature.
- The experiments in the test rig showed no buffering effect in the $Co_{2.4}Ni_{0.6}O_4$ pure and added coatings but showed a stabilization of the temperature at 916 ºC for 120 s in the case of the Co_3O_4 coating indicating endothermal reaction.
- The STA analysis of a metallic component coated with the formulations evidences the presence of chemical reactions in the coating, as it shows mass gained/lost variations for all the formulations. The DSC signal shows a clearly higher activity in the case of the Co_3O_4 coatings than in the $Co_{2.4}Ni_{0.6}O_4$ pure and added coatings.

This work confirms the presence of reactions in the active coatings developed, both in TGA and in a larger scale test rig. The presence of the reaction is especially prominent in the cobalt oxide coating, where a clear temperature damping effect has been observed in the experiments of the test rig. Nevertheless, further research must be carried out in order to better understand the effect of the coating on the reactivity of the material and its impact on the possibility to passively stabilize temperatures to finally increase service lifetime of critical components.

Future works

This research gives a proof of concept on the possibility of lowering the reaction temperatures of metal oxides. Cobalt oxide was selected as the starting material for the research since it is a widely studied material, meets the temperature range to be completed and has high reaction enthalpies. However, it is a critical material as it is detrimental to health, as well as being expensive and not very abundant on earth. The main future work should be the change of the cobalt oxide by other metal oxide with good thermochemical properties and less harmful, ideally cheap and abundant on earth's crust.

If the interest continues residing in the cobalt oxide-based materials, the continuation of this research could be done following the next paths:

- It would be interesting the synthesis of the mixed metal oxides using different routes to study the effect of the morphology in the thermochemical behavior of the material.
- The kinetic study could be completed by studying the effect of the pressure in the mechanism of the material, being able to describe reliably with the model the initial and final parts of the redox reactions.

The development of active thermal barrier coatings is a promising topic in a very early stage so there are many possibilities to continue this study. Centered in the aspects developed in this work, the next possible future works are presented:

- The sol-gel of the formulation of the active thermal coating could be modified or optimized in order to improve the mechanical resistance without harming the thermal behavior.

- Another aspect to be studied is the influence of coating manufacturing on future coating performance.
- New active TBCs can be developed using other metal oxides, less harmful than cobalt oxide.
- New application methods could be studied to obtain thicker layers, an aspect intimately linked to the protective capacity of the coating.

The assessment of the long-term behavior of the coating directly applied in a metallic component is quite difficult. New distributions of test rigs could be studied.

Chapter 3

Annex I: Dissemination

Articles

Yasmina Portilla-Nieto, Abdelali Zaki, Karmele Vidal, Marta Hernáiz, Estibaliz Aranzabe, Stefania Doppiu, Abdessamad Faik. Development of Co3-xNixO4 materials for thermochemical energy storage at lower red-ox temperature. *Solar Energy Materials and Solar Cells*. May 2021. https://doi.org/10.1016/j.solmat.2021.111194

Yasmina Portilla-Nieto, Karmele Vidal, Marta Hernaiz, Estibaliz Aranzabe, Stefania Doppiu and, Elena Palomo del Barrio. Development and stabilization of Co2.4Ni0.6O4 material for long-term thermochemical energy storage. *Journal of Energy Storage*. Special Issue: *Enerstock 2021*. May 2022. https://doi.org/10.1016/j.est.2022.104876

Yasmina Portilla-Nieto, Daniel Bielsa, Jean-Luc Dauvergne, Marta Hernaiz, Estibaliz Aranzabe, Stefania Doppiu and Elena Palomo del Barrio. Development of a Kinetic Model for the Redox Reactions of Co2.4Ni0.6O4 and SiO2/Co2.4Ni0.6O4 Oxides for Thermochemical Energy Storage. *Materials*. May 2022. https://doi.org/10.3390/ma15103695

Yasmina Portilla-Nieto, Marta Hernaiz, Marc Linder, Estibaliz Aranzabe, Stefania Doppiu, Elena Palomo del Barrio. Development of active thermochemical barrier coatings using metal oxides. Submitted to *Chemical Engineering Journal*.

Yasmina Portilla-Nieto, Julian Kaess, V.E. Sourmelis Terzopoulos, Christian Brack, Estibaliz Aranzabe, Stefania Doppiu, Elena Palomo del Barrio, Marc Linder. Active thermochemical barrier coatings using metal oxides – first experimental results. Submitted to *Chemical Engineering Journal*.

Patents

Use of Ni-Co mixed oxides for thermochemical energy storage. Nº: 19382550.2-1105. June 2019

Conferences

SOLARPACES2020: Oral contribution: Development of $Co_{3-x}Ni_xO_4$ ($0 \leq x \leq 1$) materials for thermochemical energy storage at lower red-ox temperatures.

ENERSTOCK2021: Oral contribution: Cyclability assessment of $Co_{3-x}Ni_xO_4$ ($0 \leq x \leq 1$) materials for thermochemical energy storage at lower red-ox temperatures.

Stays

German Aerospace Center (DLR). Stuttgart. Institute of Engineering Thermodynamics. 03 September 2021- 03 December 2021.

Annex II: Other research work

Enthalpy study

This section shows the enthalpy measurements carried out for both cobalt oxide and mixed cobalt and nickel oxides, pure and added with SiO_2 particles. The controversy in the enthalpy studies is high for the metal oxides as their reaction temperature range sometimes is too high to measure the enthalpies in a common DSC equipment, limited to maximum temperatures of ~ 700 ºC. The enthalpies of metal oxides use to be measured in a TGA coupled with a DSC system (simultaneous thermal analysis, STA). In this case, the main problem is the obtention of accurate values. Sometimes the layout of the equipment can also interfere with the experimental results obtained. Some authors carried out Round Robin Tests (RRT) [1] in order to measure the interference caused by the equipment. The analysis was performed by preparing a thermal treated cobalt oxide (maintaining the material overnight at 110 ºC to remove water and any other impurity) and sending aliquots of the material to different European centers with the aim of obtaining the reaction enthalpy. There was no rule regarding the equipment to be used or the calibrations. Although all the centers used TGA equipment coupled with DSC systems, the results showed high deviations in the enthalpy values obtained in different centers (see Figure 3.1).

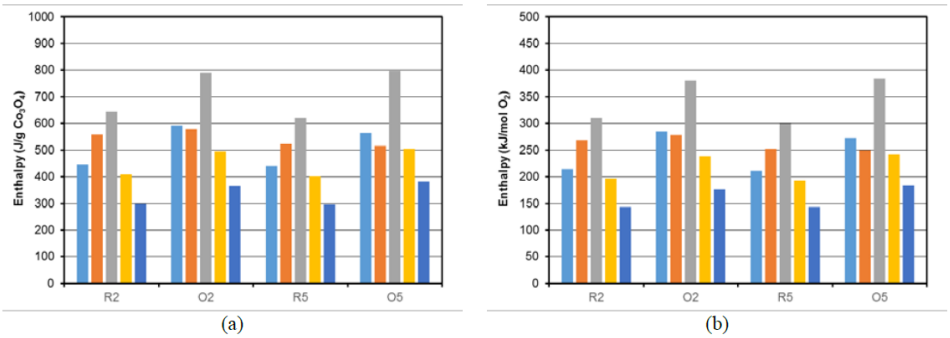

Figure 3.1. *Reaction enthalpy versus reaction temperature expressed in J/g Co_3O_4 (a) and kJ/mol O_2 (b) [1].*

As the literature shows that the enthalpy measurements are easily influenced by the instrument used, in this research work, an optimization of the STA measurement protocol was carried out by modifying the sample mass, the gas flow and the heating ramp. All the experiments were performed using platinum-rhodium crucibles (Pt-Rh), with better thermal conductivity than the Al_2O_3 ones, to obtain more accurate results. The material selected was a commercial Co_3O_4 as there is a lot of information available about this thermochemical material. The experiments consisted in 3 cycles ranging from 700 to 1000 ºC under air atmosphere.

The first step was the optimization of the sample mass. For this purpose, 4 mass values were selected: 20, 30, 40 and 50 mg. For each mass, 2 measurements were carried out. The average results can be found in Table 3.1.

Table 3.1. Enthalpy values obtained for the optimization of the sample mass.

Sample mass (mg)	Enthalpy (J/g)
20	750.3
30	771.1
40	844.7
50	761.9

The maximum values of enthalpy were obtained using a sample mass of 40 mg, reaching the theoretical enthalpy values of the pure Co_3O_4 (844 J/g) [2].

The second step was the optimization of the experimental heating rate that was performed by testing these rates: 1, 5, 10, 15 and 20 ºC/min. As in the previous case, each measurement was repeated twice. The values listed in Table 3.2 are average values.

Table 3.2. Enthalpy values obtained using different heating rate.

Heating rate (ºC/min)	Enthalpy (J/g)
1	614.5
5	748.1
10	844.7
15	671.1
20	671.2

The higher enthalpy values were obtained using a heating ramp of 10 ºC/min. This could be due to the calibration method of the instrument, which was done at 10 ºC/min. A calibration done with a different heating rate could modify the values obtained in this experiment.

The third step was the optimization of the gas flowrate. For this purpose, experiments were done using flowrates of 20, 40, 60, 80 and 100 ml/min. Each flowrate was assessed twice as in the previous cases. The results are shown in Table 3.3.

Table 3.3. Enthalpy values obtained for the optimization of the flowrate.

Gas Flowrate (ml/min)	Enthalpy (J/g)
20	745.7
40	718.8
60	844.7
80	692.5
100	706.5

As it can be observed in Table 3.3, the highest enthalpy value has been obtained using a flowrate of 60 ml/min.

In summary, in this study the best STA experimental conditions are: 40 mg of sample mass, a heating rate of 10 ºC/min and a gas flowrate of 60 ml/min.

The enthalpy measurements of the nickel cobaltites synthesized following the general formula $Co_{3-x}Ni_xO_4$ where $0<x<1$, are listed in Table 3.4. The measurements were done following the optimized parameters obtained previously. The analysis of the nickel cobaltites was done in the temperature range 600-910 ºC and the one of the pure cobalt oxide in the range 700-1000 ºC. In general, a decrease of the storage capacity is observed when adding nickel in the cobalt oxide host structure. This is linked to the decrease of the activity of the material due to sintering caused by the thermal cycling.

Table 3.4. Enthalpy values obtained for the nickel cobaltites with nickel contents (x) from 0 to 1.

Material	Enthalpy (J/g)	Mass loss (%)
Co_2NiO_4	347.4	2.69
$Co_{2.2}Ni_{0.8}O_4$	340.4	3.31
$Co_{2.4}Ni_{0.6}O_4$	594	4.86
$Co_{2.6}Ni_{0.4}O_4$	748.8	5.60
$Co_{2.8}Ni_{0.2}O_4$	586.7	5.73
Co_3O_4	631.9	6.58

New experiments were performed to measure the enthalpies of the nickel cobaltites $Co_{2.4}Ni_{0.6}O_4$ added with SiO_2 400 nm particles fresh and cycled. As a reference, the pure Co_3O_4 was also synthesized following the Pechini route used for the mixed oxides. The experiment consisted in 4 cycles under air in the STA in the temperature range 600-910 ºC in the case of the nickel cobaltites and in the temperature range 700-1000 ºC in the case of the cobalt oxide. An example of the results is depicted in Figure 3.2, while the enthalpy values obtained are listed in Table 3.5.

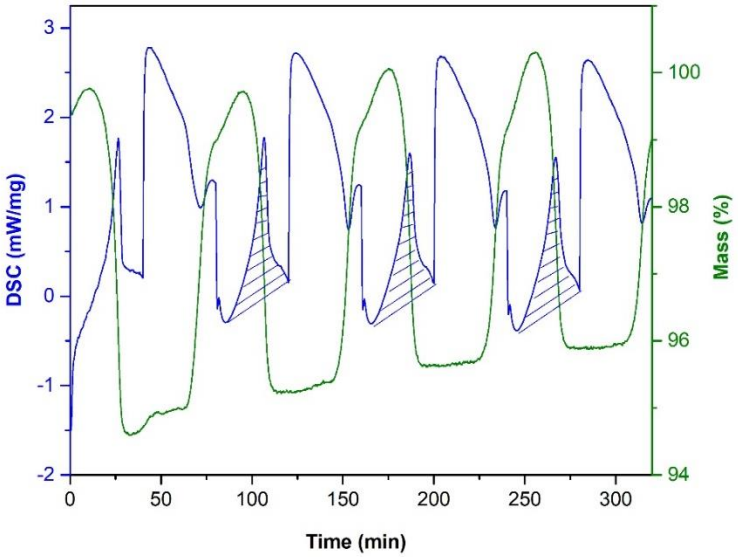

Figure 3.2. *TGA/DSC graphical result for the $Co_{2.4}Ni_{0.6}O_4$ + SiO_2 fresh material.*

Table 3.5. Enthalpy values obtained for Co_3O_4 and $Co_{2.4}Ni_{0.6}O_4$ + SiO_2, fresh and after 100 thermal cycles.

Material	N° cycles	Enthalpy (J/g)					
		C2		C3		C4	
		Reduction	Mass loss (%)	Reduction	Mass loss (%)	Reduction	Mass loss (%)
Co_3O_4	0	631.9	6.58	607.3	6.55	601.3	6.56
$Co_{2.4}Ni_{0.6}O_4$ + SiO_2	0	624	4.48	597.2	4.4	602.6	4.38
$Co_{2.4}Ni_{0.6}O_4$ + SiO_2	100	554.1	4.05	561.3	4	522	3.94

As shown in Table 3.5, there is no repeatability of the enthalpic values in the four cycles so they should be taken as approximate values, not absolute. Comparing the result obtained for the pure cobalt oxide with the nickel cobaltite with addition of silica particles it can be concluded that the addition of

particles does not influence the enthalpy values of the material but the thermal treatment decreases the storage capacity notably.

References

[1] J. González-Aguilar, J.M. Cornonado, J. Nieto-Maestre, L.F. Cabeza, M. Lanchi, S. Sau, M.E.H. Navarro, Y. Ding, C. Prieto, O. Senneca, C. Tregambi, M. Wokon, Round robin test on enthalpies of redox materials for thermochemical heat storage: Perovskites, AIP Conf. Proc. 2126 (2019). https://doi.org/10.1063/1.5117753.

[2] B. Wong, Thermochemical heat storage for concentrated solar power: Thermochemical system reactor design for thermal energy storage, Phase II Final Report for the period September 30, 2008 through April 30, 2011, (2011).

Annex III: Publications

Development of $Co_{3-x}Ni_xO_4$ materials for thermochemical energy storage at lower redox temperature

Solar Energy Materials and Solar Cells, **2021**, *230*, 111194

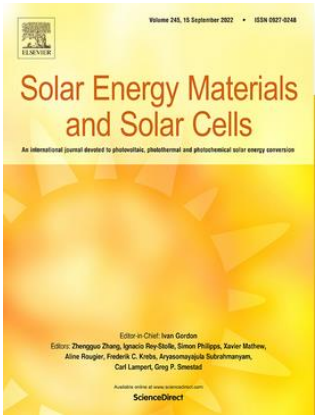

ISSN: 0927-0248

Impact Factor 2021: 7.305

Cite Score: 13.2

Q1 (Renewable energy, Sustainability and the Environment)

https://doi.org/10.1016/j.solmat.2021.111194

Solar Energy Materials & Solar Cells 230 (2021) 111194

Contents lists available at ScienceDirect

Solar Energy Materials and Solar Cells

journal homepage: www.elsevier.com/locate/solmat

Development of $Co_{3-x}Ni_xO_4$ materials for thermochemical energy storage at lower red-ox temperature

Yasmina Portilla-Nieto [a,b,c,*], Abdelali Zaki [a], Karmele Vidal [c], Marta Hernaiz [c], Estibaliz Aranzabe [c], Stefania Doppiu [a], Abdessamad Faik [a,d]

[a] Centre for Cooperative Research on Alternative Energies (CIC EnergiGUNE), Basque Research and Technology Alliance (BRTA), Alava Technology Park, Albert Einstein 48, 01510, Vitoria-Gasteiz, Spain
[b] Applied Physics II Department, Faculty of Science and Technology, University of the Basque Country (UPV/EHU), PO Box 644, 48080, Bilbao, Spain
[c] TEKNIKER, Polo Tecnológico de Eibar, C/ Iñaki Goenaga, 5, 20600, Eibar, Gipuzkoa, Spain
[d] Materials Science, Energy and Nano-Engineering, Mohammed VI Polytechnic University, Lot 660-Hay Moulay Rachid, Ben Guerir, 43150, Morocco

ARTICLE INFO

Keywords:
Thermochemical heat storage
Gas-solid reaction
Reduction/oxidation reaction
Cobalt nickel oxide

ABSTRACT

Heat storage technologies are subject of great research efforts aimed at improving the energy efficiency of power plants and heat recovery processes. In this context, the development of highly efficient and low-cost materials for thermal energy storage is imperative for a large use of this technology. The storage of thermal energy using reversible thermo-chemical reactions can provide large storage capacities especially at high temperatures. Within this class of materials, the red-ox reactions have particular interest due to the low cost of the materials involved (metal oxides) and the use of air both as reacting gas and heat transfer fluid. Therefore, many efforts are doing to improve the efficiency and reversibility of this type of reactions. In this work the synthesis and thermal performances of a novel mixed metal oxide based on cobalt/nickel metals with spinel structure $Co_{3-x}Ni_xO_4$ is reported. A deep study was carried out in order to find the best synthesis conditions and optimum relative metal content in the structure with the objective of decreasing as much as possible the red-ox temperature. The study allowed to determine the optimum Ni content in the oxide structure in order to minimize the reaction temperature. In particular, a linear relationship of the red-ox temperature as a function of the Ni content was observed, enabling reaching red-ox temperature below 700 °C. These results are very promising and open the perspective of using of these types of materials to a wider field of application.

1. Introduction

The world transition to a decarbonized energy system is underway, radically transforming the way the energy is generated, distributed, stored and consumed. This energy transition will require, among other measures, that a large part of energy comes from renewable sources and that industrial processes are more energy efficient. In this scenario, large-scale energy storage is a key factor because it makes possible a big share of renewables where their electrical production generally does not correspond to the electricity demand.

In regard to the solar energy storage and conversion, different strategies can be followed.

The sun energy is directly converted into electricity by using PV technologies [1]. This is a largely developed technology having as main drawback the intermittency in the electricity production due to the intermittency of the energy source. In this respect many strategies are being studied in order to overcome this problem exploring different types of energy storage systems such as batteries [2], pumped hydro (PH) energy storage system, Gravity ESS, superconducting magnetic ESS [3] and compressed air energy storage (CAES) together with promising hybrid systems [4].

The sun energy is transformed into valuable fuels (hydrogen, hydrocarbons, etc.) by using for example photoelectrochemical (PEC) H_2O-splitting devices for H_2 production, photocatalytic processes for CO_2 reduction or thermally driven chemical cycles [5–8]. In the last years, these fuel production technologies are receiving a large impulse both due to the need to decrease the amount of polluting agents introduced in the atmosphere and to find alternative routes to replace fossil fuels [9].

* Corresponding author. Centre for Cooperative Research on Alternative Energies (CIC EnergiGUNE), Basque Research and Technology Alliance (BRTA), Alava Technology Park, Albert Einstein 48, 01510, Vitoria-Gasteiz, Spain.
E-mail address: yportilla@cicenergigune.com (Y. Portilla-Nieto).

https://doi.org/10.1016/j.solmat.2021.111194
Received 25 November 2020; Received in revised form 13 May 2021; Accepted 15 May 2021
Available online 23 May 2021

In this respect, many challenges need still to be faced both from the materials side [10,11] with the proposition of different solutions and the system development side [12].

Another alternative is the power to heat technology. In this case, the combination of thermal energy storage (TES) systems with the use of electricity, not only from solar source but also from other renewable sources such as wind power, for heating purposes, provides the flexibility that the renewables need [13]. These energy storage technologies will play a major role not only in the renewables integration, but also in increasing energy efficiency in industrial processes by reusing stored waste heat from those same processes [14,15].

The most developed technologies in thermal energy storage are based on sensible heat storage (SHS) and latent heat storage (LHS). In the first case, the heat is stored by a temperature change of the storage material; in the second case, the heat is stored by a phase change of the storage material [16–18]. The less developed TES technology is thermochemical storage (TcES), which is based, in addition to the mass and temperature range, on the enthalpy of reversible chemical reactions, and has the highest theoretical energy storage density compared to sensible and latent heat storage [19,20]. Thermochemical energy storage is considered as the most promising technology due to (i) the high energy storage capacity; (ii) the possibility to store the heat at room temperature; (iii) the long-term storage without a significant heat loss and (iv) the heat released at a constant temperature being adjustable by the reaction conditions. The endothermic chemical reaction is used to store the heat when it is available and the reverse exothermic reaction is used to release the heat when it is needed.

In this regard, among the investigated TcES systems in the literature, red-ox reaction involving metal oxides have been considered as the most promising candidates for high temperature TES applications. Thus, these red-ox systems require suitable materials for operation in terms of complete reaction reversibility, suitable reaction temperature, high storage density, high reaction enthalpy, no-toxicity and good thermal stability during cycling in the operation temperature range [21–23].

Different research groups have investigated different materials which can be suitable for thermal energy storage at high temperatures. The most favored materials are metal oxides due to their high reaction enthalpies and high operating temperature; longer storage periods at ambient temperature and utilization of air both as reactant and as heat transfer fluid [24–26].

Although the list of metal oxides is huge and a lot of work has been done in order to identify the most performing candidates, only a few materials can fulfill the requirements, such as energy density, reversibility, kinetics and costs, in order to be considered as suitable materials for TES applications. Previous research works have demonstrated that the most promising metal oxides are cobalt oxide (Co_3O_4/CoO) and manganese oxide (Mn_2O_3/Mn_3O_4) [21,24,27,28]. Nonetheless, their high equilibrium reaction temperatures (higher than 850 °C) have been considered as the main barrier for their use in different applications such as concentrated solar power (CSP) and industrial waste heat recovery. Looking forward to a further development of TcES technology, the development of new materials with reduced red-ox temperatures which are suitable for those applications is urgently needed. Recently, several works proposed redox reactions of doped mixed oxides, spinel and perovskite oxides, aiming to tune the reaction temperature and to shed more light on the understanding of the reaction kinetics and sintering effects [29,30].

Co_3O_4 material is described as a spinel-type structure with the general formula of AB_2O_4 (A, B = Co, Zn, Ni, Fe, Cu, Mn, etc.), where A and B are divalent and trivalent metal cations, respectively. The spinel structure consists of a cubic close-packed array of oxide ions, in which one-eighth of the tetrahedral sites and one half of the octahedral sites are occupied by cations. The distribution of the cations between these two sites is highly dependent upon the nature of the cations incorporated into the structure. In normal spinel structures, the divalent A and trivalent B cations occupy the tetrahedral and octahedral sites, respectively [31–33].

The main purpose of this research is to develop advanced spinel pure mixed oxides with lower red-ox temperatures. Specifically, a solid solution between cobalt oxide and nickel oxide with the general formula $Co_{3-x}Ni_xO_4$ ($0 \leq x \leq 1$) was developed.

The most studied mixed phase of cobalt-nickel has been Co_2NiO_4 [34–36]. This material has attracted the research attention in the area of electrochemistry, especially in supercapacitors due to its low cost, environmentally friendliness, natural abundance and high theoretical capacitance. Besides, it is expected to offer more efficient redox reactions, including contributions from both nickel and cobalt ions coming from its mixed valence spinel structure where nickel occupies octahedral sites and cobalt distributes over both octahedral and tetrahedral sites [34,37–40]. It was found that the mixed phase improves both the electronic conductivity and the electrochemical activity compared to pure phases, making the material suitable for energy conversion/storage systems [35]. Also, it offers rich red-ox reactions, being an interesting property for both electrochemical and thermochemical storage applications.

In the present work, five pure nickel-cobalt mixed oxides, i.e. $Co_{2.8}Ni_{0.2}O_4$, $Co_{2.6}Ni_{0.4}O_4$, $Co_{2.4}Ni_{0.6}O_4$, $Co_{2.2}Ni_{0.8}O_4$ and Co_2NiO_4, were successfully synthesized by sol-gel method. The substitution of Co atoms by Ni atoms leads to a significant decrease in the red-ox temperature where $Co_{2.4}Ni_{0.6}O_4$ shows the lowest temperature of 685 °C (being 906 °C the one for Co_3O_4), which implies a significant decrease in the state-of-the-art red-ox temperature (by more than 220 °C). In addition, the thermal cyclability and stability of these materials was confirmed by thermogravimetric analysis (TGA) up to 100 reduction/oxidation cycles.

2. Materials and methods

2.1. Materials

The materials used during this research were: nickel nitrate hexahydrate extra-pure from *Scharlab*, cobalt nitrate hexahydrate from *Fisher Scientific* with a purity of 98+ %, citric acid from *Fisher Scientific* with a purity of 99+% and ethylene glycol anhydrous from *Sigma-Aldrich* with a purity of 99.8%.

2.2. Synthesis methods

There are three methods that can be used to synthetize Co–Ni mixed metal oxides: sol-gel method, hydrothermal route and coprecipitation and thermal decomposition of the precursors [36,41–43]. Compared in terms of production cost, purity of the final material, simplicity and process sustainability, sol-gel method seems to be the best option for eventual large-scale production:

- **Production costs**: the production cost is related to the raw material cost, but also to the different steps involved in the different synthesis routes. Concerning the precursor materials, sol-gel and hydrothermal routes use nitrates as main precursors [36], while most research works describe coprecipitation route using acetates as the main raw materials [41]. Cobalt acetate cost is 10% higher than the nitrate and nickel acetate is 50% higher than the nitrate precursor, so from the materials cost point of view sol-gel or hydrothermal routes seem to be the more appropriate. Regarding the process cost, main differences are in the washing step (only needed for the hydrothermal and coprecipitation routes) [36,41] and in the reaction conditions (very similar in terms of temperature for the three synthesis, but with notable differences in terms of pressure for the hydrothermal process). High pressure processes associated to the hydrothermal route make this process more expensive than the other routes.
- **Purity:** the production of high purity materials with hydrothermal and coprecipitation synthesis approaches requires adding a washing

step [42]. Contrary, the sol-gel route obtains a high purity material (98–100%).

- **Route complexity**: as already explained, hydrothermal route involves high pressure in the reaction step and both coprecipitation and hydrothermal include a washing step in the process, while sol-gel has no washing step associated. It must also be considered that a reflux step is used in the coprecipitation route.
- **Process sustainability**: the three methods involve similar energy consumption mainly associated to the calcination steps. However, washing steps included in the coprecipitation and hydrothermal methods involve the use of large quantities of solvents. That is why the sol-gel method is considered more environmentally friendly.

Accordingly, the technique used in this work to synthesize Co–Ni mixed metal oxides is the sol-gel method following the Pechini's route. The appropriate quantities of $Co(NO_3)_2{\cdot}6H_2O$ and $Ni(NO_3)_2{\cdot}6H_2O$ nitrates were used for the preparation of 2 g of each material, following the general formula $Co_{3-x}Ni_xO_4$. Initially, the primary precursors were dissolved in 10 mL ethylene glycol under gentle magnetic stirring to afford a homogeneous solution. Subsequently, stoichiometric citric acid, acting as a chelating ligand, was added into the reaction mixture under vigorous magnetic stirring for 60 min. The reaction mixture was dried overnight at 180 °C. The obtained powders were grinded in an agate mortar to increase their homogeneity and then calcined in air at 400 °C for 10 h to obtain the final product with the right stoichiometry.

2.3. Characterization methods

The analytical techniques used for the characterization of the different synthesized materials are described below.

X-ray diffraction (XRD). A Bruker D8 Advance diffractometer equipped with a LYNXEYE detector using Cu $K_{\alpha1}$ radiation ($\lambda = 1.5418$ Å) and θ-2θ geometry was used for XRD analysis. Data were collected at room temperature between 10° and 80° with a step size of 0.02° and a counting time of 8 s per step. The EVA software was used to determine the phase composition of the material. In order to confirm the presence of pure single structure for each material, the Rietveld refinement [44] of the structural models was performed using the WinPlotr/FullProf package [45]. The refined parameters were: background coefficients, scale factor, lattice constants, atomic positions, isotropic independent atomic displacement parameters, zero shift, peak profile and asymmetry parameters.

Insitu X-ray diffraction (in-situ XRD). XRD data were collected on a Bruker D8 Advance diffractometer operating at 30 kV and 20 mA, equipped with a Cu tube ($\lambda = 1.5418$ Å), a Vantec-1 PSD detector and an Anton Parr HTK2000 high-temperature furnace. The powder patterns were recorded in 2q steps of 0.04° in the $15 \leq 2q \leq 85$ range, counting for 1.4 s per step (total time for each temperature 42 min). Data sets were recorded at different temperatures using 0.166 °C s^{-1} heating rate.

Scanning electron microscopy (SEM). The samples were imaged by means of a scanning electron microscope Quanta 200 FEG operated in high vacuum mode at 30 kV featured with a backscattered electron detector (BSED) and Everhart-Thornley Detector (ETD). In addition, energy-dispersive X-ray spectroscopy (EDX) analyses were carried out for elemental mapping. For the evaluation of the pore size distribution of the obtained samples, SEM images were statistically examined. At least 200 measurements were collected for each sample using ImageJ software.

Thermogravimetric analysis (TGA). Two samples of each material were analyzed in a NETZSCH/TG 209 F1 Libra instrument in the temperature range from 600 °C to 950 °C with a heating/cooling rate of 10 °C/min in air atmosphere and a flow rate of 60 mL/min. The experimental error supplied by the brand of the equipment is ±2%. To ensure the quality of the measurements a calibration was carried out obtaining an error of 1.27% for the mass and 1.04% for the temperature values.

3. Results and discussion

The prepared mixed oxides of the present work are characterized by XRD, SEM, TGA analysis and in-situ XRD, and the results are shown below.

Fig. 1 shows the room temperature X-ray powder diffraction patterns obtained for the various compositions of $Co_{3-x}Ni_xO_4$ ($0 \leq x \leq 1$) in the 2Θ range of 15° – 70°. Based on the analysis of the obtained X-ray diffractograms, similar patterns were observed for Co_3O_4, $Co_{2.8}Ni_{0.2}O_4$, $Co_{2.6}Ni_{0.4}O_4$ and $Co_{2.4}Ni_{0.6}O_4$ materials, with continuous changes in the form of the peaks and their positions while increasing the amount of nickel in the structure. On the contrary, for the materials with x equal to or higher than 0.8, peaks showing an increasing of the amount of a secondary phase were observed (0.8 and 1 at. % Ni). This could suggest that following the Pechini's route of synthesis, 0.6 is the maximum amount of Ni that can dissolve in the structure of Co_3O_4 and above this value the separation of CoO·NiO occurs.

The identification of the secondary phase obtained in the diffraction patterns of $Co_{2.2}Ni_{0.8}O_4$ and Co_2NiO_4 was done by analyzing the cell parameters of the peaks obtained. The cell parameter of the secondary phase is 4.2028 ± 10^{-4} Å, while the cell parameters of CoO and NiO are 4.263 Å and 4.178 Å, respectively [46], so in base of the cell parameter values obtained the secondary phase should correspond to a mixed CoO·NiO phase.

Fig. 2 shows the results of the quantitative Rietveld refinements for the $Co_{2.4}Ni_{0.6}O_4$ ($x = 0.6$) material after synthesis, where a good agreement between the experimental and the calculated diffraction profiles was obtained. The pattern shows peaks at 43° and 63° which belong to CoO·NiO phase, being the quantity of this phase lower than 5 wt%.

Table 1 summarizes the space group, room-temperature unit-cell parameters and unit-cell volume obtained by the Rietveld's refinement analysis, for the theoretical compositions: Co_3O_4, $Co_{2.8}Ni_{0.2}O_4$, $Co_{2.6}Ni_{0.4}O_4$, $Co_{2.4}Ni_{0.6}O_4$, $Co_{2.2}Ni_{0.8}O_4$ and Co_2NiO_4. The obtained values for unit-cell parameters and unit-cell volume increase linearly with the increase of the Ni amount, which is considered as a clear evidence that the Vegard's law [47] holds for this solid solution $Co_{3-x}Ni_xO_4$ with x value from 0 to 0.6.

In order to assess the morphological properties of the prepared samples, the SEM images obtained for Co_3O_4, $Co_{2.8}Ni_{0.2}O_4$, $Co_{2.6}Ni_{0.4}O_4$, $Co_{2.4}Ni_{0.6}O_4$, $Co_{2.2}Ni_{0.8}O_4$ and Co_2NiO_4 materials are shown in Fig. 3. As it can be seen in the Figure, Co_3O_4, $Co_{2.8}Ni_{0.2}O_4$, $Co_{2.2}Ni_{0.8}O_4$ and Co_2NiO_4 materials show similar agglomerate morphologies made of particles with size around 0.80 μm. Meanwhile, $Co_{2.6}Ni_{0.4}O_4$ and $Co_{2.4}Ni_{0.6}O_4$ materials exhibit different morphologies having the first

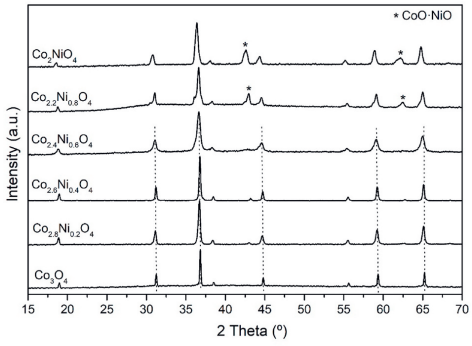

Fig. 1. Evolution of X-ray powder diffraction patterns of $Co_{3-x}Ni_xO_4$ ($0 \leq x \leq 1$) with x = 0, 0.2, 0.4, 0.6, 0.8, 1. The bullet (*) indicates the peaks corresponded to CoO·NiO phase.

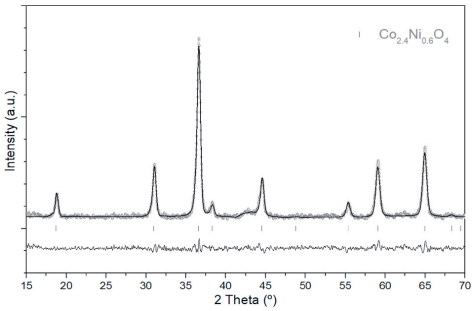

Fig. 2. Experimental (o), calculated (–) and difference profiles for the Rietveld's refinements of $Co_{2.4}Ni_{0.6}O_4$ (x = 0.6).

Table 1
Space group, room-temperature unit-cell parameters and unit-cell volume of the pure mixed structures of Co–Ni system for x from 0 to 0.6.

Composition	Material	Space group	a (Å)	V (Å^3)
x = 0	Co_3O_4	F-43m	8.0825 ± 10^{-4}	527.99
x = 0.2	$Co_{2.8}Ni_{0.2}O_4$	F-43m	8.0848 ± 10^{-4}	528.45
x = 0.4	$Co_{2.6}Ni_{0.4}O_4$	F-43m	8.0973 ± 10^{-4}	530.90
x = 0.6	$Co_{2.4}Ni_{0.6}O_4$	F-43m	8.0967 ± 10^{-4}	530.79

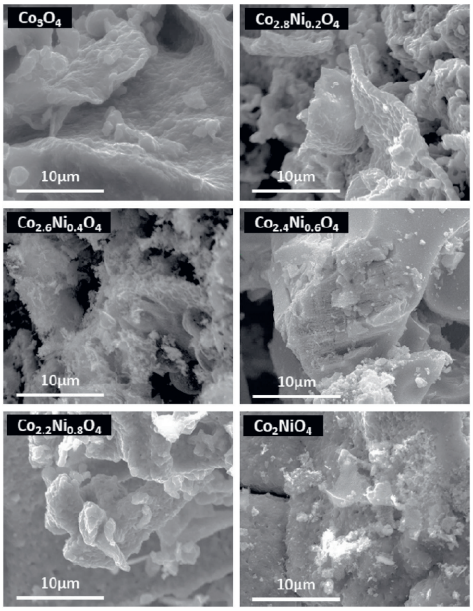

Fig. 3. SEM images of the Co_3O_4, $Co_{2.8}Ni_{0.2}O_4$, $Co_{2.6}Ni_{0.4}O_4$, $Co_{2.4}Ni_{0.6}O_4$, $Co_{2.2}Ni_{0.8}O_4$ and Co_2NiO_4 materials.

one a foamy appearance and the second one a dense structure. This fact should be taken in consideration when analyzing the thermal properties of the materials.

Thermogravimetric analyses have been done in order to study the thermal behavior of the prepared mixed metal oxides and to determine the red-ox temperatures, reaction reversibility and stability of the samples. Fig. 4a shows the STA (simultaneous thermal analysis) reduction curves obtained for Co_3O_4, $Co_{2.8}Ni_{0.2}O_4$, $Co_{2.6}Ni_{0.4}O_4$, $Co_{2.4}Ni_{0.6}O_4$, $Co_{2.2}Ni_{0.8}O_4$ and Co_2NiO_4 theoretical compositions between 600 °C and 1000 °C. A different behavior was observed for each material in regard to the reduction temperature, reaction kinetics and mass loss. As a general observation, the incorporation of nickel in the structure leads to a significant decrease in the reduction temperature. Fig. 4b shows the evolution of the reduction temperature as a function of nickel content (x), where an almost linear decrease of the reduction temperature was obtained for materials with nickel content (x) from 0 to 0.6. The reduction temperatures obtained for Co_3O_4, $Co_{2.8}Ni_{0.2}O_4$, $Co_{2.6}Ni_{0.4}O_4$, $Co_{2.4}Ni_{0.6}O_4$ are 906 °C, 852 °C, 735 °C and 685 °C, respectively. It is worth mentioning that there are no previous references of metal oxide synthesis that show such a significant decrease of the red-ox temperatures compared to the ones of Co_3O_4/CoO and Mn_2O_3/Mn_3O_4 couples. In the case of $Co_{2.2}Ni_{0.8}O_4$ (x = 0.8) and Co_2NiO_4 (x = 1), the reduction temperature obtained is 830 °C, which do not follow the trend observed for this system.

The high temperature obtained could be due to the lack of formation of the correct stoichiometry of these materials since a secondary phase of CoO·NiO was detected in their XRD diffractograms shown in Fig. 1.

In general, adding nickel to the cobalt oxide structure makes the reduction temperature tunable, being able to decrease it from 906 °C to 685 °C. Table 2 summarizes the reduction temperature, mass loss and reaction conversion ratio obtained for Co_3O_4, $Co_{2.8}Ni_{0.2}O_4$, $Co_{2.6}Ni_{0.4}O_4$, $Co_{2.4}Ni_{0.6}O_4$, $Co_{2.2}Ni_{0.8}O_4$ and Co_2NiO_4 materials.

The behavior of the different samples upon heating was studied by in-situ XRD measurements (Fig. 5).

These measurements allowed to follow the reduction reaction during heating determining the structural transformations in the material and the corresponding reduction temperature under that particular experimental conditions. This last aspect should be taken into account due to the high sensitivity of this class of reactions to the pressure change that can cause variations in the reaction temperature passing from one analysis technique to another one. Moreover, in the case of the TGA values, this is the initial reduction temperature of the samples, the point where the mass loss evidences the start of the reduction reaction. In the case of in-situ XRD, the reaction is detected only when the amount of sample reduced is enough to be detected by the diffraction technique.

This is well reflected in Table 2 where the reduction temperatures, for all the samples, obtained in the in-situ XRD results are in general higher than the ones obtained in the thermogravimetric measurements.

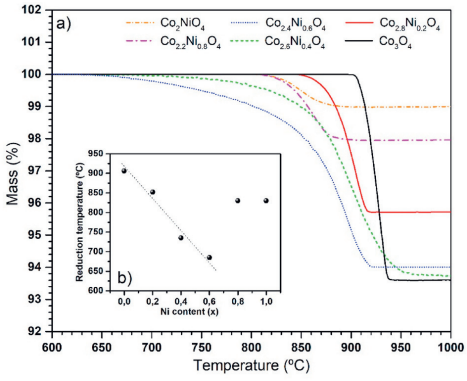

Fig. 4. a) STA experimental reduction step of the studied materials under air atmosphere with a heating/cooling rate of 10 °C/min and b) Evolution of the reduction temperature as function of nickel content.

Table 2
Reduction temperature and mass loss obtained for Co_3O_4, $Co_{2.8}Ni_{0.2}O_4$, $Co_{2.6}Ni_{0.4}O_4$, $Co_{2.4}Ni_{0.6}O_4$, $Co_{2.2}Ni_{0.8}O_4$ and Co_2NiO_4 materials.

Material	$T_{red,\ TGA}$ (°C)	$T_{red,XRDi}$ (°C)	Mass loss (%)	Conversion ratio (%)
Co_3O_4	906	950	6.4	96
$Co_{2.8}Ni_{0.2}O_4$	852	900	4.28	64
$Co_{2.6}Ni_{0.4}O_4$	735	800	6.12	92
$Co_{2.4}Ni_{0.6}O_4$	685	700	4.99	75
$Co_{2.2}Ni_{0.8}O_4$	830	900	2.05	31
Co_2NiO_4	830	850	0.72	11

The reduction temperature in the in-situ studies corresponds to the pattern where the oxidated phase starts to be detected (for each composition in bold in Fig. 5). The in-situ measurements confirm the results obtained in the STA measurements with a decrease of the reduction temperature as a function of the nickel content in the host structure (x), going from 0 to at least 0.6 at. In the case of the materials with a nickel content (x) equal or higher than 0.8, the reduction temperature maintains at a constant value of 900 °C.

The preliminary stability of the materials upon cycling was tested by performing three successive thermal cycles between 600 °C and 1000 °C under air atmosphere in the STA equipment. Fig. 6 shows TGA reduction/oxidation cycling of the studied materials between 600 °C and 1000 °C under air atmosphere with a heating/cooling rate of 10 °C/min. In the case of Co_3O_4, $Co_{2.8}Ni_{0.2}O_4$, $Co_{2.6}Ni_{0.4}O_4$, $Co_{2.4}Ni_{0.6}O_4$ and $Co_{2.2}Ni_{0.8}O_4$ materials, the TGA measurements show that, upon heating, the reduction is evidenced by the sample weight loss related to oxygen release and upon cooling the re-oxidation is accompanied by sample weight gain. In the case of $Co_{2.2}Ni_{0.8}O_4$, incomplete re-oxidation reactions were observed due to the fast cooling rate (10 °C/min) and no-dwelling step below the reduction temperature was programed. In the case of Co_2NiO_4, TGA measurement revealed small weight losses and gains (only 1%) during the three cycles, which indicates that the reduction/oxidation reaction took place in only a very small fraction of the material.

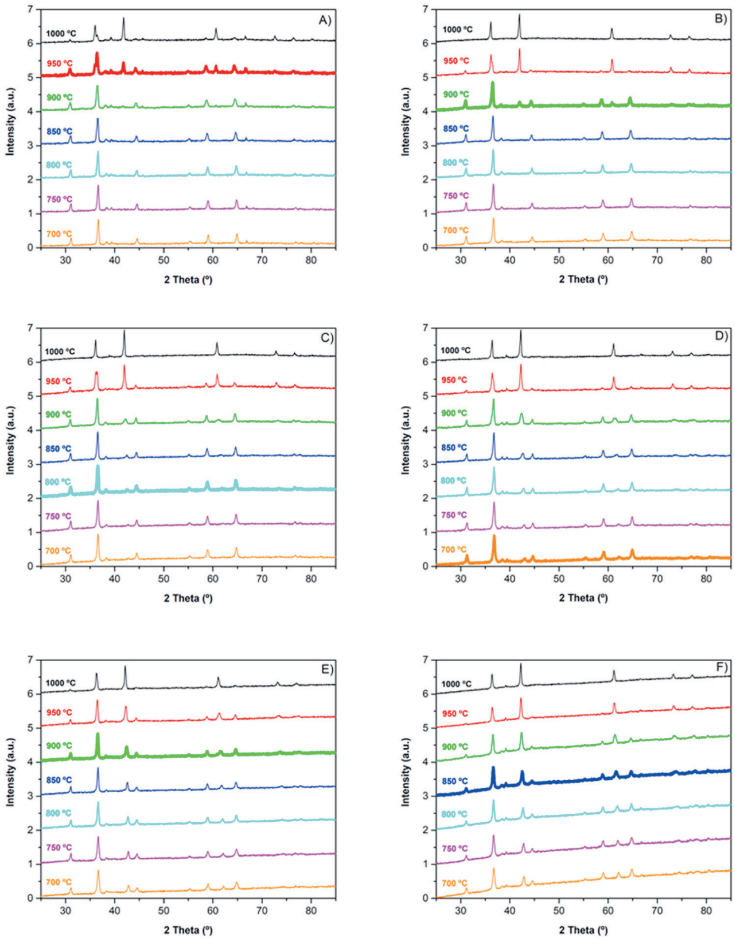

Fig. 5. In-situ XRD patterns of A) Co_3O_4, B) $Co_{2.8}Ni_{0.2}O_4$, C) $Co_{2.6}Ni_{0.4}O_4$, D) $Co_{2.4}Ni_{0.6}O_4$, E) $Co_{2.2}Ni_{0.8}O_4$ and F) Co_2NiO_4 at a temperature range of 700–1000 °C with a heating step of 50 °C. For each composition, the patterns corresponding to the reduction temperature are highlighted in bold.

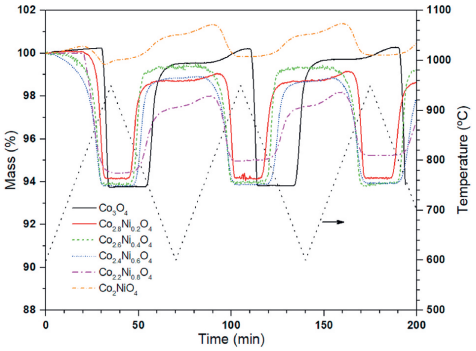

Fig. 6. TGA reduction/oxidation cycles for the studied materials between 600 °C and 1000 °C under air atmosphere with a heating/cooling rate of 10 °C/min.

The material with the best performances obtained in this study, $Co_{2.4}Ni_{0.6}O_4$, was subjected to a more extreme cycling experiment (up to 100 cycles) in order to test its stability. As shown in Fig. 7, this material exhibits an adequate reversibility even after multiple cycles, having in the first cycle a percentage of mass loss of 4.99% and in the last cycle a 3.81%.

It is worth to mention that the reproducibility of the materials was tested by performing two similar experiments with two different aliquots of the same material. Five control cycles have been analyzed in terms of mass gain/loss and reduction/oxidation temperatures. The largest error obtained has been of 1.79% but the average has been of 0.5%, which are inside the limits of the instrumental error.

The surface and structural morphology of $Co_{2.4}Ni_{0.6}O_4$ was tested after 100 cycles in TGA apparatus. The change of the morphology of the material is appreciated in Fig. 8.

The raw material showed a dense structure while the cycled material shows a porous densified structure. The thermal cycling promoted the formation of channels in the material, helping the oxygen diffusion and maintaining adequate activity levels.

The structural properties of the final material have been analyzed by XRD. The results reported in Fig. 9 show similar diffraction patterns for the samples before and after thermal cycling.

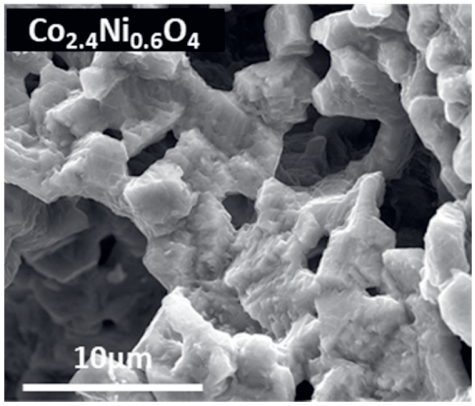

Fig. 8. SEM image of the $Co_{2.4}Ni_{0.6}O_4$ material after 100 cycles in the TGA apparatus.

The broad signal at low angle, of the cycled sample, belongs to the sample holder of the diffractometer. The main difference between the two patterns is the presence of a secondary phase of CoO·NiO after 100 thermal cycles. The refinement shows that the final composition of the material in weight fraction is 0.73 of $Co_{2.4}Ni_{0.6}O_4$ and 0.27 of CoO·NiO. This result is coherent with the activity loss obtained after thermal cycling in the TGA.

The cost of high purity $Co_{2.4}Ni_{0.6}O_4$ produced by sol-gel method at laboratory scale is estimated to be around 129 €/kg. As shown in Table 3, the reactive materials account for 38.6% of the total cost, whereas labor cost and energy consumption represent 46.2% and 15.2%, respectively.

Obviously, cost is currently one the main drawback of $Co_{2.4}Ni_{0.6}O_4$ for its final application as thermochemical material and has to be strongly reduced to compete in the TES market. It is expected that automation of the synthesis process (lower labor costs), whole sale purchasing of the reactive materials and mass production would efficiently contribute to the necessary cost reduction.

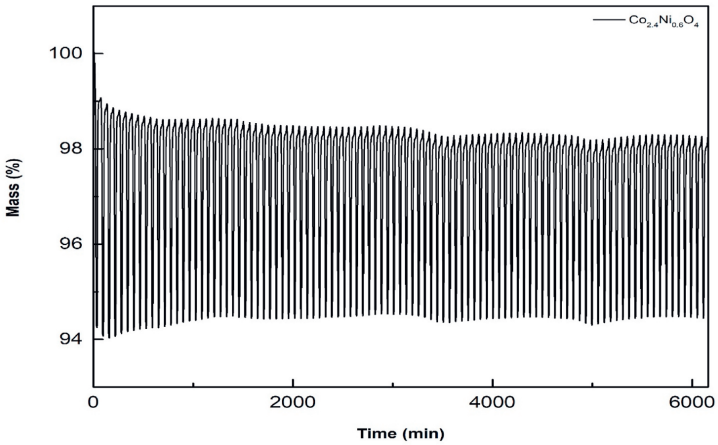

Fig. 7. 100 reduction/oxidation cycles for $Co_{2.4}Ni_{0.6}O_4$ performed between 600 °C and 1000 °C under air atmosphere with a heating/cooling rate of 10 °C/min.

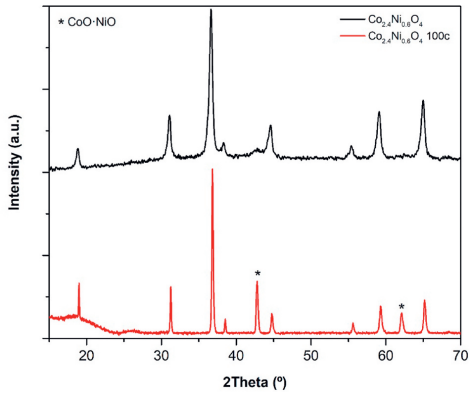

Fig. 9. X-ray powder diffraction patterns of $Co_{2.4}Ni_{0.6}O_4$ before and after 100 thermal cycles. The bullet (*) indicates the peaks corresponded to CoO·NiO phase.

Table 3
Estimated cost of high purity $Co_{2.4}Ni_{0.6}O_4$ produced by sol-gel method at laboratory scale.

		Cost (€/kg)
Reactive materials	Cobalt nitrate hexahydrate (11.7 €/kg) Nickel nitrate hexahydrate (4.06 €/kg) Citric Acid (0.76 €/kg) Ethylene glicol (1.16 €/kg)	49.57
Labor cost	2 h at 30 €/h	60
Energy	22 h at 0.9048 €/h	19.91
Total cost		129.48

4. Conclusions

In this study, the mixed oxide $Co_{3-x}Ni_xO_4$ with progressively increased amount of Ni was successfully prepared via sol-gel method following the Pechini's route.

The investigation allowed to determine the optimum amount of Ni dissolved into the cobalt oxide structure, leading to a substantial decrease of the redox temperature compared to pure Co_3O_4. In particular, the XRD measurements show that for a nickel content (x) higher than 0.6 the presence of a secondary phase of CoO·NiO is observed.

In order to determine the reactivity and redox performance of these materials, further research was carried out on the thermal behavior of all the mixed structure synthesized. In general, two main point can be highlighted, on one side the DSC/TGA results show that the thermal behavior of each mixed oxide is different from that of pure metal oxide considering the reduction temperature, oxygen loss ratio and reversibility. On the other side, it has been possible to determine the composition with the best reactivity (with Ni content (x) equal to 0.6) allowing to decrease the reduction temperature below 700 °C. This is an important achievement, opening to the possibility to use this class of reactions in applications at lower temperature.

The combination between TG measurements and in situ-XRD measurements allowed to confirm the trend in the reduction temperature even if some deviation in the absolute values of the temperature have been observed. This is probably due to a slight O_2 overpressure, consequent to the desorption process in the XRD chamber, causing a displacement of the equilibrium temperature at slightly higher values. The linear decrease of the reduction temperature with the increase of the amount of nickel in the host structure, observed in TGA, was confirmed by the in-situ XRD measurement. Finally, the preliminary cycling stability tests of the material with the best performances (Ni = 0.6) (100 cycles) confirm the good reactivity upon cycling with no modification in the reduction temperature.

The results of this work lead us to consider that this mixed oxide system could be a potential future candidate fot TcES applications, providing some flexibility in terms of reaction temperature. However, a more in depth and prolonged study of the cyclability in a lab scale test bench would be needed to confirm the thermal stability of the material.

CRediT authorship contribution statement

Yasmina Portilla-Nieto: Data curation, Methodology, Investigation, Roles/Writing original, Writing-review. **Abdelali Zaki:** Data curation, Methodology, Investigation, Writing review, Methodology. **Karmele Vidal:** Data curation, Investigation, Supervision. **Marta Hernaiz:** Conceptualization, Data curation, Funding acquisition, Project administration, Supervision, Writing review. **Estibaliz Aranzabe:** Funding acquisition, Project administration, Supervision, Writing review. **Stefania Doppiu:** Conceptualization, Data curation, Funding acquisition, Project administration, Supervision, Writing-review.

Declaration of competing interest

The authors declare that they have no known competing financial interests or personal relationships that could have appeared to influence the work reported in this paper.

Acknowledgement

The Basque Government (Elkartek CICe2017, KK-2017/00066; Elkartek CICe2019, KK-2019/00097) is acknowledged for the financial support of this work. The authors express their sincere gratitude to Leticia Martinez, Yagmur Polat and Cristina Luengo for their technical support.

References

[1] S. Kim, H. Van Quy, C.W. Bark, Photovoltaic technologies for flexible solar cells: beyond silicon, Mater. Today Energy. 19 (2021) 100583, https://doi.org/10.1016/j.mtener.2020.100583.
[2] Q. Meng, T. Liu, C. Su, H. Niu, Z. Hou, N. Ghadimi, A single-phase transformer-less grid-tied inverter based on switched capacitor for PV application, J. Control. Autom. Electr. Syst. 31 (2020) 257–270, https://doi.org/10.1007/s40313-019-00531-5.
[3] L. Kong, J. Yu, G. Cai, Modeling, control and simulation of a photovoltaic/hydrogen/supercapacitor hybrid power generation system for grid-connected applications, Int. J. Hydrogen Energy 44 (2019) 25129–25144, https://doi.org/10.1016/j.ijhydene.2019.05.097.
[4] S. Cheng, G. Zhao, M. Gao, Y. Shi, M. Huang, M. Marefati, A new hybrid solar photovoltaic/phosphoric acid fuel cell and energy storage system; Energy and Exergy performance, Int. J. Hydrogen Energy 46 (2021) 8048–8066, https://doi.org/10.1016/j.ijhydene.2020.11.282.
[5] T. Inoue, A. Fujishima, S. Konishi, K. Honda, Photoelectrocatalytic reduction of carbon dioxide in aqueous suspensions of semiconductor powders [3], Nature 277 (1979) 637–638, https://doi.org/10.1038/277637a0.
[6] J.C. Hemminger, R. Carr, G.A. Somorjai, The photoassisted reaction of gaseous water and carbon dioxide adsorbed on the SrTiO3 (111) crystal face to form methane, Chem. Phys. Lett. 57 (1978) 100–104, https://doi.org/10.1016/0009-2614(78)80359-5.
[7] P.G. Grimes, Energy depot fuel production and utilization, SAE Tech. Pap (1965), https://doi.org/10.4271/650051.
[8] J.E. Funk, Thermochemical hydrogen production: past and present, Int. J. Hydrogen Energy 26 (2001) 185–190, https://doi.org/10.1016/S0360-3199(00)00062-8.
[9] H.L. Tuller, Solar to fuels conversion technologies: a perspective, Mater. Renew. Sustain. Energy. 6 (2017), https://doi.org/10.1007/s40243-017-0088-2.
[10] N. Mariotti, M. Bonomo, L. Fagiolari, N. Barbero, C. Gerbaldi, F. Bella, C. Barolo, Recent advances in eco-friendly and cost-effective materials towards sustainable dye-sensitized solar cells, Green Chem. 22 (2020) 7168–7218, https://doi.org/10.1039/d0gc01148g.
[11] M.D. Allendorf, J.E. Miller, A.H. McDaniel, Design of materials for solar-driven fuel production by metal-oxide thermochemical cycles, Electrochem. Soc. Interface. 22 (2013) 63–68, https://doi.org/10.1149/2.F06134if.

[12] R.J. Detz, J.N.H. Reek, B.C.C. Van Der Zwaan, The future of solar fuels: when could they become competitive? Energy Environ. Sci. 11 (2018) 1653–1669, https://doi.org/10.1039/c8ee00111a.
[13] A. Bloess, W.P. Schill, A. Zerrahn, Power-to-heat for renewable energy integration: a review of technologies, modeling approaches, and flexibility potentials, Appl. Energy 212 (2018) 1611–1626, https://doi.org/10.1016/j.apenergy.2017.12.073.
[14] T. Block, N. Knoblauch, M. Schmücker, The cobalt-oxide/iron-oxide binary system for use as high temperature thermochemical energy storage material, Thermochim. Acta 577 (2014) 25–32, https://doi.org/10.1016/j.tca.2013.11.025.
[15] S. Tescari, C. Agrafiotis, S. Breuer, L. De Oliveira, M. Neises-Von Puttkamer, M. Roeb, C. Sattler, Thermochemical solar energy storage via redox oxides: materials and reactor/heat exchanger concepts, Energy Procedia 49 (2013) 1034–1043, https://doi.org/10.1016/j.egypro.2014.03.111.
[16] H.B. Dizaji, H. Hosseini, A review of material screening in pure and mixed-metal oxide thermochemical energy storage (TCES) systems for concentrated solar power (CSP) applications, Renew. Sustain. Energy Rev. 98 (2018) 9–26, https://doi.org/10.1016/j.rser.2018.09.004.
[17] B. Ehrhart, E. Coker, N. Siegel, A. Weimer, Thermochemical cycle of a mixed metal oxide for augmentation of thermal energy storage in solid particles, Energy Procedia 49 (2013) 762–771, https://doi.org/10.1016/j.egypro.2014.03.082.
[18] F. Bruno, M. Belusko, M. Liu, N.H.S. Tay, Using Solid-Liquid Phase Change Materials (PCMs) in Thermal Energy Storage Systems, Woodhead Publishing Limited, 2014, https://doi.org/10.1533/9781782420965.2.201.
[19] S. Wu, C. Zhou, E. Doroodchi, R. Nellore, B. Moghtaderi, A review on high-temperature thermochemical energy storage based on metal oxides redox cycle, Energy Convers. Manag. 168 (2018) 421–453, https://doi.org/10.1016/j.enconman.2018.05.017.
[20] M. Liu, N.H. Steven Tay, S. Bell, M. Belusko, R. Jacob, G. Will, W. Saman, F. Bruno, Review on concentrating solar power plants and new developments in high temperature thermal energy storage technologies, Renew. Sustain. Energy Rev. 53 (2016) 1411–1432, https://doi.org/10.1016/j.rser.2015.09.026.
[21] C. Agrafiotis, M. Roeb, M. Schmücker, C. Sattler, Exploitation of thermochemical cycles based on solid oxide redox systems for thermochemical storage of solar heat. Part 2: redox oxide-coated porous ceramic structures as integrated thermochemical reactors/heat exchangers, Sol. Energy 114 (2015) 440–458, https://doi.org/10.1016/j.solener.2014.12.036.
[22] C. Agrafiotis, M. Roeb, M. Schmücker, C. Sattler, Exploitation of thermochemical cycles based on solid oxide redox systems for thermochemical storage of solar heat. Part 1: testing of cobalt oxide-based powders, Sol. Energy 102 (2014) 189–211, https://doi.org/10.1016/j.solener.2013.12.032.
[23] J.H. Myung, T.H. Shin, X. Huang, G. Carins, J.T.S. Irvine, Enhancement of redox stability and electrical conductivity by doping various metals on ceria, Ce1-xMxO2-δ (M = Ni, Cu, Co, Mn, Ti, Zr), Int. J. Hydrogen Energy 40 (2015) 12003–12008, https://doi.org/10.1016/j.ijhydene.2015.05.029.
[24] C. Agrafiotis, S. Tescari, M. Roeb, M. Schmücker, C. Sattler, Exploitation of thermochemical cycles based on solid oxide redox systems for thermochemical storage of solar heat. Part 3: cobalt oxide monolithic porous structures as integrated thermochemical reactors/heat exchangers, Sol. Energy 114 (2015) 459–475, https://doi.org/10.1016/j.solener.2014.12.037.
[25] A.H. Abedin, A critical review of thermochemical energy storage systems, Open Renew. Energy J. 4 (2011) 42–46, https://doi.org/10.2174/1876387101004010042.
[26] A.J. Carrillo, J. Moya, A. Bayón, P. Jana, V.A. De La Peña O'Shea, M. Romero, J. Gonzalez-Aguilar, D.P. Serrano, P. Pizarro, J.M. Coronado, Thermochemical energy storage at high temperature via redox cycles of Mn and Co oxides: pure oxides versus mixed ones, Sol. Energy Mater. Sol. Cells 123 (2014) 47–57, https://doi.org/10.1016/j.solmat.2013.12.018.
[27] A.J. Carrillo, D.P. Serrano, P. Pizarro, J.M. Coronado, Improving the thermochemical energy storage performance of the Mn 2 O 3/Mn 3 O 4 redox couple by the incorporation of iron, ChemSusChem 8 (2015) 1947–1954, https://doi.org/10.1002/cssc.201500148.
[28] A.J. Carrillo, D.P. Serrano, P. Pizarro, J.M. Coronado, Thermochemical heat storage at high temperatures using Mn2O3/Mn3O4 system: narrowing the redox hysteresis by metal co-doping, Energy Procedia 73 (2015) 263–271, https://doi.org/10.1016/j.egypro.2015.07.686.
[29] L. André, S. Abanades, L. Cassayre, Mixed metal oxide systems applied to thermochemical storage of solar energy: benefits of secondary metal addition in Co and Mn oxides and contribution of thermodynamics, Appl. Sci. 8 (2018) 2618, https://doi.org/10.3390/app8122618.
[30] T. Block, M. Schmücker, Metal oxides for thermochemical energy storage: a comparison of several metal oxide systems, Sol. Energy 126 (2016) 195–207, https://doi.org/10.1016/j.solener.2015.12.032.
[31] R.J. Hill, J.R. Craig, G.V. Gibbs, Systematics of the spinel structure type, Phys. Chem. Miner. 4 (1979) 317–339, https://doi.org/10.1007/BF00307535.
[32] W.J. King, A.C.C. Tseung, The reduction of oxygen on nickel-cobalt oxides—II, Electrochim. Acta 19 (1974) 493–498, https://doi.org/10.1016/0013-4686(74)87030-1.
[33] D. Klissurski, E. Uzunova, Synthesis and features of binary cobaltite spinels, J. Mater. Sci. 29 (1994) 285–293, https://doi.org/10.1007/BF01162484.
[34] B. Cui, H. Lin, J.B. Li, X. Li, J. Yang, J. Tao, Core-ring structured NiCo2O4 nanoplatelets: synthesis, characterization, and electrocatalytic applications, Adv. Funct. Mater. 18 (2008) 1441–1447, https://doi.org/10.1002/adfm.200700982.
[35] M.-C. Liu, L.-B. Kong, C. Lu, X.-M. Li, Y.-C. Luo, L. Kang, X. Li, F.C. Walsh, A sol-gel process for the synthesis of NiCo 2 O 4 having improved specific capacitance and cycle stability for electrochemical capacitors, J. Electrochem. Soc. 159 (2012), https://doi.org/10.1149/2.057208jes. A1262–A1266.
[36] Z.Q. Liu, Q.Z. Xu, J.Y. Wang, N. Li, S.H. Guo, Y.Z. Su, H.J. Wang, J.H. Zhang, S. Chen, Facile hydrothermal synthesis of urchin-like NiCo2O4 spheres as efficient electrocatalysts for oxygen reduction reaction, Int. J. Hydrogen Energy 38 (2013) 6657–6662, https://doi.org/10.1016/j.ijhydene.2013.03.092.
[37] S. Kuboon, Y.H. Hu, Study of NiO-CoO and Co3O4-Ni3O 4 solid solutions in multiphase Ni-Co-O systems, Ind. Eng. Chem. Res. 50 (2011) 2015–2020, https://doi.org/10.1021/ie101249r.
[38] J. Ma, E. Guo, L. Yin, Porous hierarchical spinel Mn-doped NiCo 2 O 4 nanosheet architectures as high-performance anodes for lithium-ion batteries and electrochemical reaction mechanism, J. Mater. Sci. Mater. Electron. (2019), https://doi.org/10.1007/s10854-019-01176-5.
[39] J. Liu, S.Z. Qiao, H. Liu, J. Chen, A. Orpe, D. Zhao, G.Q. Lu, Extension of the stöber method to the preparation of monodisperse resorcinol-formaldehyde resin polymer and carbon spheres, Angew. Chem. Int. Ed. 50 (2011) 5947–5951, https://doi.org/10.1002/anie.201102011.
[40] S. Wen, Y. Liu, F. Zhu, R. Shao, W. Xu, Hierarchical MoS 2 nanowires/NiCo 2 O 4 nanosheets supported on Ni foam for high-performance asymmetric supercapacitors, Appl. Surf. Sci. 428 (2018) 616–622, https://doi.org/10.1016/j.apsusc.2017.09.189.
[41] J. Zhao, M. Li, J. Li, C. Wei, Y. He, Y. Huang, Q. Li, Porous Ni-Co-Mn oxides prisms for high performance electrochemical energy storage, Appl. Surf. Sci. 425 (2017) 1158–1167, https://doi.org/10.1016/j.apsusc.2017.07.261.
[42] I.T. Papadas, A. Ioakeimidis, G.S. Armatas, S.A. Choulis, Low Temperature Combustion Synthesis of a Spinel Nico2o4 Hole Transport Layer for Perovskite Photovoltaics, ArXiv, 2018.
[43] D.P. Dubal, P. Gomez-Romero, B.R. Sankapal, R. Holze, Nickel cobaltite as an emerging material for supercapacitors: an overview, Nanomater. Energy 11 (2015) 377–399, https://doi.org/10.1016/j.nanoen.2014.11.013.
[44] S. Petrick Casagrande, R.C. Blanco, Método de Rietveld para el estudio de estructuras cristalinas 2 (2004) 1–5.
[45] J. Rodríguez-Carvajal, Recent advances in magnetic structure determination by neutron powder diffraction, Phys. B Phys. Condens. Matter. 192 (1993) 55–69, https://doi.org/10.1016/0921-4526(93)90108-I.
[46] S. Sasaki, K. Fujino, Y. Takeuchi, Scattering factors o f their constituent atoms, Ser. B. 55 (1979) 43–48. https://www.jstage.jst.go.jp/article/pjab1977/55/2/55_2_43/_pdf.
[47] M.N. Magomedov, On the deviation from the Vegard's law for the solid solutions, Solid State Commun. 322 (2020) 114060, https://doi.org/10.1016/j.ssc.2020.114060.

Development and stabilization of $Co_{2.4}Ni_{0.6}O_4$ material for long-term thermochemical energy storage

Journal of Energy Storage, **2022**, 5*2*, 104876

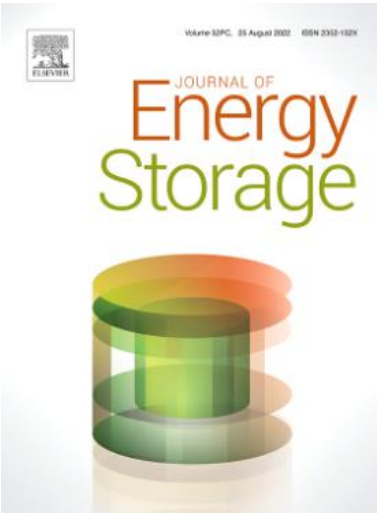

ISSN: 2352-152X

Impact Factor 2021: 8.907

Cite Score: 8.4

Q1 (Renewable energy, Sustainability and the Environment)

https://doi.org/10.1016/j.est.2022.104876

Journal of Energy Storage 52 (2022) 104876

Contents lists available at ScienceDirect

Journal of Energy Storage

journal homepage: www.elsevier.com/locate/est

Research Papers

Development and stabilization of $Co_{2.4}Ni_{0.6}O_4$ material for long-term thermochemical energy storage

Yasmina Portilla-Nieto [a,b,c,*], Karmele Vidal [c], Marta Hernaiz [c], Estibaliz Aranzabe [c], Stefania Doppiu [a], Elena Palomo del Barrio [a,d]

[a] Centre for Cooperative Research on Alternative Energies (CIC energiGUNE), Basque Research and Technology Alliance (BRTA), Alava Technology Park, Albert Einstein 48, 01510 Vitoria-Gasteiz, Spain
[b] Applied Physics II Department, Faculty of Science and Technology, University of the Basque Country (UPV/EHU), PO Box 644, Bilbao 48080, Spain
[c] TEKNIKER, Polo Tecnológico de Eibar, C/ Iñaki Goenaga, 5, 20600 Eibar, Gipuzkoa, Spain
[d] IKERBASQUE Basque Foundation for Science, Plaza Euskadi 5, 48009 Bilbao, Spain

ARTICLE INFO

Keywords:
Thermochemical heat storage
Gas-solid reaction
Redox reaction
Cobalt nickel oxide
Doped metal oxides
Silica nanoparticles
Sintering inhibition

ABSTRACT

Redox thermochemical energy storage is one of the most promising technologies to achieve dispatchability in concentrated solar power applications. Compared to commercially available thermal energy storage technologies, Redox thermochemical storage provides much higher energy storage capacity and allows energy storage at temperatures beyond 600 °C. In addition, metal oxides supporting redox reactions are usually non-critical, low-cost materials.

This paper deals with cobalt nickel mixed oxide $Co_{2.4}Ni_{0.6}O_4$ recently proposed as promising material for Redox thermochemical storage. The paper focusses on the study of $Co_{2.4}Ni_{0.6}O_4$ stability to thermal cycling and the analysis of different methods to improve it, which is a crucial issue to warrant long-term performances and durability. Three different approaches have been investigated to improve $Co_{2.4}Ni_{0.6}O_4$ stability. The first one consists in adding SiO_2 nanoparticles and particles to the $Co_{2.4}Ni_{0.6}O_4$ acting as spacer of the thermochemical material, avoiding its densification and preserving its cyclability. The second one deals with the calcination of $Co_{2.4}Ni_{0.6}O_4$ at high temperature, which aims at obtaining a more stable material without additives. The third one includes calcination and addition different size SiO_2 particles.

Deep research work has been carried out studying the effect of the three proposed alternatives to improve $Co_{2.4}Ni_{0.6}O_4$ stability. The best results achieved correspond to $Co_{2.4}Ni_{0.6}O_4$ with addition of 0.5% wt of 400 nm in size SiO_2 particles. The extrapolation of the experimental data obtained in this work indicates a conversion ratio loss of 10% in 20 years, with a temperature increase of 26.75 °C in the reduction stage and of 17.44 °C in the case of the oxidation stage.

1. Introduction

The increasing of worldwide energy demand and related environmental problems have increased the interest in the renewable energy field. Among renewable energies, concentrated solar power (CSP) is of great interest because of wide availability of solar energy, cost effectiveness and ease of hybridization [1]. It is well-known that the main drawback of solar energy is its intermittent nature, making necessary the use of energy storage systems to warrant power dispatchability. In the case of CSP, large scale and inexpensive thermal energy storage (TES) systems can be used to this end. In addition, the combination of CSP plants with TES contributes to make them economically viable [2].

Nowadays, the most developed TES technologies are sensible heat storage (SHS) and latent heat storage (LHS) technologies. In the first case, the energy is stored/released by increasing/decreasing the temperature of the storage material; whereas in the second case, energy storage relies in a phase change of the storage material [3–5]. Among all the TES technologies, thermochemical energy storage (TcES) is the less developed but the most promising one. Energy storage is achieved by means of high enthalpic, reversible chemical reactions that theoretically

* Corresponding author at: Centre for Cooperative Research on Alternative Energies (CIC energiGUNE), Basque Research and Technology Alliance (BRTA), Alava Technology Park, Albert Einstein 48, 01510 Vitoria-Gasteiz, Spain.
E-mail address: yportilla@cicenergigune.com (Y. Portilla-Nieto).

https://doi.org/10.1016/j.est.2022.104876
Received 2 September 2021; Received in revised form 27 April 2022; Accepted 10 May 2022
Available online 19 May 2022
2352-152X/

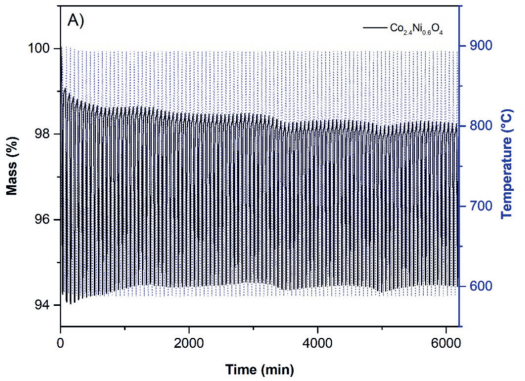

Fig. 1. Thermogravimetric analyses of pure $Co_{2.4}Ni_{0.6}O_4$. A) Variation of the mass of the sample over heating and cooling cycles and B) mass gained/lost in 5 control cycles.

Table 1
Assessment of the reversibility and the redox temperatures of the pure $Co_{2.4}Ni_{0.6}O_4$ in six control cycles.

Cycle	Mass lost (%)	T reduction (°C)	T oxidation (°C)
5	4.66	728	859
20	4.15	744	866
40	3.97	758	872
60	3.87	765	871
80	3.85	761	845
100	3.80	764	859

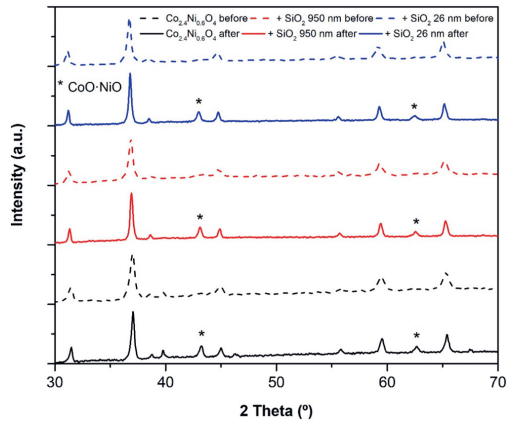

Fig. 2. X-ray diffraction patterns of the pure $Co_{2.4}Ni_{0.6}O_4$ and the ones with additions of 10% of SiO_2 of 400 nm and 26 nm before and after one thermal cycle in the diffractometer. The bullet (*) indicates the peaks corresponding to CoO·NiO phase and the (+) indicates the nickel cobaltite phase.

provide much higher energy storage density than other TES technologies [6,7]. The endothermic chemical reaction is used to store heat during the on-sun hours and during the off-sun hours the reverse exothermic reaction is used to release heat.

Redox reactions involving metal oxides have been considered suitable candidates for high temperature TES applications by many researchers.

Table 2
Lattice parameter (a) and weight fraction of the mixed oxide (X) and CoO·NiO phase (Y) in samples with different size silica particles before and after one thermal cycle in the diffractometer.

Material	a (Å)	$X_{mixed\ oxide}$	$Y_{CoO\cdot NiO}$
$Co_{2.4}Ni_{0.6}O_4$ before	8.1122 ± 10^{-4}	0.9516	0.0484
$Co_{2.4}Ni_{0.6}O_4$ after	8.1013 ± 10^{-4}	0.8099	0.1901
+10% SiO_2 400 nm before	8.1072 ± 10^{-4}	0.9370	0.0630
+10% SiO_2 400 nm after	8.0934 ± 10^{-4}	0.7262	0.2738
+10% SiO_2 26 nm before	8.1044 ± 10^{-4}	0.9697	0.0303
+10% SiO_2 26 nm after	8.0905 ± 10^{-4}	0.7542	0.2458

The redox reactions can be described as (M = metal) [8]:

Reduction reaction: $M_xO_{y+z} \rightarrow M_xO_y + z/2O_2$
Oxidation reaction: $M_xO_y + z/2O_2 \rightarrow M_xO_{y+z}$.

The materials must fulfill requirements such as complete reaction reversibility, suitable reaction temperature, high storage density, high reaction enthalpy, no-toxicity and good thermal stability during cycling [9,10].

In the case of CSP applications, there is interest in the development of new materials for energy storage at temperatures beyond the molten salt degradation temperature (~600 °C), allowing the increase of the efficiency of the heat to electricity conversion [11]. The literature shows that the most promising materials so far are cobalt oxide (Co_3O_4/CoO) and manganese oxide (Mn_2O_3/Mn_3O_4) [9,12–14]. The main barrier for their final application in technologies such as CSP and industrial waste heat recovery is their high equilibrium temperatures (higher than 850 °C). The development of stable storage materials sorting the gap of temperature application between 600 °C of the molten salts and the ~850 °C temperatures of the cobalt oxide and the manganese oxide is, therefore, of primary interest. In the last few years, several works proposed redox reactions of doped mixed oxides, spinel and perovskite oxides, being able to adjust redox temperatures and to mitigate sintering effects [8,15].

In the case of the powdered materials, such as manganese oxide, cobalt oxide or some mixed cobalt oxides [16,17], the sintering produced by the thermal cycling significantly worsens the kinetics of the material, leading to poor stability and to a significant reduction of their storage capacity and modification of their reaction equilibria over thermal cycling. In order to overcome this problem, different strategies have been applied such as the synthesis of mixed oxides and the addition of inert particles. In the first case, mixed cobalt-iron/copper/aluminum oxides have been synthesized. It has been found that these materials have superior performances than pure cobalt oxide preventing sintering. Unfortunately, the formation of mixed oxides more stable than Co_3O_4 leads to an increase of the reduction temperature [18,19]. In the second case, notable improvements in the cyclability of metal oxides by adding different types of nanoparticles without modification of the reaction temperature [20]. Other research works show notable improvements in the stability of metal oxides by adding Si. This material is one of the two most abundant elements in Earth's crust, meaning that it is cheap and easily available [11]. Moreover, authors have not reported an increase of the reduction temperature of the mixed oxide.

In a previous research work, we have proposed $Co_{3-x}Ni_xO_4$ mixed oxides as a solution to effectively reduce the reaction temperatures of cobalt and manganese oxides.

Co_3O_4 material has a spinel-type structure with the general formula of AB_2O_4 where A, B = Co, Zn, Ni, Fe, Cu, Mn, etc. A and B are divalent and trivalent metal cations, respectively. The distribution of the cations between the two sites is dependent of the nature of the cations incorporated into the structure. In normal spinel structures, the divalent A and trivalent B cations occupy the tetrahedral and octahedral sites,

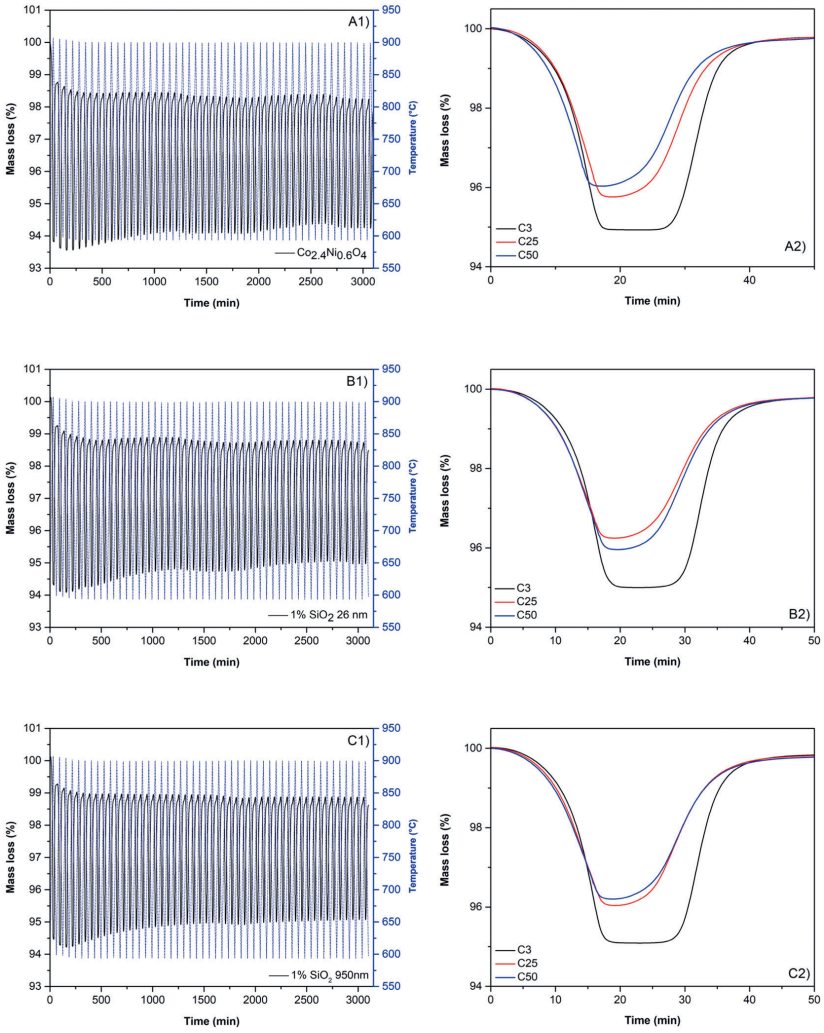

Fig. 3. Thermogravimetric analyses of A) $Co_{2.4}Ni_{0.6}O_4$ + 1% SiO_2 26 nm and B) $Co_{2.4}Ni_{0.6}O_4$ + 1% SiO_2 400 nm.

respectively. The space group obtained is the Fd-3m, proper of a cubic symmetric class [21–23].

It is proven that $Co_{3-x}Ni_xO_4$ mixed oxides allow tuning the reduction temperature until values of 685 °C [17]. However, the stability of $Co_{3-x}Ni_xO_4$ mixed oxides is insufficient due to the sintering of the material over thermal cycling.

In this work, the most promising Co-Ni mixed oxide in terms of reduction reaction temperature, the $Co_{2.4}Ni_{0.6}O_4$, has been selected for in-depth analysis of its stability and study of different approaches to improve it. In the first approach, an addition of SiO_2 nanoparticles and particles synthesized following the Stober route [24] has been done, optimizing the size and the quantity of nanoparticles to obtain the best performance. In the second one, a post-calcination process has been applied to the synthesized material to accelerate the morphological readjustment of the material and as a consequence suppressing the first unstable cycles. The results have shown that the best performance is obtained by adding SiO_2 particles to the mixed oxide. Doing so, the thermochemical material maintains the reduction and oxidation reaction temperatures in lower values than those of the pure $Co_{2.4}Ni_{0.6}O_4$. In addition, the particle size of the material remains stable after 100 thermal cycles and the conversion ratios have been improved. The lack of interactions between the thermochemical material and the nanoparticles has also been demonstrated after 100 cycles in a thermobalance.

2. Materials and methods

The materials used during this research were: Nickel nitrate hexahydrate extra-pure from Scharlab, cobalt nitrate hexahydrate from Fisher Scientific with a purity of 98+%, citric acid from Fisher Scientific

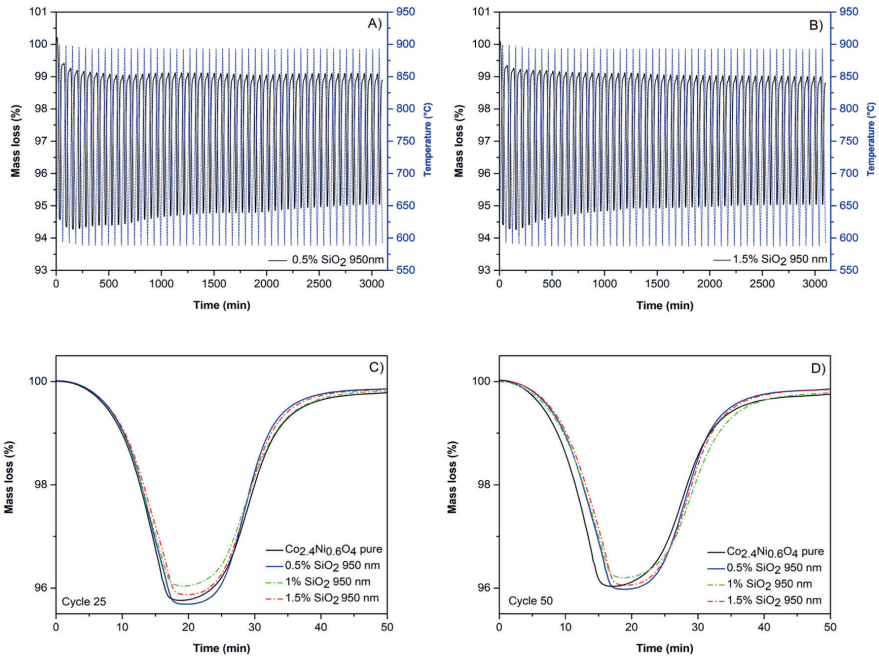

Fig. 4. Cyclability analyses of A) $Co_{2.4}Ni_{0.6}O_4$ + 0.5% SiO_2 400 nm, B) $Co_{2.4}Ni_{0.6}O_4$ + 1.5% SiO_2 400 nm, C) cycle 25 of the different percentage addition, D) cycle 50 of the different percentage addition.

Table 3
Thermogravimetric analysis of the pure material and the materials with addition of particles.

Material	Cycle 25		Cycle 50	
	Conversion ratio (%)	Mass loss (%)	Conversion ratio (%)	Mass loss (%)
$Co_{2.4}Ni_{0.6}O_4$	62.9	4.18	59.5	3.95
0.5% SiO_2 400 nm	64.2	4.27	60.1	3.99
1% SiO_2 400 nm	59.3	3.94	56.8	3.77
1.5% SiO_2 400 nm	61.9	4.10	59.5	3.94

with a purity of 99+%, ethylene glycol anhydrous from Sigma-Aldrich with a purity of 99.8%, tetraethyl orthosilicate (TEOS) from ACROS Organics with a purity of 98%, ethanol absolute form Scharlau, distilled water and an ammonia solution from EMSURE with a purity of 28–30%.

The technique used to synthesize Co-Ni mixed metal oxide is the sol-gel method following the Pechini route. To this end, appropriate quantities of precursors $Co(NO_3)_2{\cdot}6H_2O$ and $Ni(NO_3)_2{\cdot}6H_2O$ were used for the preparation of 2 g of material. First, the precursors were dissolved in 10 mL of ethylene glycol under gentle magnetic stirring to afford a homogeneous solution. Afterwards, 1 mg of citric acid was added to the reaction mixture under vigorous stirring for 60 min. The reaction mixture was dried overnight at 180 °C. The obtained powders were ground in an agate mortar to increase their homogeneity and then calcined in air at 400 °C for 10 h. The samples stabilized by calcination route were submitted to additional heating at 800 °C for 5 h in the furnace.

The silica particles and nanoparticles were synthesized following the Stober route. Appropriate quantities of tetraethyl orthosilicate, ammonia, distilled water and ethanol were used to produce 1.5 g of SiO_2 nanoparticles. The following solutions were first prepared under magnetic stirring: i) 2/3 of ethanol with ammonia and distilled water (solution A); and ii) TEOS with 1/3 of ethanol (solution B). The solution A was heated at different temperatures, in the range 25–80 °C, under magnetic stirring. Subsequently, the solution B was added in the solution A and was kept there for an hour at the corresponding temperature. After that, the mixture was submitted to magnetic stirring for 24 h at room temperature for ageing. When the particles were formed, the remaining solvent was removed in a rotary evaporator. It is worth to mention that the temperature of the process has big influence in the final particle size, obtaining in some batches nanoparticles of 26 nm and in others 400 nm particles.

The addition of the silica particles in the cobalt nickel mixed oxide was done with the help of an ultrasound tip. Appropriate amounts of nanoparticles and thermochemical material were added to 100 mL of ethanol and mixed for a minute with an ultrasound tip using an amplitude of 50%.

The experimental equipment used during the research was as follows:

In-situ *X-ray diffraction* (in-situ XRD). XRD data were collected on a Bruker D8 Advance diffractometer operating at 30 kV and 20 mA, equipped with a Cu tube (λ = 1.5418 Å), a Vantec-1 PSD detector, and an Anton Parr HTK2000 high-temperature furnace. The powder patterns were recorded in 2theta steps of 0.04° in the $15 \leq 2q \leq 85$ range, counting for 1.4 s per step (total time for each temperature 42 min). The experiment was performed in an open temperature chamber, from ambient temperature to 1000 °C, with a heating/

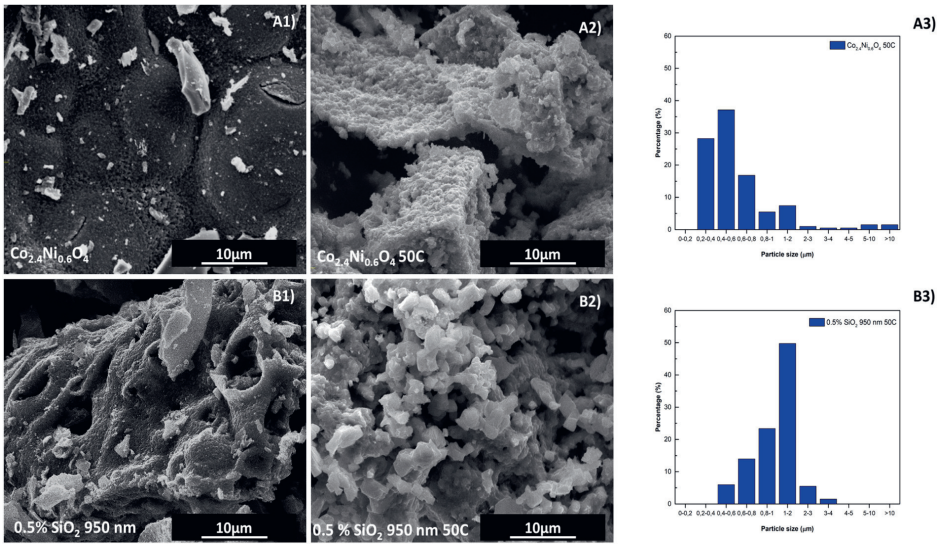

Fig. 5. SEM images of the materials fresh (A1, B1), after thermal treatment (A2, B2) and particle size distributions after thermal treatment (A3, B3).

cooling ramp of 0.166 °C/s under air. The XRD patterns were collected (1 h acquisition time) each 100 °C. The holder used for the measurements was of platinum.

Thermogravimetric analysis (TGA). The samples were analyzed in a SDT Q600 TGA from TA Instruments in the temperature range from 600 °C to 910 °C with a heating/cooling rate of 10 °C/min in air atmosphere with a flow rate of 60 mL/min. The conversion ratios of samples added with particles were calculated neglecting the amount of particles of the sample.

Scanning electron microscopy (SEM). The samples were imaged by means of a scanning electron microscope Quanta 200 FEG operated in high vacuum mode at 30 kV featured with a backscattered electron detector (BSED) and Everhart-Thornley Detector (ETD). In addition, energy-dispersive X-ray spectroscopy (EDX) analyses were carried out for elemental mapping. For the evaluation of the particle size distribution of the obtained samples, SEM images were statistically examined. At least 200 measurements were collected for each sample using ImageJ software [25].

X-ray diffraction (XRD). A Bruker D8 Advance diffractometer equipped with a LYNXEYE detector using CuKα1 radiation (λ = 1.5418 Å) and θ-2θ geometry was used for XRD analysis. Data were collected at room temperature between 10° and 80° with a step size of 0.02° and a counting time of 1 s per step. The EVA software was used to determine the phase composition of the material. In order to confirm the presence of pure single structure for each material, a full profile fitting procedure of the diffraction patterns [26] based on the Rietveld method [27] was performed using the Mau software. The refined parameters were: background coefficients, scale factor, lattice constants, atomic positions, isotropic independent atomic displacement parameters, zero shift, peak profile and asymmetry parameters. A quantitative analysis was done to obtain the composition of the materials.

3. Results and discussion

The stability of $Co_{2.4}Ni_{0.6}O_4$ was analyzed through a 100 cycles test in TGA. The results achieved are depicted in Fig. 1, where the variation of the mass of the sample over the heating and cooling cycles is displayed. We remind that the mass of the sample increases during the oxidation step (cooling stage) whereas it reduces during the reduction step (heating stage). For each heating-cooling cycle, the percentage difference between the maximum and minimum values of mass observed is referred as for mass lost (Δm) and is used hereafter to analyze the stability of the sample. Indeed, Δm is directly related to the conversion rate and must be constant over cycling in case of complete reversibility and stability of the sample. As a second indicator of stability, the onset temperatures of reduction/oxidation will be analyzed as well.

As can be seen in Fig. 1, Δm tends to decrease over the cycles, meaning that the material is not completely stable. Table 1 provides the values of mass lost (Δm) in different control cycles as well as corresponding redox temperatures of the material. It is worth to mention that the temperature values correspond to the onset temperatures. It can be seen that the cycling process is characterized by a progressive decrease of the mass lost (Δm) together with an evident augmentation of the reduction temperature. Compared to the first cycle, last cycle exhibits a Δm value 0.86% lower and a reduction temperature 35.86 °C higher. The oxidation temperatures are modified as well, but showing no clear tendency.

As already mentioned, the use of SiO_2 particles and nanoparticles as spacers is considered to improve the stability of the $Co_{2.4}Ni_{0.6}O_4$ material during thermal cycling. The choice of nanosized particles was in base to the demonstration by other authors that an amorphous structure or nanosized particles provide higher reactivity than crystalline or micro sized particles [28]. First of all, a compatibility test between the material and the particles and nanoparticles has been done by in-situ XRD. The analyses were performed using 26 nm silica nanoparticles and 400 nm silica particles with a 10% addition to facilitate the detection of eventual reaction with the thermochemical material.

Fig. 2 shows the XRD patterns of the samples before and after one thermal cycle in the diffractometer The patterns show no new phases when adding silica particles or nanoparticles in the fresh samples. On the contrary, after the first thermal cycle the high temperature phase CoO·NiO is well visible. This phase is likely formed in the initial cycles until stabilizing without deactivating further the material.

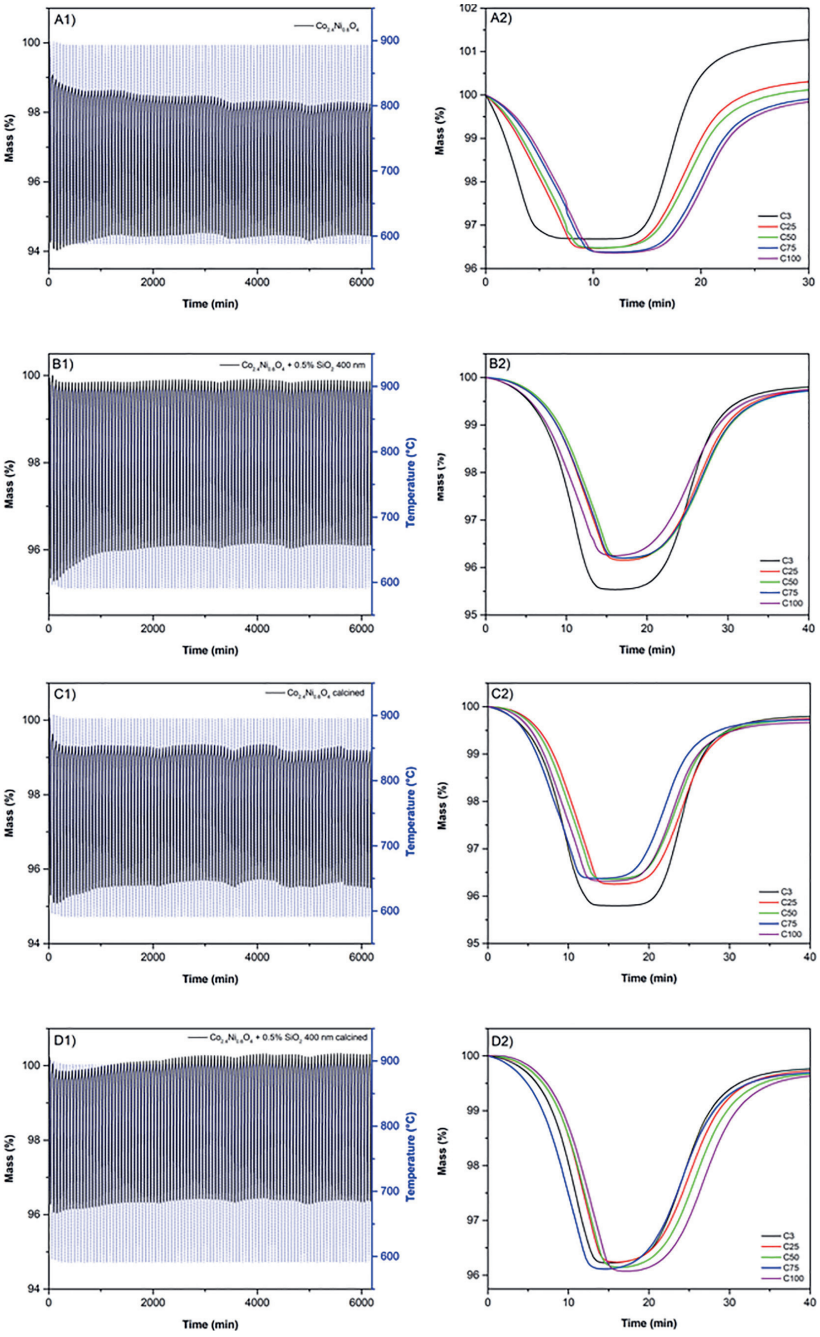

Fig. 6. Thermogravimetric analysis of A) $Co_{2.4}Ni_{0.6}O_4$, B) $Co_{2.4}Ni_{0.6}O_4$ + 0.5% SiO_2 400 nm, C) calcined $Co_{2.4}Ni_{0.6}O_4$ and D) calcined $Co_{2.4}Ni_{0.6}O_4$ + 0.5% SiO_2 400 nm.

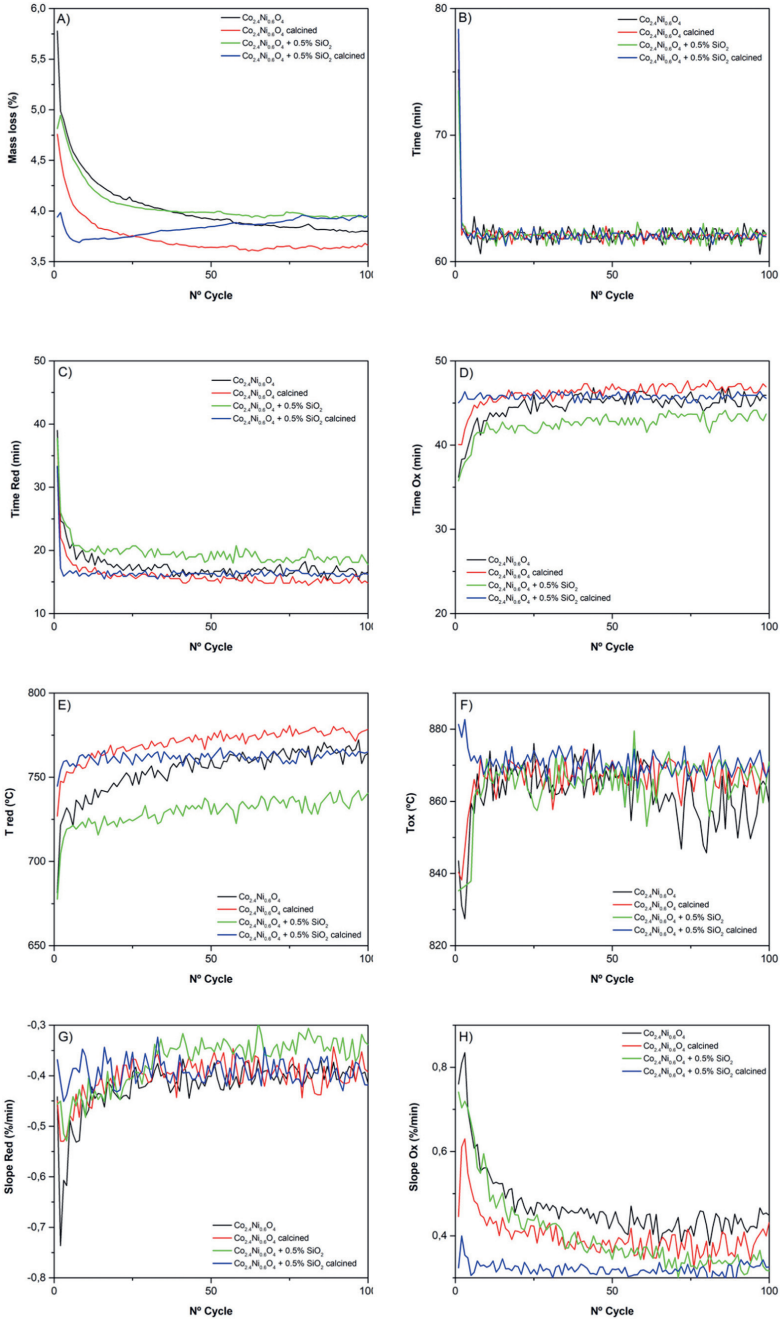

Fig. 7. Evolution of characteristic parameters of the materials in the 100-cycling test: A) Mass loss, B) total time, C) reduction step time, D) oxidation step time, E) reduction temperature, F) oxidation temperature, G) reduction slope and H) oxidation slope.

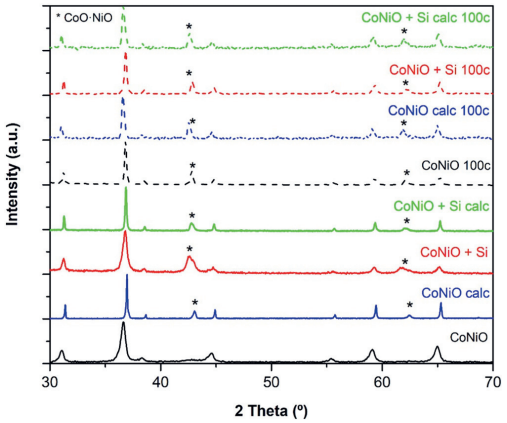

Fig. 8. X-ray diffraction patterns of $Co_{2.4}Ni_{0.6}O_4$ (CoNiO) pure fresh, pure calcined, added fresh and added calcined after thermal cycling.

Table 4
Lattice parameters (a) and weight fraction of $Co_{2.4}Ni_{0.6}O_4$ (CoNiO) pure fresh, pure calcined, with addition of particles fresh and with addition of particles calcined, after thermal cycling.

Material	a (Å)	x $Co_{2.4}Ni_{0.6}O_4$	y CoO·NiO
$Co_{2.4}Ni_{0.6}O_4$ 100c	$8{,}0811 \times 10^{-4}$	0,73	0,27
$Co_{2.4}Ni_{0.6}O_4$ calcined 100c	$8{,}0819 \times 10^{-4}$	0,71	0,29
$Co_{2.4}Ni_{0.6}O_4 + SiO_2$ 100c	$8{,}0911 \times 10^{-4}$	0,74	0,26
$Co_{2.4}Ni_{0.6}O_4 + SiO_2$ calcined 100c	$8{,}0777 \times 10^{-4}$	0,69	0,31

A refinement of the in-situ XRD patterns was performed to obtain quantitative results. As shown in Table 2, all the cycled samples show smaller lattice parameters than the fresh ones. This is due to the nickel migration out of the mixed oxide structure, resulting in the formation of the high temperature phase CoO·NiO [17]. This phase is observed in the patterns of the cycled materials and confirmed observing the weight fractions of mixed oxide (X) and CoO·NiO phase (Y) in each sample.

After confirming the lack of reactions between the mixed oxide and the particles, the effect of the size and particles loading was investigated to obtain the best possible performance of the mixed oxide in terms of densification and thermal stability. The stability and general behavior of the materials (pure mixed oxide and with additions of SiO_2 (nano)particles materials) was assessed by TGA (50 thermal cycles). The results achieved are depicted in Fig. 3. It can be seen that the pure material is not completely stable, the percentages of mass gained and lost in each cycle varying during the experiment. The same behavior is obtained for the samples with addition of (nano)particles but Fig. 3 could suggest a better behavior when adding 400 nm SiO_2 particles, obtaining sustained values of mass gained and lost. There could be a very small contribution in the initial variations of each experiment from the SiO_2 particles. As they were not calcined before the addition to the nickel cobaltite, some changes could be expected during the initial cycles even if their small amount does not justify the macroscopic effect observed mainly due to the mixed oxide structural and morphological readjustment.

The effect of the nanoparticles loading in $Co_{2.4}Ni_{0.6}O_4$ was investigated using 400 nm SiO_2 particles, that seem to stabilize the material. To this end, three different addition quantities were tested: 0.5, 1 and 1.5% wt. The results are shown below in Fig. 4.

Fig. 4A and B shows 50 thermal cycles of $Co_{2.4}Ni_{0.6}O_4$ + 0.5% SiO_2 400 nm and $Co_{2.4}Ni_{0.6}O_4$ + 1.5% SiO_2 400 nm, respectively. Fig. 4C and D shows the comparison of the behavior of each material, pure and doped, in two control cycles: the 25th and the 50th. The behavior of the pure nickel cobaltite is very similar to the one of the nickel cobaltite with addition of 400 nm SiO_2 particles. The values of mass gained/lost and the conversion listed in Table 3 could suggest a slight positive effect adding 0.5% 400 nm SiO_2 particles, reaching conversions of 64.2% instead of 62.9% obtained with the pure nickel cobaltite during the first 25 cycles, and 60.1% instead of 59.5% after 50 cycles. This potential beneficial effect will be more apparent in 100 cycles experiments that will be discussed later.

SEM analyses were performed to observe the samples of $Co_{2.4}Ni_{0.6}O_4$ pure and with addition of SiO_2 particles of 400 nm in a percentage of 0.5% before and after 50 thermal cycles. Fig. 5 shows the results obtained.

The change of morphology produced in the two materials after thermal cycling is shown in Fig. 5. In the case of the pure $Co_{2.4}Ni_{0.6}O_4$, the particles have formed big agglomerates. On the contrary, in the case of the material with addition of silica, some structural changes are appreciated, the particles are bigger but independent. However, the silica particles promote the creation of channels that ensure the oxygen flow through the material, thus resulting in better cyclability behavior compared to the pure material. The particle size distribution obtained by ImageJ software [25] (see Fig. 5B3) shows that, with an addition percentage of 0.5% wt., the particles agglomerates are always less than 4 μm. The predominant particle size in the material with addition of SiO_2 particles is of 1–2 μm.

The effect of additional calcination step at 800 °C for 5 h on the stability of pure $Co_{2.4}Ni_{0.6}O_4$ and $Co_{2.4}Ni_{0.6}O_4$ with addition of SiO_2 particles was also analyzed. Based on previous results, 400 nm SiO_2 nanoparticles and 0.5% wt. loading were selected to perform the stability study. The results of TGA experiments carried out (100 cycles of heating and cooling) are shown in Fig. 6.

The effect of the treatments is not critical, the behavior of the materials with addition of particles and calcined is very similar. The cycling repeatability of the material with addition of particles without calcination (Fig. 6B1 and B2) could be better than the fresh sample and the calcined samples repeatability. The oscillations observed during the whole cycling are lower. The results of the TGA were used to calculate the following performance indicators, which are depicted in Fig. 7:

- The mass lost (Δm) per cycle (Fig. 7A)
- The total time needed to complete the redox process for each cycle (Fig. 7B)
- The time required to complete the reduction step (Fig. 7C)
- The time required to complete the oxidation step (Fig. 7D)
- The reduction temperature for each thermal cycle (Fig. 7E)
- The oxidation temperature observed in each thermal cycle (Fig. 7F)
- The reduction rate (Fig. 7G) and the oxidation rate (Fig. 7H) for each cycle.

Based on these results, it can be concluded that the extra-calcination slows down the cycling process, increasing the total time needed to complete the redox process and reducing the maximum slope (reaction rates) of the mass vs. time curves. On the positive side, the calcination keeps the oxidation temperature more stable. Again, the use of SiO_2 particles seems to promote material stability and higher conversion, reaching higher values of mass lost per cycle after 40 cycles. More importantly, from cycle 40 onwards the decreasing of Δm along the cycles is less in the case of SiO_2-added material than in bare material. At last, but not least, SiO_2 particles help to maintain the reduction temperatures at lower values than in the case of absence of particles.

X-ray diffraction measurements were performed in order to study the possible interactions between the thermochemical material and the particles after prolonged cycling. The influence of the additional calcination process in the final stoichiometry of the material was determined too. For this purpose, Rietveld refinements [29] of all the diffractograms

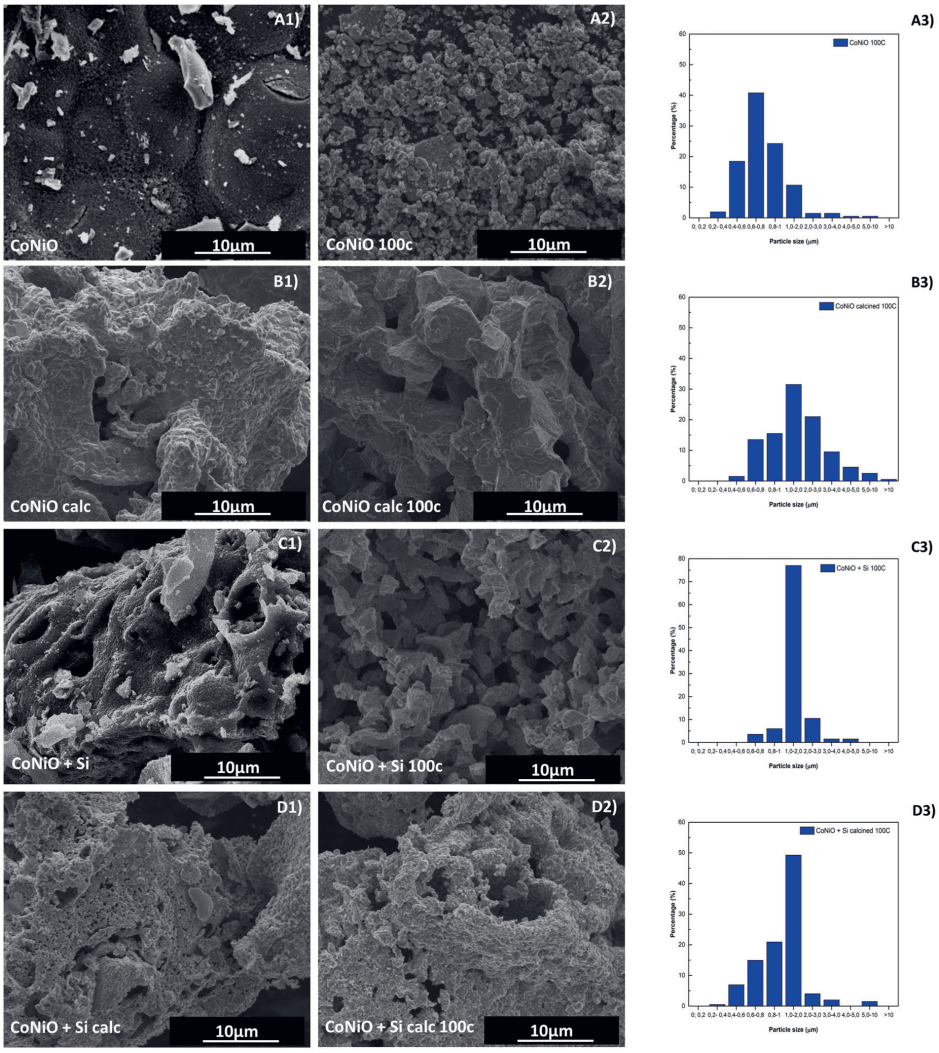

Fig. 9. SEM images of the fresh materials (A – CoNiO pure, B - CoNiO pure calcined, C – CoNiO with addition of SiO_2 particles, D - CoNiO with addition of SiO_2 particles and calcined), after 100 cycles of thermal treatment (A1, B1, C1, D1) and particle size distributions after 100 thermal cycles (A2, B2, C2, D2).

presented in Fig. 8 were done. The results are reported in Table 4.

Fig. 8 shows that the behavior of the materials after thermal cycling, with or without additional calcination step or particles addition, is the same as the one obtained by the authors in a previous research work [17]. The cycling process promotes the formation of the high temperature phase CoO·NiO until the final stoichiometry is reached and the values of weight fraction of $Co_{2.4}Ni_{0.6}O_4$ and CoO·NiO remains constant, as we observe analyzing the final fractions of both phases obtained for all the cycled materials.

The refinements do not show evidences of interaction between the SiO_2 nanoparticles and the Co-Ni based mixed oxide or the high temperature phase CoO·NiO. Indeed, the interaction between them should shift the peaks of the diffractograms to higher angles due to the smaller ionic radius of Si^{4+} (0.4 Å) in six-fold coordination, compared to the ionic radius of Co^{2+}, Co^{3+} and Ni^{2+} (0.65 Å, 0.54 Å and 0.55 Å, respectively) [30].

SEM analyses were performed in order to assess the morphology of all the materials (CoNiO pure fresh, pure calcined, with addition of particles fresh and with addition of particles calcined). Fig. 9 shows the images of the materials and the distribution of the particle size. The results of the particle size were obtained by ImageJ software [25].

The morphology of the materials changes with thermal cycling, except for the material calcined with SiO_2 particles, where the morphology does not vary. In the other cases, there are evidences of particles agglomeration (growth of particle size) after thermal cycling. The pure material shows a broad spectrum of particle sizes, while the

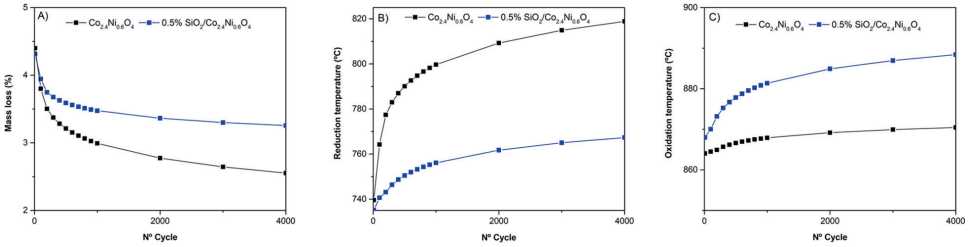

Fig. 10. $Co_{2.4}Ni_{0.6}O_4$ material and $Co_{2.4}Ni_{0.6}O_4$ + 0.5% SiO_2 400 nm material prediction results of A) mass loss, B) reduction temperature and C) oxidation temperature.

Table 5
$Co_{2.4}Ni_{0.6}O_4$ material prediction values of mass loss, conversion ratio and redox temperatures.

Cycle	Mass loss (%)	Conversion ratio (%)	Reduction temperature (°C)	Oxidation temperature (°C)
10	4.40	66	739	864
100	3.80	57	764	859
1000	2.99	45	799	867
2000	2.77	42	809	869
3000	2.64	40	814	869
4000	2.55	38	818	870

Table 6
$Co_{2.4}Ni_{0.6}O_4$ + 0.5% SiO_2 400 nm material prediction values of mass loss, conversion ratio and redox temperatures.

Cycle	Mass loss (%)	Conversion ratio (%)	Reduction temperature (°C)	Oxidation temperature (°C)
10	4.31	65	720	871
100	3.94	59	740	870
1000	3.47	52	756	881
2000	3.36	51	761	884
3000	3.30	50	765	886
4000	3.26	49	767	888

calcined one is densified and the one with addition of particles reaches a structure with a more homogeneous particle size, showing all the particles in a range of 1–2 μm.

In base to the previous results, we can conclude that extra-calcination of the mixed oxide has no beneficial effects neither in the stabilization of the thermochemical material nor in the reaction rates.

Coming back to the potential beneficial effects of SiO_2 particles in the stabilization of $Co_{2.4}Ni_{0.6}O_4$, we have extrapolated measured data of mass loss per cycle, conversion rate and oxidation temperature in the 100-cycles experiments carried our (Fig. 7) to estimate long-term behavior of doped and undoped thermochemical materials. For extrapolation, measured data have been adjusted to logarithmic functions $y = a\ ln(n) + b$, where y represents measured quantity (mass loss or reduction temperature), n is the cycle number and a and b are fitting parameters. All adjustments resulted in very good agreement with observations ($R^2 > 0.9$) and, therefore, were used to calculate mass loss, conversion rate and reduction temperature for much longer cycling periods. The results achieved are depicted in Fig. 10 and some numerical values are reported in Tables 5 and 6.

In the case of the pure material (Table 5), comparing the results of the cycle 100 and the cycle 4000 we observe that in 20 years, the material should lose a 19% of conversion ratio, increasing the reduction temperature by 54 °C and the oxidation temperature 11 °C.

In the case of the material with addition of SiO_2 particles (Table 6), comparing the results of the cycle 100 and the cycle 4000 we observe that in 20 years, the material should lose a 10.4% of conversion ratio, 8.4% less than in the case of the pure material, increasing the reduction temperature by 26 °C (54 °C for the pure material) and the oxidation temperature 17 °C (11 °C for the pure material). In general, when considering a limited number of cycles (100), the effect of particles addition in the stabilization of the material is hardly distinguished while these effects seem to be much more noticeable when considering the long-term behavior (4000 cycles). Obviously, these conclusions, which are based on extrapolation of data, although promising, should be confirmed experimentally.

4. Conclusions

In this study, the stabilization of $Co_{2.4}Ni_{0.6}O_4$ was analyzed by calcinating the synthesized material, by adding the material with SiO_2 particles and nanoparticles and by combining the two processes.

The compatibility test and the thermogravimetric analysis showed that best performance between the SiO_2 particles and nanoparticles was obtained with the ones of 400 nm and added at 0.5% wt. They improved slightly the cyclability and mitigate the densification.

The study of the calcination process to stabilize the material showed that a densification phenomenon harms the cyclability, resulting in a slowdown of the redox reactions kinetics.

The addition of silica particles improves the stability of the material, reaching better mass lost than pure material while increasing a bit the reduction temperature. The morphology of the material is more regular, obtaining the 80% of the measurements in the range of 1–2 μm.

The lack of reactions between the $Co_{2.4}Ni_{0.6}O_4$ and the SiO_2 was confirmed after 100 cycles.

The forward projection of the material with addition of SiO_2 particles has evidenced a conversion ratio loss of 10% in 20 years, with a temperature increase of 27 °C in the reduction stage and of 17 °C in the case of the oxidation stage, noticeably better results than for the pure material.

The results of this work lead us to consider this mixed oxide with addition of SiO_2 particles and the others – always in Co-Ni base- successfully synthesized in a previous research work to be a potential future candidate for TcES applications at high temperature, providing flexibility in terms of reaction temperatures and a correct stability.

CRediT authorship contribution statement

Yasmina Portilla-Nieto: Data curation, Methodology, Investigation, Roles/Writing original, Writing-review. **Karmele Vidal:** Methodology. **Marta Hernáiz:** Data curation, Investigation, Supervision. **Estíbaliz Aranzabe:** Conceptualization, Data curation, Funding acquisition, Project administration, Supervision, Writing review. **Stefania Doppiu:** Funding acquisition, Project administration, Supervision, Writing review. **Elena Palomo:** Conceptualization, Funding acquisition, Project administration, Supervision, Writing-review.

Declaration of competing interest

The authors declare that they have no known competing financial interests or personal relationships that could have appeared to influence the work reported in this paper.

Acknowledgement

The Basque Government (Elkartek CICe2019, KK-2019/00097) are acknowledged for the financial support of this work. The authors express their sincere gratitude to Cristina Luengo and Yagmur Polat for their technical support.

Appendix A. Supplementary data

Supplementary data to this article can be found online at https://doi.org/10.1016/j.est.2022.104876.

References

[1] X. Zhou, M. Mahmood, J. Chen, T. Yang, G. Xiao, M.L. Ferrari, Validated model of thermochemical energy storage based on cobalt oxides, Appl. Therm. Eng. 159 (2019), 113965, https://doi.org/10.1016/j.applthermaleng.2019.113965.
[2] M. Mahmood, A. Traverso, A.N. Traverso, A.F. Massardo, D. Marsano, C. Cravero, Thermal energy storage for CSP hybrid gas turbine systems: dynamic modelling and experimental validation, Appl. Energy 212 (2018) 1240–1251, https://doi.org/10.1016/j.apenergy.2017.12.130.
[3] H.B. Dizaji, H. Hosseini, A review of material screening in pure and mixed-metal oxide thermochemical energy storage (TCES) systems for concentrated solar power (CSP) applications, Renew. Sust. Energ. Rev. 98 (2018) 9–26, https://doi.org/10.1016/j.rser.2018.09.004.
[4] B. Ehrhart, E. Coker, N. Siegel, A. Weimer, Thermochemical cycle of a mixed metal oxide for augmentation of thermal energy storage in solid particles, Energy Procedia 49 (2013) 762–771, https://doi.org/10.1016/j.egypro.2014.03.082.
[5] F. Bruno, M. Belusko, M. Liu, N.H.S. Tay, Using Solid-Liquid Phase Change Materials (PCMs) in Thermal Energy Storage Systems, Woodhead Publishing Limited, 2014, https://doi.org/10.1533/9781782420965.2.201.
[6] S. Wu, C. Zhou, E. Doroodchi, R. Nellore, B. Moghtaderi, A review on high-temperature thermochemical energy storage based on metal oxides redox cycle, Energy Convers. Manag. 168 (2018) 421–453, https://doi.org/10.1016/j.enconman.2018.05.017.
[7] M. Liu, N.H. Steven Tay, S. Bell, M. Belusko, R. Jacob, G. Will, W. Saman, F. Bruno, Review on concentrating solar power plants and new developments in high temperature thermal energy storage technologies, Renew. Sust. Energ. Rev. 53 (2016) 1411–1432, https://doi.org/10.1016/j.rser.2015.09.026.
[8] T. Block, M. Schmücker, Metal oxides for thermochemical energy storage: a comparison of several metal oxide systems, Sol. Energy 126 (2016) 195–207, https://doi.org/10.1016/j.solener.2015.12.032.
[9] C. Agrafiotis, M. Roeb, M. Schmücker, C. Sattler, Exploitation of thermochemical cycles based on solid oxide redox systems for thermochemical storage of solar heat. Part 2: redox oxide-coated porous ceramic structures as integrated thermochemical reactors/heat exchangers, Sol. Energy 114 (2015) 440–458, https://doi.org/10.1016/j.solener.2014.12.036.
[10] C. Agrafiotis, M. Roeb, M. Schmücker, C. Sattler, Exploitation of thermochemical cycles based on solid oxide redox systems for thermochemical storage of solar heat. Part 1: testing of cobalt oxide-based powders, Sol. Energy 102 (2014) 189–211, https://doi.org/10.1016/j.solener.2013.12.032.
[11] D. Bielsa, A. Zaki, P.L. Arias, A. Faik, Improving the redox performance of Mn2O3/Mn3O4 pair by si doping to be used as thermochemical energy storage for concentrated solar power plants, Sol. Energy 204 (2020) 144–154, https://doi.org/10.1016/j.solener.2020.04.073.
[12] C. Agrafiotis, S. Tescari, M. Roeb, M. Schmücker, C. Sattler, Exploitation of thermochemical cycles based on solid oxide redox systems for thermochemical storage of solar heat. Part 3: cobalt oxide monolithic porous structures as integrated thermochemical reactors/heat exchangers, Sol. Energy 114 (2015) 459–475, https://doi.org/10.1016/j.solener.2014.12.037.
[13] A.J. Carrillo, D.P. Serrano, P. Pizarro, J.M. Coronado, Improving the thermochemical energy storage performance of the Mn2O3/Mn3O4 redox couple by the incorporation of iron, ChemSusChem. 8 (2015) 1947–1954, https://doi.org/10.1002/cssc.201500148.
[14] A.J. Carrillo, D.P. Serrano, P. Pizarro, J.M. Coronado, Thermochemical heat storage at high temperatures using Mn2O3/Mn3O4 system: narrowing the redox hysteresis by metal co-doping, Energy Procedia 73 (2015) 263–271, https://doi.org/10.1016/j.egypro.2015.07.686.
[15] L. André, S. Abanades, Investigation of metal oxides, mixed oxides, perovskites and alkaline earth carbonates/hydroxides as suitable candidate materials for high-temperature thermochemical energy storage using reversible solid-gas reactions, mater. Today, Energy 10 (2018) 48–61, https://doi.org/10.1016/j.mtener.2018.08.007.
[16] Y. Xiong, J. Zhao, Z. Zheng, W. Li, Effect of copper dopant on the mixed cobalt-iron oxides for hydrogen generation via chemical looping redox cycles, Int. J. Hydrog. Energy 45 (2020) 28372–28382, https://doi.org/10.1016/j.ijhydene.2020.07.245.
[17] Y. Portilla-Nieto, A. Zaki, K. Vidal, M. Hernaiz, E. Aranzabe, S. Doppiu, A. Faik, Development of Co3-xNixO4 materials for thermochemical energy storage at lower red-ox temperature, Sol. Energy Mater. Sol. Cells 230 (2021), 111194, https://doi.org/10.1016/j.solmat.2021.111194.
[18] T. Block, N. Knoblauch, M. Schmücker, The cobalt-oxide/iron-oxide binary system for use as high temperature thermochemical energy storage material, Thermochim. Acta 577 (2014) 25–32, https://doi.org/10.1016/j.tca.2013.11.025.
[19] U.S.D. of Energy, Thermochemical heat storage for concentrated solar power, thermochemical system reactor design for thermal energy storage, Ind. Eng. Chem. 19 (2011) 594–596.
[20] C. Roßkopf, M. Haas, A. Faik, M. Linder, A. Wörner, Improving powder bed properties for thermochemical storage by adding nanoparticles, Energy Convers. Manag. 86 (2014) 93–98, https://doi.org/10.1016/j.enconman.2014.05.017.
[21] R.J. Hill, J.R. Craig, G.V. Gibbs, Systematics of the spinel structure type, Phys. Chem. Miner. 4 (1979) 317–339, https://doi.org/10.1007/BF00307535.
[22] W.J. King, A.C.C. Tseung, The reduction of oxygen on nickel-cobalt oxides—II, Electrochim. Acta 19 (1974) 493–498, https://doi.org/10.1016/0013-4686(74)87030-1.
[23] D. Klissurski, E. Uzunova, Synthesis and features of binary cobaltite spinels, J. Mater. Sci. 29 (1994) 285–293, https://doi.org/10.1007/BF01162484.
[24] J. Liu, S.Z. Qiao, H. Liu, J. Chen, A. Orpe, D. Zhao, G.Q. Lu, Extension of the stöber method to the preparation of monodisperse resorcinol-formaldehyde resin polymer and carbon spheres, Angew. Chem. Int. Ed. 50 (2011) 5947–5951, https://doi.org/10.1002/anie.201102011.
[25] C.A. Schneider, W.S. Rasband, K.W. Eliceiri, NIH image to ImageJ: 25 years of image analysis, Nat. Methods 9 (2012) 671–675, https://doi.org/10.1038/nmeth.2089.
[26] L. Lutterotti, S. Gialanella, X-ray diffraction characterization of heavily deformed metallic specimens, Acta Mater. 46 (1998) 101–110, https://doi.org/10.1016/S1359-6454(97)00222-X.
[27] H.M. Rietveld, A profile refinement method for nuclear and magnetic structures, J. Appl. Crystallogr. 2 (1969) 65–71, https://doi.org/10.1107/s0021889869006558.
[28] J.C. Bertolini, J.L. Rousset, Reactivity of metal nanoparticles, Nanomater. Nanochem. (2007) 281–304, https://doi.org/10.1007/978-3-540-72993-8_10.
[29] S. Petrick Casagrande, R.C. Blanco, Método de Rietveld para el estudio de estructuras cristalinas 2 (2004) 1–5.
[30] R.D. Shannon, Revised effective ionic radii and systematic studies of interatomic distances in halides and chalcogenides, Acta Crystallogr. Sect. A. 32 (1976) 751–767, https://doi.org/10.1107/S0567739476001551.

Development of a Kinetic Model for the Redox Reactions of $Co_{2.4}Ni_{0.6}O_4$ and $SiO_2/Co_{2.4}Ni_{0.6}O_4$ Oxides for Thermochemical Energy Storage

Materials, **2022**, 15, 3695

ISSN: 1996-1944

Impact Factor 2021: 3.748

Cite Score: 4.2

Q2 (Material Science)

https://doi.org/10.3390/ma15103695

materials

MDPI

Article

Development of a Kinetic Model for the Redox Reactions of $Co_{2.4}Ni_{0.6}O_4$ and $SiO_2/Co_{2.4}Ni_{0.6}O_4$ Oxides for Thermochemical Energy Storage

Yasmina Portilla-Nieto [1,2,3,*], Daniel Bielsa [1], Jean-Luc Dauvergne [1], Marta Hernaiz [3], Estibaliz Aranzabe [3], Stefania Doppiu [1] and Elena Palomo del Barrio [1,4]

[1] Centre for Cooperative Research on Alternative Energies (CIC energiGUNE), Basque Research and Technology Alliance (BRTA), Alava Technology Park, Albert Einstein 48, 01510 Vitoria-Gasteiz, Spain; dbielsa@cicenergigune.com (D.B.); jldauvergne@cicenergigune.com (J.-L.D.); sdoppiu@cicenergigune.com (S.D.); e.palomo@cicenergigune.com (E.P.d.B.)
[2] Applied Physics II Department, Faculty of Science and Technology, University of the Basque Country (UPV/EHU), 48080 Bilbao, Spain
[3] TEKNIKER, Polo Tecnológico de Eibar, C/Iñaki Goenaga, 5, 20600 Eibar, Spain; marta.hernaiz@tekniker.es (M.H.); estibaliz.aranzabe@tekniker.es (E.A.)
[4] IKERBASQUE Basque Foundation for Science, Plaza Euskadi 5, 48009 Bilbao, Spain
* Correspondence: yportilla@cicenergigune.com; Tel.: +34-945-297-108

check for updates

Citation: Portilla-Nieto, Y.; Bielsa, D.; Dauvergne, J.-L.; Hernaiz, M.; Aranzabe, E.; Doppiu, S.; Palomo del Barrio, E. Development of a Kinetic Model for the Redox Reactions of $Co_{2.4}Ni_{0.6}O_4$ and $SiO_2/Co_{2.4}Ni_{0.6}O_4$ Oxides for Thermochemical Energy Storage. *Materials* **2022**, *15*, 3695. https://doi.org/10.3390/ma15103695

Academic Editors: Juan Carlos Serrano-Ruiz and Francisco de Paula Montero Chacón

Received: 19 April 2022
Accepted: 19 May 2022
Published: 21 May 2022

Publisher's Note: MDPI stays neutral with regard to jurisdictional claims in published maps and institutional affiliations.

Abstract: One of the possible solutions for the transition of the actual energetic model is the use of thermal energy storage technologies. Among them, thermochemical energy storage based on redox reactions involving metal oxides is very promising due to its high energy density. This paper deals with the development of the kinetic study based on data extracted from the thermogravimetric analysis of a cobalt-nickel mixed oxide ($Co_{2.4}Ni_{0.6}O_4$) without and with the addition of SiO_2 particles to improve the cyclability. The results show that in the reduction reaction the activation energy is not affected by the addition of SiO_2 particles while in the oxidation reaction an increase in the activation energy is observed. The theoretical models fitting with the experimental data are different for each material in the reduction reaction. The mixed oxide is controlled by a nucleation and growth mechanism for conversion ratios higher than 0.5, while the added material is controlled by diffusion mechanisms. In the oxidation reaction, the two materials are controlled by a nucleation and growth mechanism for conversion ratios higher than 0.5.

Keywords: thermochemical heat storage; gas-solid reaction; reduction/oxidation reaction; cobalt–nickel oxide; kinetic models

1. Introduction

Excessive energy use on a global scale and the associated problems have meant a focused interest in the field of renewable energy. Among these, Concentrated Solar Power (CSP) is of great interest due to the wide availability of solar energy, its cost efficiency and ease of hybridization [1]. The main drawback of this technology is its intermittency, making storage systems necessary to guarantee the availability of energy. This problem can be solved by using large-scale and inexpensive thermal energy storage (TES) systems. Moreover, the combination of CSP plants with TES contributes to making them economically viable [2].

Among the TES technologies, there are two more developed, which are sensible heat storage (SHS), where the energy is stored by increasing the temperature of the storage material and released when decreasing the temperature, and latent heat storage (LHS), where the energy storage is carried out through phase changes of the storage material [3–5]. Currently, the focus is on the development of the less studied but most promising TES technology, thermochemical storage (TcES), based on the use of high enthalpic reversible

chemical reactions to store or release energy. This technology theoretically provides a much higher energy storage density than other TES technologies [6,7]. During the on-sun hours, the endothermic chemical reaction is used to store heat and during the off-sun hours, the reverse exothermic reaction is used to release heat.

Previous research works have selected redox reactions involving metal oxides as suitable candidates for high-temperature TES applications. Therefore, redox systems need suitable materials which should fulfill requirements such as complete reaction reversibility, suitable reaction temperature, high storage density, high reaction enthalpy, no toxicity and good thermal stability during cycling in the operating temperature range [8–10].

Different research groups have investigated different materials which can be suitable for thermochemical energy storage at high temperatures. The most favored resulting materials are metal oxides due to their high reaction enthalpies, high operating temperature ranges and utilization of air at the same time as a reactant and a heat transfer fluid [11–13].

The redox reactions can be presented as [14]:

$$\text{Reduction reaction}: \ M_xO_{y+z} \rightarrow M_xO_y + z/2O_2$$

$$\text{Oxidation reaction}: \ M_xO_y + z/2O_2 \rightarrow M_xO_{y+z}$$

where *M* is a metal.

The most studied metal oxides for thermochemical applications have been cobalt oxide (Co_3O_4/CoO) and manganese oxide (Mn_2O_3/ Mn_3O_4) [8,11,15,16], but their reaction temperatures (higher than 850 °C) being too high is considered as the main barrier for their final application in technologies such as CSP or industrial waste heat recovery.

The literature shows that the development of mixed oxides is a correct alternative to tuning the reaction temperatures. The main problem is that, in most cases, the result is an increase in the reaction temperature instead of a decrease [17,18]. Sometimes, the development of mixed oxides can improve long-term cyclability. Another alternative for improving the cyclability without harming the reaction temperatures is the addition of nanoparticles to the mixed oxides [19,20].

Co_3O_4 has a spinel structure with the general formula of AB_2O_4 where A, B = Co, Zn, Ni, Fe, Cu, Mn, etc. A and B are divalent and trivalent metal cations, respectively. The nature of the cations incorporated into the structure affects the distribution of the cations between the two sites. In common spinel structures, the divalent A and trivalent B cations occupy the tetrahedral and octahedral sites, respectively [21–23].

Previous research works have demonstrated that developing mixed oxides based on Co–Ni allows for tuning the reaction temperatures depending on the amount of nickel in the cobalt oxide host structure. The most promising formulation was $Co_{2.4}Ni_{0.6}O_4$, obtaining reaction temperatures of around 700 °C during 100 thermal cycles in TGA [24]. The activity loss shown during the cycling process was studied by adding SiO_2 particles in the $Co_{2.4}Ni_{0.6}O_4$, showing no significant differences in the behavior of the material in a limited number of cycles, contrary, the 20-year predictions (4000 cycles) anticipate a notably better behavior of the mixed oxide with the addition than the one without it. This work is under review.

Several works focusing on the kinetic studies of pure cobalt oxide were published [25–28]. Some studies have found that the reduction and oxidation reactions of Co_3O_4/CoO are controlled by the heat transfer and diffusion mechanism, respectively [18]. Other studies have analyzed the effect of different additives, such as Al_2O_3 and Y_2O_3, in the cobalt oxide, demonstrating that the Co_3O_4–Al_2O_3 desorbs more oxygen than the Co_3O_4–Y_2O_3 in the same conditions, and the activation energy of Co_3O_4–Al_2O_3 and Co_3O_4–Y_2O_3 changes proportionally to the conversion fraction (α). These effects were attributed to the different ionic radii presented by the aluminum oxide and the yttrium oxide, the ability to create new compounds with different decomposition temperatures and their effect on the sintering of cobalt oxide [29].

In this work we studied, for the first time, the kinetic mechanisms of $Co_{2.4}Ni_{0.6}O_4$ and of the 0.5% $SiO_2/Co_{2.4}Ni_{0.6}O_4$ with the objective of studying the effects of Ni in the cobalt

oxide structure and to obtain a comparison of the kinetic parameters (activation energy (Ea), preexponential factor (A) and reaction model (f(α))) for the nickel cobaltite and the added nickel cobaltite.

The redox reaction of the metal oxides studied in this research is:

$$Co_{3-x}Ni_xO_4 \leftrightarrow 3Co_{1-x}Ni_xO + 1/2O_2$$

and the maximum conversion reached for the $Co_{2.4}Ni_{0.6}O_4$ material is with a mass gain/loss of 6.65%.

2. Materials and Methods

The synthesis of the mixed oxides was performed with the materials: nickel nitrate hexahydrate extra-pure from Scharlab (Barcelona, Spain, EU), cobalt nitrate hexahydrate from Fisher Scientific (Pittsburgh, PA, USA) with a purity of 98$^+$%, citric acid from Fisher Scientific with a purity of 99$^+$% and ethylene glycol anhydrous from Sigma-Aldrich (Saint Louis, MO, USA) with a purity of 99.8%.

For the synthesis of the SiO_2 particles, the used materials were: tetraethyl orthosilicate (TEOS) from ACROS Organics with a purity of 98%, ethanol absolute form Scharlau, distilled water and an ammonia solution from EMSURE with a purity of 28–30%.

The synthesis of Co–Ni mixed oxides was carried out following the sol–gel Pechini Route. For this purpose, stoichiometric quantities of $Co(NO_3)_2{\cdot}6H_2O$ and $Ni(NO_3)_2{\cdot}6H_2O$ nitrates were used. First of all, the primary precursors were dissolved in ethylene glycol under magnetic stirring to obtain a homogeneous solution. Subsequently, citric acid was added to the previous mixture under vigorous stirring for 1 h. Once the solution mixture was well mixed, it was dried overnight at 180 °C. The resulting powders were ground in an agate mortar to increase their homogeneity and then calcined in air at 400 °C for 10 h.

The Stober route was used for the synthesis of SiO_2 particles. Appropriate quantities of tetraethyl orthosilicate, ammonia, distilled water and ethanol were used to produce SiO_2 particles. Firstly, two solutions were prepared under magnetic stirring: (i) 2/3 of ethanol with ammonia and distilled water (solution A); and (ii) TEOS with 1/3 of ethanol (solution B). Solution A was maintained at ambient temperature under magnetic stirring. Subsequently, solution B was added to solution A and was kept there for 25 hours for aging. Once the particles were formed, the remaining solvent of the mixture was removed in a rotary evaporator.

The addition of a 0.5 wt. % of silica particles in the cobalt–nickel mixed oxide was carried out using an ultrasound tip using an amplitude of 50%, cooling the mixture to avoid agglomerates. The mixture was dissolved in 100 mL of ethanol and dispersed for 1 min.

The equipment used during the research was:

Thermogravimetric analysis (TGA). The samples were analyzed in a TGA/DSC 1 from Mettler Toledo, using a sensor type DSC HSS2, a furnace LF heating until 1100 °C, equipped with a sample robot standard. The gas controller is the type GC 200. The amount of material analyzed each time was 20 mg, and the temperature range was from 600 °C to 910 °C, using different heating/cooling ramps depending on the point of the model development.

The validation model was constructed using the Octave software.

3. Results

3.1. Kinetic Analysis

The kinetic models are usually determined by the intrinsic mass gained/lost regarding the oxygen absorption/desorption of metal oxides. For this purpose, the conversion ratio (α) is plotted against time (t).

The conversion ratio (α) is defined in Equation (1) [30]:

$$\alpha = \frac{m_0 - m_t}{m_0 - m_f} \quad (1)$$

where m_0 is the initial mass, m_t is the mass at time t and m_f is the final mass.

The parameters to be obtained for the development of a kinetic model are mainly: activation energy (Ea), preexponential factor (A) and reaction model ($f(\alpha)$) [31].

The reaction rate can be described by an Arrhenius type law [31]:

$$\frac{d\alpha}{dt} = k(T) \cdot f(\alpha) \tag{2}$$

$$k(T) = Ae^{-\frac{E_a}{RT}} \tag{3}$$

where R is the universal gas constant and T the temperature.

Combining Equations (2) and (3), Equation (4) is obtained:

$$\frac{d\alpha}{dt} = Ae^{-\frac{E_a}{RT}} \cdot f(\alpha) \tag{4}$$

The solution of Equation (4), and thus of the kinetic model, can be carried out using different analytical methods such as model-fitting methods, generalized kinetic models and isoconversional methods, the most used ones for metal oxides in TcES [32].

The most common isoconversional method is the Friedman method [33] and is based on the calculation of the activation energy (Ea) without knowing the kinetic model ($f(\alpha)$) by assuming that the reaction rate is a function of the temperature for an extent of the conversion (α). Equation (4) can be written in its logarithmic form as:

$$ln\left(\frac{d\alpha}{dt}\right) = ln(Af(\alpha)) - \frac{E_a}{RT} \tag{5}$$

A plot of the left term of Equation (5) vs. $1/T$ allows for obtaining Ea from the slope of the curve at different heating/cooling rates. Previous research works say that this method gives more accurate values of activation energy than the Ozawa method [34].

Once the activation energy is calculated, the next step is to obtain the reaction model $f(\alpha)$ by using the master plots method. For this purpose, the value of the activation energy obtained and the experiments carried out with the TGA, at different heating/cooling rates, need to be used. The determination of $f(\alpha)$ is based on the comparison of an experimental master plot with the theoretical ones listed in Table 1.

Table 1. Kinetic models ($f(\alpha)$) for the most representative gas–solid reactions.

Reaction Model	Name	Mechanism	$f(\alpha)$
Reaction order models	F1	Random nucleation followed by an instantaneous growth of nuclei	$1-\alpha$
	F2		$(1-\alpha)^2$
	F3		$(1-\alpha)^3$
Power law	P2	Random nucleation and growth of nuclei through different nucleation and nucleus growth models	$2\alpha^{1/2}$
	P3		$3\alpha^{2/3}$
	P4		$4\alpha^{3/4}$
Avrami–Erofeev	A2		$2(1-\alpha)[-\ln(1-\alpha)]^{1/2}$
	A3		$3(1-\alpha)[-\ln(1-\alpha)]^{2/3}$
	A4		$4(1-\alpha)[-\ln(1-\alpha)]^{3/4}$
Contracting area	R2	Phase boundary-controlled reaction	$2(1-\alpha)^{1/2}$
Contracting volume	R3		$3(1-\alpha)^{2/3}$
Diffusion	D1	Based on the penetration of reactant molecules through a layer of product	$1/2\alpha-1$
	D2		$[-\ln(1-\alpha)]^{-1}$
	D3		$3/2(1-\alpha)^{2/3}[1-(1-\alpha)1/3]^{-1}$
	D4		$3/2[(1-\alpha)-1/3-1]$

To obtain the experimental master plot is necessary to express the kinetic rate equation (Equation (4)) at infinite temperature by introducing the generalized time θ as [35–37]:

$$\theta = \int_0^t exp\left(-\frac{E_a}{RT}\right)dt \quad (6)$$

where θ denotes the reaction time taken to attain a particular α at an infinite temperature [36]. The differentiation of Equation (6) gives [35–37]:

$$\frac{d\theta}{dt} = exp\left(-\frac{E_a}{RT}\right) \quad (7)$$

By combining Equations (4) and (7), the next equation is obtained [35–37]:

$$\frac{d\alpha}{d\theta} = Af(\alpha) \quad (8)$$

Or:

$$\frac{d\alpha}{d\theta} = \frac{d\alpha}{dt}exp\left(\frac{E_a}{RT}\right) \quad (9)$$

Equation (8) can be derived using a reference point at α = 0.5 obtaining [36].

$$\frac{d\alpha/d\theta}{(d\alpha/d\theta)_{\alpha=0.5}} = \frac{f(\alpha)}{f(0.5)} \quad (10)$$

Combining Equations (9) and (10), the final equation for the obtention of the experimental master plot is reached [36]:

$$\frac{d\alpha/d\theta}{(d\alpha/d\theta)_{\alpha=0.5}} = \frac{d\alpha/dt}{(d\alpha/dt)_{\alpha=0.5}}\frac{exp(E_a/RT)}{exp(E_a/RT_{0.5})} \quad (11)$$

The experimental master plot is obtained by representing the right side vs. conversion.

If the experimental master plot does not fit completely with the theoretical models listed in Table 1, the Sestak–Berggren (SB) model [38,39] can be used, which is a mathematical description of most of the possible solid-state reaction mechanisms. In general, it does not provide information about the mechanisms involved in the reaction but allows us to model almost any reaction process [38]. This empirical model can be calculated as:

$$f(\alpha) = \alpha^m(1-\alpha)^n[-ln(1-\alpha)]^p \quad (12)$$

where m, n and p are kinetic exponents that fit with the experimental data.

Once Ea and $f(\alpha)$ are determined, the calculation of the preexponential factor A can be directly carried out by applying Equation (5).

3.2. Results and Discussion

Once the morphological and structural characterization was completed for the mixed oxide $Co_{2.4}Ni_{0.6}O_4$ [24] and for the $Co_{2.4}Ni_{0.6}O_4$ with the addition of 0.5% SiO_2 particles (under review), a kinetic study of the two materials was carried out. In the previous research work, the correct synthesis of the mixed-phase was determined by a deep structural (by XRD), and morphological (by SEM) analysis and an evaluation of the degree of reversibility (TGA measurements) [24].

The interactions between the SiO_2 particles and the $Co_{2.4}Ni_{0.6}O_4$ was studied by in situ XRD demonstrating the absence of interactions between the two materials. The XRD patterns showed no SiO_2 phases as observed in other research works [40] and the unit cell parameter shows no entry of SiO_2 into the nickel cobaltite structure. The morphology of the mixed oxide with the addition of SiO_2 was assessed by means of SEM, showing larger particles than in the case of the $Co_{2.4}Ni_{0.6}O_4$ but less compacted, allowing the oxygen to flow through the material. The cyclability was characterized by TGA, showing that the effect of the particles is not macroscopic in short cycles but helps to keep the reduction

temperatures lower than in the case of nickel cobaltite. A prediction of the material based on the experimental results showed a clear effect on long-term cycling, keeping conversion levels higher than in the case of the $Co_{2.4}Ni_{0.6}O_4$ without any addition.

It should be noted that all the materials used for the development of the kinetic models were examined by EDX to guarantee the desired stoichiometry. The theoretical Co:Ni ratio should be 80:20 in the case of $Co_{2.4}Ni_{0.6}O_4$ and the experimental value obtained was 78.55:21.45, in the range of the experimental error. The results are depicted in Figure 1 and listed in Table 2.

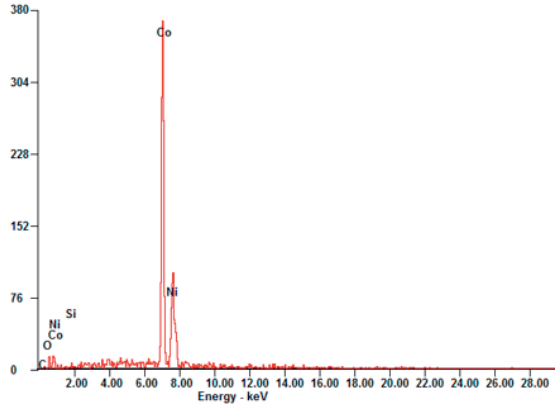

Figure 1. EDX result for the 0.5% $SiO_2/Co_{2.4}Ni_{0.6}O_4$ material.

Table 2. Elemental composition of 0.5% $SiO_2/Co_{2.4}Ni_{0.6}O_4$ obtained in EDX.

Element	Wt%	At%
SiK	0.00	0.00
NiK	78.55	78.49
CoK	21.45	21.51

The materials used underwent a previous thermal treatment based on 50 cycles in TGA to analyze the definitive kinetics of the material once it had stabilized in terms of grain size, morphology, etc.

3.2.1. Reduction Reaction Rate

For the obtainment of the kinetic parameters of the reduction reaction rate of $Co_{2.4}Ni_{0.6}O_4$ and 0.5% $SiO_2/Co_{2.4}Ni_{0.6}O_4$ and to study the effect of the silica particles in the kinetics of the mixed oxide, different heating/cooling ramped experiments were performed in a TGA. The ramps used were: 5, 10, 15 and 20 °C/min. All the experiments were performed under an N_2 atmosphere to avoid the influence of the oxygen pressure (pO_2) in the analysis.

Figure 2 shows that the mixed oxide with the addition of particles reaches the total conversions faster than the mixed oxide without the addition in most of the heating ramps. The bigger difference is shown in the 5 °C/min heating ramp, in which the pure material takes 27 min to reach the total conversion and the added one only 22 min. In the initial part of the experiment, it can be observed that the conversion ratio of the 10 °C/min experiment is slightly higher than the one of the 15 °C/min experiment. This effect is attributed to the experimental error of the instrument as the conversion values in low conversion ratios are similar.

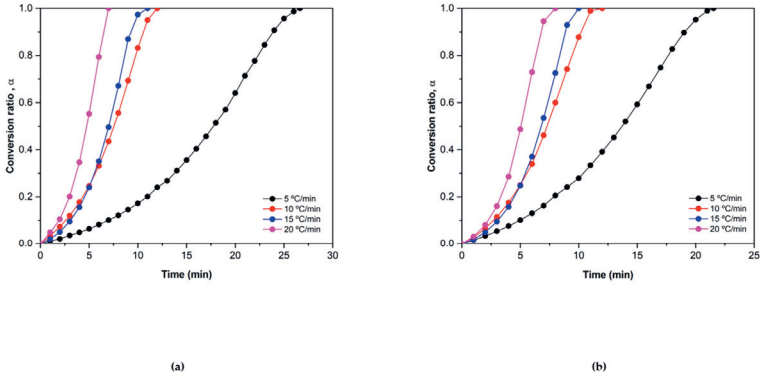

Figure 2. α vs. time plots of the reduction reaction of (**a**) $Co_{2.4}Ni_{0.6}O_4$ and (**b**) 0.5% $SiO_2/Co_{2.4}Ni_{0.6}O_4$.

The Friedman method was used for obtaining the activation energy. The data taken from TGA were treated following Equation (5). Plotting the left term of Equation (5) vs. the inverse of the temperature (1000/*T*) at different extents of reaction (*α*) and heating rates, allows us to determine the *Ea* of the material by measuring the slope of the curves.

It should be noted that for the calculation of the activation energies, the trendlines with R^2 lower than 0.97 have not been considered. In this case, the two trendlines obtained in the conversion ratio of 0.2 were discarded as their R^2 value was 0.96 for $Co_{2.4}Ni_{0.6}O_4$ and 0.71 for 0.5% $SiO_2/Co_{2.4}Ni_{0.6}O_4$.

The values of the average activation energy obtained from the slope of the curves of Figure 3 are: 450 ± 47 kJ/mol in the case of the $Co_{2.4}Ni_{0.6}O_4$ and 449 ± 32 kJ/mol for the added 0.5% $SiO_2/Co_{2.4}Ni_{0.6}O_4$. Previous research works have given very different *Ea* values for the pure Co_3O_4. Muroyama et al. report a value of 247 kJ/mol [25], while Wong et al. report 960 kJ/mol [26] and Hasanvard et al. report 158.99 kJ/mol as the maximum value for a determined α [29]. However, some authors state that the activation energy can be highly dependent on the experimental conditions, sample preparation and determination of the reaction mechanism [25]. Previous research works have determined the activation energies of some doped Co_3O_4 materials too. Wong et al. reported an activation energy of 731 kJ/mol in the case of the 5% Al_2O_3/Co_3O_4 [26] while Hasanvard et al. reported 238 kJ/mol [29] as the maximum activation energy for the same material.

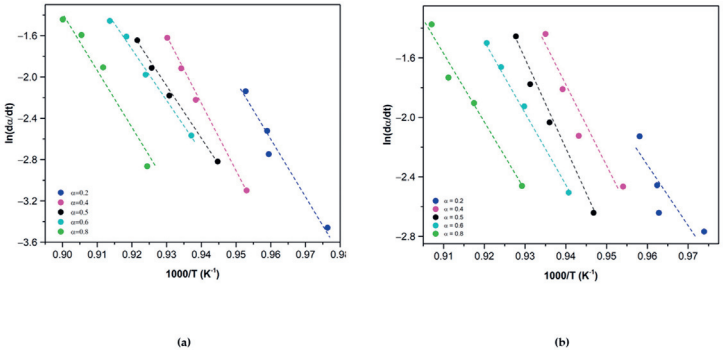

Figure 3. Friedman plot for the reduction of (**a**) $Co_{2.4}Ni_{0.6}O_4$ and (**b**) 0.5% $SiO_2/Co_{2.4}Ni_{0.6}O_4$ for different conversion ratios.

Comparing the activation energy obtained in this work for $Co_{2.4}Ni_{0.6}O_4$ and the values obtained in other research works for Co_3O_4 and doped Co_3O_4, the results are in the interval of activation energies calculated by the other authors. Taking into account that the reduction temperature of the mixed nickel cobaltite is lower than the reduction temperature of the pure cobalt oxide, the activation energy should be lower too.

Regarding the comparison between $Co_{2.4}Ni_{0.6}O_4$ and 0.5% $SiO_2/Co_{2.4}Ni_{0.6}O_4$, the same *Ea* was obtained and the deviation was quite similar for the two materials, as can be seen in Figure 4.

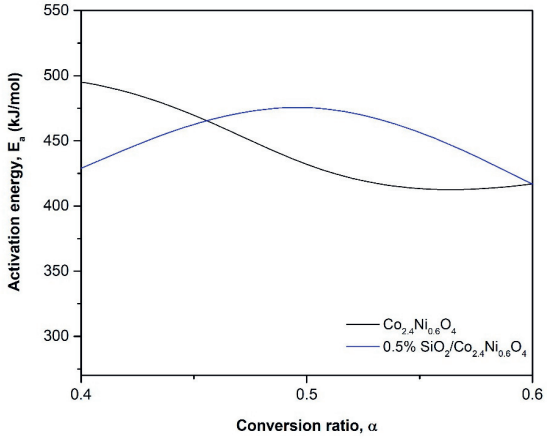

Figure 4. Evolution of the activation energy (*Ea*) with the reduction conversion ratios (*α*).

Once the average activation energy was determined, the next step was to determine the reaction mechanism using the master plot method. Introducing the activation energy obtained in Equation (11) allows us to obtain an experimental master plot and makes its comparison with the theoretical models listed in Table 1 possible. The results are depicted in Figure 5.

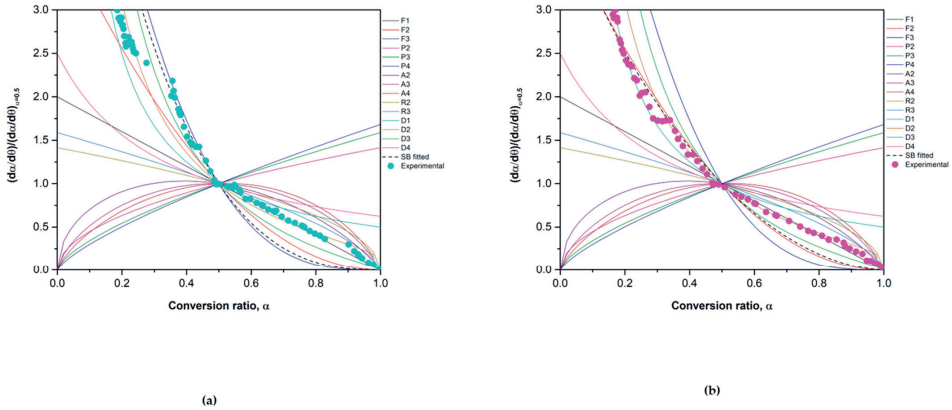

Figure 5. Theoretical master plots, SB fitted function and experimental results of (**a**) $Co_{2.4}Ni_{0.6}O_4$ and (**b**) 0.5% $SiO_2/Co_{2.4}Ni_{0.6}O_4$ using a heating ramp of 20 °C/min.

The $Co_{2.4}Ni_{0.6}O_4$ material shows a different behavior depending on the conversion ratio. When α is lower than 0.5, the experimental data fit partially with the model F3 and for an α higher than 0.5, the model F1 correctly describes the behavior of $Co_{2.4}Ni_{0.6}O_4$. These models describe instantaneous nucleation and unidimensional growth [36]. The SB model was used to define the model of the whole experiment but the only successful fitting corresponded to the α between 0.3 and 0.5, by using the exponents $m = 2$, $n = 1.7$ and $p = -2.1$, obtaining the SB equation:

$$f(\alpha) = \alpha^2(1-\alpha)^{1.7}[-ln(1-\alpha)]^{-2.1} \quad (13)$$

Regarding the 0.5% $SiO_2/Co_{2.4}Ni_{0.6}O_4$ material, when α is lower than 0.2 the best theoretical model is D1, but for α values between 0.3 and 1, the experimental data fit well with a D2 model. In any case, these two theoretical models belong to the group of diffusion models, which are quite common in this type of material. The SB model was used to obtain an accurate model of the whole reaction extent. The results show that the fitting is correct when α is lower than 0.5 and the exponents are: $m = 0.81$, $n = 1.45$, and $p = -0.87$, obtaining the SB equation:

$$f(\alpha) = \alpha^{0.81}(1-\alpha)^{1.45}[-ln(1-\alpha)]^{-0.87} \quad (14)$$

The fitting problems for the two materials are due to the oscillation that the *Ea* has in the whole range of conversions, as is depicted in Figure 4. If the activation energy is roughly constant in all the conversion ranges and there are no shoulders in the reaction rate curve, the process can be fitted by a single-step model. If not, depending on the conversion, different models describe the reaction at different stages [31].

Once the $f(\alpha)$ was defined, the "kinetic triplet" could be completed by calculating the preexponential factor (A) from the intercept of Equation (5). In the case of nickel cobaltite, the A is 9.65·1019 min^{-1}, while in nickel cobaltite with an addition, the A is 6.37·1019 min^{-1}.

To sum up, the kinetic triplets obtained for the $Co_{2.4}Ni_{0.6}O_4$ and 0.5% $SiO_2/Co_{2.4}Ni_{0.6}O_4$ materials are listed in Table 3.

Table 3. Kinetic triplet values describing the reduction reaction of the $Co_{2.4}Ni_{0.6}O_4$ and 0.5% $SiO_2/Co_{2.4}Ni_{0.6}O_4$ materials and activation energy values of pure Co_3O_4 and 5% Al_2O_3/Co_3O_4.

Material	*Ea* (kJ/mol)	$f(\alpha)$			A (min^{-1})
		m	n	p	
$Co_{2.4}Ni_{0.6}O_4$	450 ± 47	2	1.7	−2.1	$9.65{\cdot}10^{19}$
0.5% $SiO_2/Co_{2.4}Ni_{0.6}O_4$	449 ± 32	0.81	1.45	−0.87	$6.37{\cdot}10^{19}$
Co_3O_4 [25]	247	-	-	-	-
Co_3O_4 [26]	960	-	-	-	-
5% Al_2O_3/Co_3O_4 [29]	238	-	-	-	-
5% Al_2O_3/Co_3O_4 [26]	731	-	-	-	-

Thus, the equation describing the reduction reaction for the $Co_{2.4}Ni_{0.6}O_4$ is:

$$r_{red} = \frac{d\alpha_{red}}{dt} = 9.65{\cdot}10^{19} min^{-1} e^{\left(\frac{-449.82\ kJ/mol}{RT}\right)} \alpha_{red}^2 (1-\alpha_{red})^{1.7}[-ln(1-\alpha_{red})]^{-2.1} \quad (15)$$

And the resulting equation describing the model of the reduction reaction for the added 0.5% $SiO_2/Co_{2.4}Ni_{0.6}O_4$ material is:

$$r_{red} = \frac{d\alpha_{red}}{dt} = 6.37{\cdot}10^{19} min^{-1} e^{\left(\frac{-449.22\ kJ/mol}{RT}\right)} \alpha_{red}^{0.81} (1-\alpha_{red})^{1.45}[-ln(1-\alpha_{red})]^{-0.87} \quad (16)$$

3.2.2. Oxidation Reaction Rate

For the obtention of the oxidation kinetic triplet for the $Co_{2.4}Ni_{0.6}O_4$ and 0.5% $SiO_2/Co_{2.4}Ni_{0.6}O_4$ materials, isothermal programs ranging from 600 °C to 800 °C

were performed under an O_2 atmosphere (pO_2 = 1). To prevent any oxidation before doing the experiments, all the materials were firstly reduced under N_2 conditions and when the temperature of the experiment was stabilized, the atmosphere was changed to O_2 for completing the oxidation. It should be noted that in the very beginning (first minute) of the experiment, the kinetics could be slightly influenced by the gas atmosphere change from N_2 to O_2.

The conversion ratio as a function of the time is presented in Figure 6 for each isothermal experiment.

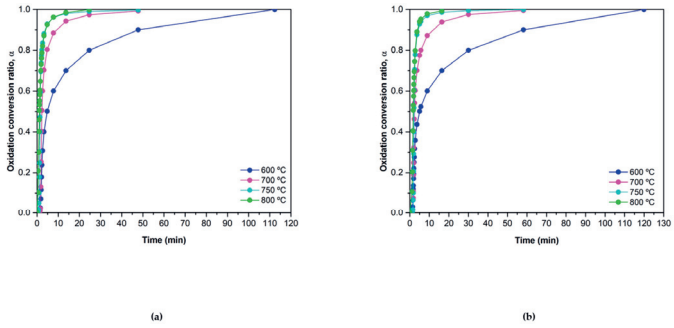

Figure 6. α vs. time plots of the oxidation reaction at pO_2 = 1 of (**a**) $Co_{2.4}Ni_{0.6}O_4$ and (**b**) 0.5% $SiO_2/Co_{2.4}Ni_{0.6}O_4$.

When the model design is performed by performing isothermal experiments instead of dynamic ones, it is not possible to follow the protocol previously followed for the obtention of the model of the reduction reaction, as in this case the temperature is constant and the activation energy cannot be calculated from Equation (5) directly. In this case, it is necessary to apply the master plots method without the *Ea* [31].

The theoretical master plot models are listed in Table 1. The obtention of the experimental master plots was carried out by using Equation (11) setting the term related to the temperatures and the activation energy as a constant:

$$\frac{d\alpha/d\theta}{(d\alpha/d\theta)_{\alpha=0.5}} = \frac{d\alpha/dt}{(d\alpha/dt)_{\alpha=0.5}} \quad (17)$$

The results are shown below in Figure 7:

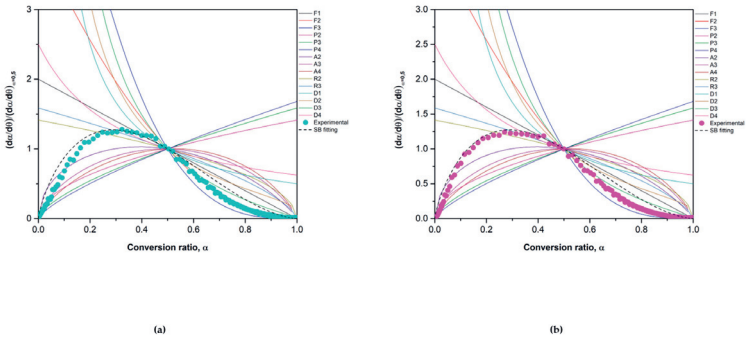

Figure 7. Comparison between theoretical models, experimental results and SB fitting of the experimental results for (**a**) $Co_{2.4}Ni_{0.6}O_4$ and (**b**) 0.5% $SiO_2/Co_{2.4}Ni_{0.6}O_4$.

The experimental data obtained for $Co_{2.4}Ni_{0.6}O_4$ do not present exactly the same tendency as any theoretical model listed in Table 1. In this case, both the material without addition and the material with the addition of silica shows a very similar experimental trend. Both materials fit well with the F2 model for α above 0.5. The F2 theoretical model corresponds to a reaction of second-order, where random nucleation is followed by an instantaneous growth of nuclei [32]. In order to obtain a model that fits well with the whole experimental data, the SB equation was used [38]. The behavior of $Co_{2.4}Ni_{0.6}O_4$ and 0.5% $SiO_2/Co_{2.4}Ni_{0.6}O_4$ is so similar that the resulting exponents in the fit were the same for both materials. The exponents obtained were $m = 2.8$, $n = 1$ and $p = -2.01$. The SB equation obtained for both materials was:

$$f(\alpha) = \alpha^{2.8}(1-\alpha)^{1}[-ln(1-\alpha)]^{-2.01} \quad (18)$$

In the case of the $Co_{2.4}Ni_{0.6}O_4$ (Figure 7A), the SB equation fits with the experimental data in the α range from 0.25 to 0.5. In the rest of the range, the empirical method is close to the experimental results but does not fit completely well. This is a detriment when calculating the activation energies of the materials since the calculated $f(\alpha)$ has to be used. In the case of the added 0.5% $SiO_2/Co_{2.4}Ni_{0.6}O_4$ material (Figure 7B), the empirical calculation fits well with the experimental data from $\alpha = 0$ to $\alpha = 0.5$. The result of the rest of the range is quite similar but it does not fit perfectly. However, the oxidation reaction was further modeled using the values obtained for $f(\alpha)$, as it was the model that better described the whole experiment.

So then, for the obtention of an average value of *Ea*, the isoconversional method of Friedman was applied [33]. The isothermal experiments used for the calculation of the reaction model under the O_2 atmosphere were used for the obtention of the Friedman plots.

It is worth mentioning that the trendlines observed in Figure 8 were obtained using four points, each one obtained from a different temperature isothermal analysis. In some cases, in the figure, one of the points overlapped for different conversion ratios.

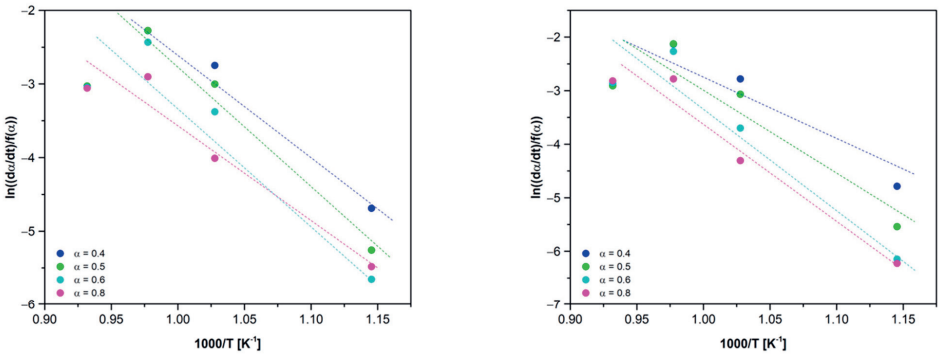

Figure 8. Friedman plots of (**a**) $Co_{2.4}Ni_{0.6}O_4$ and (**b**) 0.5% $SiO_2/Co_{2.4}Ni_{0.6}O_4$ at different α.

The average oxidation activation energy obtained for the $Co_{2.4}Ni_{0.6}O_4$ material was 100 ± 22 kJ/mol. The results obtained in this research work are quite similar to the ones reported in the bibliography regarding the Co_3O_4. Muroyama et al. report an oxidation activation energy of 58.07 ± 0.26 kJ/mol [25]. In the case of Reti et al., the oxidation activation energy obtained was 60.19 kJ/mol [41] and in the work of Tomlinson and

Esterlow, the value was 80 ± 15 kJ/mol [42]. Regarding the doped Co_3O_4, Wong et al. reported an oxidation activation energy of 165 kJ/mol for the material 5%Al_2O_3/Co_3O_4 [26]. The result obtained in this research work is in between the values previously reported for pure and doped cobalt oxides. Regarding the 0.5% $SiO_2/Co_{2.4}Ni_{0.6}O_4$ material, an average oxidation *Ea* of 124 ± 36 kJ/mol was obtained. It is worth mentioning that the method selected for the obtention of the kinetic model can lead to different values of activation energy. The model $f(\alpha)$ selected previously can affect the results obtained too.

As with what happened in the reduction reaction, the activation energy of the oxidation reaction changes for each conversion ratio, as it can be observed in Figure 9. In the oxidation reaction, the two materials fitted well with the theoretical model F2 but only for a concrete conversion range, so the change of activation energy fits well with the result obtained for the model.

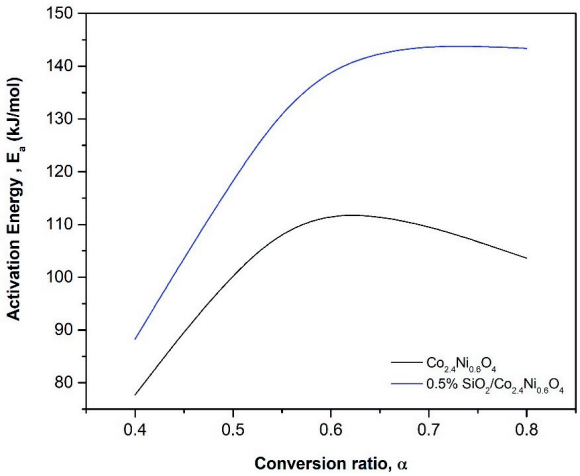

Figure 9. Evolution of the activation energy (*Ea*) with the oxidation ratio (α).

The preexponential factor (*A*) was calculated from the order at the origin of the Friedman plots shown in Figure 8 and the results obtained were 7·103 min^{-1} for the $Co_{2.4}Ni_{0.6}O_4$ and 7.81·105 min^{-1} for the 0.5% $SiO_2/Co_{2.4}Ni_{0.6}O_4$.

To sum up, the "kinetic triplet" obtained for the oxidation reaction of the $Co_{2.4}Ni_{0.6}O_4$ and $SiO_2/Co_{2.4}Ni_{0.6}O_4$ materials are listed in Table 4:

Table 4. Kinetic triplet values describing the oxidation reaction of the $Co_{2.4}Ni_{0.6}O_4$ and 0.5% $SiO_2/Co_{2.4}Ni_{0.6}O_4$ materials and activation energy values of pure Co_3O_4 and 5% Al_2O_3/Co_3O_4.

Material	*Ea* (kJ/mol)	$f(\alpha)$			*A* (min^{-1})
		m	*n*	*p*	
$Co_{2.4}Ni_{0.6}O_4$	100 ± 22	2.8	1	−2.01	$7{\cdot}10^3$
0.5% $SiO_2/Co_{2.4}Ni_{0.6}O_4$	134 ± 36	2.8	1	−2.01	$7.81{\cdot}10^5$
Co_3O_4 [25]	58 ± 0.26	-	-	-	-
Co_3O_4 [41]	60	-	-	-	-
5% Al_2O_3/Co_3O_4 [26]	165	-	-	-	-

Thus, the equation describing the oxidation reaction for the $Co_{2.4}Ni_{0.6}O_4$ is:

$$r_{ox} = \frac{d\alpha_{ox}}{dt} = 7{\cdot}10^3 min^{-1} e^{\left(\frac{-100\ kJ/mol}{RT}\right)} \alpha_{ox}^{2.8} (1-\alpha_{ox})^1 [-ln(1-\alpha_{ox})]^{-2.01} \quad (19)$$

And the resulting equation describing the model of the oxidation reaction for the added 0.5% SiO_2/ $Co_{2.4}Ni_{0.6}O_4$ material is:

$$r_{ox} = \frac{d\alpha_{ox}}{dt} = 7.81 \cdot 10^5 \text{min}^{-1} e^{\left(\frac{-124\,\text{kJ/mol}}{RT}\right)} \alpha_{ox}^{2.8} (1-\alpha_{ox})^1 [-ln(1-\alpha_{ox})]^{-2.01} \quad (20)$$

The concordance of the experimental results and the theoretical values were assessed by using the OCTAVE software. The theoretical equations (Equations (15), (16), (19) and (20)) were implemented in the program to obtain the predicted behavior of the materials and were compared with the experimental data obtained in the TGA. Figures 10 and 11 show this comparison for the reduction and oxidation reactions, respectively.

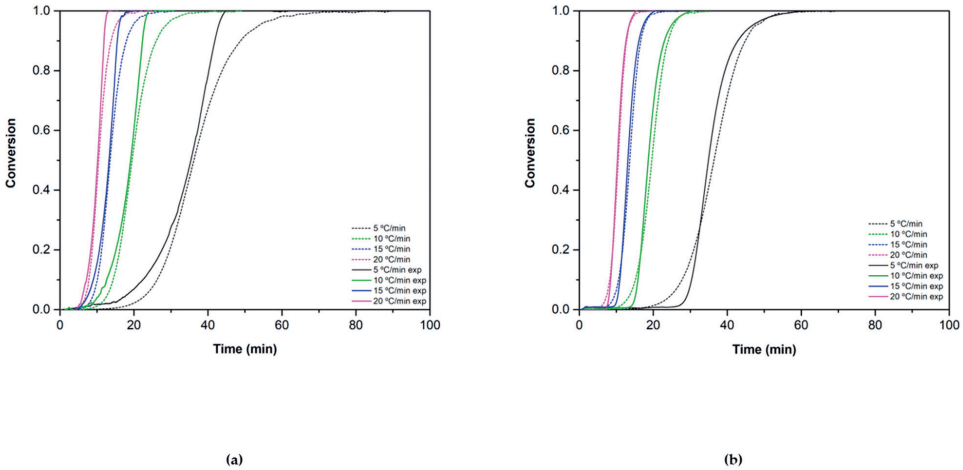

Figure 10. Reduction conversion validation for (**a**) $Co_{2.4}Ni_{0.6}O_4$ and (**b**) 0.5% SiO_2/$Co_{2.4}Ni_{0.6}O_4$. The dotted lines correspond to the theoretical values and the solid ones to the experimental ones.

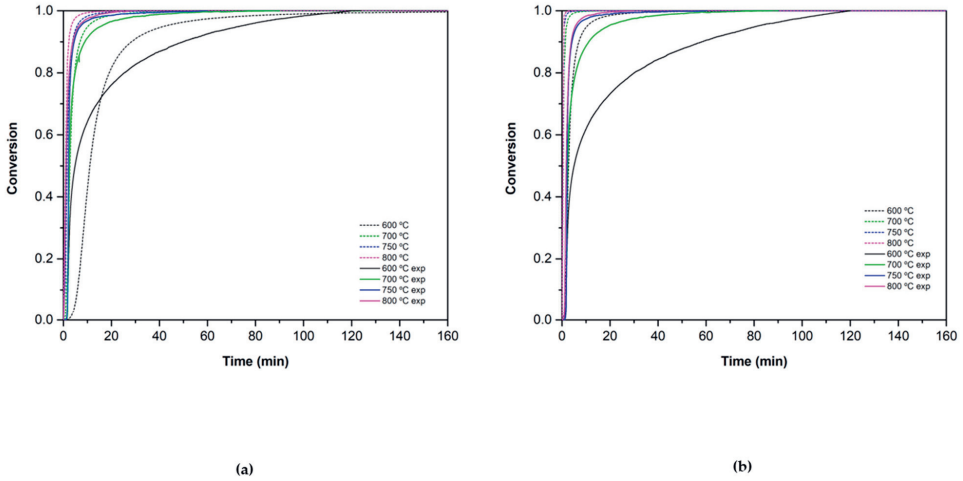

Figure 11. Oxidation conversion validation for (**a**) $Co_{2.4}Ni_{0.6}O_4$ and (**b**) 0.5% SiO_2/ $Co_{2.4}Ni_{0.6}O_4$. The dotted lines correspond to the theoretical values and the solid ones to the experimental ones.

In the case of $Co_{2.4}Ni_{0.6}O_4$ (Figure 10A), the theoretical values obtained fit well with the experimental data until conversion ratios of 0.8, where a drop in the speed in the model is observed. This may be because, at conversion ratios above 0.5, the nucleation and growth model governs the course of the reaction, so the SB equation does not fully define the trend of the experimental data. In the case of the 0.5% $SiO_2/Co_{2.4}Ni_{0.6}O_4$ (Figure 10B), the experimental data fit well with the theoretical one as diffusion mechanisms govern the whole reaction extent range. For both cases, the calculated model does not fit completely with the experimental data using a heating ramp of 5 °C/min. In this case, the heating ramp could be too slow to observe the normal course of the reaction.

The oxidation reaction validation is shown in Figure 11. Experimental and theoretical data of $Co_{2.4}Ni_{0.6}O_4$ show a good concordance in all the reaction extent. In the case of the added 0.5% $SiO_2/Co_{2.4}Ni_{0.6}O_4$, the theoretical trend corresponds well until conversion values of 0.8. The conversion ranges from 0.8 to 1 are not fully adjusted with the SB equation. In both materials, different behavior is observed between theoretical and experimental results at a temperature of 600 °C. As was the case with the reduction step, the isotherm at 600 °C may not have a fully adequate temperature for the normal course of the reaction without interference or limitations from the process temperature.

4. Conclusions

In this work, the development of a kinetic model of $Co_{2.4}Ni_{0.6}O_4$ and of 0.5% $SiO_2/Co_{2.4}Ni_{0.6}O_4$ materials for thermochemical energy storage applications was firstly reported. The results obtained for these materials were compared with the data from the pure cobalt oxide available from previous research works.

In the reduction reaction, the activation energy of the two materials (450 kJ/kg for $Co_{2.4}Ni_{0.6}O_4$ and 449 kJ/kg for 0.5% $SiO_2/Co_{2.4}Ni_{0.6}O_4$) is in the range of the pure Co_3O_4 one (158–960 kJ/kg), so neither the nickel substitution in the cobalt oxide structure nor the addition of SiO_2 particles affects this parameter.

The theoretical models $f(\alpha)$ fitting with the reduction experimental data are different nucleation and growth mechanisms in the case of the $Co_{2.4}Ni_{0.6}O_4$ and different diffusion models in the case of 0.5% $SiO_2/Co_{2.4}Ni_{0.6}O_4$.

In the oxidation reaction, the activation energy of the two materials (99 kJ/kg for $Co_{2.4}Ni_{0.6}O_4$ and 123 kJ/kg for 0.5% $SiO_2/Co_{2.4}Ni_{0.6}O_4$) is in agreement with the values published in regard to other mixed oxides (165 kJ/kg for 5% Al_2O_3/Co_3O_4) but higher than the value reported in the bibliography for Co_3O_4 (~60 kJ/kg).

The behavior of the two materials fits with the same theoretical models $f(\alpha)$ describing nucleation and growth mechanisms when the conversion ratios are higher than 0.5. The SB equation was used to obtain the model of the whole experiment.

The developed model confirms a good agreement between the experimental data and the theoretical ones in most of the measurement conditions.

Author Contributions: Conceptualization, M.H., D.B. and S.D.; methodology, Y.P.-N., S.D., E.A. and E.P.d.B.; software, Y.P.-N. and J.-L.D.; validation, Y.P.-N., J.-L.D., S.D., E.A. and E.P.d.B.; formal analysis, Y.P.-N., S.D. and E.A.; investigation, Y.P.-N.; resources, S.D., E.A. and E.P.d.B.; data curation, Y.P.-N., D.B. and S.D.; writing—original draft preparation, Y.P.-N.; writing—review and editing, Y.P.-N., D.B. and S.D.; visualization, M.H.; supervision, S.D., E.A., E.P.d.B. and M.H.; project administration, S.D. and M.H.; funding acquisition, S.D., E.A. and E.P.d.B. All authors have read and agreed to the published version of the manuscript.

Funding: This research was funded by the Basque Government, grant number KK-2019/00097 in the project ELKARTEK CICe2019.

Institutional Review Board Statement: Not applicable.

Informed Consent Statement: Not applicable.

Acknowledgments: The Basque Government (Elkartek CICe2019, KK-2019/00097) are acknowledged for the financial support of this work. The authors express their sincere gratitude to Cristina Luengo for her technical support.

Conflicts of Interest: The authors declare no conflict of interest.

References

1. Zhou, X.; Mahmood, M.; Chen, J.; Yang, T.; Xiao, G.; Ferrari, M.L. Validated Model of Thermochemical Energy Storage Based on Cobalt Oxides. *Appl. Therm. Eng.* **2019**, *159*, 113965. [CrossRef]
2. Mahmood, M.; Traverso, A.; Traverso, A.N.; Massardo, A.F.; Marsano, D.; Cravero, C. Thermal Energy Storage for CSP Hybrid Gas Turbine Systems: Dynamic Modelling and Experimental Validation. *Appl. Energy* **2018**, *212*, 1240–1251. [CrossRef]
3. Dizaji, H.B.; Hosseini, H. A Review of Material Screening in Pure and Mixed-Metal Oxide Thermochemical Energy Storage (TCES) Systems for Concentrated Solar Power (CSP) Applications. *Renew. Sustain. Energy Rev.* **2018**, *98*, 9–26. [CrossRef]
4. Ehrhart, B.; Coker, E.; Siegel, N.; Weimer, A. Thermochemical Cycle of a Mixed Metal Oxide for Augmentation of Thermal Energy Storage in Solid Particles. *Energy Procedia* **2013**, *49*, 762–771. [CrossRef]
5. Bruno, F.; Belusko, M.; Liu, M.; Tay, N.H.S. *Using Solid-Liquid Phase Change Materials (PCMs) in Thermal Energy Storage Systems*; Woodhead Publishing Limited: Thorston, UK, 2014; ISBN 9781782420965.
6. Wu, S.; Zhou, C.; Doroodchi, E.; Nellore, R.; Moghtaderi, B. A Review on High-Temperature Thermochemical Energy Storage Based on Metal Oxides Redox Cycle. *Energy Convers. Manag.* **2018**, *168*, 421–453. [CrossRef]
7. Liu, M.; Steven Tay, N.H.; Bell, S.; Belusko, M.; Jacob, R.; Will, G.; Saman, W.; Bruno, F. Review on Concentrating Solar Power Plants and New Developments in High Temperature Thermal Energy Storage Technologies. *Renew. Sustain. Energy Rev.* **2016**, *53*, 1411–1432. [CrossRef]
8. Agrafiotis, C.; Roeb, M.; Schmücker, M.; Sattler, C. Exploitation of Thermochemical Cycles Based on Solid Oxide Redox Systems for Thermochemical Storage of Solar Heat. Part 1: Testing of Cobalt Oxide-Based Powders. *Sol. Energy* **2014**, *102*, 189–211. [CrossRef]
9. Myung, J.H.; Shin, T.H.; Huang, X.; Carins, G.; Irvine, J.T.S. Enhancement of Redox Stability and Electrical Conductivity by Doping Various Metals on Ceria, Ce1-XMxO2-δ (M = Ni, Cu, Co, Mn, Ti, Zr). *Int. J. Hydrogen Energy* **2015**, *40*, 12003–12008. [CrossRef]
10. Agrafiotis, C.; Roeb, M.; Schmücker, M.; Sattler, C. Exploitation of Thermochemical Cycles Based on Solid Oxide Redox Systems for Thermochemical Storage of Solar Heat. Part 2: Redox Oxide-Coated Porous Ceramic Structures as Integrated Thermochemical Reactors/Heat Exchangers. *Sol. Energy* **2015**, *114*, 440–458. [CrossRef]
11. Agrafiotis, C.; Tescari, S.; Roeb, M.; Schmücker, M.; Sattler, C. Exploitation of Thermochemical Cycles Based on Solid Oxide Redox Systems for Thermochemical Storage of Solar Heat. Part 3: Cobalt Oxide Monolithic Porous Structures as Integrated Thermochemical Reactors/Heat Exchangers. *Sol. Energy* **2015**, *114*, 459–475. [CrossRef]
12. Abedin, A.H. A Critical Review of Thermochemical Energy Storage Systems. *Open Renew. Energy J.* **2011**, *4*, 42–46. [CrossRef]
13. Carrillo, A.J.; Moya, J.; Bayón, A.; Jana, P.; De La Peña O'Shea, V.A.; Romero, M.; Gonzalez-Aguilar, J.; Serrano, D.P.; Pizarro, P.; Coronado, J.M. Thermochemical Energy Storage at High Temperature via Redox Cycles of Mn and Co Oxides: Pure Oxides versus Mixed Ones. *Sol. Energy Mater. Sol. Cells* **2014**, *123*, 47–57. [CrossRef]
14. Block, T.; Schmücker, M. Metal Oxides for Thermochemical Energy Storage: A Comparison of Several Metal Oxide Systems. *Sol. Energy* **2016**, *126*, 195–207. [CrossRef]
15. Carrillo, A.J.; Serrano, D.P.; Pizarro, P.; Coronado, J.M. Thermochemical Heat Storage at High Temperatures Using Mn_2O_3/Mn_3O_4 System: Narrowing the Redox Hysteresis by Metal Co-Doping. *Energy Procedia* **2015**, *73*, 263–271. [CrossRef]
16. Carrillo, A.J.; Sastre, D.; Serrano, D.P.; Pizarro, P.; Coronado, J.M. Revisiting the BaO2/BaO Redox Cycle for Solar Thermochemical Energy Storage. *Phys. Chem. Chem. Phys.* **2016**, *18*, 8039–8048. [CrossRef] [PubMed]
17. Block, T.; Knoblauch, N.; Schmücker, M. The Cobalt-Oxide/Iron-Oxide Binary System for Use as High Temperature Thermochemical Energy Storage Material. *Thermochim. Acta* **2014**, *577*, 25–32. [CrossRef]
18. Wong, B. Energy, U.S.D. of Thermochemical Heat Storage for Concentrated Solar Power, Thermochemical System Reactor Design for Thermal Energy Storage. *Ind. Eng. Chem.* **2011**, *19*, 594–596.
19. Roßkopf, C.; Haas, M.; Faik, A.; Linder, M.; Wörner, A. Improving Powder Bed Properties for Thermochemical Storage by Adding Nanoparticles. *Energy Convers. Manag.* **2014**, *86*, 93–98. [CrossRef]
20. Bielsa, D.; Zaki, A.; Arias, P.L.; Faik, A. Improving the Redox Performance of Mn_2O_3/Mn_3O_4 Pair by Si Doping to Be Used as Thermochemical Energy Storage for Concentrated Solar Power Plants. *Sol. Energy* **2020**, *204*, 144–154. [CrossRef]
21. Hill, R.J.; Craig, J.R.; Gibbs, G.V. Systematics of the Spinel Structure Type. *Phys. Chem. Miner.* **1979**, *4*, 317–339. [CrossRef]
22. King, W.J.; Tseung, A.C.C. The Reduction of Oxygen on Nickel-Cobalt Oxides—II. *Electrochim. Acta* **1974**, *19*, 493–498. [CrossRef]
23. Klissurski, D.; Uzunova, E. Synthesis and Features of Binary Cobaltite Spinels. *J. Mater. Sci.* **1994**, *29*, 285–293. [CrossRef]
24. Portilla-Nieto, Y.; Zaki, A.; Vidal, K.; Hernaiz, M.; Aranzabe, E.; Doppiu, S.; Faik, A. Development of Co3-XNixO4 Materials for Thermochemical Energy Storage at Lower Red-Ox Temperature. *Sol. Energy Mater. Sol. Cells* **2021**, *230*, 111194. [CrossRef]

25. Muroyama, A.P.; Schrader, A.J.; Loutzenhiser, P.G. Solar Electricity via an Air Brayton Cycle with an Integrated Two-Step Thermochemical Cycle for Heat Storage Based on Co3O4/CoO Redox Reactions II: Kinetic Analyses. *Sol. Energy* **2015**, *122*, 409–418. [CrossRef]
26. Wong, B. *Thermochemical Heat Storage for Concentrated Solar Power: Thermochemical System Reactor Design for Thermal Energy Storage, Phase II Final Report for the Period September 30, 2008 through April 30, 2011*; U.S. Department of Energy: Washington, DC, USA, 2011.
27. Hutchings, K.N.; Wilson, M.; Larsen, P.A.; Cutler, R.A. Kinetic and Thermodynamic Considerations for Oxygen Absorption/Desorption Using Cobalt Oxide. *Solid State Ion.* **2006**, *177*, 45–51. [CrossRef]
28. Pagkoura, C.; Karagiannakis, G.; Zygogianni, A.; Lorentzou, S.; Kostoglou, M.; Konstandopoulos, A.G.; Rattenburry, M.; Woodhead, J.W. Cobalt Oxide Based Structured Bodies as Redox Thermochemical Heat Storage Medium for Future CSP Plants. *Sol. Energy* **2014**, *108*, 146–163. [CrossRef]
29. Hasanvand, A.; Pourabdoli, M. Theoretical thermodynamics and practical kinetics studies of oxygen desorption from Co_3O_4-5 wt% Al_2O_3 and Co_3O_4-5 wt% Y_2O_3 composites. *J. Part. Sci. Technol.* **2019**, *5*, 13–21. [CrossRef]
30. Carrillo, A.J.; Serrano, D.P.; Pizarro, P.; Coronado, J.M. Understanding Redox Kinetics of Iron-Doped Manganese Oxides for High Temperature Thermochemical Energy Storage. *J. Phys. Chem. C* **2016**, *120*, 27800–27812. [CrossRef]
31. Vyazovkin, S.; Burnham, A.K.; Criado, J.M.; Pérez-Maqueda, L.A.; Popescu, C.; Sbirrazzuoli, N. ICTAC Kinetics Committee Recommendations for Performing Kinetic Computations on Thermal Analysis Data. *Thermochim. Acta* **2011**, *520*, 1–19. [CrossRef]
32. Bielsa, D.; Zaki, A.; Arias, P.L.; Faik, A. Development of a Kinetic Reaction Model for Reduction and Oxidation of Si Doped Mn_2O_3 for Thermochemical Energy Storage in Concentrated Solar Power Plants. *J. Energy Storage* **2021**, *43*, 103271. [CrossRef]
33. Friedman, H.L. Kinetics of Thermal Degradation of Char-Forming Plastics from Thermogravimetry. Application to a Phenolic Plastic. *J. Polym. Sci. Part C Polym. Symp.* **2007**, *6*, 183–195. [CrossRef]
34. Criado, J.M.; Sánchez-Jiménez, P.E.; Pérez-Maqueda, L.A. Critical Study of the Isoconversional Methods of Kinetic Analysis. *J. Therm. Anal. Calorim.* **2008**, *92*, 199–203. [CrossRef]
35. Ozawa, T. Kinetic Analysis of Derivative Curves in Thermal Analysis. *J. Therm. Anal.* **1970**, *2*, 301–324. [CrossRef]
36. Gotor, F.J.; José, M.C.; Malek, J.; Koga, N. Kinetic Analysis of Solid-State Reactions: The Universality of Master Plots for Analyzing Isothermal and Nonisothermal Experiments. *J. Phys. Chem. A* **2000**, *104*, 10777–10782. [CrossRef]
37. Ozawa, T. Non-Isothermal Kinetics and Generalized Time. *Thermochim. Acta* **1986**, *100*, 109–118. [CrossRef]
38. Šesták, J.; Berggren, G. Study of the Kinetics of the Mechanism of Solid-State Reactions at Increasing Temperatures. *Thermochim. Acta* **1971**, *3*, 1–12. [CrossRef]
39. Criado, J.M.; Málek, J.; Gotor, F.J. The Applicability of the Šesták-Berggren Kinetic Equation in Constant Rate Thermal Analysis (CRTA). *Thermochim. Acta* **1990**, *158*, 205–213. [CrossRef]
40. Ali, G.A.M.; Fouad, O.A.; Makhlouf, S.A.; Yusoff, M.M.; Chong, K.F. Co3O4/SiO2 Nanocomposites for Supercapacitor Application. *J. Solid State Electrochem.* **2014**, *18*, 2505–2512. [CrossRef]
41. Reti, A.R.; Brian, P.L.T.; Hoagland, L.C. Short-time, High Temperature Oxidation of Cobaltous Oxide. *Ind. Eng. Chem. Process Des. Dev.* **2000**, *5*, 171–177. [CrossRef]
42. Tomlinson, W.J.; Easterlow, A. Kinetics and Microstructure of Oxidation of CoO to Co3O4 at 700-800 °C. *J. Phys. Chem. Solids* **1985**, *46*, 151–153. [CrossRef]

Development of active thermochemical barrier coatings using metal oxides

Submitted to: Chemical Engineering Journal

ISSN: 1385-8947

Impact Factor 2021: 16.744

Cite Score: 19.4

Q1 (Chemical Engineering, Environmental Chemistry)

Retirado a solicitud de su autora

Active thermochemical barrier coatings using metal oxides – first experimental results

Submitted to: Chemical Engineering Journal

ISSN: 1385-8947

Impact Factor 2021: 16.744

Cite Score: 19.4

Q1 (Chemical Engineering, Environmental Chemistry)